COMILLAS

UNIVERSIDAD PONTIFICIA

ICAI ICADE CIHS

Multi-agent control strategies for the islanded and grid-connected operation of microgrids with 100% electronic generation

Author:
Andrés Tomás Martín

Supervisors:
Prof. Dr. Aurelio García Cerrada
Prof. Dr. Lukas Sigrist

ICAI School of Engineering
Comillas Pontifical University

To Tania,
thank you for your unconditional support.

The wise man will want
to be ever with him who is
better than himself.
Plato

An empty stomach is not
a good political adviser.
Albert Einstein

Resumen

Los efectos de la actividad humana sobre el cambio climático son una de las preocupaciones más importantes en la actualidad. Para mitigar estos efectos, se deben reducir las emisiones de gases de efecto invernadero. Esto está transformando profundamente la industria hacia un aumento masivo de la electrificación y la introducción de fuentes de energía sin emisiones de carbono (o cero emisiones netas) en la matriz energética. Este cambio está impulsando el desarrollo de recursos de energía renovable y tecnologías relacionadas.

El incremento de recursos de energía renovable está transformando la estructura, planificación, modelado, análisis y control de los sistemas eléctricos. Tradicionalmente, los sistemas eléctricos convencionales han estado compuestos por grandes plantas de generación que producen la energía transportada por el sistema de transmisión hasta el lado de la demanda en el nivel del sistema de distribución. Los recursos renovables desafían naturalmente esta estructura, ya que las plantas eólicas y solares se conectan frecuentemente al nivel de distribución de los sistemas eléctricos. Además, el desarrollo de recursos renovables ha incrementado el número de regiones dentro de los sistemas eléctricos capaces de operar de forma aislada, además de estar conectadas a la red principal. Estas regiones se denominan *microrredes*.

El control de microrredes en corriente alterna (CA), inspirado en el control de los sistemas eléctricos convencionales, se realiza de forma jerárquica. La literatura suele identificar tres capas principales de control en microrredes: control primario, secundario y terciario. Los controladores internos de dispositivos (control de tensión, control de corriente, etc.) no se consideran en esta clasificación. La capa de control primario se encarga de estabilizar la tensión y la frecuencia de la microrred después de perturbaciones. Esta capa es importante para garantizar el equilibrio entre generación y demanda y la estabilidad de la microrred. Sin embargo, el control primario provoca desviaciones respecto a los valores nominales de frecuencia y tensión de los generadores tras una perturbación. El control secundario es responsable de recuperar la tensión y la frecuencia de la microrred, considerando el reparto de potencia activa y reactiva entre los generadores. En otra escala temporal, el control terciario se encarga de la operación óptima de la microrred. Ejemplos de control terciario incluyen sistemas de gestión energética, algoritmos de despacho económico y el control del intercambio de potencia con la red principal en modo conectado a red.

Este control jerárquico se realiza habitualmente de manera centralizada, en la cual un controlador central recibe mediciones de distintos agentes (por ejemplo, generadores, cargas, nudos piloto) en la microrred y toma decisiones de control usando su propio algoritmo centralizado, actualizando los puntos de consigna para los actuadores (por ejemplo, generadores). Esta es también la estructura más común en el control de sistemas eléctricos tradicionales, con muchos ejemplos en el control terciario (por ejemplo, despacho económico, programación de generación) y en el control secundario (por ejemplo, control automático de generación, control de tensión en nudos piloto). Esta estructura de control ha sido la mejor solución durante décadas y hoy en día también se utiliza en microrredes, aunque podría no ser la alternativa más adecuada para todos los escenarios.

Recientemente, se han propuesto y analizado estructuras de control jerárquico descentralizadas basadas en consenso para microrredes. Esta es una estructura multiagente en la que ya no es necesario un coordinador central. En su lugar, los agentes individuales toman decisiones de control basadas únicamente en su información local y la información compartida con un grupo reducido de agentes, llamados "vecinos". Este tipo de control parece especialmente adecuado para microrredes debido a la naturaleza distribuida de sus recursos. De hecho, las estructuras de control centralizado sufren de cuellos de botella, puntos únicos de fallo y falta de flexibilidad cuando aumenta el número de agentes.

Los recursos renovables se conectan habitualmente a redes de CA o CC mediante convertidores electrónicos con respuestas muy rápidas de tensión, frecuencia y corriente. Esto se conoce comúnmente como "generación electrónica".

El objetivo principal de esta tesis es modelar, evaluar y proponer estrategias de control descentralizado multiagente para la operación de microrredes con un 100 % de generación electrónica, tanto en modo aislado como en modo conectado a red.

A diferencia de los sistemas eléctricos convencionales con generadores lentos, en este caso, las dinámicas rápidas de las líneas pueden no ser despreciables en comparación con las dinámicas de los generadores. En este escenario, esta tesis propone un algoritmo para calcular, de forma sistemática, la relevancia de cada estado de un sistema lineal en la respuesta entrada–salida del sistema. Se explora su aplicación a un modelo linealizado de una microrred eléctrica para decidir qué dinámicas son relevantes para incluir en el análisis y/o simulación. Este algoritmo utiliza una realización balanceada no física del sistema lineal, donde se puede calcular la energía de cada variable de estado en la salida del sistema. Tanto la realización balanceada como el sistema original comparten los mismos autovalores. Se define un "coeficiente de relevancia" para cada variable de estado del sistema lineal original combinando la relevancia de los estados de la realización balanceada con los factores de participación de los modos en los estados para los autovalores de ambos sistemas. La utilidad del coeficiente de relevancia propuesto se ha validado comparando simulaciones no lineales detalladas de una microrred con simulaciones de modelos reducidos según las recomendaciones del coeficiente. Los resultados muestran que el coeficiente de relevancia proporciona recomendaciones claras y sensatas, incluso en sistemas sin una separación clara de tiempos

entre dinámicas.

Las microrredes eléctricas en CA deben funcionar, alternativamente, conectadas o desconectadas (formando una isla) de la red principal. Por tanto, la resincronización sin interrupciones es una característica importante que debe estar incorporada en los controladores de microrredes. Un controlador secundario centralizado parece la opción obvia para la resincronización, pero recientemente se han propuesto controladores secundarios descentralizados multiagente en la literatura porque simplificarían las comunicaciones necesarias. Sin embargo, varios aspectos de esta funcionalidad deben investigarse más a fondo. En esta tesis, se presenta y analiza la implementación de un control secundario multiagente que resincroniza una microrred en isla con la red principal. Se estudia en profundidad la importancia de los retardos de comunicación para la estabilidad general de la microrred, junto con los flujos instantáneos de potencia durante la resincronización. Los resultados muestran que la influencia de los retardos y el control del flujo de potencia durante los transitorios pueden gestionarse razonablemente bien mediante un diseño adecuado de los parámetros de control. Los resultados fueron validados en una microrred real compuesta por cuatro convertidores de 15 kVA, un emulador de red de 75 kVA y una infraestructura de comunicación industrial.

Aunque también se han propuesto esquemas de control distribuido para el control terciario de microrredes (problema de despacho económico), la mayoría aún necesita un controlador centralizado para coordinar la operación entre generadores distribuidos. Esta tesis también propone un control jerárquico de microrred completamente descentralizado con un despacho económico basado en consenso en su capa terciaria, desacoplado de las dinámicas del sistema eléctrico para hacerlo robusto a los retardos de comunicación. Utiliza una novedosa formulación incremental (para gestionar las desviaciones respecto a los puntos de consigna del control terciario) y considera los límites de potencia activa de los generadores. La robustez y el rendimiento del control jerárquico propuesto se compararon con el enfoque centralizado convencional y con un enfoque descentralizado previamente publicado. Su estabilidad se demuestra mediante simulación no lineal en tiempo real, análisis de estabilidad basado en Lyapunov y análisis modal.

Los fallos críticos en los sistemas eléctricos, como caídas de tensión, cortocircuitos o desconexión de unidades de generación, pueden provocar interrupciones del suministro que causan pérdida de demanda si el apagón es parcial o, en el peor de los casos, un colapso total del sistema eléctrico. El operador del sistema debe definir un plan de reposición de tensión para recuperar el servicio lo más rápido posible. Este plan es una lista de operaciones que deben ejecutarse secuencialmente para restablecer el servicio en una región específica del sistema eléctrico. Dado que el estado completo de la red puede ser desconocido, el plan puede modificar sus decisiones a medida que avanza (reposición de tensión adaptativa).

Los planes convencionales de reposición de tensión son enfoques de arriba hacia abajo, empezando desde grandes plantas en el nivel de transmisión y luego incorporando cargas y elementos generadores secuencialmente. En estos casos, la única opción para el sistema de distribución es esperar hasta que se restaure la

tensión en el nivel de transmisión.

Alternativamente, esta tesis explora un método distribuido para el arranque en negro de una microrred dentro del nivel de distribución de un sistema eléctrico. Las operaciones de red se realizan de manera centralizada por el operador del sistema de distribución, pero la generación y su control se coordinan de forma descentralizada. Se emplea un enfoque de *control activado por eventos* en la capa de control secundario descentralizado del método propuesto.

Todas las simulaciones y análisis realizados en esta tesis se implementaron usando modelos propios basados en ecuaciones diferenciales no lineales, construidos en MATLAB Simulink. El trabajo realizado en el modelado y análisis de sistemas eléctricos (en esta tesis, aplicado a microrredes) ha llevado al desarrollo de una herramienta de código abierto en MATLAB Simulink, VFlexP, que ha sido utilizada para modelar, analizar y simular todos los casos de estudio incluidos en esta tesis. A diferencia de otras herramientas, VFlexP permite una representación flexible de dispositivos y soporta la integración sencilla de nuevos modelos. Incluye un módulo para analizar la relevancia de las variables de estado con el fin de ayudar a la simplificación del modelo, y garantiza una inicialización eficiente desde el análisis de flujo de carga para evitar transitorios iniciales no deseados. Su interfaz gráfica agrupa de manera organizada los elementos similares del sistema eléctrico. Esta herramienta fue desarrollada pensando en el análisis de sistemas híbridos CA/CC. Por ahora, VFlexP está limitado a una representación d-q del sistema a estudiar.

Esta tesis presta especial atención a los efectos de los retardos temporales en las comunicaciones entre agentes en todas las estructuras de control descentralizadas multiagente propuestas o analizadas. Algunos trabajos previos ya señalaban la importancia de considerar estos retardos en el análisis de estabilidad de sistemas multiagente basados en consenso. Tras el trabajo desarrollado en esta tesis, se concluye que considerarlos y modelarlos es de crucial importancia. El coeficiente de relevancia de estado presentado es útil para analizar si un retardo de comunicación es o no despreciable. Además, puede ser útil para decidir el orden de la aproximación de Padé (una aproximación lineal) para modelar el retardo de comunicación en una aproximación lineal del sistema.

En el estudio de la sincronización de una microrred con la red principal, los retardos de comunicación, aunque pequeños, son muy importantes en el rendimiento del sistema. Este aspecto no es tan crítico para la estabilidad de pequeña señal, pero sí muy relevante para la estabilidad transitoria, ya que afecta significativamente el transitorio de potencia activa entre convertidores durante la sincronización. Estos transitorios deben estar limitados a las capacidades nominales de los convertidores. Por tanto, omitir este retardo en los estudios podría hacer inviable el proceso de sincronización. Como se mencionó antes, el coeficiente de relevancia de estado puede ser una herramienta poderosa para analizar qué dinámicas (incluyendo retardos) son relevantes en la respuesta del sistema. Considerar los retardos de comunicación en el estudio de simulación debería facilitar mucho la implementación del algoritmo. Para validar esta conclusión, el algoritmo propuesto fue implementado en un entorno real con cuatro convertidores CC/CA de 15 kVA y una infraestructura de

comunicación industrial.

En el control jerárquico completamente descentralizado presentado en esta tesis, el control terciario está diseñado de manera que su convergencia no se vea afectada por los retardos de comunicación en el sistema. No obstante, estos retardos sí se consideran en la capa de control secundario del control jerárquico descentralizado propuesto.

Las debilidades y fortalezas del control descentralizado multiagente para microrredes se comprenden mejor después del trabajo desarrollado en esta tesis. El control centralizado sigue siendo más adecuado para la mayoría de los casos en la actualidad. Sin embargo, con el crecimiento de la generación distribuida, el control centralizado puede dejar de ser práctico, principalmente debido a cuellos de botella y problemas de eficiencia. En este escenario, la investigación en la implementación de capacidades de control tradicionales sin necesidad de control centralizado resulta esencial.

Summary

The effects of human activity on climate change are some of the most important concerns nowadays. To mitigate these effects, the greenhouse gas emissions should be reduced. This is greatly transforming industry towards a massive increase of electrification and the introduction of zero-carbon (net zero) energy source in the generation mix. This is pushing the development of renewable energy resources and related technologies.

The increment of renewable energy resources is transforming the structure, planning, modelling, analysis and control of power systems. Conventional power systems have been traditionally composed of big power plants generating the energy transported by the transmission system to the demand side at the distribution system level. Renewable energy resources naturally challenge this structure, as wind and solar energy are often connected at the distribution level of power systems. Moreover, the development of renewable energy resources has increased the number of regions within power systems capable of operating as islands, apart from being connected to the main grid. These regions are called *microgrids*.

The control of AC microgrids, inspired by the conventional power system control, is done hierarchically. Literature typically identifies three main control layers in microgrids, namely, primary, secondary and tertiary control. Internal device controllers (voltage control, current control, etc.) are not considered in this classification. The primary control layer is in charge of stabilising the voltage and frequency of the microgrid after perturbations. This layer is important to guarantee the generation-demand balance and the stability of the microgrid. However, the primary control layer causes deviations from the nominal frequency and voltage values of generators after a perturbation. The secondary control layer is responsible for recovering the voltage and frequency of the microgrid, considering the active- and reactive-power sharing of the generators in the microgrid. In a different time scale, the tertiary control layer is in charge of the optimal operation of the microgrid. Examples of the tertiary control layer include energy management systems, economic dispatch algorithms and the control of the power exchange with the main grid in grid-connected mode.

This hierarchical control is usually carried out in a centralised way, in which a central controller receives measurements from different agents (e.g., generators, loads, pilot buses) in the microgrid and takes control actions using its own centralised control algorithm, updating the set points for actuators in the microgrid

(e.g., generators). This is also the most common structure for the control of traditional power system, with a lot of examples of applications in tertiary control (e.g., unit commitment, economic dispatch) and in secondary control (e.g., automatic generation control, voltage control of pilot buses). This control structure has been the best solution for decades and is nowadays used for microgrids, too although it may not be the best alternative.

Recently, decentralised consensus-based control structures have been proposed and analysed for microgrid hierarchical control. This is a multi-agent structure in which no central coordinator is longer needed. Instead, individual agents make control decisions based only on their local information and the information shared by a reduced group of agents, called "neighbours". This type of control seems especially suitable for microgrids due to the often distributed nature of their resources. In fact, centralised control structures suffer from bottlenecks, single points of failure and lack of flexibility when the number of agents increases.

Renewable energy resources are most often interfaced with AC or DC grids by means of electronic converters with very fast voltage, frequency, and current responses. This is commonly referred as "electronic generation".

The main objective of this thesis is to model, evaluate and propose decentralised multi-agent control strategies for the islanded and grid-connected operation of microgrids with 100% electronic generation.

Unlike in conventional power systems with slow generators, fast power-line dynamics may not always be negligible compared to generators' dynamics. In this scenario, this thesis proposes an algorithm to calculate the relevance of each state of a linear system in the system input–output response, systematically. It explores its application to a linearised model of an electrical microgrid to decide which dynamics are relevant to be included for analysis and/or simulation. This algorithm uses a non-physical balanced realisation of the linear system, where the energy of each state variable in the system output can be calculated. Both the balanced realisation and the original system have the same eigenvalues. A "relevance coefficient" of each one of the state variables of the original linear system has been defined by combining the relevance of the states of the balanced realisation with the mode-in-state participation factors of the eigenvalues of both systems. The usefulness of the proposed relevance coefficient was validated by comparing detailed non-linear simulations of an electrical microgrid with non-linear simulations of reduced models as informed by the relevance coefficient. Results show that the proposed relevance coefficient gives sensible and clear recommendations, even in systems without a clear time separation between system dynamics.

Electrical AC microgrids are required to work, alternatively, either connected to or disconnected from (forming an island) the main grid. Therefore, seamless re-synchronisation is a relevant feature to be built in microgrid controllers. A centralised secondary microgrid controller is the obvious choice for re-synchronisation, but recently, decentralised multi-agent secondary controllers have been proposed in the literature because they would simplify the communications required. However, several aspects of this functionality need to be investigated further. In this

thesis, the implementation of a multi-agent secondary control that re-synchronises an island microgrid with the main grid is presented and analysed. The importance of communication delays for the overall microgrid stability, together with the instantaneous power flows in the microgrid during re-synchronisation, have been studied thoroughly. Results show that the influence of the communication delays and the power flow control during transients can be tackled reasonable well by an appropriate design of the control parameters. The results of this work were validated in a real microgrid comprising four 15 kVA converters, a 75 kVA grid emulator, and an industrial communication infrastructure.

Although there have also been distributed-control proposals for microgrid tertiary control (economic dispatch problem), most of them still need a centralised controller to coordinate the operation between distributed generators. This thesis also proposes a fully decentralised hierarchical microgrid control with a consensus-based economic dispatch problem in its tertiary layer, decoupled from the dynamics of the power system to make it robust to communication delays. It uses a novel incremental (i.e., to manage the deviations from the tertiary control set points) formulation and considers the active-power limits of the generators. The robustness and performance of the proposed hierarchical control were compared with the conventional centralised approach and a previously published decentralised approach. Its stability is proved with non-linear real-time simulation, Lyapunov-based stability analysis, and modal analysis.

Critical failures in power systems, such as voltage sags, faults or disconnection of generating units, can lead to power outages which cause a loss of supply to some demand if the blackout is partial or, in the worst case, the total zero of the power system. The system operator must define a voltage restoration plan to recover the service as fast as possible. This plan is a list of the grid operations that must be done sequentially to recover the service on a specific region of the power system. Since the complete grid status may be unknown, the voltage restoration plan can change its decisions as it progresses (online voltage restoration).

Conventional voltage restoration plans are top-down approaches, starting from large power plants at the transmission system level and then adding demand and generator elements, sequentially. In such cases, the only option for the distribution system is to wait until the voltage is restored at the transmission system level.

Alternatively, this thesis explores a distributed method for the black start of a microgrid within the distribution level of a power system. The grid operations are carried out centrally by the distribution system operator, but generations and their control are coordinated in a decentralised manner. A *triggered control* approach is used in the decentralised secondary control layer of the proposed method.

All the simulations and analyses carried out in this thesis are implemented using their own models based on non-linear differential equations, constructed using MATLAB Simulink. The work done on the modelling and analysis of power systems (in this thesis, applied to microgrids) has led to the development of an open-source MATLAB Simulink tool, VFlexP, which has been used to model, analyse and simulate all the case studies included in this thesis. Unlike other tools, VFlexP

allows flexible device representation and supports easy integration of new models. It includes a module for analysing the relevance of state variables to aid model simplification and ensures efficient initialisation from power-flow analysis to avoid inconvenient initial transients. Its user-friendly interface organises similar power system elements together. This tool was developed beaing in mind the analysis of AC/DC hybrid systems. So far, VFlexP is limited to a d-q representation of the system to be studied.

This thesis gives a special attention to the effects of the communication time delays between agents in all the decentralised multi-agent control structures proposed or analysed. Some of the previous work stated the importance of considering those communication time delays for stability analysis of consensus-based multi-agent systems. After the work done in this thesis, it is concluded that considering and modelling these delays is of crucial importance. The state relevance coefficient presented is useful for analysing if a communication time delay is negligible or not. Moreover, it may be helpful to decide the order of the Padé approximation (a linear approximation) to model the communication time delay in a linear approximation of the system.

In the study of the synchronisation of a microgrid to the main grid, the communication time delays, although small, are very important in the system performance. This issue is not clear for small signal stability but it is very relevant for transient stability because it greatly affects the active-power transient between grid-forming converters during the synchronisation process. These transients must be limited to converter nominal capabilities. Therefore, omitting this time delay in the studies could make the synchronisation process unfeasible. As mention before, the state relevance coefficient can be a powerful tool to analyse which dynamics (including delays) are relevant in the system response. Considering the communication delays in the simulation study should greatly easy the implementation of the algorithm. To validate this conclusion, the proposed algorithm was implemented in a real setup with four 15 kVA DC/AC converters and an industrial communication infrastructure.

In the fully decentralised hierarchical control presented in this thesis, the tertiary control is designed in a way in which its convergence is not affected by the communication time delays in the system. Nevertheless, these time delays were still considered in the secondary control layer of the proposed decentralised hierarchical control.

The weaknesses and strengths of decentralised multi-agent control for microgrids are clearer after the work done in this thesis. A centralised control is nowadays more suitable for the majority of cases. However, with the growth of a distributed generation, centralised control may not be practical, mainly due to bottlenecks and efficiency issues. In this scenario, research on the implementation of traditional control capabilities without centralised control is essential.

Agradecimientos/Acknowledgements

En primer lugar, quiero agradecer a mis directores de tesis Aurelio García Cerrada y Lukas Sigrist por la oportunidad que me brindaron, y la confianza depositada en mí para realizar esta tesis. Gracias por su esfuerzo y dedicación en la supervisión de cada paso importante de esta investigación, y sus revisiones y consejos.

A Aurelio, por su insistencia para que me centrase durante los momentos más complicados, por dedicar tanto tiempo a tantas explicaciones y clases al inicio de esta tesis, por su rigurosidad en las correcciones de mi inglés, mi código LaTeX, mis ecuaciones, los colores de las figuras, ... (¡Cuántas cosas corregidas!). Gracias por sus consejos, en lo profesional y en lo personal, por los cafés a primera hora, a media mañana, por la tarde, ... (¡Cuántos cafés!), y por sus lecciones de electrónica de potencia mientras tomamos cervecita fría (¡pero bien fría!). No puedo imaginarme un mejor director de tesis.

A Lukas, por mostrarme que se puede disfrutar del proceso y por ingeniárselas para sacar siempre tiempo cuando lo necesitaba. Gracias por enseñarme que es posible ser experto en pequeña señal, estabilidad transitoria, despacho económico y deslastre de cargas, todo a la vez. Esa pasión ha despertado en mí interés por temas ajenos a mi investigación principal.

A Javier Roldán, por compartir conmigo sus conocimientos de control de convertidores y por sus consejos sobre la escritura académica. Gracias a él y a Njegos Jankovic por su inestimable ayuda en el montaje experimental en el laboratorio de IMDEA energía.

To Behzad Kazemtabrizi, for his warm welcome and support during my PhD stay at Durham University and for his kind introduction to optimisation problems, economic dispatch, and Lyapunov analysis.

A Luis Rouco, por su consejos sobre análisis de pequeña señal en sistemas eléctricos, y por sus charlas sobre la vida.

A los investigadores del área Modelado, Análisis y Control del IIT, por sus consejos sobre análisis de sistemas eléctricos, gracias Paco, Nacho, Álvaro, Enrique, Ana, Fidel, Javi y Juan Luis.

A Jorge Suárez Porras, por ser más que un compañero de trabajo durante estos años. Gracias por su inestimable ayuda en trabajos incluidos en esta tesis. Gracias por hacerme tan amenos los días de laboratorio.

A Carlo de Paolis, gracias por ser el mejor representante que uno pueda tener, por sus consejos y por acompañarme día a día, por enseñarme a valorar un buen

expresso y por tantas discusiones técnicas.

A Carlos David Zuluaga, por su generosidad y compromiso personal y profesional, y por tanto conocimiento compartido, por ejemplo, sobre redes neuronales. Gracias por su colaboración en el desarollo de la herramienta de simulación utilizada en esta tesis.

A Régulo Enrique Ávila, por sus discusiones sobre convertidores *grid-forming* y por sus consejos sobre estabilidad transitoria y LaTeX.

A Mohammad Rajabdorri, por sus consejos sobre despacho económico, publicaciones y planificación de la tesis. Gracias también por organizar los partidillos de fútbol en los que mostrar mi calidad.

A Javier García Aguilar, por su compañerismo durante los primeros años de mi tesis. Su trabajo inspiró la idea inicial para el desarollo de la herramienta de simulación utilizada en esta tesis. Gracias también por sus consejos sobre LaTeX.

A Nacho de Rodrigo, por sus consejos sobre inteligencia artificial, LLMs y GitHub. Gracias también por todos los momentos que me has hecho pasar durante el desarrollo de la tesis.

Gracias a Álvaro, Hadi, Miad, y al resto de los investigadores en formación del área Modelado, Análisis y Control del IIT, por las charlas, comidas y cafés en Ricci, y después en Rey Francisco. Habéis hecho este trabajo mucho más ameno.

Gracias a a Diana, Dion, Marco, Milan y el resto la unidad de Sistemas Eléctricos del grupo IMDEA energía, por acogerme como a uno más el tiempo que estuve allí.

Gracias a Isa, Belén, Cristina, Marisa, Ajda, Paula y Aurora por su amabilidad y ayuda en las gestiones administrativas durante la tesis.

Gracias a Manuel y Jose, de ICAI, y a Álex y Josemi, de IMDEA, por su ayuda y consejos sobre implementaciones en laboratorio.

A Tania, el amor de mi vida, por todo lo que haces y por ser como eres. Gracias por darme un buen motivo para sonreír al volver a casa sin importar como fuera el día.

A mi madre, por su sacrificio para permitirme llegar hasta aquí.

A mi padre, por sus consejos en cada decisión.

A mi familia, por tantos momentos de felicidad en los que el estrés de la investigación se desvanecía.

A mi familia política, por hacerme sentir partícipe de sus tradiciones.

Quiero agradecer a la Comunidad de Madrid, al Ministerio de Ciencia e Innovación del Gobierno de España y a la Universidad Pontificia Comillas, por la financiación de los siguientes proyectos y ayudas que han hecho posible la realización de esta tesis doctoral:

- El programa de investigación S2018/EMT-4366 PROMINT-CAM sobre microrredes inteligentes de la Comunidad de Madrid, España, con un apoyo del 50 % del Fondo Social Europeo.

- El proyecto MIG-20201002, "FLEXENER, Nuevo sistema energético 100 % renovable, flexible y robusto para la integración de nuevas tecnologías en generación, redes y demanda. Estudios técnicos de redes" financiada por el

Centro para el Desarrollo Tecnológico Industrial (CDTI) y respaldada por el Ministerio de Ciencia e Innovación.

- El proyecto TED2021-130610B-C22, "Mejora de las herramientas para el análisis de sistemas eléctricos híbridos CC/CA con penetración masiva de fuentes renovables y casos de estudio", del Ministerio de Ciencia e Innovación.

- La colaboración con el Prof. Dr. Behzad Kazemtabrizi de la Universidad de Durham mediante una estancia de de investigación de 3 meses ha sido posible gracias a una beca de la Universidad Pontificia Comillas, destinada a estancias de movilidad de profesores e investigadores en centros de investigación extranjeros.

In the preparation of this manuscript, generative AI tools such as *ChatGPT* (OpenAI, 2024) and *Grammarly* (Grammarly, 2024) were instrumental in improving the writing and coding processes. ChatGPT was used for rephrasing and revising sections and for assisting in refining the language, structure, and vocabulary to ensure clarity and coherence. Grammarly further supported this process by providing grammar and syntax checks, improving the overall readability and correctness of the text.

Additionally, ChatGPT and GitHub Copilot (GitHub & OpenAI, 2024) were employed to expedite coding tasks in MATLAB and LaTeX, offering insights into algorithm optimisation and debugging, which accelerated technical aspects of the research. The use of these tools contributed to a more efficient workflow.

Contents

List of Figures xxi

List of Tables xxvii

Acronyms xxix

1 Introduction 1
- 1.1 Control of microgrids . . . 1
  - 1.1.1 Context of microgrids . . . 1
  - 1.1.2 Hierarchical control of microgrids . . . 2
- 1.2 Decentralised control of microgrids . . . 5
- 1.3 Objectives of the thesis . . . 7
  - 1.3.1 Main objective . . . 7
  - 1.3.2 Specific objectives . . . 8
- 1.4 Outline of the thesis . . . 9

2 Multi-agent secondary control of microgrids. Preliminaries and fundamentals 11
- 2.1 Introduction . . . 11
- 2.2 The importance of simulation in microgrid studies and the main assumptions adopted . . . 11
- 2.3 Modelling of microgrids. Fundamentals and tools . . . 14
  - 2.3.1 Working in a d-q reference frame . . . 14
  - 2.3.2 Basic element modelling and per unit values . . . 17
  - 2.3.3 Modelling with several different reference frames . . . 20
- 2.4 Inner controls of grid-forming and grid-following converters . . . 21
- 2.5 Primary control of GFr-VSCs . . . 24
  - 2.5.1 Selection of a droop control method . . . 25
  - 2.5.2 Virtual impedance loop . . . 27
- 2.6 Decentralised consensus-based multi-agent control. . . . 30
- 2.7 Multi-agent secondary control of microgrids . . . 33
  - 2.7.1 Secondary control . . . 33
  - 2.7.2 Influence of communication delays in the stability of the consensus algorithm . . . 39

2.7.3 Event-triggered multi-agent secondary control 43
2.8 Decentralised incremental secondary control 48
2.8.1 Proof of convergence of the proposed secondary control using a Lyapunov function 49
2.8.2 Cost-based secondary control 50
2.8.3 Case study: Hybrid DC/AC microgrid 51

3 State relevance of linear models of microgrids 59
3.1 Introduction 59
3.2 Modal analysis of the system 61
3.2.1 Eigenvalues and eigenvectors of a matrix 62
3.2.2 Eigenvalue sensitivities 62
3.2.3 Participations of a mode in a state 62
3.3 The proposed method: State relevance calculation 63
3.3.1 Balanced state-space realisation of a linear system 64
3.3.2 Eigenvalue-relevance analysis 64
3.3.3 State relevance 65
3.4 Case study 1: Small microgrid 66
3.4.1 Description of the case study 66
3.4.2 Illustration of the RC 67
3.4.3 Applying the state RC to MOR 69
3.4.4 Impact of control time-scale separation 74
3.5 Case study 2: a larger microgrid 75
3.5.1 Analysis of the importance of the communication graph . . . 79
3.5.2 Analysis of the selection of the input and output variables . . 80
3.6 Applying state relevance on the IEEE 69 bus test system case study . 84
3.6.1 Performance of the algorithm in a case with clear time-scale separation between control layers. 84
3.6.2 Performance of the algorithm in a system close to its stability limit 84
3.7 Conclusions 88

4 Application of consensus among agents for reconnecting a microgrid of grid-forming converters to the main grid 89
4.1 Introduction 89
4.2 Application overview 92
4.2.1 System description 92
4.2.2 Droop control and consensus final value 93
4.2.3 Steady-state operation 95
4.2.4 Synchronisation with the main grid 95
4.2.5 Tracking of power set points 96
4.3 Synchronisation controller design 96
4.3.1 Dynamic equivalent of the consensus algorithm 96
4.3.2 Modelling and effect of communication delays 97

4.3.3 Power exchanged between two DGs . . . 98
4.3.4 A complete model of the synchronisation process . . . 99
4.3.5 PI controller design . . . 100
4.4 Active-power flow characterisation during transients and its control . 102
4.4.1 Characterising the active-power flow between DGs . . . 102
4.4.2 Reduction of the transient active-power peak . . . 103
4.5 Further details of the case study and analysis . . . 103
4.5.1 MG description and parameters . . . 103
4.5.2 Effect of the derivative droop term . . . 104
4.5.3 Numerical simulation to validate the secondary controller . . 106
4.6 Experimental validation . . . 108
4.6.1 Laboratory description . . . 108
4.6.2 Experimental results . . . 111
4.7 A large case study: IEEE 69 bus test system . . . 113
4.8 Summary and conclusion . . . 116

5 Multi-agent optimal energy management in microgrids 119
5.1 Introduction . . . 119
5.2 Economic dispatch formulation . . . 121
5.2.1 Centralised economic dispatch problem . . . 121
5.2.2 The economic dispatch as a consensus problem . . . 122
5.3 Case study and results . . . 126
5.3.1 Convergence of the proposed decentralised economic dispatch algorithm under communication delays . . . 126
5.3.2 Case study for the implementation of the proposed fully-decentralised hierarchical control: Hybrid AC/DC microgrid 130
5.3.3 Real-time validation of the proposed fully decentralised hierarchical control . . . 133
5.4 Large case study: IEEE 69 bus test system . . . 135
5.5 Conclusion and future work . . . 135

6 Multi-agent-based black start of a microgrid 139
6.1 Introduction . . . 139
6.1.1 Technical considerations during the black start . . . 140
6.1.2 Specific problems in distribution networks . . . 141
6.2 Distributed vs centralised service restoration in power systems . . . 142
6.2.1 Dynamic analysis of the restoration process . . . 144
6.2.2 Examples of actual service restoration plans . . . 145
6.3 Exploring a distributed restoration procedure . . . 145
6.3.1 Synchronisation of grid-forming converters with the main grid 150
6.4 Case study: Black start of the IEEE 69 bus test system . . . 153
6.5 Summary and Conclusions . . . 158

7 Conclusions, contributions, publications and future work 161
7.1 Conclusions: Decentralised vs centralised control of microgrids . . . 161
7.2 Contributions: Towards an electronically-fed electric microgrid . . . 162
7.2.1 State relevance in electronically-fed microgrids . . . 162
7.2.2 VFlexP . . . 163
7.2.3 Decentralised control of microgrids . . . 163
7.3 Future work . . . 165
7.4 Publications . . . 166
7.4.1 Articles published in journals . . . 166
7.4.2 Articles presented in conferences . . . 167
7.4.3 Papers under review . . . 168

Bibliography 169

A A Vector-Based Flexible-Complexity Power System Tool for Simulation, Static and Modal Analysis of Hybrid AC/DC Power Systems 187
A.1 Introduction . . . 187
A.2 Vector-based modelling of hybrid power systems with flexible complexity . . . 191
A.2.1 Scalable and Vectorisable Modelling of power systems . . . 191
A.2.2 Flexible-complexity models for power systems . . . 192
A.3 Simulation of hybrid power systems and SSA in VFlexP . . . 193
A.3.1 Powerflow and Initialisation . . . 195
A.3.2 Linearisation . . . 196
A.3.3 Small signal analysis . . . 196
A.3.4 Simulation of non-linear and linear models . . . 196
A.4 Case studies using VFlexP . . . 197
A.4.1 Case study: small power systems . . . 197
A.4.2 Case study: Large hybrid AC/DC power system . . . 203
A.5 Conclusion . . . 211
A.6 Test System Parameters . . . 213
A.7 Electronic converter modelling . . . 213

B Elimination of dynamics for model order reduction 217
B.1 Reducing the number of states in linear models . . . 217
B.2 Reducing the number of states in the nonlinear models used . . . 218

C IEEE 69 bus test system 221

List of Figures

1.1 AC microgrid hierarchical control. Adapted from Bidram, Nasirian, Davoudi, and Lewis, 2017. . . . 2
1.2 Structure of a conventional power system. . . . 5
1.3 Structure of a modern power system. Generation is connected at both transmission and distribution levels. . . . 6
1.4 Comparison of the features of centralised and decentralised control structures. . . . 7

2.1 An example of microgrid composed of grid-forming voltage source converters and loads. The typical system studied in this thesis. . . . 13
2.2 $\alpha - \beta$ reference frame . . . 14
2.3 $d - q$ reference frame . . . 16
2.4 A 3-phase inductor. . . . 17
2.5 Multiple $d - q$ reference frames . . . 21
2.6 Grid-following voltage source converter control structure. Adapted from Bidram, Nasirian, Davoudi, and Lewis (2017). . . . 22
2.7 Block diagram of the phase-locked-loop. . . . 22
2.8 Grid-following voltage source power controller structure. . . . 22
2.9 Grid-following voltage source converter control structure. The abc/dq block is the so-called Park Transform. Adapted from Bidram et al. (2017). . . . 23
2.10 Diagram of a GFr-VSC. . . . 23
2.11 Voltage and current controllers of a GFr-VSC (i). . . . 24
2.12 Power controller of a GFr-VSC . . . 25
2.13 Two GFr-VSCs connected through a transmission line . . . 25
2.14 Block diagram of the output virtual impedance loop . . . 28
2.15 Virtual impedance with low-pass filter . . . 29
2.16 Transient virtual resistor block diagram . . . 30
2.17 Diagram of the ω-P secondary control of a grid-forming converter. . . . 35
2.18 Diagram of the v-Q secondary control of a grid-forming converter. . . . 36
2.19 Frequency, voltage, active and reactive power of all GFr converters in the modified IEEE 69-bus test system during the simulation in the case of seeking reactive-power-sharing consensus ($B = 1;\ \beta = 0$). . . . 38

2.20 Frequency, voltage, active and reactive power of all GFr converters in the modified IEEE 69-bus test system during the simulation in the case of seeking voltage consensus ($B = 0;\ \beta = 1$). 40
2.21 Frequency, voltage, active and reactive power of all GFr converters in the modified IEEE 69-bus test system during the simulation in the case of seeking both voltage and reactive-power-sharing consensus ($B = 1;\ \beta = 1$). 41
2.22 Movement of the eigenvalues of the linear approximation of the modified IEEE 69-bus test system when increasing the communication time delay between GFr-VSCs. 43
2.23 Frequency, voltage, active and reactive power of all GFr-VSCs, and total number of messages sent in the modified IEEE 69-bus test system during the simulation with a threshold function with $A^v_{sec} = A^f_{sec} = A^P_{sec} = A^Q_{sec} = 10^2$ for the triggered secondary control. 45
2.24 Frequency, voltage, active and reactive power of all GFr-VSC, and total number of messages sent in the modified IEEE 69-bus test system during the simulation with a threshold function with $A^v_{sec} = A^f_{sec} = A^P_{sec} = A^Q_{sec} = 10^3$ for the triggered secondary control. 46
2.25 Frequency, voltage, active and reactive power of all GFr-VSC, and total number of messages sent in the modified IEEE 69-bus test system during the simulation with a threshold function with $A^v_{sec} = A^f_{sec} = A^P_{sec} = A^Q_{sec} = 10^4$ for the triggered secondary control. 47
2.26 6 bus system with a point-to-point VSC-based DC link between buses 2 and 5. 51
2.27 Variation of the root loci of the system in relation to the constant communication delay between agents, varied from 50 to 200 ms. . . 53
2.28 Active power response of DGs 1-4 to a 5.85% reduction in both loads for the three cases studied with lost communication links. 55
2.29 Active power response of DGs 1-4 to the outage of DG4 when there are communication links lost 56
2.30 Cost increment from the optimal one with different levels of active-power demand. Blue line: secondary control seeks an equal power share. Red line: secondary control seeks a cost-based share. 57

3.1 Diagram of a GFr-VSC. 66
3.2 A case study with two GFr-VSCs and two loads 67
3.3 Relevance of the most relevant delay-related states 69
3.4 Illustrating the participation factors of the eigenvalues in the states of the system. 71
3.5 Accumulated relevance of the states of the original system. Case study 1 with no clear time-scale separation. States are ordered from most relevant to least relevant. 73
3.6 Response of DG2 in case study 1 to a 50% reduction in the impedance of Load 1 (but constant X/R ratio). 74

3.7 Accumulated relevance of the states of the original system. Case study 1 with a clear time-scale separation between control layers. . . 75
3.8 Response of DG2 in case study 1 to a 50% reduction in the impedance of Load 1 but constant X/R ratio with a clear time-scale separation between control layers. 77
3.9 Simplified diagram of the microgrid with ten GFr-VSCs (case study 2). A dashed line shows the communication graph, including the direction of the information flow. 78
3.10 Accumulated relevance of the states of the original system. Microgrid with ten GFr-VSCs (case study 2). 78
3.11 Response of electrical variables of DG10 in the microgrid with ten GFr-VSCs (case study 2) to a 50% reduction of Load 1 impedance while maintaining its X/R ratio. 79
3.12 Evolution of the state RC of the most relevant state of each line when changing the X/R ratio of line 3 while keeping its impedance modulus constant. 80
3.13 Evolution of the state RC of the most relevant state of each line when changing the X/R ratio of line 3 while keeping its impedance modulus constant. Graph from DG10 (leader) to DG1. 82
3.14 Response of the frequency of the COI of the complete and reduced models in case study 2 (10 GFr-VSCs) to a 5% increment in the frequency set point of DG1 (leader). 83
3.15 Bode diagram of the system using the increment in the frequency set point of DG1 (leader) as input and the frequency of the COI as output. 83
3.16 Normalised state relevance of the base case study. 86
3.17 Comparison of the time response of the complete and reduced models of the microgrid to a load change. 86
3.18 Normalised state relevance of the study case with abnormal time-scale separation. 87
3.19 Comparison of the time response of the complete and reduced models of the microgrid to a load change. 87

4.1 Electrical and control system diagram of the microgrid (MG) studied in this work. Four distributed generators (DGs) with a decentralised secondary controller. 93
4.2 Primary and secondary controller of a distributed generator (DG). In (a), for any DG except the leader (k). In (b), for the leader ($k = 1$ in this work). 94
4.3 Evolution of the state relevance of the low-pass filter (LPF) state variables in (4.15), while changing the integral gain. 97
4.4 Block diagram representing the dynamic model of the agent-based secondary controller applied in this work. 99
4.5 Fundamental study of the powerflow between two DGs. 101

4.6 (blue) Active power peak needed for synchronisation and (black) synchronisation time, for different values of m_D. (dashed) Simplified and (solid) detailed microgrid (MG) model. 105
4.7 Angle versus modulus of the MG eigenvalues, for different values of m_D (see the text for explanations). 106
4.8 Simulation results of (blue) the proposed method and (red) the method based on saturation. From top to bottom, active power, reactive power and frequency of $DG1$, and θ_{diff}. The events are explained in the text. 107
4.9 Pictures of the elements of the laboratory. (a) Line impedances, (b) AC busbars, (c) DC busbars, (d) 75 kVA voltage-source converters (VSCs), (e) 15 kVA VSCs, (f) real-time computers, (g) communication network switch, (h) single-board RIO and (i) two compactRIO. . . . 109
4.10 Interconnection of the hardware elements in the laboratory. (Green) Power converters, (yellow) auxiliary power converter, (blue) network impedances, (red) AC busbars, (orange) DC busbars and (purple) resistive load. 110
4.11 Communication infrastructure of the laboratory facilities. 111
4.12 Histogram of the experimental measures of the communication delay between $DG1$ and $DG2$ in the laboratory. 112
4.13 Experimental results. Resynchronisation and grid-connected control modes. From top to bottom, active power (P_i), frequency (f_i) and angle difference (θ_{diff}). 113
4.14 Comparison of the switched model, the averaged model and the experimental results. From top to bottom, active power (P_1), frequency (f_1) and angle difference (θ_{diff}). 114
4.15 Single-line diagram of the modified version of the IEEE 69 bus test system. 115
4.16 Simulation results of the synchronisation of the IEEE 69 bus test system to an infinite grid with the control proposed in this Chapter. 117

5.1 Overview of the proposed decentralised hierarchical control for a microgrid, implemented for each generator of the microgrid 121
5.2 6 bus system with a point-to-point VSC-based DC link between buses 2 and 5. 127
5.3 Communication graph used for the decentralised economic dispatch algorithm 127
5.4 Comparison of the evolution of the global operation cost and the power balance obtained using the different approaches for Case I. . . 128
5.5 Same comparison of Figure 5.4 but for Case II. 129
5.6 Same comparison of Figure 5.4 but for Case III. 129
5.7 Evolution of the virtual cost and power set point of each agent during the consensus process for the communication delay on case I. 131
5.8 Study with demand variation 132

5.9 Diagram of the process for the real-time simulation of the proposed hierarchical control in the OPAL-RT OP4510 simulator. 133
5.10 Results of the real-time validation of the proposed decentralised hierarchical control. 134
5.11 Communication graph used for the 69 bus case study. 135
5.12 Study with demand variation in the large system. 136

6.1 Flow chart of the proposed distributed algorithm for the optimal restoration of a microgrid. "Grid action" means closing a controllable switch. 147
6.2 Diagram of the modified IEEE 69 bus test system used as the case study. "GFr" stands for grid-forming converter. 154
6.3 Graph of available communication between DGs for the study of the black-start of a microgrid. 155
6.4 Frequency, active power, voltage and reactive power of all DGs in the microgrid. 156
6.5 Sequence of the messages between DGs in the microgrid. 157
6.6 Final communication graph among all the DGs in the microgrid after the restoration process has finished. 158
6.7 Number of secondary control messages sent by each DG during the restoration procedure 159
6.8 Percentages of the messages sent by each DG during the restoration procedure 160

A.1 Loads, selectors and assignments. Array dimensions are indicated in square brackets. 193
A.2 Summary of elements included in VFlexP. 195
A.3 Single-line diagram of a synchronous generator feeding a load 198
A.4 (a) Bus-1 voltage, (b) Speed of the SG in pu, (c) Active power of the SG, (d) Reactive power of the SG, (e) eigenvalues of the system and (f) Comparison of the frequency response of non-linear and linearised system shown in Figure A.3. 199
A.5 Single-line diagram of a synchronous generator feeding a load through a transmission line. 200
A.6 (a) Bus-1 voltage, (b) Speed of the SG in pu, (c) Active power of the SG, (d) Reactive power of the SG, (e) eigenvalues of the system and (f) Comparison of the system (Figure A.5) frequency with non-linear and linearised models. 201
A.7 Single-line diagram of the 4-bus hybrid AC-DC system 202
A.8 (a) Bus-1 voltage, (b) Speed of the synchronous generator in pu, (c) Active power, (d) Reactive power and (e) Frequency in the non-linear and linearised simulations of the system in Figure A.7. 204
A.9 Graph representing the grid used for the case study. Buses highlighted in red include generation. 205

A.10 Screenshot of the Simulink workspace for the hybrid system implemented in VFlexP. . . . 206
A.11 State relevance of the linearised system, grouped by element. The state relevance is normalised to sum one and shown in a logarithmic scale for clarity. . . . 207
A.12 Evolution of the state relevance of the voltage and current controllers for all converters of the system under study when varying the voltage controller of converter DG1. . . . 208
A.13 Response of the frequency of DG1 to a load change. Comparison between the complete model and different reduced-order non-linear models. . . . 210
A.14 Response of the frequency measured by the PLL of the grid-following converter to an increment of the active power injected by the grid-following converter. . . . 212

B.1 Relevant and less relevant dynamics . . . 217

C.1 One-phase diagram of the modified IEEE 69 bus test system used as the case study. . . . 222
C.2 Model of a grid-forming converter . . . 223
C.3 Communication graph used for the modified IEEE 69 bus test system used as the case study. . . . 224

List of Tables

1.1 Limitations and gaps of decentralised control solutions for microgrids applied to several topics. Column "**Decent.**" includes the existing level of development of decentralised solutions in that specific topic. 8

2.1 Droop method selection. 27
2.2 Different approaches to model time delay. 39
2.3 Cost coefficients and power range for every agent in Figure 5.2. . . . 52
2.4 Eigenvalues of the Laplacian matrix for each communication-graph case of the communication-link loss study. 54
2.5 Parameters used for the simulation of the microgrid in Figure 2.26. . 57

3.1 Parameters used for the simulation of the microgrid. 68
3.2 Operating point of the microgrid of case 1. $i \in [1-2]$. 68
3.3 State relevance for case study 1 (2 GFrs) with no clear time-scale separation. 72
3.4 State relevance for case study 1 (2 GFrs) with clear time-scale separation. 76
3.5 Operating point of the microgrid of case 2. $i \in [1-10]$. 77
3.6 State relevance analysis for different output choices. 81
3.7 Nomenclature used for the group of states 85

4.1 Comparison of existing approaches for synchronising MGs. 92
4.2 Parameters used in the simulation study in Section 4.4. 102
4.3 MG hardware and control parameters. 104

5.1 Cost coefficients and power range for every agent in Figure 5.2. . . . 128
5.2 Communication delay implemented for each test case. 128
5.3 Comparison of the performance of different energy distpach algorithms under different communication delays 130

6.1 Black start of distribution systems in the literature, specifying the software used for the modelling. 141

6.2 Comparison of existing reviews for restoration methods. D: distributed, C: centralised, DS: distribution system, TS: transmission system. . . . 143
6.3 Connection times . . . 155

A.1 Overview of simulation and analysis tools for hybrid AC/DC power systems. . . . 189
A.2 Summary of elements included in VFlexP. . . . 194
A.3 Eigenvalues for the system shown in Figure A.3. . . . 200
A.4 Eigenvalues for the system shown in Figure A.5. . . . 202
A.5 Computation time when Simplus and VFlexP simulate the systems shown in Figures A.3, A.5 and A.7. . . . 203
A.6 Parameters for the system shown in Figure A.3. . . . 213
A.7 Parameters for the system depicted in Figure A.7. . . . 214
A.8 Parameters used for the simulation of the large hybrid power system. 215

C.1 Parameters used for the simulation of the modified IEEE 69 bus test system. . . . 224
C.2 IEEE 69-bus system data. . . . 225

Acronyms

AGC	automatic generation control	34
BESS	battery energy storage system	166
BS	black-start	140
COI	centre of inertia	80
CSC	current-source converter	21
DG	distributed generator	165
DSO	distribution system operator	165
FACTS	flexible alternating current transmission system	59
FUBM	flexible universal branch model	9
GA	genetic algorithm	143
GFl	grid-following converter	21
GFl-VSC	grid-following voltage-source converter	142
GFr	grid-forming converter	221
GFr-VSC	grid-forming voltage-source converter	221
HSV	Hankel singular value	60
HVDC	high-voltage direct-current	59
LPF	low-pass filter	90
MAS	multi-agent system	30
MG	microgrid	164
MILP	mixed integer linear programming	143
MOR	model order reduction	61
OPF	optimal power flow	39
PCC	point of common coupling	145
PI	proportional+integral	90
PLL	phase locked loop	60
RC	relevance coefficient	60

RER renewable energy resource 139
RMS root mean square 18
SCR short circuit ratio 60
TSO transmission system operator 145
TVR transient virtual resistor 29
VPP virtual power plant 121
VSC voltage-source converter 92
VSM virtual synchronous machine 4

This chapter introduces the thesis topic, its context, motivation and objectives, summarises its contributions, and describes the outline of this document.

1 Introduction

1.1 Control of microgrids

1.1.1 Context of microgrids

Mitigating climate change is one of the most important challenges in the history of the energy sector, responsible for almost three-quarters of the greenhouse gas emissions (International Energy Agency, 2021). Fighting climate change is calling for a fast decarbonisation of the world economy, and this will require the electrification of industry activities still using fossil fuels, cleaning or eliminating current fuel-consuming means of production of electricity and a massive integration of renewable energy resources (RERs).

The implementation of these strategies is transforming existing electrical power systems and the way these systems are planned all around the world at an unprecedented pace.

The traditional structure was characterized by fully-dispatchable large power plants connected to transmission grids with unidirectional power flow from those plants to loads through distribution grids. In contrast, modern power systems are evolving towards a more flexible scenario where not fully-dispatchable power plants are also connected to transmission grids and small power plants are connected to distribution grids. Consequently, uncertainty is becoming a prominent factor, distribution grids must now admit bidirectional power flows since they also host electricity generation. Moreover, islanded operation can improve the resiliency of regions of the power system. This is driving the development of microgrids.

The *Conseil International des Grandes Réseaux Électriques* (CIGRÉ) Working Group C6.22 defined the microgrid concept in one sentence in Marnay et al. (2015):

> Microgrids are electricity distribution systems containing loads and distributed energy resources (such as distributed generators, storage devices, or controllable loads) that can be operated in a controlled,

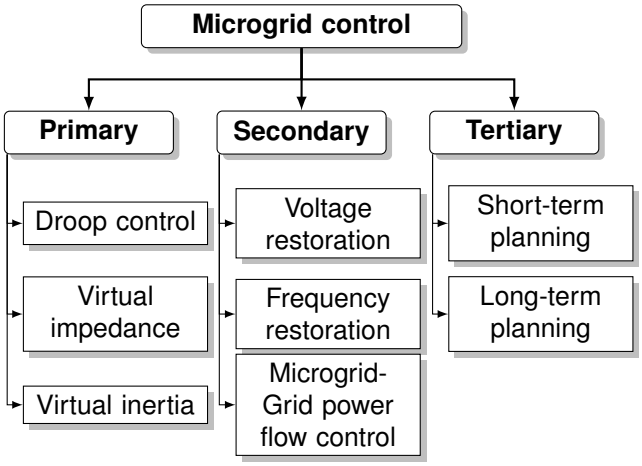

Figure 1.1: AC microgrid hierarchical control. Adapted from Bidram, Nasirian, Davoudi, and Lewis, 2017.

coordinated way either while connected to the main power network or while islanded.

Since most distributed generation involves renewable energy resources, microgrids are bound to have a large contribution of electronic converters, allowing fast and flexible control systems. Like in the control of conventional electric power systems, the match between generation and load must always be guaranteed, but the distributed nature, variability and uncertainty of renewable generation resources complicate this matching.

1.1.2 Hierarchical control of microgrids

However, in spite of their differences with traditional power systems, microgrids have inherited the traditional hierarchical control structure of those systems, although with some possible additions. Microgrid control consists of three layers, namely, primary, secondary and tertiary, as described in Bidram and Davoudi (2012). Figure 1.1 gives an idea of the elements involved in these three control layers.

Renewable energy resources are commonly connected to the power systems by electronic DC/AC converters. These converters are, in general, voltage-source converters (VSCs), which means that the output voltage of the converter is imposed by the converter itself, thanks to a stable voltage at the DC side[1]. In general, the DC/AC transformation is done using ON/OFF-controllable solid-state fast switches which

[1] called voltage sourced converters by Yazdani and Iravani (2010)

are used to generate a flexible variable-frequency, variable-voltage source in response to the control system of the converter. There are several techniques to obtain the ON and OFF signals for the switches (e.g., pulse-width modulation, sliding mode control, etc.) and a filter is usually connected to the output of the converter to reduce the harmonic content of the output voltage. Harmonics and unbalance effects are technical challenges in the design and control of electronic converters, but are out of the scope of this thesis. Moreover, converter switching will be ignored, and an average-switching model will always be used. Chapter 4 includes a comparison between an average-switching model and a model considering switching for the results on the resynchronisation of a microgrid with the main grid, and it is shown that for the timescales studied in this thesis, both models give similar results. In general, all high-frequency harmonics are neglected, considering the effect of the converters' filters. In the case of large unbalances in the microgrid, it must be considered in the design of the converter's inner controllers with techniques described in Yagüe Yagüe (2024), but the proposed algorithms can still be applied.

Broadly speaking, VSCs are controlled either as grid-forming voltage-source converters (GFr-VSCs) (Avila-Martinez et al., 2022) or as grid-following voltage-source converters (GFl-VSCs) (Singhal, Vu, & Du, 2021).

GFr-VSCs impose the AC voltage and frequency at their point of connection, while GFl-VSCs measure the voltage (magnitude and angle) at their point of connection (e.g., using a phase locked loop (PLL)) and orientate the injected current with respect to that voltage to meet a required active and reactive power injection. The fast current and/or voltage control in VSCs are not normally included within the hierarchical control of microgrids, and it is often referred to as level-0 control of electronic power converters. Recent studies have proposed adding a virtual impedance loop (J. He & Li, 2011) to GFr-VSCs (Wang, Li, Blaabjerg, & Loh, 2015). Since it is normally included above the voltage and current controller, in this thesis, the virtual impedance loop is included in the primary control layer. The virtual impedance loop emulates the voltage drop in the output impedance due to the output current, but without electrical losses. It can be used to enhance the stability of the system when connecting a grid-forming converter to a strong grid, but it can also be used for other purposes. For example, Paquette and Divan (2015) propose to use the virtual impedance loop to limit the output current of the converter; Avila-Martinez et al. (2022) use the virtual impedance only during transients to enhance transient stability; and T. Liu, Liu, Liu, and Liu (2016) propose to use the virtual impedance to damp the resonance of the output *LCL* filter of the converter.

Excluding level 0 of control, primary control is the first and fastest control layer of a microgrid. The main objective of the primary control is to stabilise the voltage and frequency across the microgrid after any change in the generation-load balance (e.g., an islanding event or a change in generated or demanded power).

In conventional power systems, the primary control includes speed governors and voltage regulators of synchronous generators. Kundur, Balu, and Lauby (1994) explain the most common structures for primary control of synchronous gener-

ators. When the active-power demand increases (decreases), a synchronous machine slows down (accelerates) due to the imbalance between the electrical and mechanical torque applied. This situation continues until the balance is recovered, normally because the speed governor modifies the mechanical torque applied to the synchronous machine.

Similarly, a GFr-VSC reduces its output frequency when its active-power demand increases and increases its output frequency when its active-power demand decreases, thus mimicking the behaviour described by a synchronous generator. A similar strategy is used with voltage and reactive power (i.e., the converter reduces its output voltage when the reactive-power demand rises and increases its output voltage when reactive power demand decreases). These control loops are inherently stable in systems with inductive transmission lines since the active-power flow depends mainly on the angle difference between the two ends (related to the frequency), and the reactive-power flow depends mainly on the voltage amplitude difference. This type of primary control of GFr-VSCs is commonly called virtual synchronous machine (VSM) or droop control, depending on its specific structure.

GFl-VSCs can also provide support when any active- or reactive-power disturbance takes place within a microgrid by injecting more (less) active power if their measured frequency is below (above) its nominal value; and more (less) reactive power if the voltage is below (above) its nominal value. Converters with this operation mode are also called grid-supporting voltage source converters.

As a result of disturbances, frequency and voltage move from their nominal values even after the primary control reaction. This is permissible during transients, but the frequency and voltage must be forced to return to their nominal values during normal operation. The layer in charge of recovering the frequency and voltage to their nominal values is the secondary control.

In conventional power systems, the secondary control layer is implemented in a centralised manner. It takes care of the generation-demand balance in a zone of the grid, and the exchanged active power between zones after a disturbance. Egido, Fernandez-Bernal, and Rouco (2009) explain the structure of the automatic generation control (AGC) of the Spanish system, where the active power set points of the generators in each zone are adjusted by a central zone coordinator. Since frequency deviations are produced by an imbalance between the active power set points of the units and the demand in a zone, adjusting the active power set points recovers the nominal value of the frequency.

The tertiary control layer is in charge of the optimal operation of the grid, optimising the active-power sharing of units to minimise global costs (i.e., economic dispatch) and the unit commitment of units (e.g., day-ahead problem). Although it can handle some considerations about the dynamics of the units in the system, like ramp constraints or frequency constraints, the tertiary control layer usually ignores the dynamics of the system. It is a discrete problem run periodically to ensure the optimal operation of the system. Traditionally, the tertiary control layer runs centralised, which allows a conventional implementation of the optimisation problem. In grid-connected mode, the power injection to the main grid can be

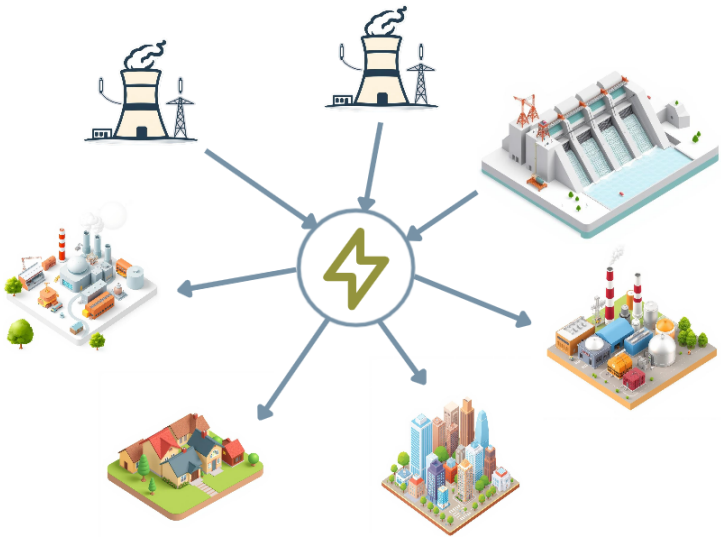

Figure 1.2: Structure of a conventional power system.

considered in the dispatch of the main grid, considering the microgrid as a whole. When a group of RERs is grouped as one power plant for planning purposes, it is called virtual power plant (VPP), as described by Naval and Yusta (2021).

1.2 Decentralised control of microgrids

In conventional power systems, a relatively small number of large generators were connected at the transmission level, a large number of loads were connected at the distribution level, and there was always a unidirectional power flow: from generation to consumption. In general, conventional power systems were composed of a single entity controlling generation, transmission and distribution. This arrangement naturally suggested a centralised generation dispatch, and centralised algorithms for frequency and voltage secondary control, as illustrated in Figure 1.2.

With the development of RERs, microgrids are gaining weight in power systems. Moreover, generation at the distribution level is increasing, and the number of units to be coordinated, even from different entities, is increasing rapidly. In this scenario, the conventional centralised structure for the control of the power system may not be the most adequate for all cases. Instead, a decentralised structure, like the one shown in Figure 1.3, may be adequate.

This thesis uses the definition of centralised and decentralised control of Hatziargyriou (2014) and the definition of distributed control of Cruz Victorio, Kazemtabrizi, and Shahbazi (2022), in the context of secondary and tertiary control of microgrids:

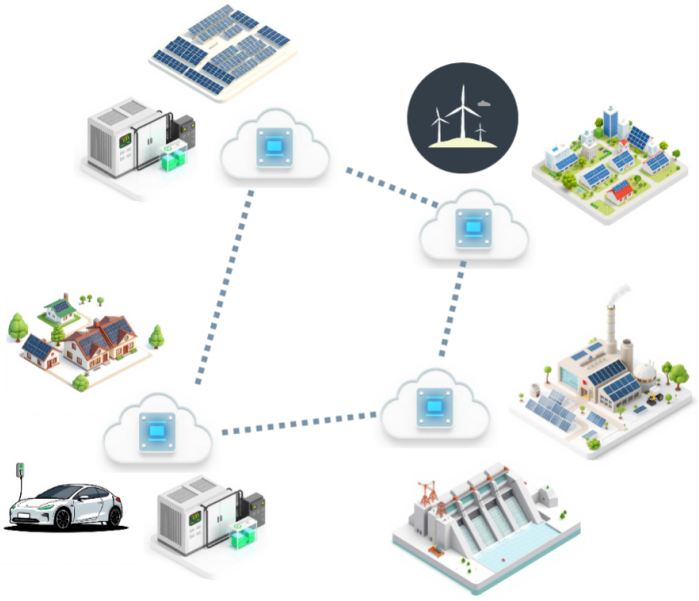

Figure 1.3: Structure of a modern power system. Generation is connected at both transmission and distribution levels.

- **Centralised control:** It is a control structure in which one central agent receives information from different agents or sensors and uses its own control algorithm to calculate the set points (i.e., instructions or references) for the agents or actuators.
- **Decentralised control:** It is a control structure in which each agent calculates its own control decisions, either with only local information or with local and external information.
- **Distributed control:** It is a control structure in which each agent calculates its own control decisions by considering local and external information, and a centralised agent ensures the coordination among agents.

An "agent", as used above, is generally defined as an autonomous entity that can perceive its environment and make decisions. Secondary and tertiary control systems in microgrids are multi-agent environments with a given communication structure.

Figure 1.4 compares centralised and decentralised structures for control systems, including the main advantages and drawbacks of each structure. A centralised structure suffers from a single point of failure, limited scalability and adaptability. In a decentralised structure, control speed and performance must be sacrificed to a certain extent.

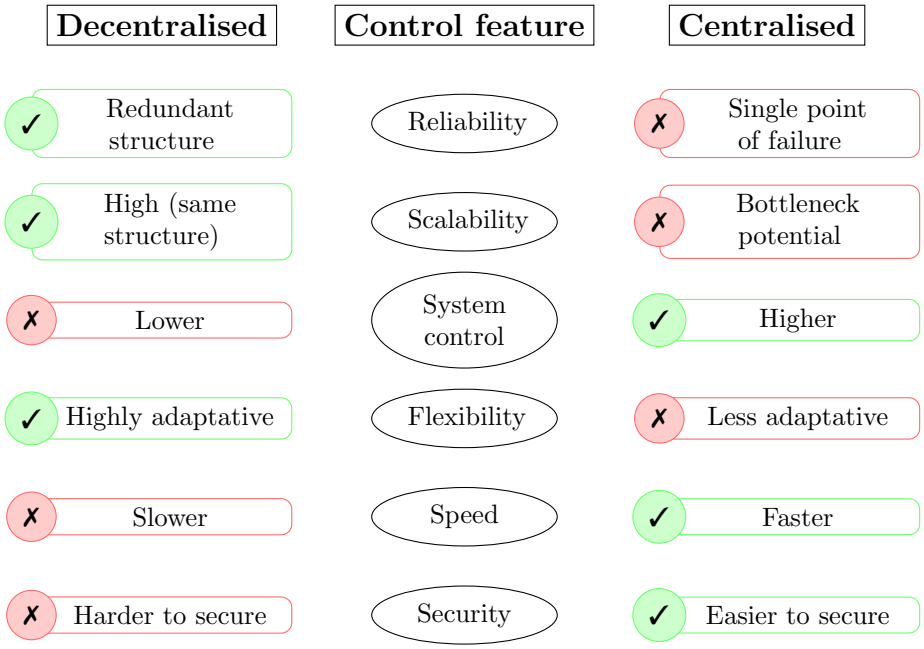

Figure 1.4: Comparison of the features of centralised and decentralised control structures.

Regarding decentralised multi-agent control systems (multi-agent algorithms include communications among agents for coordination), the most used control structure is consensus, although there are some other structures, as described by Dorri, Kanhere, and Jurdak (2018).

In the context of microgrid control, the most extended multi-agent control structure is consensus-based control. There are some studies implementing other structures, like distributed model-predictive control, applied in secondary frequency control by Yi, Xu, Gu, and Fei (2021), and game theory, applied in energy management by Javanmard, Tabrizian, Ansarian, and Ahmarinejad (2021).

This thesis focuses on first-order consensus-based control, since it is the main decentralised multi-agent control structure applied in microgrids.

1.3 Objectives of the thesis

1.3.1 Main objective

The main objective of this thesis is to evaluate the performance of decentralised control structures for microgrids to clarify in which situations this type of control could be a valid design option.

Centralised control structures have been widely adopted in power systems for secondary and tertiary control. This thesis proposes and evaluates different multi-agent decentralised control structures for the secondary and tertiary control of a microgrid.

The performance of multi-agent decentralised control will be investigated in several situations of the operation of microgrids, such as island operation, re-synchronisation with the main grid or black start in a distribution grid.

1.3.2 Specific objectives

The performance of multi-agent control structures is analysed for different topics in Chapter 2 (secondary control in islanded operation), Chapter 4 (synchronisation to the main grid and grid-connected operation), Chapter 5 (decentralised economic dispatch of a microgrid) and Chapter 6 (black-start) of this thesis. After the review of the state of the art of each topic, included in the introduction of each chapter, the research gaps shown in Table 1.1 were identified. This table serves as a summary on the specific objectives on decentralised control that were set during the PhD work.

Table 1.1: Limitations and gaps of decentralised control solutions for microgrids applied to several topics. Column "**Decent.**" includes the existing level of development of decentralised solutions in that specific topic.

Topic	**Decent.**	**Limitation/gap**	**Chapter**
Secondary Control	High	No consideration of the tertiary-secondary control link	Chapter 2
Synchronisation	Medium	No experimental validation or delay consideration	Chapter 4
Economic dispatch	Medium	Algorithm Convergence is limited by communication delay	Chapter 5
Black-start	Low	Nothing much done	Chapter 6

In the analysis and simulations done in Chapter 2, the models of large microgrids with electronic generation were very large to handle efficiently, with a lot of variables. After review of the existing approaches, no systematic studies were found on the influence of the state variables on the input-output response of systems with a high percentage of electronic generation. Therefore, an extra specific objective was set to analyse systematically the important variables in the input-output response of a linear system. Chapter 3 includes a review of the state of the art and the proposal to fill this gap, namely, the "state relevance" coefficient.

1.4 Outline of the thesis

The rest of the thesis document is structured in 7 chapters. Chapter 2 describes how the main system components (e.g., lines, loads converters, etc.) have been modelled. In all cases, models well-accepted in the literature were used. It also introduces and analyses the multi-agent secondary control of microgrids based on consensus and serves as a general overview of graph theory.

The simulation and analysis of microgrids with the algorithms proposed were carried out using a custom-made tool developed by the author using MATLAB and Simulink (MathWorks, 2024). Appendix A includes a detailed description of the tool. The tool is flexible enough to implement all the techniques and analyses presented in this thesis. For the initialisation of the dynamic models of the power systems studied, the tool uses the flexible universal branch model (FUBM) proposed by Alvarez-Bustos, Kazemtabrizi, Shahbazi, and Acha-Daza (2021), an extension of MATPOWER (Zimmerman, Murillo-Sánchez, & Thomas, 2011).

Chapter 3 proposes an algorithm to measure the relevance of each state variable of a linear system in its input-output response and illustrates how the relevance of state variables can be used in a microgrid case study with a secondary-control layer.

Chapter 4 proposes a method to synchronise a microgrid working with a multi-agent consensus-based secondary control with the main grid. For the experimental validation of the method, the laboratory facilities of IMDEA Energy were used (Prodanovic, Rodríguez-Cabero, Jiménez-Carrizosa, & Roldán-Pérez, 2017). The collaboration with IMDEA Energy institute was possible thanks to the PROMINT program of the Madrid government.

Chapter 5 proposes a fully decentralised hierarchical control structure for a microgrid with a consensus-based economic dispatch algorithm and an incremental secondary control. For real-time validation of this algorithm, the simulation model constructed in MATLAB Simulink was compiled and loaded on one OPAL-RT box, using HYPERSIM software (OPAL-RT TECHNOLOGIES, Inc., 2024).

Chapter 6 studies the distributed black-start of a microgrid with multi-agent triggered secondary control based on consensus, and Chapter 7 includes the conclusions, spells out the contributions and suggests possible future work of this thesis.

Appendix A includes the description of the MATLAB/Simulink tool used for the simulation and modal analysis of electrical power systems in this thesis.

Appendix B describes the procedure used for the elimination of non-relevant states in linear and non-linear models during this thesis.

Appendix C describes a modified version of the IEEE 69-bus test system presented by Baran and Wu (1989) and used in Chapters 2 to 6.

In this thesis, the microgrids used as test cases vary among chapters. In Chapter 3, several microgrids are used as illustrative examples for the proposed method, because their properties clarified the results. In Chapter 4, the small microgrid is used because it could be implemented in the laboratory setup. In Chapters 2, 5

and Appendix A, hybrid microgrids are used to validate the modelling tool with DC elements. To validate the scalability and applicability of the proposed methods, all of them are applied to the modified IEEE 69-bus test system described in Appendix C.

The choice of validation methods other than conventional simulation, i.e., the laboratory setup in Chapter 4 and the real-time simulation in Chapter 5, is based on the availability of hardware from the collaborations with the IMDEA Energy Institute and Durham University, respectively.

This chapter investigates decentralised multi-agent secondary control in microgrids based on consensus. Special attention has been given to the effect of communication time delays on the stability of the consensus algorithm and to an event-triggered control alternative to counteract this effect. However, to start with, this chapter summarises important elements and tools that have to be understood before the control problem can be discussed.

2 Multi-agent secondary control of microgrids. Preliminaries and fundamentals

2.1 Introduction

As described in Chapter 1 the hierarchical control proposed for microgrids has a structure similar to the one in classical power systems, i.e., three control layers: primary control, secondary control and terciary control. However, in generation based on electronic power converters it is important to recall that the behaviour of those generators relies on a well-designed level-0 control system which has already been given a lot of attention in the literature. Drawing from the literature review on hierarchical control of microgrids in Chapter 1 the present chapter will investigate the principles of use of consensus-based secondary control in microgrids as the most popular alternative for decentralized control in this field of application. Cases of application of this form of control will be investigated in later chapters.

Before dealing with the main topic of this chapter (decentralised secondary control), it is worth describing the modelling approach used, some useful tools, and lower control layers in order to have a comprehensive picture of the problem in hands.

2.2 The importance of simulation in microgrid studies and the main assumptions adopted

Simulation has always been an essential tool for the analysis and design of power systems. It helps to understand the behaviour of the system under different con-

ditions and to test control and protection strategies safely. The focus of models for power system simulation varies from device-level models that focus on the behaviour of individual components to system-level models that focus on the behaviour of the entire system. Model details very much depend on the dynamic phenomena to be studied and the related control and protection dynamics.

Device-level models include very detailed modelling of the physical behaviour of specific components. They are used to study the performance and reliability of those components in different operating conditions (e.g., thermal, mechanical or electrical behaviour). Manufacturers mainly use device-level models to design and test new components.

System-level models are used mainly by system operators, regulators, and researchers to study the behaviour of the system as a whole. System-level models typically include a simplified representation of the physical behaviour of individual components.

This chapter includes an explanation of the modelling approach used in this thesis for the elements of electrical power systems. The following restrictions apply to the models used:

- DC-AC switching converters are represented as ideal balanced voltage sources.
- The primary energy source of electronic converters is treated as ideal, i.e, instantaneous response with no limitations.
- Designing the level-0 voltage and current control loops of the converters is not the main concern of this study because this loops have been extensively treated in the literature; it is assumed that these control loops are effectively designed and finely tuned.
- The electric current limits of the converters are not addressed in this thesis either, as the focus is on the normal operation of the system, under the assumption that it will not encounter critical conditions such as faults. Although the current limitation is essential for controlling electronic converters, especially in the presence of faults, it mainly influences the transient stability of the system, which is outside the scope of this research. The multi-agent control algorithms analysed in this thesis function at higher, and thus slower, control levels.

Figure 2.1 shows a possible example of a microgrid composed of grid-forming voltage source converters with unidirectional communications between converters, many other configurations are possible.This chapter describes how all components of such a system will be modelled for the studies carried out.

Each distributed generator (DG) is connected to the grid by means of an LCL filter and electrical lines. Loads are represented by admittances. DGs interchange information among them ("Sec. vars" in the figure) for secondary and tertiary control purposes. Note that the information flow in the figure is arbitrary and serves only as an example.

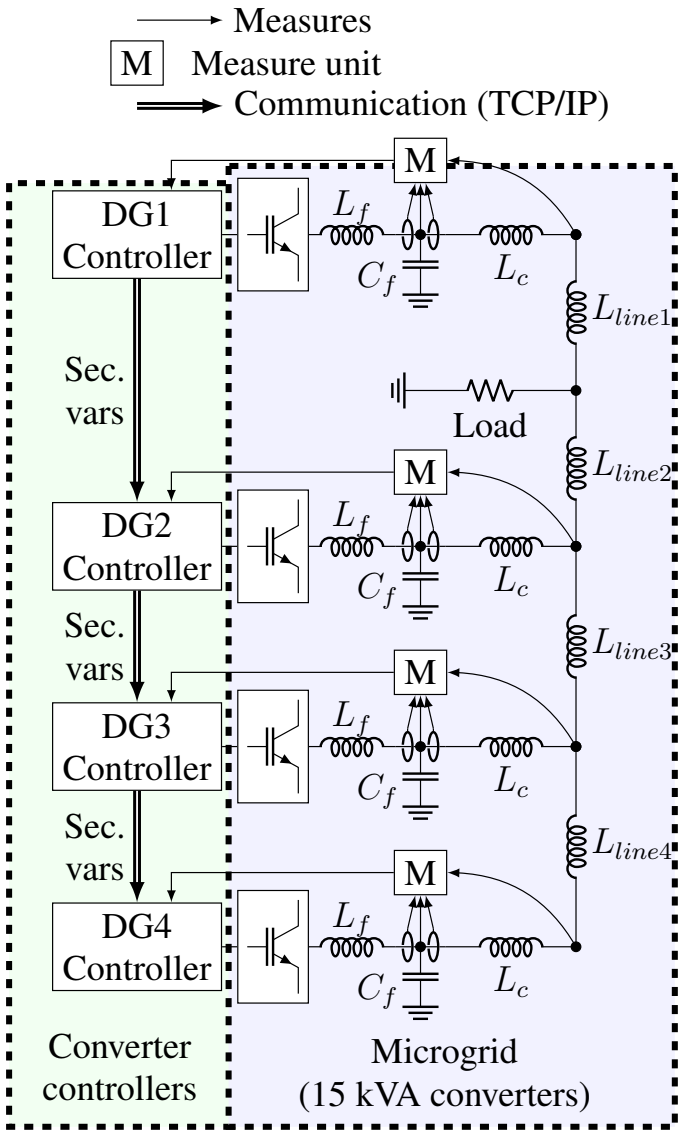

Figure 2.1: An example of microgrid composed of grid-forming voltage source converters and loads. The typical system studied in this thesis.

2.3 Modelling of microgrids. Fundamentals and tools

2.3.1 Working in a $d-q$ reference frame

Let us consider a positive-sequence 3-phase balanced voltage with the following phase-voltage components: a, b, and c:

$$v_{a,b,c}(t) = \begin{cases} v_a(t) = V_0 \cos(\omega_1 t + \varphi) \\ v_b(t) = V_0 \cos(\omega_1 t + \varphi - 2\pi/3) \\ v_c(t) = V_0 \cos(\omega_1 t + \varphi + 2\pi/3) \end{cases} \tag{2.1}$$

and the complex number:

$$\mathbf{v}^s(t) = v_\alpha + j v_\beta = \frac{2}{3} K \left(v_a(t) + e^{j2\pi/3} v_b(t) + e^{-j2\pi/3} v_c(t) \right) \tag{2.2}$$

Applying (2.2) to the positive sequence 3-phase balanced voltage in (2.1) results:

$$\mathbf{v}^{s+}(t) = K \cdot V_0 e^{j(\omega_1 t + \varphi)} \tag{2.3}$$

which is a complex number with amplitude KV_0 rotating anti-clockwise with angular speed ω_1 in the complex plane, and initial position in $t = 0$ equal to φ (see Figure 2.2).

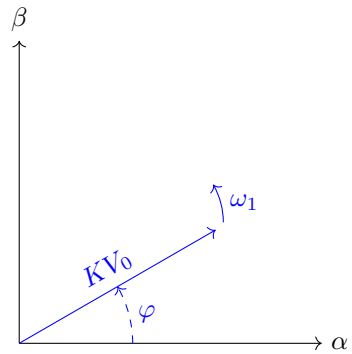

Figure 2.2: Positive-sequence 3-phase voltage (rotating with angular speed ω_1) in $\alpha - \beta$ static reference frame

The transformation in (2.2) can also be written in matrix form:

$$\begin{bmatrix} v_0 \\ v_\alpha \\ v_\beta \end{bmatrix} = \underbrace{K \begin{bmatrix} a & a & a \\ 2/3 & -1/3 & -1/3 \\ 0 & 1/\sqrt{3} & -1/\sqrt{3} \end{bmatrix}}_{\mathbf{T}_{abc \to \alpha\beta 0}} \cdot \begin{bmatrix} v_a \\ v_b \\ v_c \end{bmatrix} \tag{2.4}$$

where a is an arbitrary constant and v_0 is the "homopolar" component (or 0 component) of the voltage in α-β axes. In three-wire systems, the homopolar component does not transmit power because $i_a(t) + i_b(t) + i_c(t) = 0$. Moreover, if the three-phase voltage is balanced, as considered in this thesis, the homopolar component of the voltage is also 0 because $v_a(t) + v_b(t) + v_c(t) = 0$. Therefore, this component is not considered in this thesis any more, leading to:

$$\begin{bmatrix} v_\alpha \\ v_\beta \end{bmatrix} = \underbrace{K \begin{bmatrix} 2/3 & -1/3 & -1/3 \\ 0 & 1/\sqrt{3} & -1/\sqrt{3} \end{bmatrix}}_{\mathbf{T}_{abc\to\alpha\beta}} \cdot \begin{bmatrix} v_a \\ v_b \\ v_c \end{bmatrix} \tag{2.5}$$

The inverse transform can be proposed as:

$$\begin{bmatrix} v_a \\ v_b \\ v_c \end{bmatrix} = \underbrace{\frac{1}{K} \cdot \begin{bmatrix} 1 & 0 \\ -1/2 & \sqrt{3}/2 \\ -1/2 & -\sqrt{3}/2 \end{bmatrix}}_{\mathrm{T}_{\alpha\beta\to abc}} \cdot \begin{bmatrix} v_\alpha \\ v_\beta \end{bmatrix} \tag{2.6}$$

where $T_{abc\to\alpha\beta} \cdot T_{\alpha\beta\to abc} = I_{2x2}$.

Park Transformation

As shown above, with no homopolar component, a positive-sequence 3-phase balanced voltage is represented in an $\alpha - \beta$ reference frame as a complex number with amplitude KV_0 rotating with angular speed ω_1 (see Figure 2.2). If one projects this complex number onto a pair of orthogonal axes $d - q$, which also rotate with angular speed ω_1, the complex number has constant components on the new $d - q$ axes (see Figure 2.3). This transformation is called "Park Transformation" because it was introduced by Park (1929), derived from the two-reaction theory of Blondel (1913). Park Transformation is used to have a useful reference frame for the analysis and control of an electrical synchronous machine.

The transformation between the "stationary" frame $\alpha - \beta$ ($\mathbf{v}^{s+}$) and the "rotating" frame $d - q$ ($\mathbf{v}$) can be written as:

$$\mathbf{v} = e^{-j\omega_1 t}\mathbf{v}^{s+} = KV_0 e^{j\varphi} = KV_0 \cos\varphi + jKV_0 \sin\varphi \tag{2.7}$$

or in matrix form:

$$\begin{bmatrix} v_d \\ v_q \end{bmatrix} = \begin{bmatrix} \cos(\omega_1 t) & \sin(\omega_1 t) \\ -\sin(\omega_1 t) & \cos(\omega_1 t) \end{bmatrix} \cdot \begin{bmatrix} v_\alpha \\ v_\beta \end{bmatrix} \tag{2.8}$$

Complex numbers such as $\mathbf{v} = v_d + jv_q$ are often called "space vectors" and should not be mistaken for the so-called "phasors" which are also represented in the complex plane and whose attributes resemble those of space vectors.

The direct transformation from abc to dq is:

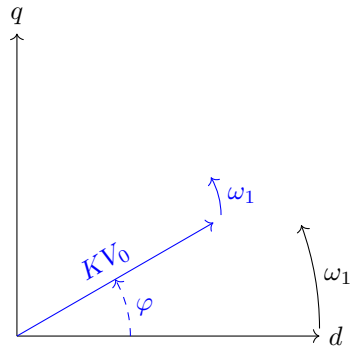

Figure 2.3: Positive-sequence 3-phase voltage in $d-q$ reference frame

$$\begin{bmatrix} v_d \\ v_q \end{bmatrix} = T_{abc\to dq} \begin{bmatrix} v_a \\ v_b \\ v_c \end{bmatrix} \tag{2.9}$$

where:

$$T_{abc\to dq} = K \begin{bmatrix} \frac{2}{3}\cos(\omega_1 t) & \frac{2}{3}\cos\left(\omega_1 t - \frac{2\pi}{3}\right) & \frac{2}{3}\cos\left(\omega_1 t - \frac{4\pi}{3}\right) \\ -\frac{2}{3}\sin(\omega_1 t) & -\frac{2}{3}\sin\left(\omega_1 t - \frac{2\pi}{3}\right) & -\frac{2}{3}\sin\left(\omega_1 t - \frac{4\pi}{3}\right) \end{bmatrix} \tag{2.10}$$

If the 0 component is also of interest:

$$v_0 = K \cdot a \cdot (v_a(t) + v_b(t) + v_c(t)) \tag{2.11}$$

Power invariant Park transform

In a 3-phase power system, the instantaneous power drawn by a current $i_{abc}(t)$ is calculated as:

$$p(t) = v_a(t)i_a(t) + v_b(t)i_b(t) + v_c(t)i_c(t) \tag{2.12}$$

If $K = \sqrt{3/2}$ and $a = \sqrt{2}/3$ in (2.10) and (2.11):

$$p(t) = v_0(t)i_0(t) + v_d(t)i_d(t) + v_q(t)i_q(t) \tag{2.13}$$

Therefore, with this choice of K and a, the instantaneous power using $dq0$ components has a similar expression as the one using abc components. This is why this choice is called "the power invariant Park Transform", and it will be the one used in this thesis. Notice that, after the transformation in (2.10), an ideal 3-phase voltage source of rms value V_{rms} would be represented by a space vector v_{dq} of modulus equal to $\sqrt{3} \cdot V_{rms}$.

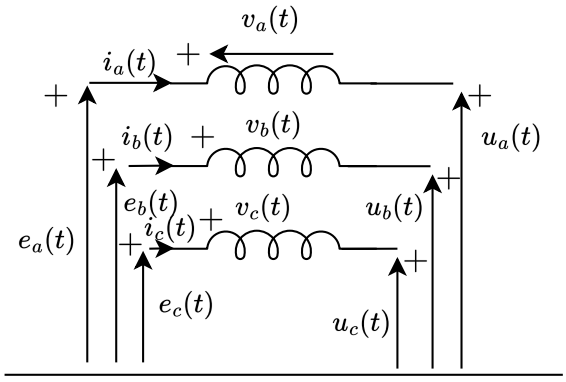

Figure 2.4: A 3-phase inductor.

2.3.2 Basic element modelling and per unit values

A common way to analyse and control power systems is using the d-q reference frame since it transforms sinusoidal 3-phase signals into constants in steady state. This greatly simplifies the control of any electrical variable.

Equations of basic electrical components in the d-q reference frame

All the equations that model the power systems are based on a d-q reference frame. To illustrate the derivation of those equations, the equations of a 3-phase balanced inductor of inductance L and series resistance R without magnetic coupling (see Figure 2.4) are derived from the three-phase model (abc) that follows:

$$L\frac{di_{abc}}{dt} = v_{abc} - R \cdot i_{abc} \tag{2.14}$$

where i_{abc} is the 3-phase current through the inductor, and $v_{abc} = e_{abc} - u_{abc}$ is the 3-phase voltage across the inductor. Expanding (2.14) to the three-phase vector form:

$$L \cdot \frac{d}{dt}\begin{bmatrix} i_a \\ i_b \\ i_c \end{bmatrix} = \begin{bmatrix} v_a \\ v_b \\ v_c \end{bmatrix} - R \cdot \begin{bmatrix} i_a \\ i_b \\ i_c \end{bmatrix} \tag{2.15}$$

Applying (2.6) to (2.15):

$$L\cdot\mathbf{T}_{\alpha\beta\rightarrow abc}\cdot\frac{d}{dt}\begin{bmatrix} i_\alpha \\ i_\beta \end{bmatrix}=\mathbf{T}_{\alpha\beta\rightarrow abc}\cdot\begin{bmatrix} e_\alpha \\ e_\beta \end{bmatrix}-R\cdot\mathbf{T}_{\alpha\beta\rightarrow abc}\cdot\begin{bmatrix} i_\alpha \\ i_\beta \end{bmatrix}-\mathbf{T}_{\alpha\beta\rightarrow abc}\cdot\begin{bmatrix} u_\alpha \\ u_\beta \end{bmatrix} \tag{2.16}$$

Multiplying (2.16) by $\mathbf{T}_{abc\rightarrow\alpha\beta}$ from the left-hand side, and since,

$$\mathbf{T}_{abc\rightarrow\alpha\beta}\cdot T_{\alpha\beta\rightarrow abc}=I_{2x2}; \tag{2.17}$$

$$L\cdot\frac{d}{dt}\begin{bmatrix} i_\alpha \\ i_\beta \end{bmatrix}=\begin{bmatrix} e_\alpha \\ e_\beta \end{bmatrix}-R\cdot\begin{bmatrix} i_\alpha \\ i_\beta \end{bmatrix}-\begin{bmatrix} u_\alpha \\ u_\beta \end{bmatrix} \tag{2.18}$$

Applying (2.7) and the fact that,

$$\frac{d\mathbf{i}_{\alpha\beta}}{dt}=\frac{d}{dt}\left(e^{j\omega_1 t}\mathbf{i}_{dq}\right)=j\omega_1\cdot e^{j\omega_1 t}\cdot\mathbf{i}_{dq}+e^{j\omega_1 t}\cdot\frac{d\mathbf{i}_{dq}}{dt} \tag{2.19}$$

leads to:

$$L\frac{d\mathbf{i}_{dq}}{dt}=\mathbf{e}_{dq}-R\cdot\mathbf{i}_{dq}-\mathbf{u}_{dq}-jL\omega_1\mathbf{i}_{dq} \tag{2.20}$$

Recalling that dq variables are complex numbers such as $\mathbf{v}_{dq}=v_d+j\cdot v_q$, the equations of an inductive element in a d-q reference frame are:

$$\begin{cases} v_d=L\dfrac{di_d}{dt}-\omega_1 Li_q+Ri_d \\ \\ v_q=L\dfrac{di_q}{dt}+\omega_1 Li_d+Ri_q \end{cases} \tag{2.21}$$

Analogously, the equations of a capacitor in a d-q reference frame are:

$$\begin{cases} i_d=C\dfrac{dv_d}{dt}-\omega_1 Cv_q+\dfrac{1}{R}v_d \\ \\ i_q=C\dfrac{dv_q}{dt}+\omega_1 Cv_d+\dfrac{1}{R}v_q \end{cases} \tag{2.22}$$

where C is the capacitance, R is its parallel resistance, $\mathbf{i}_{dq}$ is the current entering the capacitor, $\mathbf{v}_{dq}$ is the voltage across the capacitor.

In power systems, voltages, currents, power, impedances, etc., are often expressed in per-unit (pu) instead of using volts, amperes, watts, ohms, etc. Per-unit values are obtained by dividing the actual variables by their "base" values.

In this thesis, the base values for voltage and power are selected as the root mean square (RMS) nominal (subscript *N*) line-to-line voltage and the three-phase apparent power of the system:

$$V_b=\sqrt{3}\cdot V_{N,a}^{RMS},\quad S_b=3\cdot V_{N,a}^{RMS}\cdot I_{N,a}^{RMS} \tag{2.23}$$

Consequently, the base current has been selected as:

$$I_b = \sqrt{3} \cdot I_{N,a}^{RMS} \tag{2.24}$$

so that[1],

$$S_b = V_b \cdot I_b \tag{2.25}$$

and, it makes sense defining the base impedance for the per-phase equivalent system as:

$$Z_b = \frac{V_{N,a}^{RMS}}{I_{N,a}^{RMS}} = \frac{V_b/\sqrt{3}}{I_b/\sqrt{3}} = \frac{V_b}{I_b} \tag{2.26}$$

or, in other words, using (2.25) and (2.26)

$$Z_b = \frac{V_b^2}{S_b} \tag{2.27}$$

Since, using the power-invariant Park transform,

$$|x_{dq}| = \sqrt{3} \cdot x_a^{RMS} \tag{2.28}$$

for a three-phase variable x_{abc} (phase voltages or currents), the moduli of the complex numbers v_{dq} and i_{dq} will be $1\,pu$ when the line voltage and the phase current reach their nominal values.

Some examples of how natural variables and parameters can be put in p.u., follow:

$$\begin{cases} v_{pu} = \dfrac{v}{V_b}, \quad i_{pu} = \dfrac{i}{I_b}, \\ L_{pu} = \dfrac{L}{L_b}, \quad R_{pu} = \dfrac{R}{Z_b}, \\ Z_b = L_b \omega_b, \quad \omega_{pu} = \dfrac{\omega}{\omega_b} \end{cases} \tag{2.29}$$

where the base frequency in rad/s is the nominal frequency of the system.

With the choices for base values, the equations of an inductor in the d-q reference frame using per-unit variables are:

$$\begin{cases} L_{pu} \dfrac{di_{d,pu}}{dt} = \omega_b \left(e_{d,pu} - R_{pu} i_{d,pu} - u_{d,pu} + L_{pu} \omega_{1,pu} i_{q,pu} \right) \\ L_{pu} \dfrac{di_{q,pu}}{dt} = \omega_b \left(e_{q,pu} - R_{pu} i_{q,pu} - u_{q,pu} - L_{pu} \omega_{1,pu} i_{d,pu} \right) \end{cases} \tag{2.30}$$

Analogously, the equations of a capacitor in a d-q reference frame using per-unit variables are:

[1] Not the most common choice!

$$\begin{cases} C_{pu}\dfrac{dv_{d,pu}}{dt} = \omega_b\left(i_{1d,pu} - \dfrac{v_{d,pu}}{R_{pu}} - i_{2d,pu} + C_{pu}\omega_{1,pu}v_{q,pu}\right) \\ C_{pu}\dfrac{dv_{q,pu}}{dt} = \omega_b\left(i_{1q,pu} - \dfrac{i_{q,pu}}{R_{pu}} - i_{2q,pu} - C_{pu}\omega_{1,pu}v_{d,pu}\right) \end{cases} \tag{2.31}$$

Finally (forgetting the 0 component, for simplicity),

$$p_{pu} = i_{d,pu}\cdot v_{d,pu} + i_{q,pu}\cdot v_{q,pu} \tag{2.32}$$

$$q_{pu} = i_{d,pu}\cdot v_{q,pu} - i_{q,pu}\cdot v_{d,pu} \tag{2.33}$$

where $v_{dq,pu} = v_{d,pu} + jv_{q,pu}$ are the components of the 3-phase voltage, $i_{dq,pu} = i_{d,pu} + ji_{q,pu}$ are the components of the 3-phase current, p_{pu} is the instantaneous real power and q_{pu} is the instantaneous reactive power. In steady state, p_{pu} is equal to the active power (P_{pu}) and q_{pu} is equal to the reactive power (Q_{pu}). In addition, the complex power can be written as:

$$S_{pu} = P + jQ = v_{dq,pu}\cdot i^*_{dq,pu} \tag{2.34}$$

where $i^*_{dq,pu} = i_{d,pu} - ji_{q,pu}$.

2.3.3 Modelling with several different reference frames

In a microgrid with several voltage-source converters (VSCs), every converter sets a frequency, even grid-following voltage-source converters (GFl-VSCs). Although all frequencies are equal in steady state, each VSC may set a different frequency during transients. As explained in Subsection 2.3.1, all components of a positive-sequence 3-phase voltage with frequency ω_1 are constant only on a d-q reference frame rotating with angular speed ω_1. Therefore, to keep the VSC model simple, the control system of each converter must be simulated in a d-q reference frame rotating with an angular speed equal to the frequency of the converter. In order to simulate all other elements of the microgrid jointly with all the converters, a common d-q reference frame must be chosen and all variables measured in or affecting one converter must be referred from this common frame to the converter own one, while all converter output electrical variables must be referred fromits own reference frame to the common one. For example, the voltage components in a d2-q2 rotating reference frame (v_{d2} and v_{q2}) can be calculated from those in a d1-q1 reference frame, as follows:

$$v_{d2} + jv_{q2} = (v_{d1} + jv_{q1})e^{-j\varphi_d} = (v_{d1} + jv_{q1})(\cos\varphi_d - j\sin\varphi_d) \tag{2.35}$$

$$\begin{cases} v_{d2} = v_{d1}\cos\varphi_d + v_{q1}\sin\varphi_d \\ v_{q2} = v_{q1}\cos\varphi_d - v_{d1}\sin\varphi_d \end{cases} \tag{2.36}$$

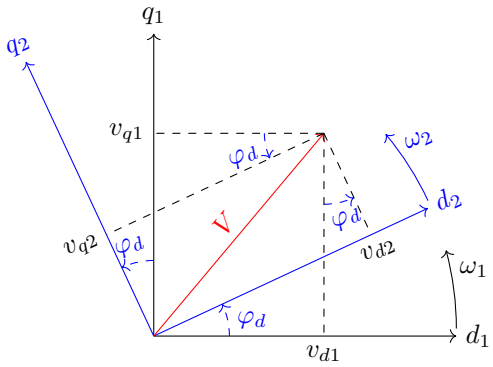

Figure 2.5: Multiple $d-q$ reference frames

where φ_d is the angle from axis $d1$ to axis $d2$ (see Figure 2.5). Angles are positive when anticlockwise.

2.4 Inner controls of grid-forming and grid-following converters

Renewable energy resources (RERs) are often connected to the power system through electronic converters which are classified into VSCs and current-source converters (CSCs), as described and compared in Monteiro, Pinto, Exposto, and Afonso (2015). However, most converters in actual power systems are of the VSCs type. Within VSC technology, converters are classified into grid-forming converters (GFrs) and grid-following converters (GFls).

GFl-VSCs are connected to a bus or point of common coupling (PCC) through a filter, track the voltage moduli and angles of their PCCs, and adjust their inner voltages to inject a controlled current, oriented to meet certain active and reactive power requirements. A diagram depicting the control of a GFl-VSC is shown in Figure 2.6. Subscript i stands for "the i-th converter". The phase locked loop (PLL) block tracks the voltage amplitude and angle of the PCC of the converter, in general using a PI control, as shown in Figure 2.7.

The abc/dq block in Figure 2.10 is the Park Transform, which makes the use of a PI current controller possible and natural since d and q components are constant values in steady state. Typically, a PI current controller in a $d-q$ reference frame guarantees that the current d and q components follow their set points. Other control approaches for VSCs are possible or even necessary[2], including sliding mode control (Gholami, Pilloni, Pisano, & Usai, 2021) and proportional-resonant

[2]For example, proportional-resonant controllers are necessary in unbalanced systems to control negative sequences, and when harmonic control is required.

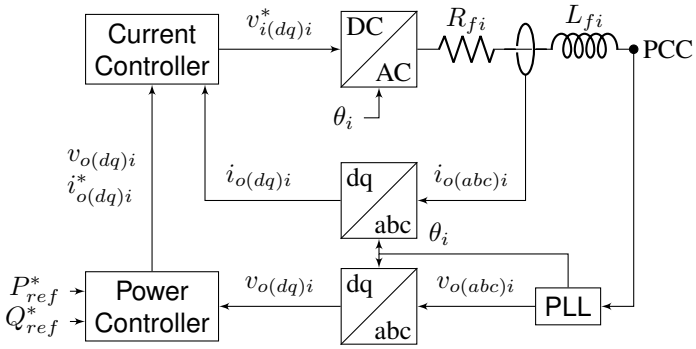

Figure 2.6: Grid-following voltage source converter control structure. Adapted from Bidram, Nasirian, Davoudi, and Lewis (2017).

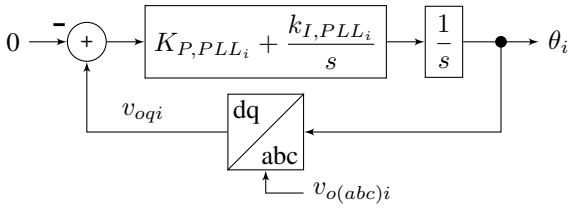

Figure 2.7: Block diagram of the phase-locked-loop.

control (Yagüe Yagüe, 2024). However, the inner controllers of VSCs are not the main focus of this thesis, and only conventional PI controllers are considered in this layer. The power controller, shown in Figure 2.8, calculates the set-point values for the d and q components of the current, considering the active- and reactive-power set points and the d and q components of the measured voltage. The structure of the current controller is detailed in Figure 2.9. This structure is for the positive sequence (in case of unbalances, oscillations appear in the feedback signal and dedicated filtering is needed, or controls for the negative sequence could be added).

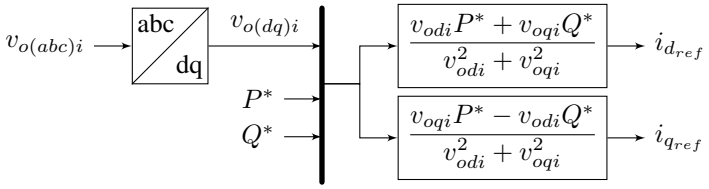

Figure 2.8: Grid-following voltage source power controller structure.

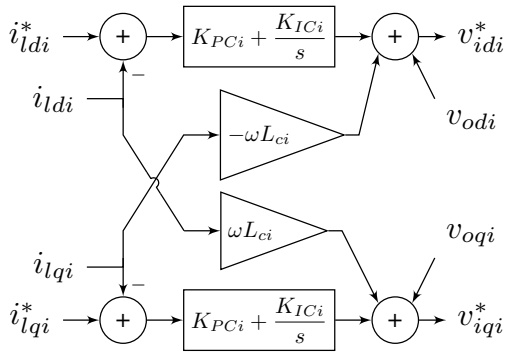

Figure 2.9: Grid-following voltage source converter control structure. The abc/dq block is the so-called Park Transform. Adapted from Bidram, Nasirian, Davoudi, and Lewis (2017).

Grid-forming voltage-source converters (GFr-VSCs) impose the voltage and frequency at their PCCs. A diagram depicting the control of a GFr-VSC is shown in Figure 2.10. It is connected to a bus or PCC through a filter and imposes the voltage and frequency on its point of control (PC). For several important reasons, this type of electronic converter is usually equipped with inner current and voltage controllers. The structure of PI voltage and current controllers is detailed in Figure 2.11.

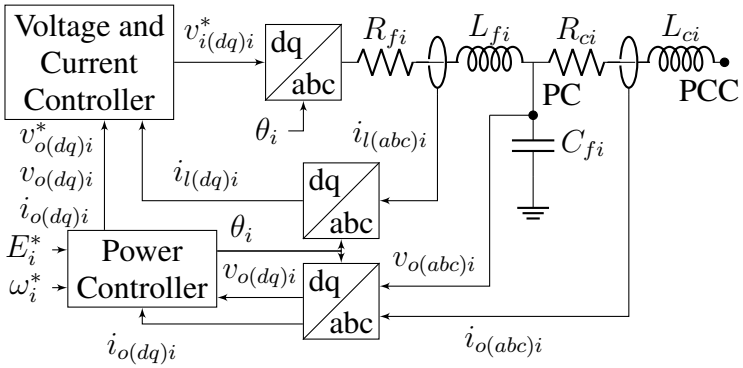

Figure 2.10: Diagram of a GFr-VSC. Adapted from Bidram, Davoudi, and Lewis, 2014.

Each GFr-VSC uses its own reference frame for the Park transform for control purposes so that the set point for its q voltage component is zero ($v^*_{oqi} = 0$). Applying a power-invariant Park Transform, active and reactive power drawn from a GFr-VSC have a similar expression to the one using three-phase (abc) electrical

variables. As previously discussed, for modelling and simulation purposes of the whole system, one of the $d-q$ synchronous reference systems is taken as the angle reference, and all other state variables are referred to it.

The simplest model of a GFr-VSC is an ideal voltage source that imposes the voltage and frequency at its PC. Including the voltage and current controllers makes the model more detailed, which is, in general, necessary for stability studies related to converter interactions. Typically, the converter itself (i.e., the DC/AC conversion block in Figure 2.10) is modelled as a controlled ideal sinusoidal voltage source by neglecting the PWM-driven control of the switches (e.g., IGBTs) because switching transients are much faster than the dynamics of voltage and current controllers. Given the rather fast controller dynamics, the line dynamics of the microgrid cannot be neglected a priori. Obviously, the presence of several GFr-VSCs and other elements, together with the inclusion of line dynamics, significantly increases the size of the problem with respect to traditional power systems where power-line and generator-stator dynamics are most often neglected.

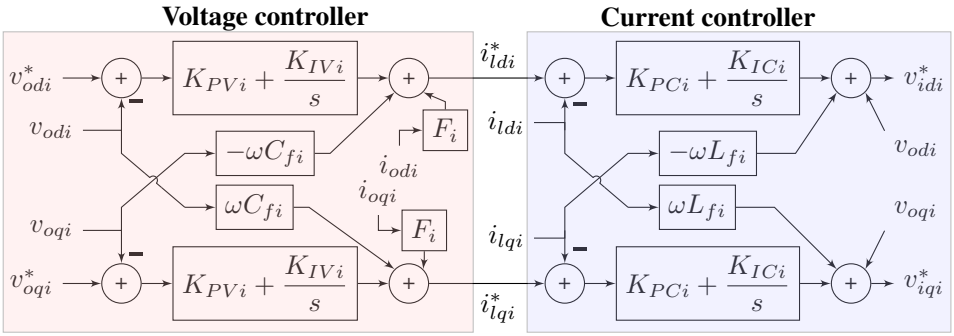

Figure 2.11: Voltage and current controllers of a GFr-VSC (i), including the decoupling of the output LC filter and current feed-forward. Adapted from Bidram, Davoudi, Lewis, and Guerrero, 2013.

2.5 Primary control of GFr-VSCs

If more than one GFr-VSC must work connected to the same grid, some form of self-synchronisation and power-sharing should be applied, for example, by means of droop control. Figure 2.12 illustrates the most typical $\omega - P$ and $v - Q$ droop controllers of a GFr-VSC used, where the actual active and reactive powers delivered by each converter i (P_i and Q_i, respectively) are calculated from its output voltage and current. The filtered results are used to manipulate the output voltage and frequency set-point values.

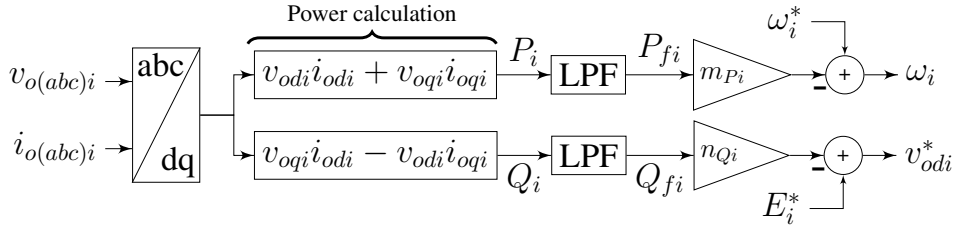

Figure 2.12: Power controller of a GFr-VSC (i), including droop control for frequency and voltage. Low-pass filters (LPFs) are usually included to reduce measurement noise.

2.5.1 Selection of a droop control method

Let us consider two GFr-VSC G1 and G2 with output voltage phasors $E_1\angle\gamma_1$ and $E_2\angle\gamma_2$, and frequencies ω_1 and ω_2, respectively ($\omega_1 = \omega_2$ in steady state). The active (P) and reactive (Q) power flow going from G1 to G2 through a transmission line of impedance $Z\angle\theta$ can be calculated as follows: (see Figure 2.13)

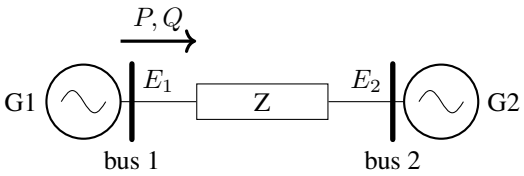

Figure 2.13: Two GFr-VSCs connected through a transmission line

$$\begin{cases} P = \dfrac{E_1 E_2}{Z}\cos(\theta - \delta) - \dfrac{{E_2}^2}{Z}\cos(\theta) \\ Q = \dfrac{E_1 E_2}{Z}\sin(\theta - \delta) - \dfrac{{E_2}^2}{Z}\sin(\theta) \end{cases} \tag{2.37}$$

where:

- δ is the angle between bus 1 and bus 2 voltage phasors.
- θ is the angle of the impedance of the transmission line (Z is its module).
- E_1 is the RMS[3] voltage of bus 1
- E_2 is the RMS voltage of bus 2.

[3]Root Mean Square value

- P and Q are the active and reactive powers transferred between buses 1 and bus 2.

Setting $E_2 = 1$ as a voltage reference and naming $V = E_1 - E_2$ the voltage difference:

$$\begin{cases} P = \dfrac{V+1}{Z}\cos(\theta-\delta) - \dfrac{1}{Z}\cos(\theta) \\ Q = \dfrac{V+1}{Z}\sin(\theta-\delta) - \dfrac{1}{Z}\sin(\theta) \end{cases} \tag{2.38}$$

Splitting the fraction:

$$\begin{cases} P = \dfrac{V}{Z}\cos(\theta-\delta) + \dfrac{1}{Z}\cos(\theta-\delta) - \dfrac{1}{Z}\cos(\theta) \\ Q = \dfrac{V}{Z}\sin(\theta-\delta) + \dfrac{1}{Z}\sin(\theta-\delta) - \dfrac{1}{Z}\sin(\theta) \end{cases} \tag{2.39}$$

To choose the best droop method, one must calculate the derivative of the active and reactive power in relation to the voltage and angle difference between the two nodes. The derivative of the active and reactive power when the the voltage difference between the two nodes changes, is:

$$\begin{cases} \dfrac{\partial P}{\partial V} = \dfrac{1}{Z}\cos(\theta-\delta) \\ \dfrac{\partial Q}{\partial V} = \dfrac{1}{Z}\sin(\theta-\delta) \end{cases} \tag{2.40}$$

Whether the "sensitivity" of Q with respect to V (voltage difference) is bigger than the "sensitivity" of P to changes in V, can be quantified as:

$$\left|\frac{\partial Q/\partial V}{\partial P/\partial V}\right| = |\tan(\theta-\delta)| > 1 \tag{2.41}$$

which, if δ is small, implies:

$$|\tan(\theta-\delta)| \approx |\tan\theta| = \frac{X}{R} > 1 \text{ and } X > R \tag{2.42}$$

Similarly, one can show that, with a small δ:

$$\left|\frac{\partial Q/\partial \delta}{\partial P/\partial \delta}\right| = \left|\frac{-\cos\theta}{\sin\theta}\right| < 1 \;\rightarrow\; |\tan\theta > 1| \text{ and } X > R \tag{2.43}$$

Therefore, the droop-method selection can be suggested as outlined in Table 2.1.

In high-voltage lines, the situation in the first row of Table 2.1 is the most typical one and the droop control is implemented as described in Figure 2.12. However, in low-voltage lines (i.e. distribution systems) the most common situation is the

X/R ratio	Results	Droop-selection method
$X > R$	$\lvert\partial Q/\partial V\rvert > \lvert\partial P/\partial V\rvert$ $\lvert\partial Q/\partial \delta\rvert < \lvert\partial P/\partial \delta\rvert$	f changes to change P, V changes to change Q.
$X = R$	$\lvert\partial Q/\partial V\rvert = \lvert\partial P/\partial V\rvert$ $\lvert\partial Q/\partial \delta\rvert = \lvert\partial P/\partial \delta\rvert$	?? ??
$X < R$	$\lvert\partial Q/\partial V\rvert < \lvert\partial P/\partial V\rvert$ $\lvert\partial Q/\partial \delta\rvert > \lvert\partial P/\partial \delta\rvert$	V changes to change P, f changes to change Q

Table 2.1: Droop method selection.

one described in the last row of Table 2.1. In this case, some authors propose to follow the recommendations included in that table but some others (e.g. Y. Li and Li (2009) propose the compensation of the effect of the line impedance using two auxiliary inputs, namely, V' and δ' as:

$$\begin{bmatrix} V \\ \delta \end{bmatrix} = \begin{bmatrix} -\sin\theta & \cos\theta \\ \cos\theta & \sin\theta \end{bmatrix} \cdot \begin{bmatrix} V' \\ \delta' \end{bmatrix} \tag{2.44}$$

so that, now:

$$\left|\frac{\partial P/\partial \delta'}{\partial Q/\partial \delta'}\right| > 1 \;\; \& \;\; \left|\frac{\partial Q/\partial V'}{\partial P/\partial V'}\right| > 1 \tag{2.45}$$

very much like in high-voltage lines using V and δ, with the disadvantage of having to know the impedance at the PCC.

2.5.2 Virtual impedance loop

As shown in Section 2.5.1, droop control methods are designed in different ways depending on the inductive or resistive nature of electrical lines in the power system. More specifically, the impedance to be considered in the design of the droop control technique is the impedance seen from the electronic converters to other voltage sources. Therefore, adding one inductive output impedance to the converter can ensure that the most conventional active-power vs frequency droop control is still valid for low-voltage applications, where electrical lines connecting converters are more resistive. However, including this output impedance increases the electrical losses of the system. Alternatively, some authors propose adding a "virtual output impedance" instead of a physical one. This is carried out by changing the actual converter output voltage as a function of its output current.

Harnefors, Zhang, and Bongiorno (2008) propose VSC controller designs for passivity. Some of those designs are defined by Wang et al. (2015) as virtual impedance topologies. In one of them, a low-pass filter is included in the voltage set point for the direct and quadrature components in the current controller. It is clear that this approach does not affect the system in steady state since the low pass filter is designed to have unity DC gain. However, during transients, if the voltage

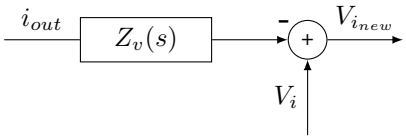

Figure 2.14: Block diagram of the output virtual impedance loop

of the PCC changes rapidly, the converter will not change its voltage and therefore, active and reactive power injections will not follow their set points. This approach seems to focus on improving the system damping.

Bidram and Davoudi (2012) summarise some designs of virtual impedance loops. In the first design, proposed by J. M. Guerrero, Vasquez, Matas, de Vicuna, and Castilla (2011), the voltage drop in the set point of the voltage controller depends on the converter output current as:

$$V_{i_{new}} = V_i - Z_v(s) i_{out} \tag{2.46}$$

where $V_{i_{new}}$ is the new set point for the voltage controller, V_i is the voltage set point calculated by a droop controller, $Z_v(s)$ is the transfer function of the virtual impedance and i_{out} is the measured output current. The block diagram of the output virtual impedance loop is shown in Figure 2.14.

If $Z_v(s) = R$, the converter sees a resistive output impedance which, although it mimics the response of a physical impedance, it does not introduce electrical losses. If the output virtual impedance is designed as $Z_v(s) = sL$, the converter sees an inductive output impedance. However, since a transfer function with a higher order in the numerator than in the denominator can not be implemented in a real system, J. Guerrero, de Vicuna, Miret, Matas, and Cruz (2004) propose a virtual impedance block as:

$$Z_v(s) = \frac{s}{s + \omega_c} Z_{v0} \tag{2.47}$$

where ω_c is the cutoff frequency of the high-pass filter and Z_{v0} is the nominal value of the virtual impedance.

Moreover, J. M. Guerrero et al. (2011) propose a strategy to prevent current spikes when the converter is connected to the microgrid (soft start) where the virtual impedance varies gradually from an initial value Z_i to a final value Z_f with a T time constant, as:

$$Z_{v0}(t) = Z_f - (Z_f - Z_i)\, e^{-t/T} \tag{2.48}$$

D'Arco, Suul, and Fosso (2015) propose a virtual impedance method with the scheme shown in Figure 2.15, recalling the equations of an inductive element in dq components:

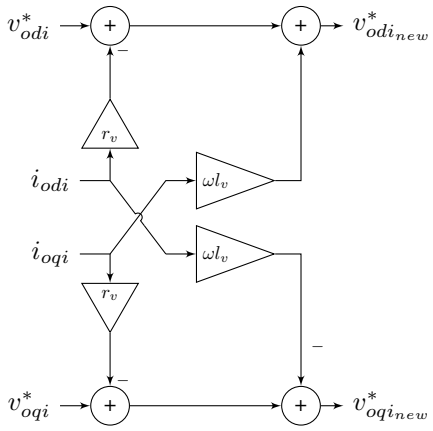

Figure 2.15: Virtual impedance approach in D'Arco, Suul, and Fosso, 2015, where r_v and l_v are the resistance and inductance values of the virtual impedance.

$$\begin{cases} v_d = L\dfrac{di_d}{dt} - \omega L i_q + R i_d \\ \\ v_q = L\dfrac{di_q}{dt} + \omega L i_d + R i_q \end{cases} \tag{2.49}$$

The comparison of (2.49) with Figure 2.15 reveals that the virtual impedance voltage drop obtained by D'Arco et al. (2015) is like the one of an inductive element in steady state:

$$\frac{di_{odi}}{dt} = \frac{di_{oqi}}{dt} = 0 \tag{2.50}$$

A similar approach to the virtual impedance is called transient virtual resistor (TVR), and was proposed by Qoria, Gruson, Colas, Kestelyn, and Guillaud (2020) and used by Avila-Martinez et al. (2022) to avoid a particular resonance around the grid frequency. The TVR block diagram is depicted in Figure 2.16.

The transient virtual impedance used by Paquette and Divan (2015) leads to a voltage drop on the voltage set points given by:

$$\begin{cases} v_{d,\mathrm{VI}} = R^0_{\mathrm{VI}} i_{od} s/\left(s+\omega_{c,\mathrm{hpf}}\right) - \omega L^0_{\mathrm{VI}} i_{oq} s/\left(s+\omega_{c,\mathrm{hpf}}\right) \\ \\ v_{q,\mathrm{VI}} = R^0_{\mathrm{VI}} i_{oq} s/\left(s+\omega_{c,\mathrm{hpf}}\right) - \omega L^0_{\mathrm{VI}} i_{od} s/\left(s+\omega_{c,\mathrm{hpf}}\right) \end{cases} \tag{2.51}$$

The first component, similar to the one used by Qoria et al. (2020), can be applied to improve the system damping. The whole virtual impedance voltage drop is similar to the one used by D'Arco et al. (2015) (see Figure 2.15) with a washout filter. Thus, the virtual impedance loop can also be applied to improve the system damping.

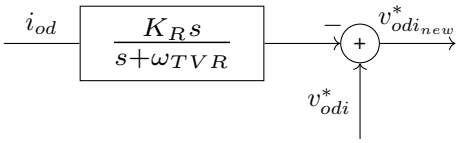

Figure 2.16: Transient virtual resistor block diagram, where i_{od} is the d component of the output current, v^*_{odi} is the d component of the voltage set point calculated by the droop control and $v^*_{odi_{new}}$ is the d component of the new voltage set point for the voltage controller. K_R (gain) and ω_{TVR} (cutoff frequency) are parameters of the washout filter. An analogous diagram was applied to the q component.

Regarding where to apply the voltage drop obtained by the virtual impedance loop, there are two main approaches: before the voltage and current controllers (D'Arco et al., 2015), and after the voltage and current controllers (J. M. Guerrero et al., 2011). If applied before the voltage and current controllers, the voltage drop passes through the two PI controllers and, therefore, can be considered in the saturation block. However, the PI controllers can slow down the virtual impedance response.

2.6 Decentralised consensus-based multi-agent control.

Kanerica (2024) defines a multi-agent system (MAS) as:

> "a collection of autonomous agents that interact and work together to solve complex problems or achieve a specific goal. Each agent in the system is a self-contained entity capable of making decisions and performing tasks independently. Additionally, these agents can communicate, cooperate, and even compete with each other to complete tasks that might be too complex for a single agent to handle."

There exist distributed architectures of MASs with an agent coordinator that manages the other agents, as shown in Andreadis, Klazoglou, Niotaki, and Bouzakis, 2014. However, in recent years, much more attention has been paid to decentralised multi-agent control where there is no central coordinator and "agents" collaborate (i.e., they exchange information) to achieve a desired behaviour, although each agent executes its own control actions. A specific type of multi-agent control where agents agree on a common value without the intervention of a central control is called "consensus-based" (Kanerica, 2024). In this thesis, the study of decentralised control structures will focus only on the first-order consensus protocol, as it is the most commonly used approach for microgrids.

The idea of decentralised control suits decentralised generation well and can be facilitated by modern technologies such as smart communications.

In consensus multi-agent control, each agent communicates only with a small group of agents called "neighbours". A "leader" who knows set-point values may or may not exist. In any case, the leader does not talk to every other agent in a MAS.

Consensus-based control strongly relies on graph theory, of which a brief summary follows. Interested readers can see Diestel (2000), for example, where graph theory is explained in detail.

Let $G = (V, E, A)$ be a graph of order N, where $V = \{v_1, v_2, \ldots, v_N\}$ is the set of the vertices or nodes of the graph (generally DGs in a microgrid are nodes of the graph), and $e_{ij} \in E \subseteq V \times V$ are pairs of nodes or edges of the graph (communication links between nodes). If edges are ordered pairs of nodes, they are said to be directed and information travels in only one direction from one node to the other one. Edges have weights which are collected in the so-called adjacency matrix of the graph A. Apart from these very general definitions, the graphs used in this thesis will have the following characteristics:

1. Only directed graphs or digraphs (graphs with directed edges) will be considered.
2. The element of the *ith* row and *jth* column of A is the weight of the communication link from j to i. If information travels from node j to node i, $a_{ij} > 0$ and $e_{ij} \in E$.
3. In the adjacency matrix of the graphs of interest $a_{ii} = 0 \; \forall \; i$.

The in-degree d_i of a node i is defined as,

$$d_i = \sum_{j=1}^{N} a_{ij} \tag{2.52}$$

in other words, d_i is the sum of the weights of those edges delivering information to node v_i.

The diagonal in-degree matrix D is:

$$D = \text{diag}(d_i) \text{ with } i = 1, 2 \ldots, N \tag{2.53}$$

and the Laplacian matrix L of the graph is:

$$L = D - A \tag{2.54}$$

Most approaches use (2.54) to model the graph Laplacian. However, the adjacency matrix construction and the Laplacian matrix differ between references. For example,

- Bidram, Davoudi, Lewis, and Sam Ge (2014), Dehkordi et al. (2021), Wong, Lim, Cruden, Rotaru, and Ray (2021) and Y. Zhang, Mohammadpour Shotorbani, Wang, and Mohammadi-Ivatloo (2021) use a_{ij} for the weight from j to i. It is the notation used in this thesis.

- Olfati-Saber and Murray (2004), Mohammadi et al. (2021) and Q. Sun, Han, Zhang, Zhou, and Guerrero (2015) use a_{ij} for the weight from i to j.
- Finally, Simpson-Porco et al. (2015), Zhou, Kim, Zhang, Sun, and Han (2018) and Khayat et al. (2020) always use bidirectional communications with $a_{ij} = a_{ji}$.

If each node v_i has an agent with an associated control variable x_i with first-order dynamics (i.e., their dynamic response can be modelled through first-order differential equations), the local control protocol is defined as:

$$\dot{x}_i = \sum_{j \in N_i} a_{ij} \left(x_j - x_i \right) \tag{2.55}$$

where N_i is the subset of nodes in V sending information to node i. In matrix form:

$$\begin{gathered} \dot{x} = -Dx + Ax = -(D - A)x \\ \dot{x} = -Lx \end{gathered} \tag{2.56}$$

Equation (2.55) means that the agent placed at node v_i changes its state x_i based on the state information (x_j) received from some (not all!) of its neighbours $v_j \in N_i$, where $N_i = \{v_j | a_{ij} > 0\}$[4].

Agents will reach a "consensus" if, in steady state,

$$x_i(t \to \infty) = x_j(t \to \infty) = \text{constant, c} \tag{2.57}$$

with,

$$\dot{x}_i = 0 \quad \text{and} \quad \sum_{j \in N_i} a_{ij} \left(x_j - x_i \right) = 0 \tag{2.58}$$

and this happens, if and only if, the graph has a spanning tree, i.e., there exist a path between every two nodes. This is equivalent to having all-but-one L eigenvalues with positive real part, and one eigenvalue with zero real part. Under these conditions, the consensus value c is (Bidram et al., 2017):

$$c = \sum_{i=1}^{N} p_i x_i(0) \tag{2.59}$$

where $x_i(0)$ is the initial value of x_i and

$$\begin{gathered} w_1 = [p_1, p_2, \ldots, p_N]^T \\ w_1^T \cdot L = 0 \\ ||w_1|| = 1 \end{gathered} \tag{2.60}$$

[4]Strictly speaking, any node with a connection with v_i (sending or receiving information) is its neighbour, but (2.55) excludes those who receive information from v_i ($a_{ji} > 0$) but do not send information to v_i ($a_{ij} = 0$). Recall the definition of digraph in this work. In fact, this thesis will often refer to N_i as the neighbours of v_i.

or, in other words, all agents evolve from an initial state to a final state (consensus value) that is the mean value of all agents' initial states (average-based consensus) (Rokrok, Shafie-khah, Siano, & Catalão, 2017).

If there is a "leader" (let us call it node v_0) who knows the "set point" for its state variable $x_0(\infty) = x_{ref}$ and communicates its value to, at least, one of the nodes of the rest of the graph (i.e., there is at least one edge $(v_0, v_i) \in E$) with a weight $g_i > 0$[5], the problem of finding a distributed control to drive all states to x_{ref} is know as the *synchronization and the cooperative tracker problem* (Bidram et al., 2017). In this case, (2.55) can be modified to:

$$\dot{x}_i = g_i(x_{ref} - x_i) + \sum_{j \in N_i} a_{ij} (x_j - x_i) \tag{2.61}$$

Lewis, Zhang, Hengster-Movric, and Das (2014) demonstrate that, in steady state,

$$x_i(t) = x_j(t) = x_{ref} \tag{2.62}$$

if, and only if, every node of the graph can be reached from the leader following the graph edges (i.e., the graph has a spanning tree with the leader as the root node). This condition is satisfied if, and only if, all the eigenvalues of matrix $L + G$ have a positive real part. G is a diagonal matrix:

$$G = diag(g_1, g_2, \ldots, g_N) \tag{2.63}$$

where, at least there is one $g_i > 0$.

2.7 Multi-agent secondary control of microgrids

In a multi-agent-based decentralised secondary control, unlike in a centralised controller, generators (agents) must collaborate to reach a solution, (the "consensus value"). Multi-agent-based control is attractive for microgrids, given the dispersed nature of RERs. The control proposed and analysed in this thesis is based on the one presented by Bidram et al. (2017).

2.7.1 Secondary control

The droop controllers (one for active-power and frequency control and another one for reactive-power and voltage control) used by Bidram, Davoudi, and Lewis (2014), shown in Figure 2.12, are of the form:

$$\begin{aligned} \omega_i &= \omega_{0,i} - m_{P_i} P_i \\ v_i &= v_{0,i} - n_{Q_i} Q_i \end{aligned} \tag{2.64}$$

where ω_i and v_i are, respectively, the frequency and voltage imposed by the GFr converter i, $\omega_{0,i}$ and $v_{0,i}$ its no-load frequency and voltage, m_{P_i} and n_{Q_i} its active

[5]Weights g_i between the leader and any other node are called *pinning gains*.

and reactive droop coefficients, and P_i and Q_i its measured output active and reactive power.

Although the previous droop, without explicit active and reactive power set points, is already used by Bidram et al. (2014) in microgrids with electronic-based generation, there is a different formulation for droop control based on active power set points, as the one used by Simpson-Porco, Dörfler, and Bullo (2013):

$$\begin{aligned} \omega_i &= \omega_{ref,i} - m_{P_i}\left(P_i - P_{ref,i}\right) \\ v_i &= v_{ref,i} - n_{Q_i}\left(Q_i - Q_{ref,i}\right) \end{aligned} \tag{2.65}$$

where ω_i and v_i are, respectively, the frequency and voltage imposed by the GFr converter i, $\omega_{ref,i}$ and $v_{ref,i}$ its frequency and voltage set points, m_{P_i} and n_{Q_i} its active and reactive droop coefficients, P_i and Q_i its measured output active and reactive power and $P_{ref,i}$ and $Q_{ref,i}$ its active and reactive power set points.

The secondary control in (2.64) modifies $\omega_{0,i}$ and $v_{0,i}$ to control ω_i and v_i. This is equivalent to modifying $\omega_{ref,i}$ and $v_{ref,i}$ in (2.65). However, in general, traditional centralised secondary control modifies the active power set point of generation units instead of their frequency set points (see, for example, the automatic generation control (AGC) described by Egido et al. (2009)). Putting (2.64) and (2.65) together,

$$\omega_{0,i} - m_{P_i}P_i = \omega_{ref,i} - m_{P_i}\left(P_i - P_{ref,i}\right) \tag{2.66}$$

which leads to:

$$P_{ref,i} = \frac{\omega_{0,i} - \omega_{ref,i}}{m_{P_i}} \tag{2.67}$$

The relationship in (2.67) implies that the active power set point is implicit in the frequency set point $\omega_{0,i}$ in (2.64). The same applies to the reactive power set point and the voltage set point.

Secondary frequency control

Figure 2.17 shows how a given $GFr - VSC_i$ changes the set points of its output frequency (ω_i^*) as a function of (a) the actual output values of its active power and frequency; and (b) information from its neighbours (subscript j). The algorithm tries to achieve a steady-state consensus on the system frequency and the way in which converters share changes in the demanded active power.

The controller presented in Figure 2.17 is like the one in Bidram et al. (2017) but adds a constant communication time delay from DGj to DGi, represented by transfer function $T_d(s)$.

In the case of active-power and frequency control (Figure 2.17):

1. There is a leader converter (and only one) that knows the frequency set point to be reached in the grid (ω_{ref}). Without loss of generality, let us assume that $\mathrm{GFr} - \mathrm{VSC}_1$ is the leader converter, in which case $g_1 = 1$ [6]($g_j = 0\ j \neq 1$) and

[6]Pinning gain as defined by Bidram et al. (2017).

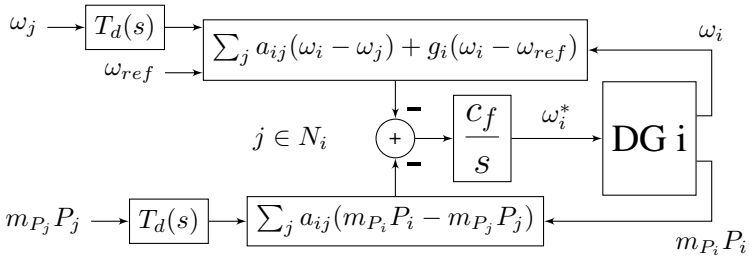

Figure 2.17: Diagram of the ω-P secondary control of a grid-forming converter. ω_i^* is the frequency set point for the primary control. Adapted from Bidram, Davoudi, and Lewis (2014).

$N_1 = \emptyset$, because the leader does not receive information from neighbours (there is no $a_{1j} \neq 0$).

2. The input of the integral block (c_f/s) in Figure 2.17 must be zero in steady state, in all converters. Therefore:

   - For the leader ($g_1 = 1$ and $a_{1j} = 0,\ \forall j$),

   $$\omega_1 = \omega_{ref} \tag{2.68}$$

   - For any other GFr $-$ VSC$_i$ ($g_i = 0$):

   $$\sum_{\forall j} a_{ij} \left(\omega_i + m_{P_i}P_i - \omega_j - m_{P_j}P_j\right) = 0 \tag{2.69}$$

3. If steady state is reached after a disturbance, the system frequency is unique (a global parameter) and, in Figure 2.17,

   $$\omega_i = \omega_j = \omega_{ref}\ \forall\ i, j \tag{2.70}$$

   where ω_{ref} is the frequency set point (e.g., $\omega_{ref} = 2\pi \cdot 50$ rad/s).

4. Taking (2.70) to (2.69) yields,

   $$m_{P_i}P_i \sum_{\forall j} a_{ij} = \sum_{\forall j} m_{P_j}P_j \ \Rightarrow\ P_i = \frac{\sum_{\forall j} m_{P_j}P_j}{m_{P_i} \sum_{\forall j} a_{ij}} \tag{2.71}$$

that quantifies the way in which GFr-VSCs in the grid share the active-power load.

Secondary voltage control

Figure 2.18 shows how a given $GFr - VSC_i$ changes the set points of its output voltage magnitude (v_i^*) as a function of (a) the actual output values of its reactive

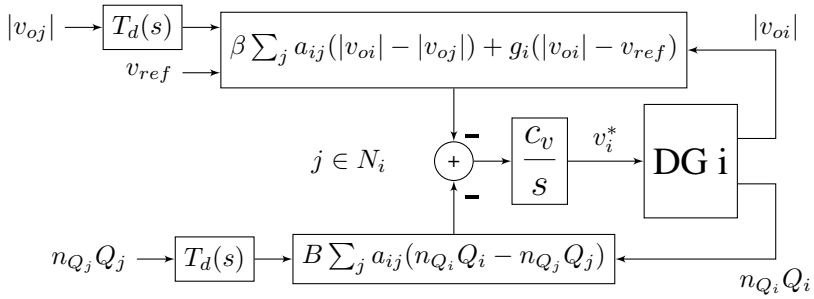

Figure 2.18: Diagram of the v-Q secondary control of a grid-forming converter. v_i^* is the voltage set point for the primary control. Two parameters are introduced to ensure either consensus in reactive power sharing (B) or in voltage amplitude consensus (β). Adapted from Bidram, Davoudi, and Lewis (2014).

power and voltage; and (b) information from its neighbours (subscript j). The algorithm tries to achieve a steady-state consensus on the way in which converters share changes in the demanded reactive power and their output voltages.

Things are quite different in the case of voltage and reactive-power control because not all buses will have the same voltage in steady state (voltage is not a global variable) and because the reactive power flows across the grid are closely related to the voltage profile of the grid buses in grids with mainly inductive lines.

1. Nevertheless, the input signal of the integrator (c_v/s) in Figure 2.18 must be zero. Therefore,

$$\sum_{\forall j} \left[\beta a_{ij} \left(|v_{oi}| - |v_{oj}|\right) + B a_{ij} \left(n_{Q_i} Q_i - n_{Q_j} Q_j\right)\right] + g_i \left(|v_{oi}| - v_{ref}\right) = 0 \quad (2.72)$$

2. In this case, one may accept having several leaders with different voltage set points. Then, if z is a "voltage leader" bus ($a_{zj} = 0,\ \forall j$ and $g_z = 1$), and its voltage set point is $v_{ref,z}$, it yields,

$$v_{oz} = v_{ref,z} \quad (2.73)$$

3. Meanwhile, in any other GFr $-$ VSC$_i$ (non leader, $g_i = 0$):

$$\sum_{\forall j} \left[\beta a_{ij} \left(|v_{oi}| - |v_{oj}|\right) + B a_{ij} \left(n_{Q_i} Q_i - n_{Q_j} Q_j\right)\right] = 0 \quad (2.74)$$

   - If in (2.74), $\beta = 0$, and $B \neq 0$:

$$Q_i = \frac{\sum_{\forall j} a_{ij} n_{Q_j} Q_j}{n_{Q_j} \sum_{\forall j} a_{ij}} \quad (2.75)$$

     that describes the way in which GFr-VSCs share the reactive-power load across the grid.

- If in (2.74), $\beta \neq 0$, and $B = 0$:

$$|v_{oi}| = \frac{\sum_{\forall j} a_{ij} |v_{oj}|}{\sum_{\forall j} a_{ij}} \tag{2.76}$$

that describes the grid voltage profile in steady state.

Since the control dynamics in Figures 2.17 and 2.18 are of the first order, they can be modelled by the graph Laplacian matrix with (2.56). Therefore, graph theory can be applied to this control structure. The two gains (β and B, with value 0 or 1) introduced in Figure 2.18, weigh voltage consensus and reactive power sharing and can be used to select one of them, as stated by Simpson-Porco et al. (2015). In this thesis, GFr converters will not seek voltage consensus ($B = 1;\ \beta = 0$) to make consensus in reactive-power sharing possible. In the case of voltage consensus, voltages can be weighted using constants to have a consensus on the desired voltage profile; not all voltages have to be the same value, since voltage is a local variable.

The performance of the consensus-seeking control algorithms described above was investigated in a modified version of the IEEE 69-bus test system, in which the generation units are seven GFr-VSCs. The structure and parameters of the test system, the controllers of the grid-forming converters, and the initial operating point for the simulations are included in Appendix C.

The microgrid was modelled, initialised and linearised using the author-developed Simulink®-based tool described in Appendix A. The inputs chosen are current injections into each bus, and the outputs chosen are the frequencies, voltages, and generated active and reactive power of each DG.

Figures 2.19 to 2.21 show the difference between seeking reactive-power-sharing consensus ($B = 1;\ \beta = 0$), voltage consensus ($B = 0;\ \beta = 1$) or both ($B = 1;\ \beta = 1$). These figures show the response of the frequency, voltage, active and reactive power of all GFr-VSCs in the modified IEEE 69-bus test system to the following events:

- At $t = 10$ s, the secondary control layer is activated (on frequency, voltage, active and reactive power).
- At $t = 30$ s, the load on bus 1 is increased by 300 kW.

Clearly, after the activation of the secondary control layer, the consensus is achieved on frequency, active power, and voltage or reactive power, depending on the selected case. After the demand variation, the frequency, active power sharing and reactive power sharing (or voltage) change, and are later recovered by the secondary control. Note that the existing oscillations are related to consensus control dynamics and are not the focus of this analysis. They can be reduced by slowing down the secondary control.

1. Figure 2.19 ($B = 1;\ \beta = 0$). Reactive-power consensus is achieved while the voltage profile of the GFr-VSCs is determined by the grid structure and

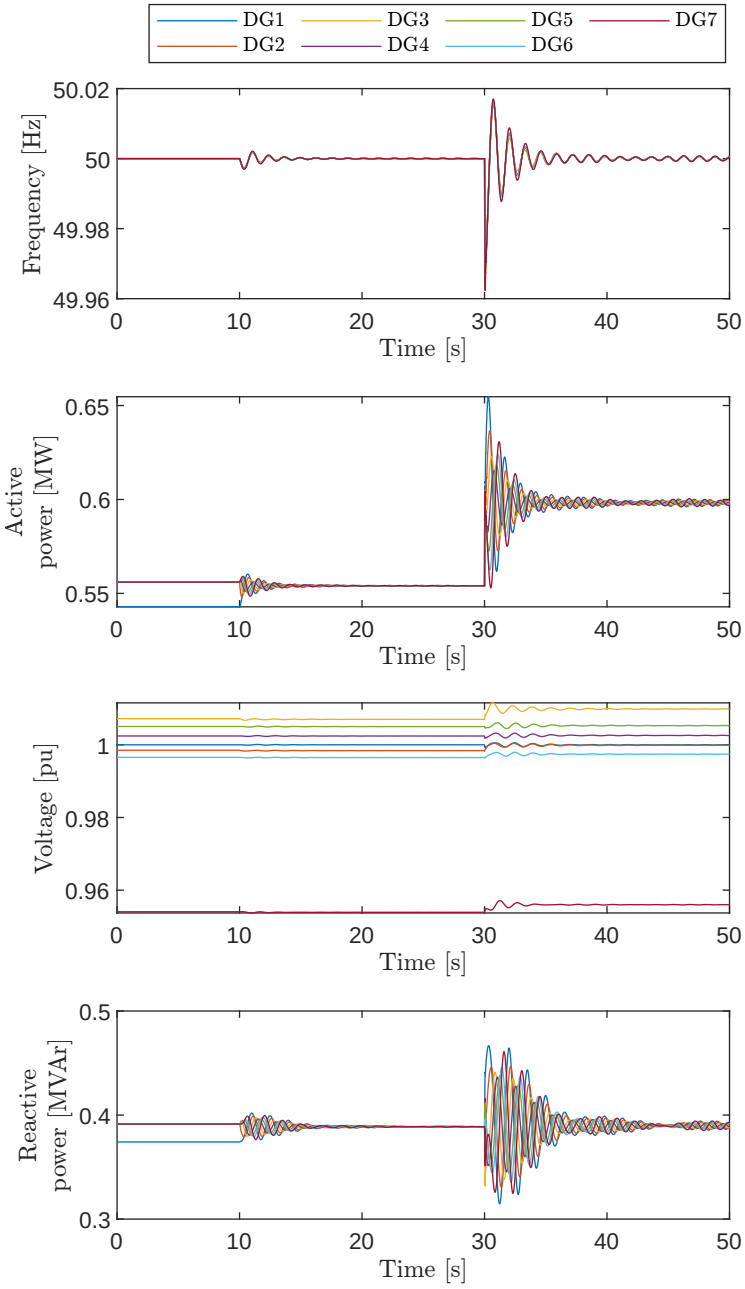

Figure 2.19: Frequency, voltage, active and reactive power of all GFr converters in the modified IEEE 69-bus test system during the simulation in the case of seeking reactive-power-sharing consensus ($B = 1;\ \beta = 0$).

parameters. Notice that DG7 has a considerably lower voltage amplitude than the others due to its location in the microgrid (see Appendix C).

2. Figure 2.20 ($B = 0;\ \beta = 1$). Note that, in this case, all converters are forced to follow the same voltage. In a real implementation, the optimal voltage profile may be sought using an optimal power flow (OPF). Clearly, when voltage consensus is sought, the reactive power sharing among GFr-VSCs is determined by the grid structure and parameters.

3. Finally, Figure 2.21 ($B = 1;\ \beta = 1$). Clearly, when both the consensus in voltage and reactive-power-sharing are sought, none of them are met. In case of both, voltage profile is closer to consensus than in the case of reactive-power consensus only. Analogously, in case of both, reactive-power profile is closer to consensus than in the case of voltage-consensus only.

2.7.2 Influence of communication delays in the stability of the consensus algorithm

In centralised or decentralised secondary control, there are several communication links. Since communication between different devices can be carried out using several protocols (e.g., TCP) and communication links can have different lengths, the time lapse for data transmission can vary considerably. Therefore, some references include a communication delay in their secondary control model. Different models of communication delays in the literature are compared in Table 2.2.

Table 2.2: Different approaches to model time delay. "C" column indicates if the reference includes a consensus algorithm. "S/D" column indicates whether the reference includes a stochastic (S) or deterministic (D) model of the time delay.

Reference	C	Delay model	S/D
Shahab et al. (2019)	✓	constant delay with white noise	S
Dehkordi et al. (2021)	✓	time-varying with white noise	S
Coelho et al. (2016)	✓	delay differential equations	D
Milano and Anghel (2012)	×	delay differential equations	D
Olfati-Saber and Murray (2004)	✓	Padé approximation	D
Olfati-Saber, Fax, and Murray (2007)	✓	Laplace exponential	D
Manshang et al. (2018)	✓	self (processing) and communication	D
Wong, Lim, Cruden, Rotaru, and Ray (2021)	✓	constant delay	D

Delay models can be deterministic (delay differential equations, Padé approximation, Laplace exponential), which can be studied analytically, and stochastic

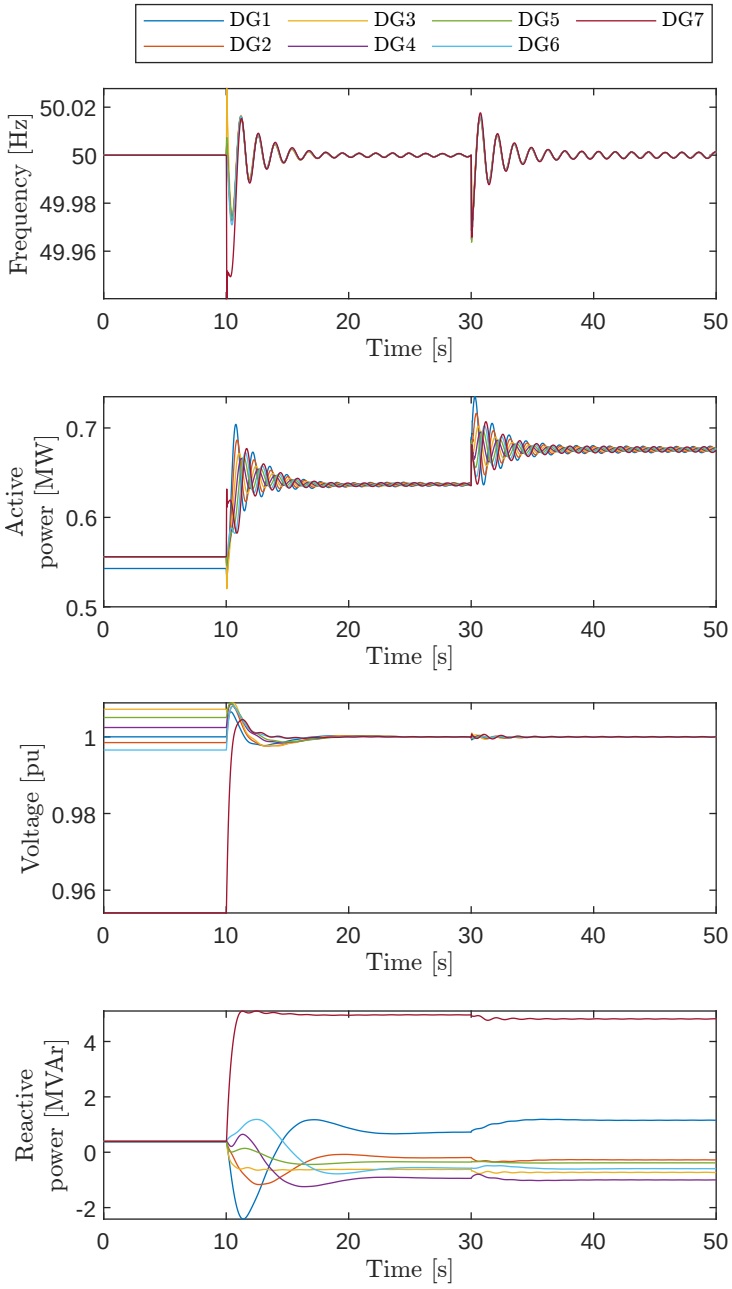

Figure 2.20: Frequency, voltage, active and reactive power of all GFr converters in the modified IEEE 69-bus test system during the simulation in the case of seeking voltage consensus ($B = 0;\ \beta = 1$).

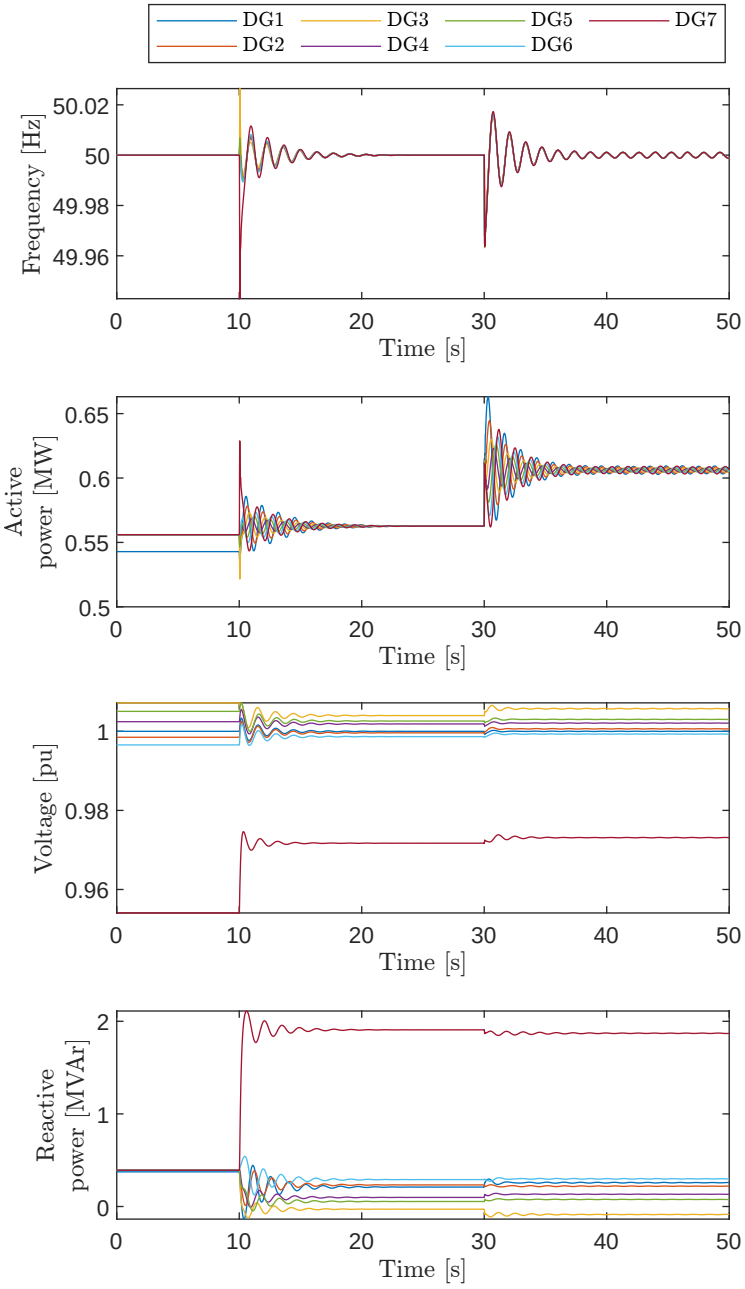

Figure 2.21: Frequency, voltage, active and reactive power of all GFr converters in the modified IEEE 69-bus test system during the simulation in the case of seeking both voltage and reactive-power-sharing consensus ($B = 1;\ \beta = 1$).

(time-varying with white noise, constant delay with white noise), which can be characterised by their mean and variance values. The former category is used in linear analysis, such as in small-signal stability studies, and the latter is often used in non-linear time-domain simulation. However, recently, Jankovic, Roldán-Pérez, Prodanovic, and Rouco (2024) demonstrated that the consideration of the delay mean value is enough for most stability and performance studies of systems with high penetration of electronic converters.

As stated by Olfati-Saber and Murray (2004), the graph topology has a strong influence on the robustness of a consensus algorithm to time delays. That work states that, considering an undirected graph, the delay (τ) must be bounded to guarantee stability:

$$\tau \leq \frac{\pi}{4d_{\max}(G)} \tag{2.77}$$

where $d_{\max}$ is the maximum out-degree of the agents included in the graph.

This theoretical delay limit does not apply to the consensus algorithms that will be proposed and analysed in this thesis, due to three reasons:

- The graphs used for the consensus algorithms proposed and analysed in this thesis are directed[7].
- The graphs used have a leader-follower structure, with a pinning gain (and only one).
- Unlike in Olfati-Saber and Murray (2004), this thesis explores several consensus problems simultaneously and there are inner control structures that may also have something to say.

Therefore, in this thesis, the delay limit below which the consensus algorithm is stable is calculated by modal analysis of the complete linearised system, modelling the delay, in every communication link, with a third-order Padé approximation (Olfati-Saber & Murray, 2004). Figure 2.22 shows the pole loci of the complete linearised system of the modified IEEE 69-bus test system when increasing the communication time delay between GFr-VSCs. Eigenvalues are shown using a magnitude-phase representation that allows the simultaneous representation of eigenvalues with large and small magnitudes. In case of a pair of conjugate eigenvalues, only the one with positive imaginary part has been included. Eigenvalues with phase between 90 and 270 degrees are stable (i.e., they have negative real parts). With the data used, the results obtained by the analysis presented in this section demonstrate thatthe delay limit below which the consensus algorithm is stable is around 60 ms.

[7] In a directed graph, having communication from node i to node j does not imply having communication from node j to node i

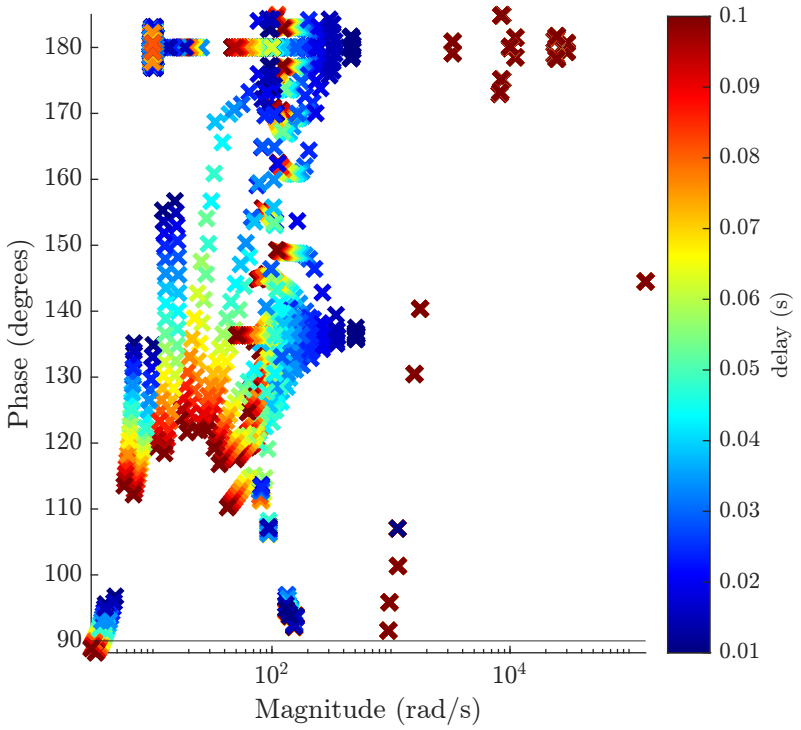

Figure 2.22: Movement of the eigenvalues of the linear approximation of the modified IEEE 69-bus test system when increasing the communication time delay between GFr-VSCs converters. The delay was modified between 0.01 s and 0.1 s.

2.7.3 Event-triggered multi-agent secondary control

Communications in consensus-based secondary control can use continuous messages or triggered messages. In the former case, messages are sent as soon as the communication channel is available, keeping the communication channel used all the time but easing the modelling, analysis, design and implementation of the secondary control layer. In the latter case, messages are sent after an event occurs, for example, only when the absolute value of the difference between the measurement value ($x(t)$) and the last value sent by the agent ($x(\tau)$) exceeds a threshold (th), as follows (Jamali, Baghaee, Sadabadi, Gharehpetian, & Anvari-Moghaddam, 2023).

$$|x(t) - x(\tau)| > th \tag{2.78}$$

This alternative should require a smaller channel bandwidth than the former, and can even reduce the communication time delay in cases with congestion with continuous messages. The threshold used in consensus-based triggered secondary

control can be either a constant value or a variable one and can be applied to continuous variables or discrete (sampled) ones (Khayat et al., 2020).

The sum of the square of errors between the last sent value and the actual measured value is compared by Jamali et al. (2023) with the threshold to establish the trigger function. A similar trigger mechanism is applied to the secondary control of a hybrid AC/DC microgrid by C. Yang, Zheng, Bu, Li, and Guerrero (2024).

Using a variable threshold allows for more advanced message reduction. A time-dependent threshold is introduced in J. Zhang, Sun, and Zhao (2023). The algorithms for triggered consensus-based secondary control normally use an event-based (i.e., threshold-based) trigger mechanism. However, a hybrid scheme is presented by K. Zhao, Xiao, Li, Wang, and Wei (2024), switching between time-based (i.e., a message is sent every time interval) and event-based trigger mechanisms.

The event-triggered secondary control proposed here activates the communication if:

$$\psi = A^{v}_{sec}|v(t)-v(\tau)| + A^{\omega}_{sec}|\omega(t)-\omega(\tau)| + A^{P}_{sec}|P(t)-P(\tau)| + A^{Q}_{sec}|Q(t)-Q(\tau)| > 1 \tag{2.79}$$

where A^{v}_{sec}, A^{ω}_{sec}, A^{P}_{sec} and A^{Q}_{sec} are threshold gains, t is the time instant and τ is the time of the last message sent. A new message is sent when $\psi > 1$. In this case, a constant communication delay of 10 ms is introduced in all communication links. Along this thesis, communication delays are varied from a few milliseconds, realistic delays for the best communication case, as shown in Chapter 4, to hundreds of milliseconds, a realistic case in a worse communication condition.

Figures 2.23 to 2.25 show the influence of the threshold value on the dynamic response of the system. The figures shows the response of frequency, voltage, and active and reactive power of all GFr converters in the modified IEEE 69-bus test system to the same events as before.

Figure 2.23 shows frequency, voltage, and active and reactive power of all GFr-VSCs, and total number of messages sent in the modified IEEE 69-bus test system during the simulation with a threshold function with $A^{v}_{sec} = A^{f}_{sec} = A^{P}_{sec} = A^{Q}_{sec} = 10^2$ (value decided by simulation) for the triggered secondary control.

Clearly, consensus is not fully reached with the threshold function used. However, the system remains stable and the number of messages sent is low.

Figure 2.24 shows frequency, voltage, active and reactive power of all GFr-VSCs, and total number of messages sent in the modified IEEE 69-bus test system during the simulation with a threshold function with $A^{v}_{sec} = A^{f}_{sec} = A^{P}_{sec} = A^{Q}_{sec} = 10^3$ for the triggered secondary control. Clearly, the consensus in active and reactive power improves. However, the number of messages sent is higher than before.

Finally, Figure 2.25 shows frequency, and voltage, active and reactive power of all GFr-VSCs, and total number of messages sent in the modified IEEE 69-bus test system during the simulation with a threshold function with $A^{v}_{sec} = A^{f}_{sec} = A^{P}_{sec} = A^{Q}_{sec} = 10^4$ for the triggered secondary control. Now, consensus is fully reached with those thresholds, but it has the highest number of messages sent.

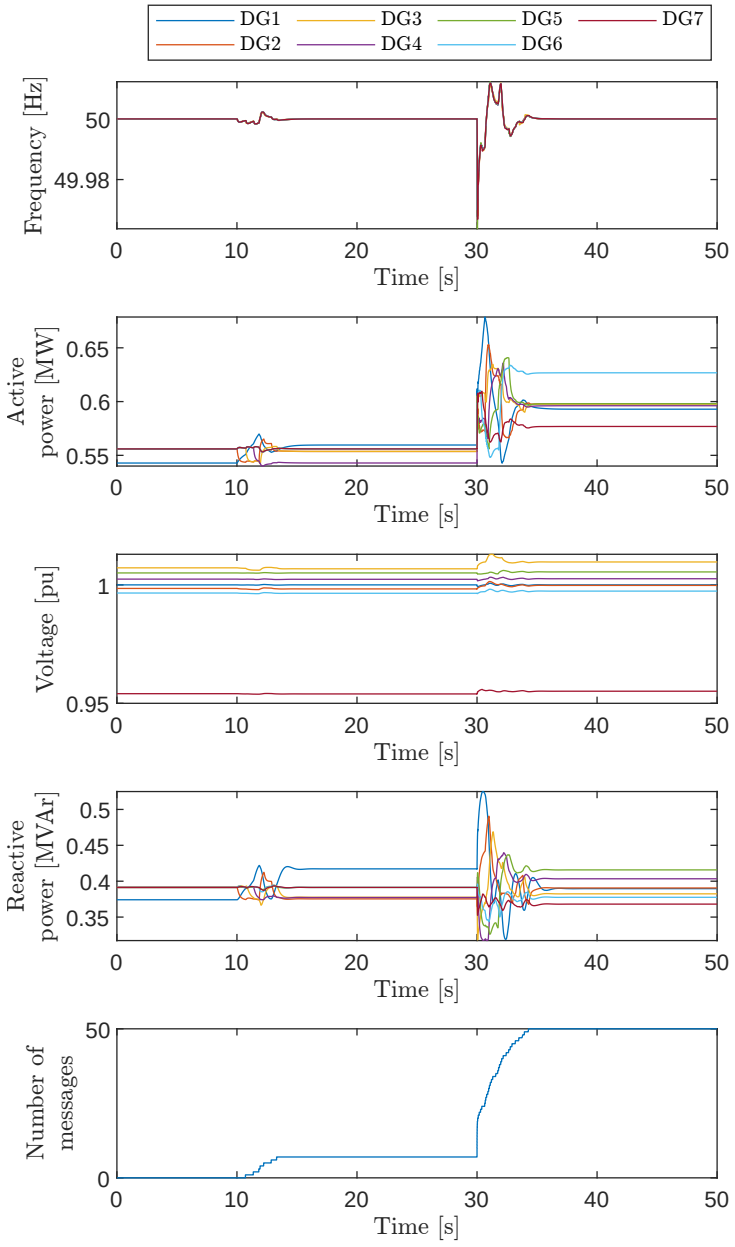

Figure 2.23: Frequency, voltage, active and reactive power of all GFr-VSCs, and total number of messages sent in the modified IEEE 69-bus test system during the simulation with a threshold function with $A^v_{sec} = A^f_{sec} = A^P_{sec} = A^Q_{sec} = 10^2$ for the triggered secondary control.

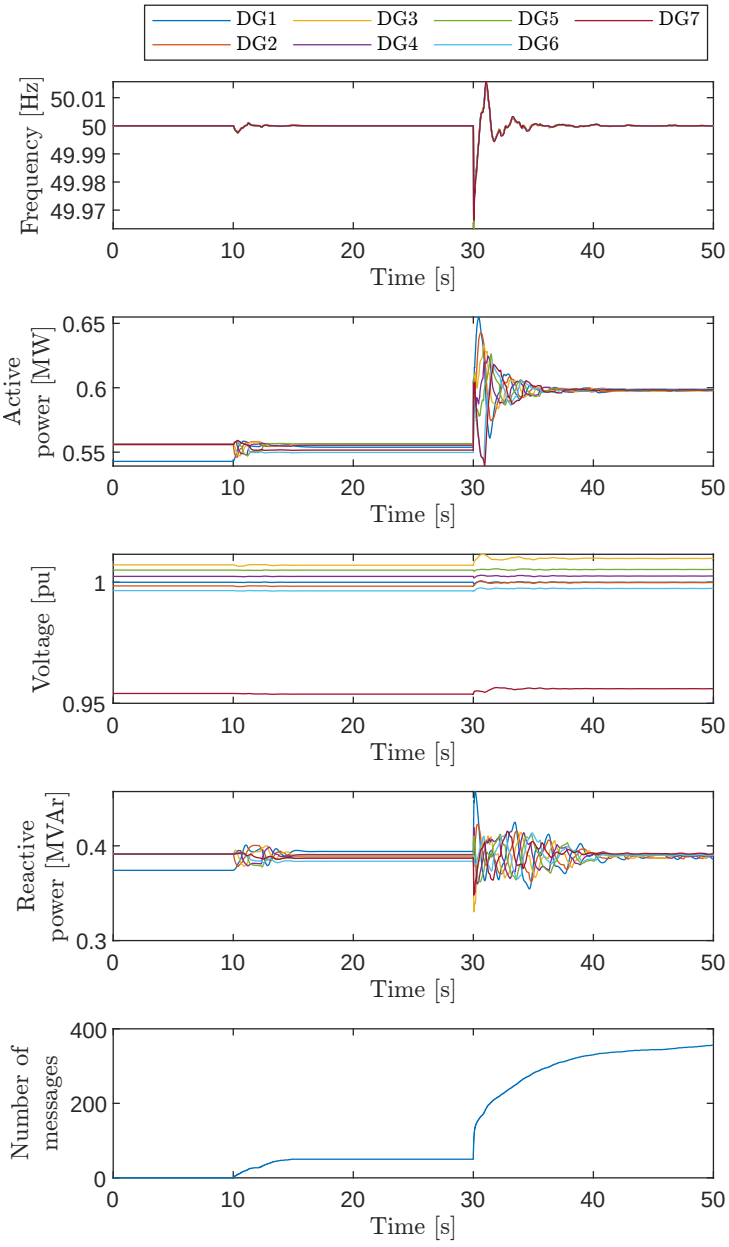

Figure 2.24: Frequency, voltage, active and reactive power of all GFr-VSC, and total number of messages sent in the modified IEEE 69-bus test system during the simulation with a threshold function with $A^v_{sec} = A^f_{sec} = A^P_{sec} = A^Q_{sec} = 10^3$ for the triggered secondary control.

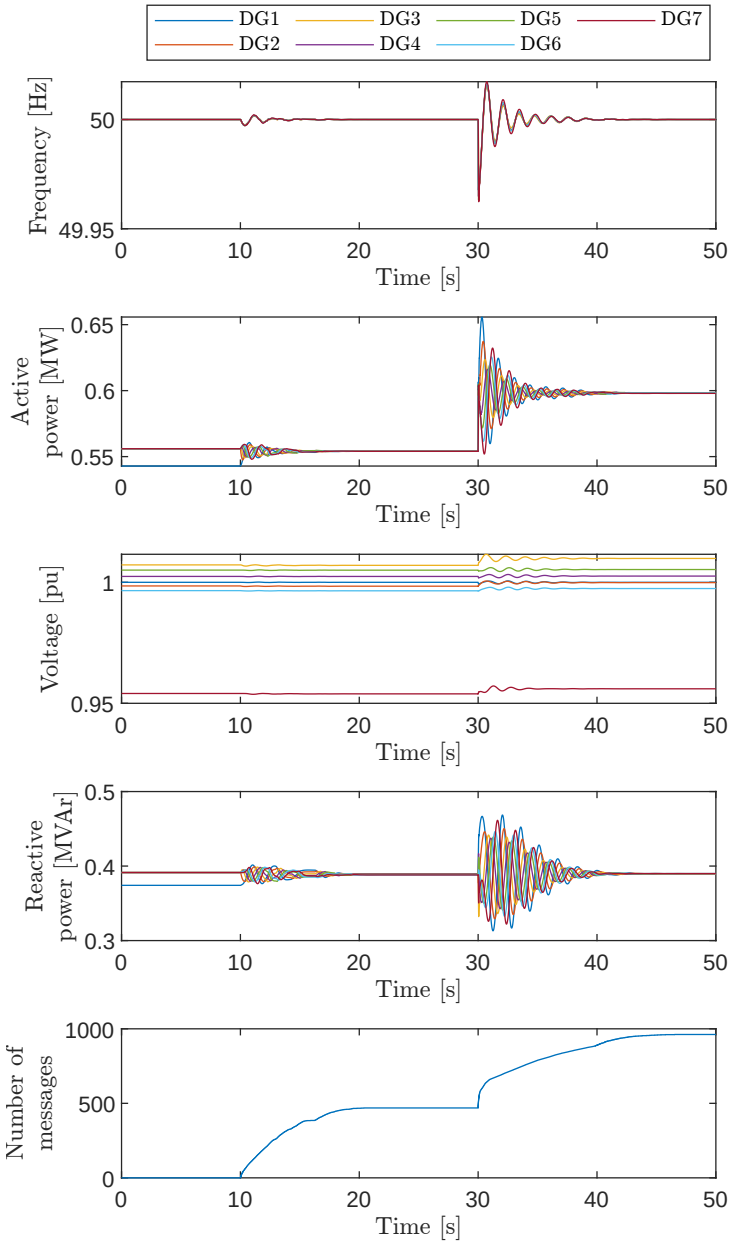

Figure 2.25: Frequency, voltage, active and reactive power of all GFr-VSC, and total number of messages sent in the modified IEEE 69-bus test system during the simulation with a threshold function with $A^v_{sec} = A^f_{sec} = A^P_{sec} = A^Q_{sec} = 10^4$ for the triggered secondary control.

The threshold function parameters must be carefully designed to limit the number of messages without significantly affecting the overall performance of the secondary control. This design is system-dependent and can be carried out ad hoc (i.e., for each case)with simulation. The stability of triggered secondary control is validated in this thesis by simulation. Therefore, it is only guaranteed for the tested conditions, similarly to eigenvalue stability analysis with constant communication delays in the case of continuous communications.More about the performance of event-triggered consensus control can be found in Chapter 6.

2.8 Decentralised incremental secondary control

The existing algorithms for decentralised secondary control either do not consider the tertiary control set points (Espina, Cárdenas-Dobson, Simpson-Porco, Kazerani, & Sáez, 2023) or involve the economic dispatch on the dynamic control of the system (Dorfler, Simpson-Porco, & Bullo, 2016). The latter makes the tertiary control layer vulnerable to communication time delays.

This chapter proposes an incremental secondary control layer based on consensus. This formulation eases its implementation as a slave of a tertiary control layer while maintaining separate dynamics. Details of a consensus-based tertiary control will be discussed in Chapter 5. The incremental approach acts only on deviations from the tertiary control set points, similarly to a centralised AGC (Egido et al., 2009). This novel incremental formulation considers the active-power limits of the units. If the secondary control is cost-orientated, its achieves a lower cost than the conventional secondary control, as will be shown in the results of this chapter. Generation or demand variations from the dispatched values and power losses cause these deviations. The incremental notation used for secondary control is described by equations (2.80)-(2.83):

$$\frac{d\Delta\omega_i^{ref}}{dt} = \sum_{j\in N} a_{ij}^{\omega}(\Delta\omega_j^{ref} - \Delta\omega_i^{ref}) - g_i^{\omega}\Delta\omega_i^{ref} \tag{2.80}$$

$$\begin{aligned}\frac{d\Delta P_i^{ref}}{dt} = &\sum_{j\in N} a_{ij}^{P}\left(\frac{\Delta\omega_j - \Delta\omega_i}{m_{P_i}} + k_j\Delta P_j - k_i\Delta P_i\right)\\ &- g_i^{P}\Delta P_i - g_i^{\omega}\Delta\omega_i\end{aligned} \tag{2.81}$$

where k_i is a constant with the information for the desired power sharing. Initially $k_i = m_{P_i}$.

$$\frac{d\Delta v_i^{ref}}{dt} = \sum_{j\in N} a_{ij}^{v}(\Delta v_j - \Delta v_i) - g_i^{v}\Delta v_i \tag{2.82}$$

$$\frac{d\Delta Q_i^{ref}}{dt} = \sum_{j \in N} a_{ij}^{Q}(\Delta Q_j - \Delta Q_i) - g_i^{Q}\Delta Q_i \tag{2.83}$$

where, if x is the frequency, active power, reactive power, or voltage, Δx_i^{ref} is the increment for the set-point value given by the tertiary control[8], $\Delta x_i = x_i - x_i^{ref,T}$ is the measured deviation of x_i from the tertiary control set point, g_i^x are the pinning gains for frequency, active and reactive power, and voltage and a_{ij}^x are the elements of the adjacency matrices for frequency, active and reactive power, and voltage.

2.8.1 Proof of convergence of the proposed secondary control using a Lyapunov function

Let us define the state vector:

$$\Delta\omega^{\text{ref}} = \begin{bmatrix} \Delta\omega_1^{\text{ref}} \\ \Delta\omega_2^{\text{ref}} \\ \vdots \\ \Delta\omega_n^{\text{ref}} \end{bmatrix} \tag{2.84}$$

The Laplacian matrix (L^ω) of a graph is:

$$L^\omega = D^\omega - A^\omega \tag{2.85}$$

where A is the adjacency matrix, and D is the in-degree matrix whose elements are defined as:

$$d_{ii}^\omega = \sum_{\forall j \in N} a_{ij}^\omega \tag{2.86}$$

and the pinning matrix of the graph is:

$$G^\omega = \text{diag}\left(g_1^\omega, g_2^\omega, \ldots, g_n^\omega\right) \tag{2.87}$$

One can rewrite the consensus in equation (2.80) in vector form as:

$$\frac{d\Delta\omega^{ref}}{dt} = -\left(L^\omega + G^\omega\right)\Delta\omega^{ref} \tag{2.88}$$

Let us now define the following Lyapunov function candidate:

$$J\left(\Delta\omega^{ref}\right) = \frac{1}{2}\left(\Delta\omega^{ref}\right)^T \Delta\omega^{ref} \tag{2.89}$$

which is definite positive for $\Delta\omega^{ref} \neq 0$ and $J(0) = 0$.

The derivative of $J\left(\Delta\omega^{ref}\right)$ is:

[8] the set point for the primary control layer is $x_i^{ref} + \Delta x_i^{ref}$

$$\frac{dJ}{dt} = \left(\Delta\omega^{ref}\right)^T \frac{d\Delta\omega^{ref}}{dt} = -\left(\Delta\omega^{ref}\right)^T \left(L^{\omega} + G^{\omega}\right) \Delta\omega^{ref} \tag{2.90}$$

Therefore, J is a Lyapunov function (that is, the consensus is guaranteed) if $(L^{\omega} + G^{\omega})$ has all its eigenvalues with positive real part ($\mathrm{Real}(\lambda_i) > 0 \; \forall \; i$).

Similarly, one can demonstrate the convergence of (2.83) and (2.82) given that v_i and Q_i are directly affected by v_i^{ref} and Q_i^{ref} respectively.

The convergence of (2.81) can also be demonstrated if the system is assumed to remain synchronised in steady state ($\omega_i = \omega_j \; \forall \; i, j$).

This chapter adopts the leader-based pinning gain procedure used by Bidram et al. (2014), in which only the DGs playing a leader's role have non-zero pinning gains. In this case, without loss of generality, only one leader will be considered in the system. The leader is in charge of recovering the voltage and frequency of the system after any disturbance. Therefore, if the leader is the DG k:

$$g_k^{\omega} = g_k^{v} = 1 \qquad\qquad g_i^{\omega} = g_i^{v} = 0 \;\; \forall \;\; i \neq k \tag{2.91}$$

Since in island operation the active power and reactive power served must satisfy the demand, there cannot be fixed power set points for the leaders and the proposed method does not involve pinning gains for active and reactive power:

$$g_i^{P} = g_i^{Q} = 0 \;\; \forall \;\; i \tag{2.92}$$

As discussed in Section 2.7.1, consensus on voltage profile and reactive power can not be achieved simultaneously. Here, only reactive power consensus has been sought in the secondary control layer.

The active power set points calculated by the secondary control are saturated to comply with the DGs operating range. If the leader is with its active power set point saturated, its role is passed to the next DG that is not saturated because it needs some active-power margin to recover the frequency.

2.8.2 Cost-based secondary control

The cost of the active power provided by DG_i is calculated as:

$$c_i = c_{A_i} P_i^2 + c_{B_i} P_i + c_{C_i} \tag{2.93}$$

where c_{A_i}, c_{B_i} and c_{C_i} are the quadratic, linear and constant cost coefficients, respectively.

The consensus problem can also be formulated in terms of the costs to operate each DG (c_i) by modifying the active-power-sharing coefficients as:

$$k_i^{cost} = k_i \frac{dc_j}{dc_i \sum_j \frac{dc_j}{dc_i}} \tag{2.94}$$

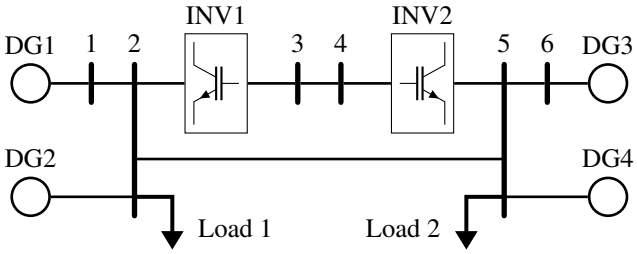

Figure 2.26: 6 bus system with a point-to-point VSC-based DC link between buses 2 and 5.

where:

$$dc_i = \frac{\partial c_i}{\partial P_i} = 2c_{A_i}P_i + c_{B_i} \tag{2.95}$$

If the measured active power of the units is above their scheduled active power (i.e., the demand is higher than the dispatched, the unit must increase its power), the most expensive unit must have the lowest increment. If the measured active power of the units is below their scheduled active power (i.e., the demand is lower than the dispatched, the unit must decrease its power), the most expensive unit must have the highest decrement. To change the active-power sharing, if the scheduled active power is above the measured one, a_{ij}^P can be modified further as:

$$dc_i = \begin{cases} \dfrac{\partial c_i}{\partial P_i} = 2c_{A_i}P_i + c_{B_i} & \Delta P_i > 0 \\ \dfrac{1}{\dfrac{\partial c_i}{\partial P_i}} = \dfrac{1}{2c_{A_i}P_i + c_{B_i}} & \Delta P_i < 0 \end{cases} \tag{2.96}$$

2.8.3 Case study: Hybrid DC/AC microgrid

The secondary control proposed here is applied to a hybrid DC/AC microgrid. For simplicity, continuous messages are used instead of event-triggered control. However, the proposed control structure can also be used with event-triggered control. The electric system to be used is depicted in Figure 2.26. It is a hybrid AC/DC microgrid with four grid-forming converters DG1-4 and two DC/AC interface converters INV1 and INV2, controlled as grid-following converters on the AC side. The control structure for the interface converters INV1 and INV2 is the one shown in Figure 2.6. The parameters of the system model used are shown in Table 2.5.

As a novelty (in the previous case studies presented in this thesis, the DC voltage of the grid-forming converter was considered ideal), the DC part of the

Table 2.3: Cost coefficients and power range for every agent in Figure 5.2.

DG	$\mathbf{C_{B_i}}$ $[\$/\mathbf{MW}]$	$\mathbf{C_{A_i}}$ $[\$/\mathbf{MW^2}]$	$\mathbf{P_{min}}$ $[\mathbf{MW}]$	$\mathbf{P_{max}}$ $[\mathbf{MW}]$
1	2	0.04	0	80
2	3	0.03	0	80
3	4	0.035	0	80
4	4	0.03	0	80

system is modelled in this case study. Active-power losses involved in the DC/AC conversion are modelled as:

$$P_{loss,i} = \alpha_i + \beta_i P_i^{AC} + \gamma_i (P_i^{AC})^2 \tag{2.97}$$

The active and reactive power set points P_i^{ref} and Q_i^{ref} for INV1 and the reactive power set point for INV2 are kept constant to the ones obtained with the power flow. The active power set point for INV2 is modified to maintain its DC voltage with a PI controller:

$$P_2^{ref}(s) = (v_{DC,2} - v_{DC,2}^{ref}) \left(K_{P,DC,2} + \frac{K_{I,DC,2}}{s} \right) \tag{2.98}$$

DGs 1-4 are grid-forming converters working with droop control.

The adjacency matrices of the communication graph used for this case study are:

$$A^P = A^Q = A^\omega = \begin{bmatrix} 0 & 1 & 0 & 1 \\ 1 & 0 & 1 & 0 \\ 0 & 1 & 0 & 1 \\ 1 & 0 & 1 & 0 \end{bmatrix} \tag{2.99}$$

with DG1 set as the leader at the beginning of the simulation (the one with pinning gain equal to one in frequency and voltage).

In this application, voltage consensus was not implemented. Instead, reactive power sharing was applied.Therefore:

$$A^v = \mathbf{0}^{4\times 4} \tag{2.100}$$

Table 2.3 includes each agent's cost coefficients (linear and quadratic terms) and its minimum and maximum active-power limits.

For the non-linear simulation, the dynamic models were initialised from the power flow solution of the hybrid microgrid obtained using the flexible universal branch model in Alvarez-Bustos et al. (2021), an extension of MATPOWER (Zimmerman et al., 2011).

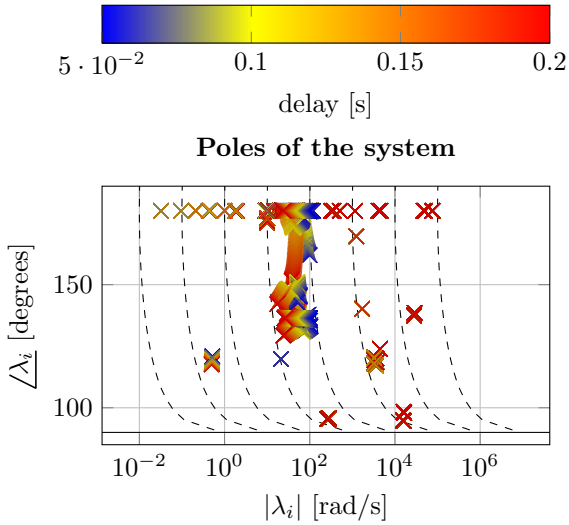

Figure 2.27: Variation of the root loci of the system in relation to the constant communication delay between agents, varied from 50 to 200 ms.

Non-linear dynamic simulations of the microgrid shown in Figure 2.26 were carried out to evaluate the proposed secondary control formulation and its robustness.

Communication delays and loss of communication links

Firstly, the robustness of the secondary control structure against communication time delays and link loss was investigated by modal analysis and non-linear simulation, respectively.

Figure 2.27 shows how the root loci of the system move when the communication delay between agents is varied from 50 to 200 ms in 100 equal steps. The communication delay was modelled by a 3rd-order Padé approximation when linearising the system equations, as suggested in Olfati-Saber and Murray (2004).

The eigenvalues of the linear system are shown in Figure 2.27 using their magnitude and phase.

Figure 2.27 shows that the system remains stable for the range of communication delay tested. However, some complex eigenvalues move closer to the stability limit (90 degrees) when increasing the communication delay. If the delay is increased further, those eigenvalues could make the system unstable. To avoid the delay effect, the secondary control algorithm could introduce a delay compensation (Jankovic et al., 2024). As an alternative, here we propose to slow down the secondary control until the stability of the system is not affected by the expected communication time delays. The communication delay was set to 100 ms.

Table 2.4: Eigenvalues of the Laplacian matrix for each communication-graph case of the communication-link loss study.

Case	$\mathbf{L} = \mathbf{L}^{\omega} + \mathbf{G}^{\omega}$	L eig.
1	$\begin{bmatrix} 3 & -1 & 0 & -1 \\ -1 & 2 & -1 & 0 \\ 0 & -1 & 2 & -1 \\ -1 & 0 & -1 & 2 \end{bmatrix}$	$\begin{bmatrix} 0.1864 \\ 2 \\ 2.4707 \\ 4.3429 \end{bmatrix}$
2	$\begin{bmatrix} 2 & 0 & 0 & -1 \\ -1 & 2 & -1 & 0 \\ 0 & 0 & 1 & -1 \\ -1 & 0 & -1 & 2 \end{bmatrix}$	$\begin{bmatrix} 0.1981 \\ 1.555 \\ 2 \\ 3.247 \end{bmatrix}$
3	$\begin{bmatrix} 1 & 0 & 0 & 0 \\ -1 & 2 & -1 & 0 \\ 0 & 0 & 0 & 0 \\ -1 & 0 & -1 & 2 \end{bmatrix}$	$\begin{bmatrix} 0 \\ 1 \\ 2 \\ 2 \end{bmatrix}$

To evaluate the robustness of the proposed secondary control against the loss of communication links between agents, the system response was compared in three scenarios:

1. No link loss.
2. The links starting at DG2 are lost.
3. The links starting at DG2 and the links starting at DG4 are lost.

The perturbations simulated consisted in a 5.85% reduction in both loads of the system (results in Figure 2.28) and the outage of DG4 (results in Figure 2.29).

Table 2.4 includes the Laplacian matrix and its eigenvalues for the communication graphs in the cases detailed above. Only the third case has an L matrix with one zero eigenvalue, and consensus is not guaranteed. This means that the graph does not have a spanning tree (i.e., not all the nodes can be reached from the leader node), and the consensus is not guaranteed.

Figure 2.28 includes the simulation results of the dynamic response of the active power of DGs 1-4 to a 5.85% reduction in both loads for the three scenarios considered.

Clearly, results confirm the theoretical conclusions drawn from the Laplacian matrix: Consensus convergence is only guaranteed if the Laplacian matrix has only one zero eigenvalue, corresponding to the leader node (i.e., the communication graph has a spanning tree). Figure 2.28 shows that when four communication links are lost (graph with no spanning tree), the steady-state active power sharing

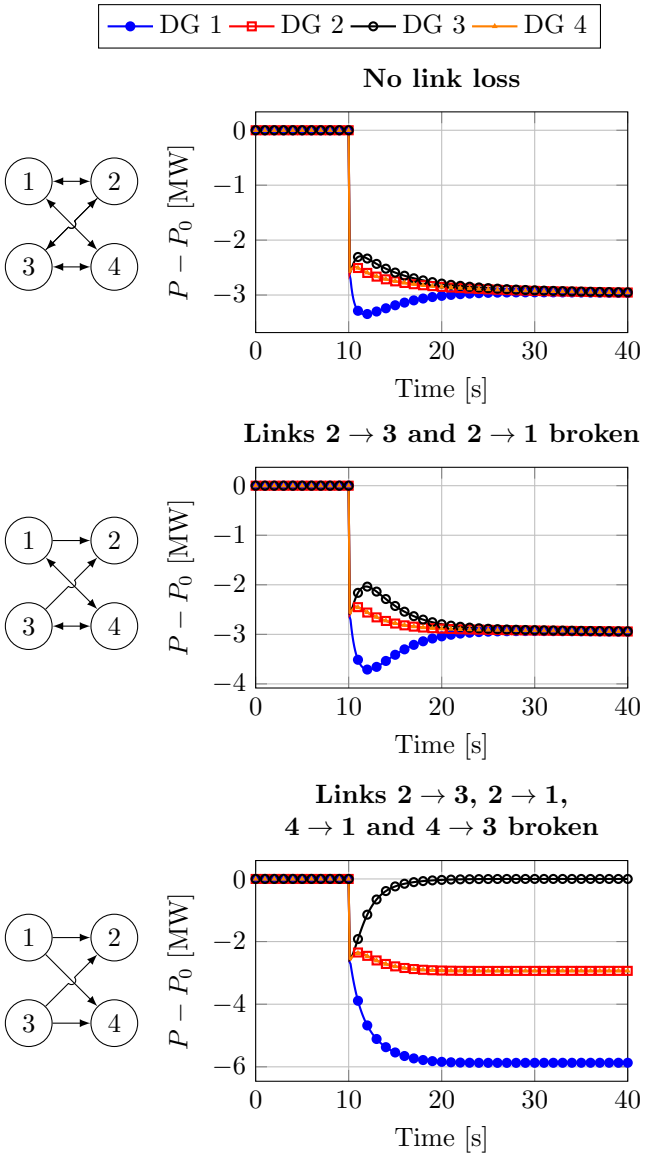

Figure 2.28: Active power response of DGs 1-4 to a 5.85% reduction in both loads for the three cases studied with lost communication links.

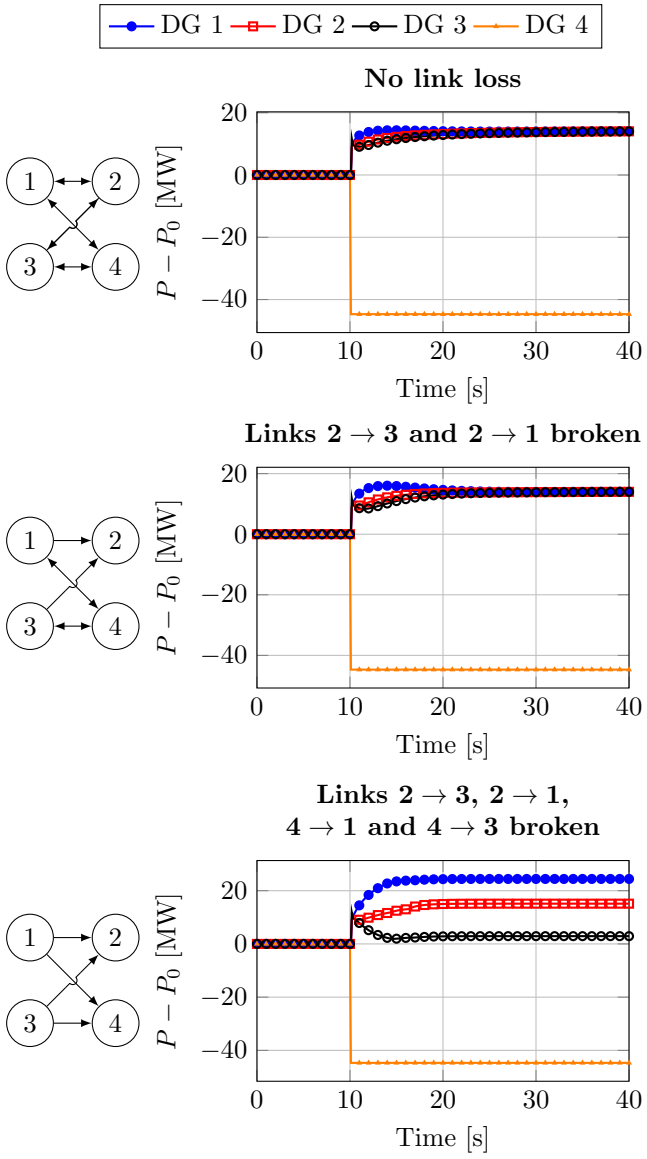

Figure 2.29: Active power response of DGs 1-4 to the outage of DG4 when there are communication links lost

Table 2.5: Parameters used for the simulation of the microgrid in Figure 2.26.

Grid-forming converters			
m_P (pu)	0.05	n_Q (pu)	0.05
R_f (pu)	0.01	L_f (pu)	0.1
C_f (pu)	0.1	R_{cf} (pu)	10^3
R_c (pu)	0.05	L_c (pu)	0.5
K_{PV}	1	K_{IV}	10
K_{PC}	1	K_{IC}	10
F_i	1	LPF_{const} (s)	0.01

Interface converters			
R_{f_1} (pu)	0.0001	L_{f_1} (pu)	0.15
R_{f_2} (pu)	0.0002	L_{f_2} (pu)	0.35
K_{PC}	1	K_{IC}	10
$K_{P,PLL}$	1	$K_{I,PLL}$	20
$\alpha_{1,2}$	0.0001	$\beta_{1,2}$	0.015
γ_1	0.2	γ_2	0.2
$K_{P,DC,2}$	0.5	$K_{I,DC,2}$	10

Lines (pu)			
R_{2-5}	0.05	$L_{1-2} = L_{5-6}$	0.1
R_{3-4}	0.05	$R_{1-2} = R_{5-6}$	0.001
L_{2-5}	0.5	L_{3-4}	0

Loads			
P_{load_1}	122.9 MW	Q_{load_1}	0.3 MVAr
P_{load_2}	80 MW	Q_{load_2}	0.5 MVAr

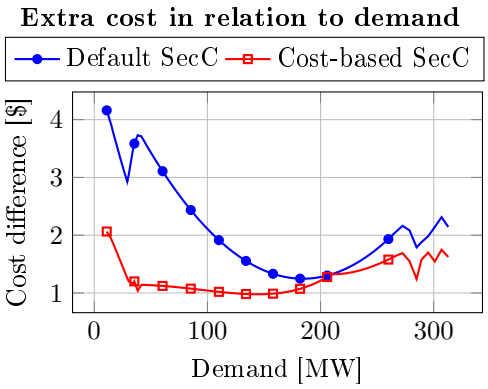

Figure 2.30: Cost increment from the optimal one with different levels of active-power demand. Blue line: secondary control seeks an equal power share. Red line: secondary control seeks a cost-based share.

after the disturbance is not the same as in the other two cases, which means that consensus is not reached.

Figure 2.29 includes the simulation results of the dynamic response of the active power of DGs 1-4 to the outage of DG4 for the three scenarios considered.

Similarly to the results obtained in Figure 2.28, when four communication links are lost, the graph does not include a spanning tree, consensus is not guaranteed, and the steady-state active power sharing after the disturbance is not the same as in the other two cases.

Table 2.5 includes the parameters used for the models of the microgrid.

Figure 2.30 shows the cost increment from the optimal operating point (*i.e.*, updating the tertiary control set points for the active power after each load disturbance) in the operation of the proposed secondary control under demand varia-

tions from the initially dispatched point. Results with a secondary control based on active power sharing (*Default SecC*) are compared with those of a cost-based secondary control (*Cost-based SecC*) in that Figure.

As expected, Figure 2.30 shows that the cost-based secondary control is always cheaper than the one based on active power sharing. However, the cost increment resulting from both methods is small for the tests carried out, even in cases with an active power demand that is very different from the scheduled one. In these cases, the tertiary control layer should update its active power set points.

This chapter proposes an algorithm to measure systematically the relevance of each state variable in the input-output response of a linear system and applies the algorithm to two microgrids of different sizes with a hierarchical control system.

3 State relevance of linear models of microgrids

3.1 Introduction

The analysis and simulation of conventional power systems have relied on a clear time-scale separation between slowly-varying electromechanical variables, such as voltage and speed of synchronous generators, and fast-varying electromagnetic variables, such as line currents and bus voltages. This has led to the use of algebraic equations to describe the latter, and differential equations to describe the former when studying stability problems (most noticeably, small-signal and transient frequency and angle stability) (Kundur et al., 1994). Since the order of a dynamic system is measured by the number of differential equations used to describe it, this separation naturally provides a reduction in the order of the model (Ghosh & Senroy, 2012). However, when looking at the literature of microgrid control, with the growing use of fast voltage-source converter (VSC)-based generation, it soon became obvious that it was unclear whether model reduction based solely on time-scale separation was still applicable. This was the reason why the focus of this work was temporarily diverted towards a systematic approach to determine what level of detail was necessary when modelling microgrid components. This chapter explains how this problem was tackled and what the results were.

Qoria et al. (2018) simplify the level-0 of converter control by considering no dynamics in either the current control or both voltage and current control. Karawita and Annakkage (2010) propose the use of hybrid network models for small-signal stability analysis of power systems with fast-acting VSC-based stations of high-voltage direct-current (HVDC) and flexible alternating current transmission systems (FACTSs): algebraic equations are used to describe lines far away from a VSC, whereas detailed differential equations are used to describe lines close to VSCs. Results in Karawita and Annakkage (2010) show that this hybrid approach produces more accurate modal results than the traditional one and prevents the computational complexity that would arise if all power lines were modelled in detail. More

recently, Grdenić, Delimar, and Beerten (2020) assessed the impact that a simplified model of the AC network has on the accuracy of small-signal stability analysis of AC systems with VSC-based HVDC. Grdenić et al. (2020) revisit the use of hybrid models such as the ones proposed by Karawita and Annakkage (2010) and reveals the importance of detailed models of AC lines and phase locked loops (PLLs) in critical situations with low short circuit ratio (SCR) or very long lines in the vicinity of VSCs. Finally, recent work by Grdenić, Delimar, and Beerten (2022) goes further and shows that complex AC line models are necessary to study the dynamics of power systems with VSCs if high-frequency phenomena such as harmonic stability (Wang & Blaabjerg, 2019) or electromagnetic converter interactions (Bayo Salas, 2018) are to be reliably addressed. This reference proposes an algorithm to determine how far one can go simplifying complex AC-line models as proposed by Beerten, D'Arco, and Suul (2016) while satisfying a given accuracy threshold. The simplification of AC-line models has probably been the topic that has received the most attention in the literature. Still, the ever-increasing complexity of the application and control of VSCs calls for a more comprehensive analysis of whether the dynamics of some parts of modern power systems can be neglected for simulation, analysis, or control purposes, leading to reduced-order models.

In the scenario described above, this chapter presents a systematic algorithm to extract the relevant physical states of a dynamic system in its input-output response, and applies it to microgrids with electronic power sources. Once the relevant states are identified, one can proceed to apply any model-reduction technique to include the dynamics of those variables in a reduced-order model of the microgrid. This model can then be used for nonlinear simulation or modal analysis, for example. In general, the selection of relevant states is usually made in terms of the associated time constants only, neglecting other state characteristics. The proposed algorithm combines the energy-in-state information provided by a balanced linear approximation of the nonlinear system of the microgrid and the mode-in-state participation factors of a linear approximation of that nonlinear system to determine the *relevance coefficient (RC)*[1]. Notice that the dynamics of nonlinear systems are often studied by using the eigenvalues (or modes) of a linear approximation of that system.

Given a nonlinear state variable description of a dynamic system, a balanced linear approximation (or realisation) of the model is often used to assess which states participate with more energy in the output response of the system. This information is obtained by using the so-called Hankel singular values (HSVs) and can be used to decide, by eliminating low-energy states (truncation), which state variables one should include in the next step, namely, the order reduction of the model (Laub, Heath, Paige, & Ward, 1987). Unfortunately, the state variables of the balanced realisation are not those of the original system but are obtained by using a linear transformation from the latter. Nevertheless, this method has been used

[1]Details of the calculation of the RC will be discussed briefly in Section 3.2.3. A more detailed explanation of the algorithm can be found in Tomás-Martín, García-Cerrada, Sigrist, Yagüe, and Suárez-Porras (2023)

for model order reduction (MOR) in power systems (Ramirez et al., 2016), resulting in a much lower-order reduced system. If the error between the response of the original system and the reduced-order one is to be minimised, the Hankel-norm (sum of the HSVs of the neglected states) must be minimised (Antoulas, 2005).

MOR techniques applied to dynamic systems include the so-called "moment-matching techniques" (also known as Krylov-based techniques), which are transfer-function-based methods whose objective is to match the behaviour of the first terms of the power series expansions of the system. A moment-matching method commonly used to approximate communication delays is Padé's approximation (Olfati-Saber & Murray, 2004). These techniques are widely used to have a reduced-order model that precisely describes the frequency response of the original model; however, the relation between the original states and the system dynamics is unclear.

Singular perturbation techniques are also popular MOR algorithms (Kokotović, Khalil, & O'Reilly, 1999). They have been applied to microgrids by Rasheduzzaman, Mueller, and Kimball (2015), where the authors identify as relevant states those strongly participated by a selection of eigenvalues with slow time constants. This reference also computes a reduced-order model (not a simple truncation) with eigenvalues that are close to the selected ones in the original model. However, only the time constants of the system eigenvalues are considered to select which variables must be included in the reduced-order model. Neither eigenvalue damping nor its weight in the system response is taken into account, and this shortcoming can be tackled by using the RC proposed in the present chapter. A similar MOR algorithm using singular perturbation can be found in Durić, Radojević, and Turković (1997). Ghosh and Senroy (2012) compare balanced truncation and Krylov-based techniques to reduce the order of the model in power systems. The so-called balanced residualisation calculates the balanced realisation of the model and then reduces the model using singular perturbation (Parang, Mohammadi, & Arefi, 2019).

Jayawardena, Meegahapola, Robinson, and Perera (2015) use a state-space transformation that clarifies the eigenvalue-state dependence; however, they also focus only on the time constants of the eigenvalues to consider them in the subsequent model reduction. In fact, approaches that keep the system structure and the physical meaning of the states in reduced models, either make assumptions valid for conventional power systems but not necessarily for electronics-dominated power systems, or they focus on selecting the eigenvalues with the slowest time constants and the states participated by those eigenvalues (modal analysis). The present chapter systematises the selection of relevant states by evaluating the RC.

3.2 Modal analysis of the system

Modal analysis has been chosen to study the small-signal stability of AC/DC hybrid microgrids because it has been used often in the past to study the small-signal stability of conventional electric power systems. Here, it will also be used to work

out the relevance of each state variable in the input-output response of a microgrid. A brief description of the main elements to be considered follows.

3.2.1 Eigenvalues and eigenvectors of a matrix

Any linear dynamic system has a matrix form, given by:

$$\begin{cases} \dot{\mathbf{x}} = \mathbf{A}\mathbf{x} + \mathbf{B}\mathbf{u} \\ \mathbf{y} = \mathbf{C}\mathbf{x} + \mathbf{D}\mathbf{u} \end{cases} \tag{3.1}$$

where $\mathbf{x}$ are the state variables of the system, $\mathbf{u}$ are the inputs of the system, and $\mathbf{y}$ are the outputs of the system. $\mathbf{A}$, $\mathbf{B}$, $\mathbf{C}$ and $\mathbf{D}$ are matrices of appropriate dimensions.

The most important characteristics of the dynamic response of (3.1) are contained in matrix $\mathbf{A}$ and its eigenvalues or system modes.

3.2.2 Eigenvalue sensitivities

The sensitivity of an eigenvalue of matrix $\mathbf{A}$ to changes in a parameter α, introduced by Van Ness, Boyle, and Imad (1965), can be calculated as in Pagola, Perez-Arriaga, and Verghese (1989):

$$\frac{\partial \lambda_i}{\partial \alpha} = \frac{\mathbf{w}_i^{\mathrm{T}} \cdot \dfrac{\partial \mathbf{A}}{\partial \alpha} \cdot \mathbf{v}_i}{\mathbf{w}_i^{\mathrm{T}} \cdot \mathbf{v}_i} = \mathbf{w}_i^{\mathrm{T}} \cdot \frac{\partial \mathbf{A}}{\partial \alpha} \cdot \mathbf{v}_i \tag{3.2}$$

where superscript T means transpose, λ_i is the ith eigenvalue of the system, and $\mathbf{v}_i$ and $\mathbf{w}_i^T$ are the right and left eigenvectors[2] associated with λ_i, respectively. In this thesis, the left-eigenvector matrix is calculated as:

$$\mathbf{W} = \mathrm{inv}(\mathbf{V}), \text{ with } \begin{cases} \mathbf{V} = [\mathbf{v}_1, \cdots, \mathbf{v}_n] \\ \mathbf{W} = \begin{bmatrix} \mathbf{w}_1^T \\ \vdots \\ \mathbf{w}_n^T \end{bmatrix} \end{cases} \tag{3.3}$$

which implies $\mathbf{w}_i^T \cdot \mathbf{v}_i = 1$ and $\mathbf{w}_i^T \cdot \mathbf{v}_j = 0$, if $i \neq j$.

3.2.3 Participations of a mode in a state

The definition of the participation of a mode λ_i in a state x_j introduced by Pérez-Arriaga, Verghese, and Schweppe (1982) is based on the free response ($\mathbf{u}(t) = 0$) of each state j of the system with initial conditions $\mathbf{x}(0)$:

$$x_j(t) = \sum_{\forall i} \mathbf{w_i}^T \mathbf{x}(0) e^{\lambda_i t} v_{ji} \tag{3.4}$$

[2]Notice that eigenvectors are written as column vectors. Therefore, $\mathbf{w}_i^T \cdot \mathbf{A} = \lambda_i \cdot \mathbf{w}_i^T$.

where v_{ji} is the j-th element of the column vector $\mathbf{v}_i$ and, if only initial condition $x_m(0)$ is non-zero (considering $x_m(0) = 1$ for simplicity):

$$x_j(t) = \sum_{\forall i} w_{mi} v_{ji} \cdot e^{\lambda_i t} \tag{3.5}$$

where w_{mi} is the m-th element of the column vector $\mathbf{w}_i$. The number $p_{ji,m} = w_{mi} v_{ji}$ could be named "participation of mode λ_i in state $x_j(t)$ when only initial condition $x_m(0)$ is non-zero", as stated by Yagüe Yagüe (2024). Normally, the specific case $m = j$ is used for the calculation of participation factors. Participation factors are clearly related to a specific initial condition but are universally accepted to quantify how the dynamic characteristics of an eigenvalue (or mode) affect the behaviour of a state variable of the system. Since p_{ji} is a complex number, there are several ways of considering the participation factors in order to understand better their importance. One of them is to calculate their normalised magnitude. This thesis uses the normalisation of Milano (2010), in which "the participation factor of mode i in state variable j" is calculated as follows:

$$p_{ji} = \frac{|w_{ji}|\,|v_{ji}|}{\sum_{\forall k} |w_{ki}|\,|v_{ki}|} \quad \text{so that} \quad \sum_{\forall j} p_{ji} = 1 \tag{3.6}$$

i.e., if mode λ_i participates only in one state variable j, then $\bar{p}_{ji} = 1$, and $\bar{p}_{ji} < 1$ otherwise. In other words, $\bar{p}_{ji}$ quantifies the relative participation of λ_i in one state variable compared to its partition in the rest of the state variables. Notice that whereas v_{ji} and w_{ij} are complex numbers, in general, p_{ij} is always a real number greater than 0. A decentralised calculation of eigenvalues and eigenvectors is outside the scope of this chapter. Some results can be found in the literature (Gusrialdi & Qu, 2017).

As will be shown later, sensitivities and participation factors are tools that can be used for the analysis of the stability of microgrids.

3.3 The proposed method: State relevance calculation

MOR in any linear system involves:

1. Identification of relevant dynamics.
2. Identification of the states in which those relevant dynamics participate.
3. Reduction of the model to include the dynamics of the relevant states, plus the algebraic equations to calculate the non-relevant states.

The proposed algorithm focuses on the first two items of the list above, namely, the identification of relevant dynamics and states of the system. To calculate the proposed state-relevance coefficient, the algorithm includes three steps: (a) calculation of a balanced realisation of the linear system; (b) calculation of the relevance of its eigenvalues; and (c) calculation of the relevance of the states of the original system.

3.3.1 Balanced state-space realisation of a linear system

Let us recall the typical description of a linear system of the form:

$$\begin{cases} \dot{\mathbf{x}} = \mathbf{A}\mathbf{x} + \mathbf{B}\mathbf{u} \\ \mathbf{y} = \mathbf{C}\mathbf{x} + \mathbf{D}\mathbf{u} \end{cases} \tag{3.7}$$

where $\mathbf{x}$ is the system state column vector, $\mathbf{u}$ is the input vector, $\mathbf{y}$ is the output vector, and $\mathbf{A}$, $\mathbf{B}$, $\mathbf{C}$ and $\mathbf{D}$ are the system matrices.

If the system in (3.7) is asymptotically stable, the controllability ($\mathbf{W}_c^2$) and observability ($\mathbf{W}_o^2$) Gramians are defined as, (Moore, 1981):

$$\begin{cases} \mathbf{W}_c^2 \triangleq \displaystyle\int_0^\infty e^{\mathbf{A}t}\mathbf{B}\mathbf{B}^{\mathrm{T}}e^{\mathbf{A}^{\mathrm{T}}t}\,\mathrm{d}t \\ \mathbf{W}_o^2 \triangleq \displaystyle\int_0^\infty e^{\mathbf{A}^{\mathrm{T}}t}\mathbf{C}^{\mathrm{T}}\mathbf{C}e^{\mathbf{A}t}\,\mathrm{d}t \end{cases} \tag{3.8}$$

where superscript T means the transposed of a matrix or vector.

The linear system in (3.7) can be transformed into another one whose states $\overline{x}$ are a linear combination of the states of the original system (x) given by a transformation matrix $\mathbf{T}$ such that $\overline{x} = \mathbf{T}x$ and $x = \mathbf{T}^{-1}\overline{x}$ (Laub et al., 1987). The original linear system is consequently transformed into:

$$\begin{cases} \dot{\overline{x}} = \mathbf{T}\mathbf{A}\mathbf{T}^{-1}\overline{x} + \mathbf{T}\mathbf{B}u \\ y = \mathbf{C}\mathbf{T}^{-1}\overline{x} + \mathbf{D}u \end{cases} \tag{3.9}$$

and the new controllability and observability Gramians are:

$$\overline{\mathbf{W}}_c^2 = \mathbf{T}\mathbf{W}_c^2\mathbf{T}^T \qquad \overline{\mathbf{W}}_o^2 = (\mathbf{T}^{-1})^T\mathbf{W}_o^2\mathbf{T}^{-1} \tag{3.10}$$

A balanced realisation is achieved when a transformation matrix T in (3.9) is used such that:

$$\overline{\mathbf{W}}_c^2 = \overline{\mathbf{W}}_o^2 = diag(g_i) \tag{3.11}$$

where g_i are the HSVs. Small entries in g_i indicate those states that can be removed to simplify the model since both their observability and controllability are small, whereas large entries indicate the most relevant states, (Moore, 1981). In this thesis, MATLAB command `balreal` is used to calculate the balanced transformation of a linear system. Since the states of the balanced system are a combination of the states of the original system, the former states may not have physical meaning any more.

3.3.2 Eigenvalue-relevance analysis

Since the balanced transformation is linear, the transformed system has the same eigenvalues as the original system; therefore, relevant eigenvalues of the transformed system will also be relevant eigenvalues of the original system. The relevant states of the transformed system can be chosen based on the values of g_i after

the transformation in (3.9)-(3.11), and relevant eigenvalues can be determined by checking which eigenvalues have high participation factors in the relevant states. The mode-in-state participation factors calculated and normalised as in (3.6) are used here.

Since each state of the transformed system has a different relevance, it is proposed that the participation factor of each eigenvalue in the states of the transformed system should be weighted with the state relevance (*i.e.*, an eigenvalue having a high participation factor in a relevant state is not necessarily more relevant than an eigenvalue having a low participation factor in a more relevant state). The value of g_j can then be used to weight $\bar{p}_{ij}$ using:

$$\hat{\mathbf{R}}_\lambda = [\hat{R}_\lambda(\lambda_1), \cdots, \hat{R}_\lambda(\lambda_n)]^T = \left([g_1, \cdots, g_n] \cdot \overline{\mathbf{P}}\right)^T \tag{3.12}$$

where $\hat{R}(\lambda_i)$ will be called the "relevance of eigenvalue λ_i" and $\overline{\mathbf{P}}$ is the participation matrix of the transformed system which has $\bar{p}_{ij}$ in its $i-th$ row and $j-th$ column. The bar above $\mathbf{P}$ and its elements has been used to indicate that they have been calculated using the balanced realisation in (3.9). Normalising yields:

$$\mathbf{R}_\lambda = [R_\lambda(\lambda_1), \ldots, R_\lambda(\lambda_n)]^T = \hat{\mathbf{R}}_\lambda / max(\hat{\mathbf{R}}_\lambda) \tag{3.13}$$

The normalised value will be used unless otherwise stated.

3.3.3 State relevance

Let us now weigh each column of the participation matrix of the original system ($\mathbf{P}$) with the relevance of its associated eigenvalue ($\hat{R}(\lambda_i)$). By summing all these weighted columns, the resulting column vector can be used to quantify the "relevance of each state":

$$\hat{\mathbf{R}}_x = \mathbf{P} \cdot \mathbf{R}_\lambda \tag{3.14}$$

which can be normalised as follows:

$$\mathbf{R}_x = [R_x(x_1), \ldots, R_x(x_n)]^T = \hat{\mathbf{R}}_x / max\left(\hat{\mathbf{R}}_x\right) \tag{3.15}$$

where $R_x(x_i)$ will be called the "relevance coefficient (RC) of state x_i". The normalised value will be used unless otherwise stated.

This chapter includes the application of the state relevance algorithm presented to two microgrids of different sizes. These microgrids are powered by grid-forming voltage-source converters (GFr-VSCs) and have a hierarchical control system composed of consensus-based secondary control (presented in Chapter 2) and droop-based primary control above voltage and current control loops (as described for GFr-VSCs in Chapter 2).

A very small, constant communication delay between converters is included in the study to analyse if the state relevance finds it negligible. Delays are modelled

using a third-order Padé approximation in the linear model and an exact delay in the nonlinear model.

The rest of this chapter is organised as follows: Section 3.4 presents the results obtained when applying the proposed state RC to a small microgrid and explores the impact of varying system and control parameters on RCs. A larger microgrid is studied in Section 3.5, with some further applications of RCs, and the proposed algorithm is validated in the modified IEEE 69 bus test system in Section 3.6.Finally, Section 3.7 concludes the chapter.

3.4 Case study 1: Small microgrid

3.4.1 Description of the case study

Figure 3.1 shows the diagram of a GFr-VSC (see Chapter 2 for a detailed explanation of the diagram). The detailed model of a GFr-VSC used in this chapter can be found in Figure C.2, included in Appendix C. The secondary control used in this first case study is the one described in Chapter 2, with only one leader and one follower agent.

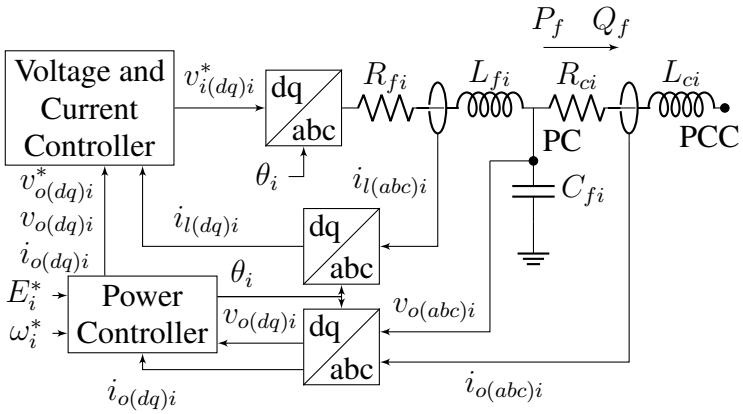

Figure 3.1: Diagram of a GFr-VSC. Adapted from Bidram, Davoudi, and Lewis, 2014.

The RC described above is used to investigate a small microgrid consisting of two GFr-VSCs (DG1 and DG2) connected to two buses, a load connected to each bus (Load 1 and Load 2) and a power line connecting the two buses (see Figure 3.2).

The current case study results in a very simple graph in which DG1 has been made leader and angle reference, with set points $v_{ref} = 1$ pu and $\omega_{ref} = 1$ pu, and in which DG2 follows the frequency and active and reactive power sharing of DG1. Table 3.1 shows control level-0 parameters, droop-controller parameters,

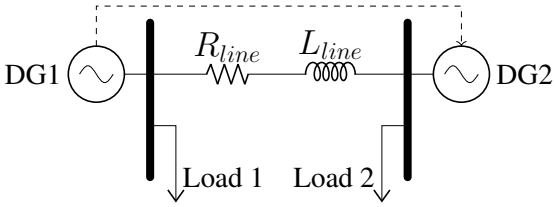

Figure 3.2: A case study with two GFr-VSCs and two loads. A dashed line represents a communication link between the two GFr-VSC.

decentralised secondary control parameters, and system parameters. The parameters of the test system are based on those in Bidram, Davoudi, Lewis, and Guerrero (2013).

The complete model for a GFr-VSC has 14 states, corresponding to the inner and outer inductor currents ($i_{l(dq)}$ and $i_{o(dq)}$), the capacitor voltage ($v_{o(dq)}$), the filters for active and reactive power (P_f and Q_f), integrators of the frequency (ω^*) and voltage (E^*) secondary controllers, integrators of the voltage and current controllers ($PIv_{(dq)}$ and $PIi_{(dq)}$). The leader distributed generator (DG) has been chosen as the angle reference, which will be assigned here without loss of generality to DG1, i.e., for any other converter,

$$\theta_i = \int (\omega_i - \omega_{DG1}) \tag{3.16}$$

This simple case study will be used to illustrate the use of RC. Firstly, the impact of varying parameters on the RC is shown. Secondly, the RC is used to support the MOR of the small microgrid. Nonlinear simulations are used to compare the proposed approach with other approaches to select relevant states. Finally, the impact of the time-scale separation of the controls on the RC is analysed.

3.4.2 Illustration of the RC

The system in Figure 3.2 has been linearised around the operating point shown in Table 3.2 by using MATLAB® and Simulink® for different cases to illustrate the use of the state RC. Line, loads, and controller dynamics have all been included. To linearise the system, the set points for the frequency and voltage of the leader and the load disturbance have been set as inputs, while frequency, voltage, and active and reactive power of the two converters have been set as outputs. Notice that the calculation of the balanced realisation of the linear model depends on the input-output choice.

The value of the RC has been calculated for all the state variables of the model in Figure 3.2, once linearised, by following the procedure described in Sections 3.3.1-3.3.3 and the relevance of some states has been investigated in various circumstances. For example, Figure 3.3a shows the value of the RC for the most relevant of

Table 3.1: Parameters used for the simulation of the microgrid.

GFr-VSCs			
m_P	$9.42 \cdot 10^{-4}$ rad/s·W	n_Q	$1.14 \cdot 10^{-3}$ V/VAr
R_f	0.4332 Ω	L_f	13.7892 mH
C_f	73.4787 μF	R_{cf}	4332 Ω
R_c	0.4332 Ω	L_c	13.7892 mH
K_{PV}	0.023084	K_{IV}	0.23084
K_{PC}	43.32	K_{IC}	433.2
F_i	1	LPF_{const}	0.01 s
Secondary control parameters and bases			
c_f	100	c_v	100
f_{base}	50 Hz	S_{base}	10 kVA
delay (T_d)	$1.00 \cdot 10^{-3}$ s	$V_{nom} = V_{base}$	380 V
Z_{base}	43.32 ω	$\beta = 0$	$B = 1$
$g_1 = 1$	$g_i = 0 \; \forall \; i \neq 1$	$a_{ij} = 1 \; \forall \; i \neq 1, j = i - 1$	
Lines			
R_{line}	0.4332 Ω	L_{line}	13.7892 mH
Load 1			
R_{load}	21.66 Ω	L_{load}	68.9459 mH
Load 2 in case study 1, loads 2-10 in case study 2			
R_{load}	43.32 Ω	L_{load}	137.8918 mH

Table 3.2: Operating point of the microgrid of case 1. $i \in [1 - 2]$.

State name	Value	State name	Value
DGi/P	0.50457 pu	DGi/Q	0.53963 pu
$DG1/v$	1 pu	$DG1/\theta$	0 rad
$DG2/v$	1.0452 pu	$DG2/\theta$	0.034023 rad

the delay-related states as the delay transmitting the value of ω from DG1 to DG2 changes from 0.001 to 0.1 s while maintaining the delay transmitting the values of P and Q equal to 0.001 s. Note that the states mpP and nqQ are related to the secondary control of active power and reactive power, respectively, as presented in Chapter 2.Clearly, the larger the delay, the more relevant its related state is, whereas the relevance of constant delays does not change much. In fact, when the delay of transmitting ω is increased to around 0.04 s, its states are the most important ones in the input-output response of the system (highest RC).

Similarly, Figure 3.3b (blue line) shows the value of the relevance coefficient for the most relevant of the power-line-related states as the X/R ratio changes from 0.2 to 20 while maintaining the line impedance modulus equal to 0.1005 pu.

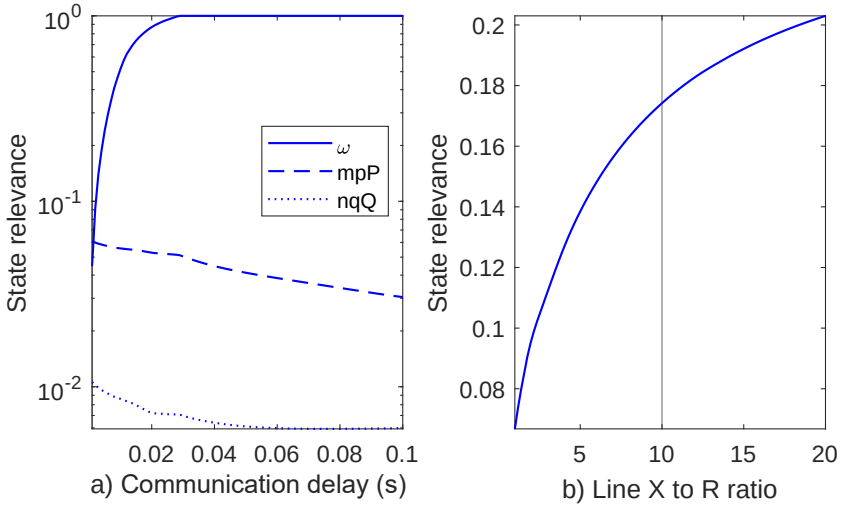

Figure 3.3: a) Relevance of the most relevant delay-related states in the transmission of ω (continuous line), mpP (dashed line), and nqQ (dotted line), separately. b) Relevance of the transmission-line-related state when changing its X/R ratio. The vertical line represents the original value of the X/R.

Clearly, the transmission-line dynamics can be neglected if its X/R ratio is low; however, it must be taken into account if the X/R ratio increases (the line time constant also increases).

3.4.3 Applying the state RC to MOR

This section investigates whether the state RC is helpful in the reduction of the linear model of a microgrid. The detailed procedure for the reduction of state variables in the system is described in Appendix B. Three approaches have been used:

1. The state RC has been used to decide which states should be removed from the model. This approach has been labelled as "Rel.".

2. The states participated by eigenvalues with small time constants (fast dynamics) have been eliminated. This approach has been labelled as "Eig.". It is used by conventional MOR techniques, including Rasheduzzaman et al. (2015).

3. Since fast dynamics are often neglected in MORs, strategy "Rel." has been simplified by assessing eigenvalue relevance as $\hat{\mathbf{R}}_\lambda = -1/\mathrm{Real}(\lambda_i)$ instead of using (3.12). The eigenvalue relevance is then used to calculate the state relevance using (3.14) and (3.15). The state-relevance coefficients $\mathbf{R}_x$ calculated this way have been used to decide which states can be eliminated. This approach has been labelled as "Rel. ap.".

Figure 3.4 illustrates how the system eigenvalues participate in the states of the original system. Mode-in-state participation factors have been calculated by using the procedure described in Chapter 2. Notice that a dark grey colour indicates those states with a large participation of a given mode. Each tick in the X-axis represents an eigenvalue. They have been sorted in ascending order according to their time constants ($-1/\mathrm{Real}(\lambda_i)$), which have been explicitly recorded at the bottom of the figure to show which states are participated by the fast or slow eigenvalues. States have been grouped on the Y-axis (for example, delay states and d-q axes in currents and voltages).

Figure 3.4 shows that eigenvalues 1 to 4 have an exponential time constant just above 10^{-6} seconds. Furthermore, states of the time-delay blocks ($Delay\,\omega$, $Delay\,m_pP$, $Delay\,n_qQ$) are participated by the eigenvalues with small time constants. Notice that $Delay\,n_qQ$ has no participation factors recorded, as they are smaller than 0.01. Voltage- and current-controller states (named $DG1-2PIi$ or $DG1-2PIv$) are participated by the eigenvalues with the largest time constants. Transmission line, low-pass power filters, and secondary-control states are participated by eigenvalues with time constants from just above 10^{-5} s to just below 10^{-1} s. Intentionally, time scales between primary and level-0 controls have not been separated.

Figure 3.5 shows the accumulated relevance of the states of the original system following the procedure described in Sections 3.3.1-3.3.3. The accumulated relevance of the states can help to decide how many states to include in the reduced system. After state number 8, there is a visible change in the slope of the curve, and taking 14 states one reaches 90% of the final value of the accumulated relevance.

Table 3.3 compares the three different approaches to select relevant states. Columns $R_{x,1}$ and $R_{x,2}$ in Table 3.3 show the state relevance calculated in approaches "Rel." and "Rel. ap.", respectively. Motivated by the slope change in Figure 3.5, eight states will be chosen to be included in a reduced-order model. From columns $R_{x,1}$ and $R_{x,2}$, the eight most relevant states have been chosen and highlighted in Table 3.3. The eight states chosen by looking only at the largest time

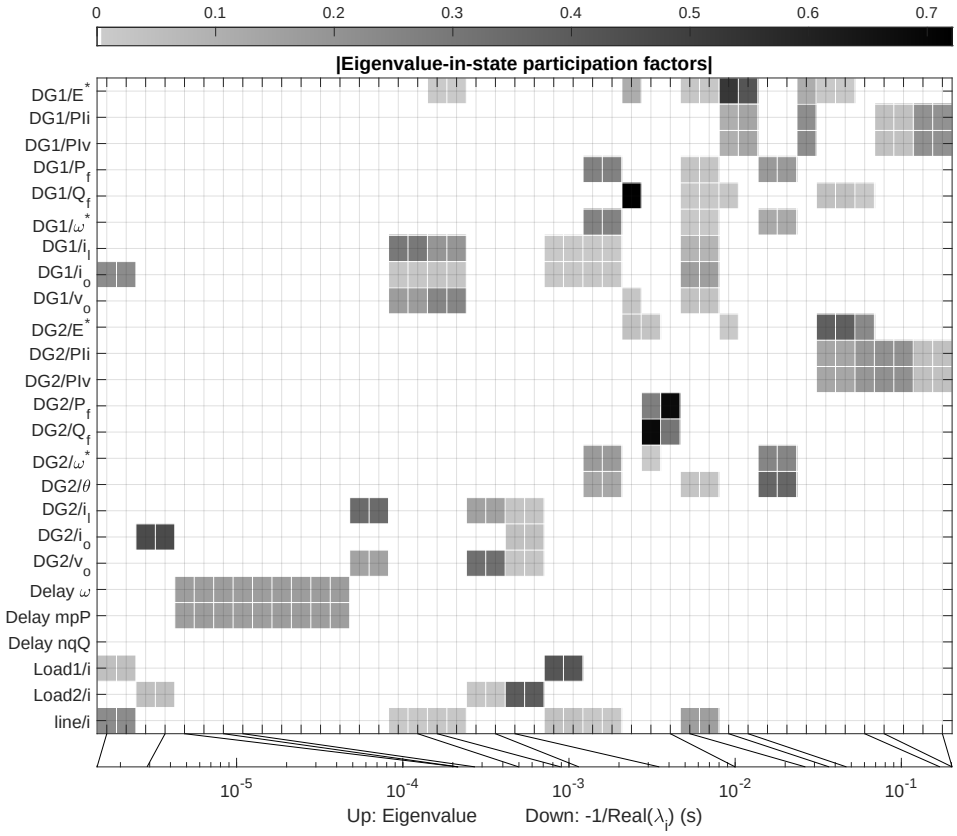

Figure 3.4: Illustrating the participation factors of the eigenvalues in the states of the system. For clarity, participation factors below 0.01 are not shown.

Table 3.3: State relevance for case study 1 (2 GFrs). R_{x_1} and R_{x_2} are the state relevance calculated by "Rel" and "Rel. ap." approaches, respectively. x_3 gives the state order obtained by "Eig" approach. No clear time-scale separation.

State name	$R_{x,1}$	$R_{x,2}$	x_3
$DG2/\theta$	**1**	0.20265	9
$DG2/E^*$	**0.80611**	**0.84812**	**6**
$DG2/\omega^*$	**0.7537**	0.14393	10
$DG1/P_f$	**0.66905**	0.11802	18
$DG2/PIv_d$	**0.59128**	**0.76333**	**5**
$DG2/PIi_d$	**0.5815**	**0.75303**	**7**
$DG1/\omega^*$	**0.51843**	0.085096	19
$DG1/E^*$	**0.46321**	0.29667	11
$DG1/PIi_d$	0.21128	**0.38871**	12
$DG1/PIv_d$	0.20369	0.3861	**8**
$DG1/Q_f$	0.1972	0.1216	17
$DG1/i_{oq}$	0.18067	0.049342	13
$line/i_d$	0.1742	0.049568	43
$DG1/i_{od}$	0.17374	0.049969	44
$line/i_q$	0.17058	0.047488	14
$DG1/i_{ld}$	0.11985	0.031824	27
$DG1/i_{lq}$	0.10294	0.027054	28
$DG1/v_{od}$	0.074896	0.022417	26
$Delay - mpP(3)$	0.061444	0.013688	37
$DG1/v_{oq}$	0.045319	0.026989	29
$Delay - \omega(3)$	0.044722	0.0091235	36
$DG2/v_{od}$	0.027841	0.027275	24
$Load1/i_q$	0.025238	0.017029	20
$Load1/i_d$	0.023709	0.016606	21
$DG2/Q_f$	0.020457	0.066592	16
$DG2/P_f$	0.019911	0.051659	15
$Load2/i_q$	0.012315	0.016433	22
$Load2/i_d$	0.011226	0.015891	23
$Delay - nqQ(3)$	0.0106	0.008306	39
$DG2/i_{oq}$	0.010234	0.00342	42
$DG2/i_{od}$	0.0062695	0.0031477	41
$DG2/i_{lq}$	0.0036369	0.0053899	30
$DG1/PIi_q$	0.0027129	**0.98425**	**2**
$DG1/PIv_q$	0.0025971	**1**	**1**
$DG2/i_{ld}$	0.0024959	0.0053131	31
$Delay - \omega(2)$	0.0013242	0.0026039	32
$Delay - mpP(2)$	0.001292	0.0025898	33
$DG2/v_{oq}$	0.0012146	0.020922	25
$Delay - \omega(1)$	0.00076035	0.001508	35
$Delay - mpP(1)$	0.00074536	0.0014999	34
$DG2/PIv_q$	0.00025056	**0.99918**	**3**
$DG2/PIi_q$	0.00022255	**0.9834**	**4**
$Delay - nqQ(2)$	3.9989e-05	5.1843e-05	38
$Delay - nqQ(1)$	1.9983e-05	2.9065e-05	40

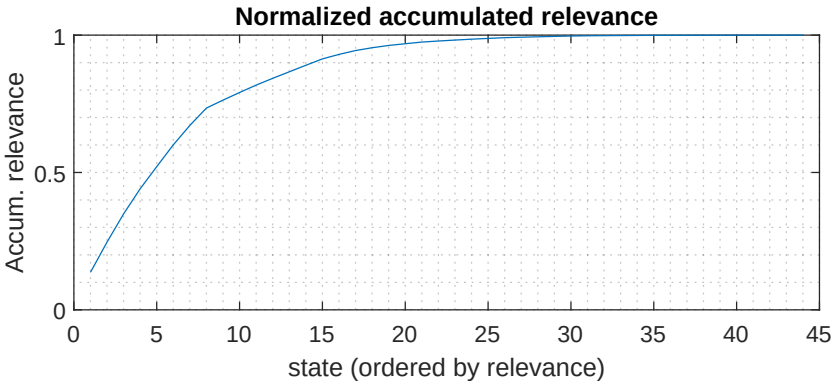

Figure 3.5: Accumulated relevance of the states of the original system. Case study 1 with no clear time-scale separation. States are ordered from most relevant to least relevant.

constants of the linear system eigenvalues and the mode-in-state participation of those eigenvalues have been highlighted in column x_3 in Table 3.3.

According to Table 3.3, the reduced systems obtained by the three different methods include the following states:

- "Rel." includes the reference frame of DG2, the secondary control of both converters, the low-pass filter (LPF) of the active power of DG1, the output inductance of DG1, and the voltage and current controller of DG2.
- "Rel. ap." and "Eig." include the voltage secondary control of DG2 and the voltage and current controllers of both converters.

Clearly, several states that the proposed method finds negligible in the system response are included in the other two approaches. The question arises whether the RC-informed selection outperforms the other two approaches. The accuracy of the reduced models suggested by the three approaches presented will be investigated by means of simulations of the reduced nonlinear models. The procedure followed to reduce the nonlinear models, according to the relevant states identified by the three approaches, is described in Appendix B.

Now, the response of several electrical variables of DG2 in the original (complete) and reduced nonlinear models to a change in Load 1 is studied. The load change is simulated by reducing the impedance of Load 1 a 50% suddenly while keeping its X/R ratio; therefore, the active and reactive powers consumed by Load 1 increase, supposing the voltage remains constant.

The reduced models used for the simulation include the states highlighted in Table 3.3 plus some additional ones because the reduction was done respecting natural blocks (*e.g.*, if the d axis of the voltage and current controller of a converter are suggested to be included in the reduced model, the q axis must also be included).

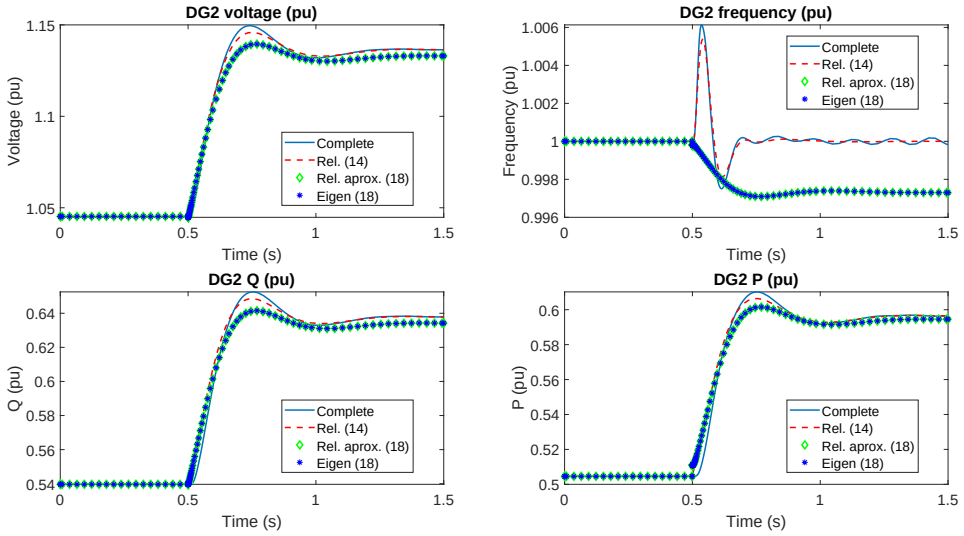

Figure 3.6: Response of DG2 in case study 1 to a 50% reduction in the impedance of Load 1 (but constant X/R ratio) without a clear time-scale separation between control layers. In legend, enclosed within brackets, are the numbers of states included in the reduced models.

The total number of states used in the simulation of each of the reduced-order models has been noted, enclosed within brackets, in Figure 3.6.

Clearly, the proposed method "Rel." can represent the original system dynamics more accurately with fewer states than the other two methods. Furthermore, the proposed method is the only one having a response of DG2 frequency similar to the original system response.

3.4.4 Impact of control time-scale separation

The microgrid shown in Figure 3.2 was linearised with the parameters shown in Table 3.1, except for the following modifications in some GFr-VSC parameters:

$$m'_p = 10 \cdot m_p, \quad n'_q = 10 \cdot n_q, \quad c'_f = c'_v = 2,$$
$$T'_f = 1\,\text{s}, \quad \text{delay}' = 1 \cdot 10^{-5}\,\text{s}.$$

These changes slow down the secondary control and the power-filter dynamics and strengthen the time-scale separation of the system dynamics.

Figure 3.7 shows the accumulated relevance of the states of the original system. Clearly, the first nine states are the most relevant ones, and the rest of the states do not contribute much. It should be noted that the normalised accumulated relevance saturates more quickly than in the previous case with a weaker time-scale separation.

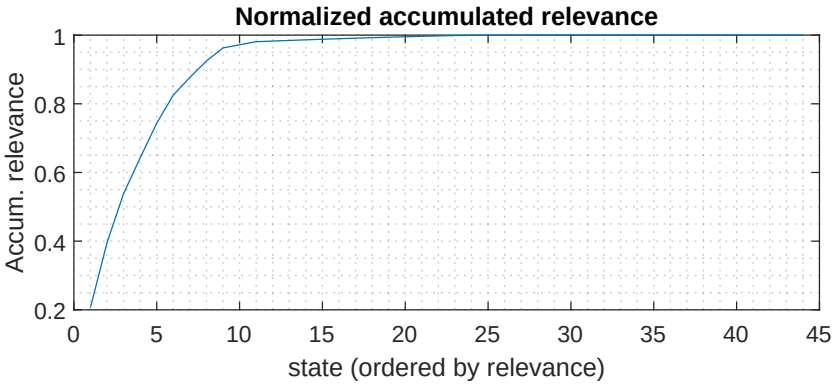

Figure 3.7: Accumulated relevance of the states of the original system. Case study 1 with a clear time-scale separation between control layers.

Columns $R_{x,1}$ and $R_{x,2}$ in Table 3.4 include the state relevance for the test system calculated according to alternatives 1 and 3 in Section 3.4.3 and the nine states with the highest relevance have been highlighted to be selected in reduced models. Column x_3 of the same table shows that the dynamics with high participation factors of the nine slowest eigenvalues coincide with those selected by the other two algorithms, unlike in Table 3.3. The three approaches suggest the inclusion of the same nine states, namely, the secondary control, and the power filter dynamics of both converters. The state involved in the reference frame calculation for DG2 must also be included.

Figure 3.8 shows the response of several electrical variables of DG2 in the original and reduced nonlinear models to a change in Load 1 (a 50% reduction of load impedance but constant X/R ratio). The three reduced models include the same states and produce the same results.

3.5 Case study 2: a larger microgrid

A microgrid test system including ten GFr-VSCs has been used to investigate the application of the proposed state relevance coefficient in a larger system, where MOR techniques may be more helpful. The diagram of the microgrid for this case study is shown in Figure 3.9. It is a radial extension of the small microgrid built with several blocks like the one in Figure 3.2. The system in Figure 3.9 has been linearised around the operating point shown in Table 3.5 by using MATLAB® and Simulink®to illustrate the use of the state RC.

With the communication graph shown in Figure 3.9 (dashed line), the values of a_{ij} and g_i for this case study are: $a_{ij} = 1$ if $i \neq 1$ and $j = i - 1$, otherwise $a_{ij} = 0$, and $g_i = 1$ if $i = 1$, otherwise $g_i = 0$. For simplicity, the microgrid was designed as a radial microgrid with equal converters and with each converter connected to the

Table 3.4: Case study 1 (2 GFrs). R_{x_1} and R_{x_2} are the state relevance calculated by "Rel" and "Rel. ap." approaches, respectively. x_3 gives the state order obtained by "Eig" approach. Clear time-scale separation.

State name	$R_{x,1}$	$R_{x,2}$	x_3
$DG1/\omega^*$	**1**	**0.96606**	**1**
$DG2/\omega^*$	**0.91326**	**0.91722**	**2**
$DG2/E^*$	**0.69113**	**1**	**3**
$DG1/P_f$	**0.50268**	**0.59417**	**5**
$DG2/\theta$	**0.48854**	**0.57902**	**6**
$DG1/E^*$	**0.39584**	**0.52737**	**4**
$DG2/Q_f$	**0.24991**	**0.65226**	**7**
$DG2/P_f$	**0.23146**	**0.455**	**8**
$DG1/Q_f$	**0.1837**	**0.26013**	**9**
$DG1/PIv_d$	0.043904	0.099938	10
$DG1/PIi_d$	0.043367	0.098454	11
$DG2/PIi_d$	0.0088186	0.089091	13
$DG2/PIv_d$	0.0087562	0.09028	12
$DG1/i_{ld}$	0.0087091	0.004619	29
$Load1/i_d$	0.0078151	0.0023619	21
$Load1/i_q$	0.0077397	0.002271	20
$DG1/i_{od}$	0.0073217	0.0073633	43
$DG1/i_{lq}$	0.0073141	0.003001	28
$line/i_q$	0.0066516	0.0065061	19
$line/i_d$	0.0064484	0.0062382	18
$DG1/v_{od}$	0.0061259	0.0030799	26
$DG1/i_{oq}$	0.0057181	0.0055408	44
$DG1/v_{oq}$	0.0051427	0.0023077	27
$DG2/i_{oq}$	0.0017761	0.0022288	33
$Load2/i_q$	0.0013125	0.0027668	22
$Load2/i_d$	0.0010476	0.0025129	23
$DG1/PIi_q$	0.00058978	0.085032	17
$DG1/PIv_q$	0.00056472	0.086395	16
$DG2/i_{od}$	0.00033632	0.00053219	32
$DG2/v_{od}$	0.00019634	0.0019809	24
$DG2/PIv_q$	4.3818e-05	0.086013	14
$DG2/PIi_q$	4.3158e-05	0.084655	15
$Delay-mpP(3)$	1.5463e-05	1.6877e-05	40
$Delay-\omega(3)$	1.4707e-05	1.6103e-05	41
$DG2/i_{ld}$	4.5115e-06	0.0004148	31
$Delay-nqQ(3)$	3.2894e-06	5.0874e-06	42
$DG2/v_{oq}$	7.4e-07	0.0017938	25
$DG2/i_{lq}$	7.0284e-07	0.00042746	30
$Delay-mpP(1)$	3.3645e-08	9.8701e-07	39
$Delay-nqQ(1)$	2.4814e-08	7.5812e-07	37
$Delay-\omega(1)$	4.6621e-09	9.1807e-07	35
$Delay-mpP(2)$	1.0086e-11	1.6358e-06	38
$Delay-\omega(2)$	3.607e-12	1.5729e-06	34
$Delay-nqQ(2)$	1.4872e-12	1.2682e-06	36

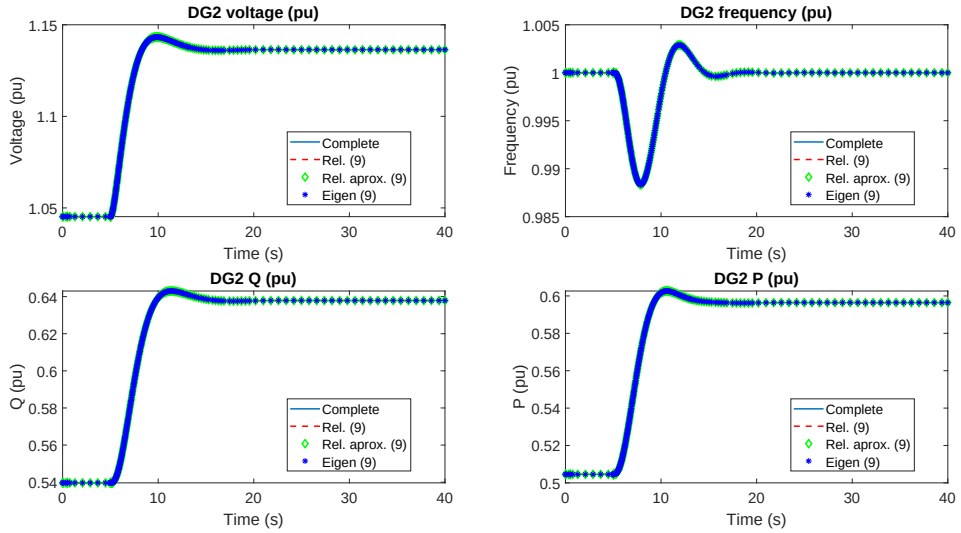

Figure 3.8: Response of DG2 in case study 1 to a 50% reduction in the impedance of Load 1 but constant X/R ratio with a clear time-scale separation between control layers. Numbers enclosed within brackets in the legends show the number of states included in the reduced models.

Table 3.5: Operating point of the microgrid of case 2. $i \in [1-10]$.

State name	**Value**	**State name**	**Value**
DGi/P	0.58174 pu	DGi/Q	0.63089 pu
$DG1/v$	1 pu	$DG1/\theta$	0 rad
$DG2/v$	1.0349 pu	$DG2/\theta$	0.026235 rad
$DG3/v$	1.0606 pu	$DG3/\theta$	0.042931 rad
$DG4/v$	1.0792 pu	$DG4/\theta$	0.053505 rad
$DG5/v$	1.0927 pu	$DG5/\theta$	0.060102 rad
$DG6/v$	1.1024 pu	$DG6/\theta$	0.064119 rad
$DG7/v$	1.1091 pu	$DG7/\theta$	0.06648 rad
$DG8/v$	1.1137 pu	$DG8/\theta$	0.067801 rad
$DG9/v$	1.1165 pu	$DG9/\theta$	0.068483 rad
$DG10/v$	1.1178 pu	$DG10/\theta$	0.068768 rad

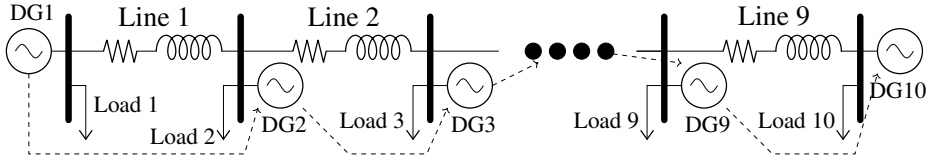

Figure 3.9: Simplified diagram of the microgrid with ten GFr-VSCs (case study 2). A dashed line shows the communication graph, including the direction of the information flow.

same bus as its local load. Radial microgrids could arise in distribution networks in which distributed generation is connected to intermediate nodes (Hossain, Pota, Hossain, & Blaabjerg, 2019).

The parameters of the GFr-VSCs, lines and loads are the same as those in case study 1 (Table 3.1). The operating point around which the nonlinear system is linearised is shown as the power flow solution in Table 3.5.

Figure 3.10 shows the accumulated relevance of the states of the original system. In this case, the choice of how many states must be included in the reduced system is not very clear. The optimal value is between 50 and 100 states. To test the accuracy of the proposed method against others, even considering fewer states, three nonlinear reduced-order models have been compared: (a) a model including the 57 states with the largest relevance coefficients according to strategy 1 in Section 3.4.3; (b) a model including the 90 states with the largest relevance coefficients according to strategy 3 in Section 3.4.3, and (c) a model including the 90 states participated by the eigenvalues with the largest time constants. Again, the final number of states needed in the reduced models may differ (it may be higher due to structural considerations).

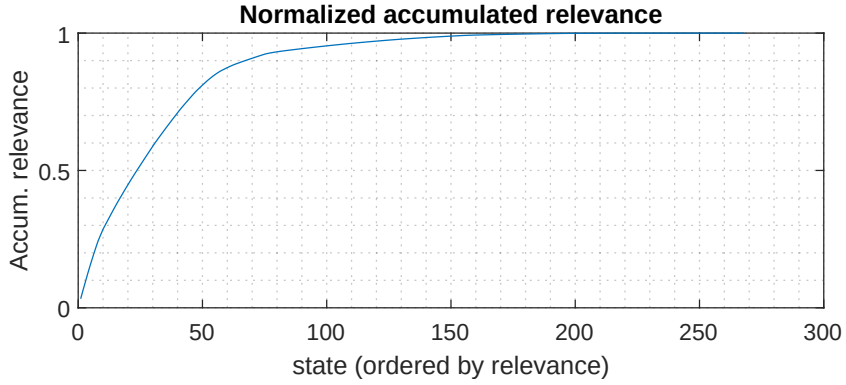

Figure 3.10: Accumulated relevance of the states of the original system. Microgrid with ten GFr-VSCs (case study 2).

Figure 3.11 shows the response of several electrical variables of DG10 in the original and reduced nonlinear models to a change in Load 1. The load change is simulated by reducing the impedance of Load 1 a 50% while keeping its X/R ratio.

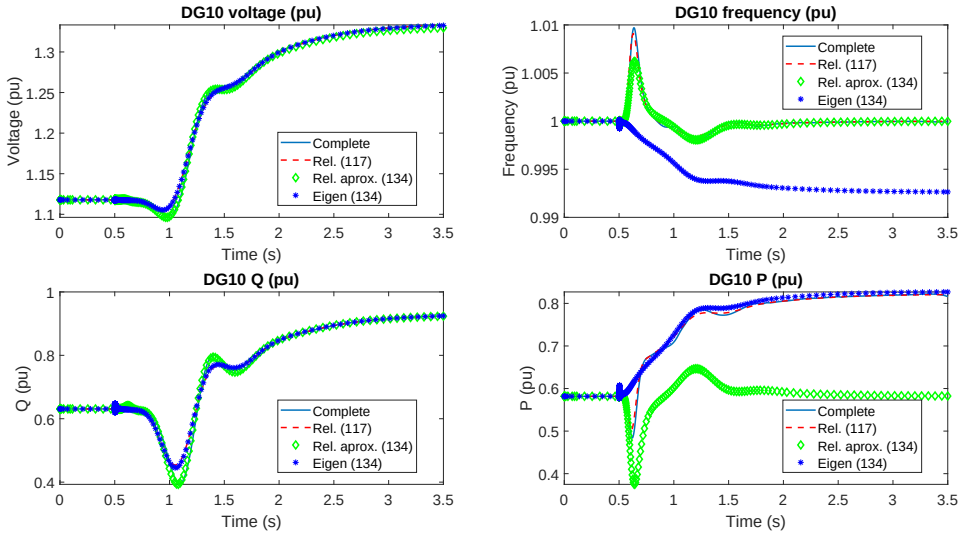

Figure 3.11: Response of electrical variables of DG10 in the microgrid with ten GFr-VSCs (case study 2) to a 50% reduction of Load 1 impedance while maintaining its X/R ratio. The numbers enclosed within brackets in the legends show the number of states included in each reduced nonlinear model.

Since the proposed method is the only one that finds the secondary control of all converters relevant, it is the only one having correct steady-state values. Moreover, it is the one with the best accuracy in the input-output response.

3.5.1 Analysis of the importance of the communication graph

In addition to the identification of relevant states for MOR, the state RC can help to analyse the importance of each state in the input-output response of the system. For example, let us consider the microgrid with ten GFr-VSCs (shown in Figure 3.9) and let us change the X/R ratio of line 3 while keeping its impedance modulus and the X/R ratio of all the other lines.

Figure 3.12 shows the evolution of the state RC of the most relevant state of each line. It clearly shows that lines 1, 2 and 3 are much more relevant than lines 7, 8 and 9. The communication graph (from DG_i to DG_{i+1}, $i \in [1, 9]$) affects this result. In fact, if the communication graph is reversed (from DG_i to DG_{i-1}, $i \in [2, 10]$) the relevance of the lines is also inverted (see Figure 3.13). This result may be caused by the radial structure of the microgrid and its communication graph. Notice that the relevance of the line with an increasing X/R ratio always increases. This

information can help choose systematically which lines need detailed modelling and which ones can be simplified for each case study, allowing more informed decisions for reduced models.

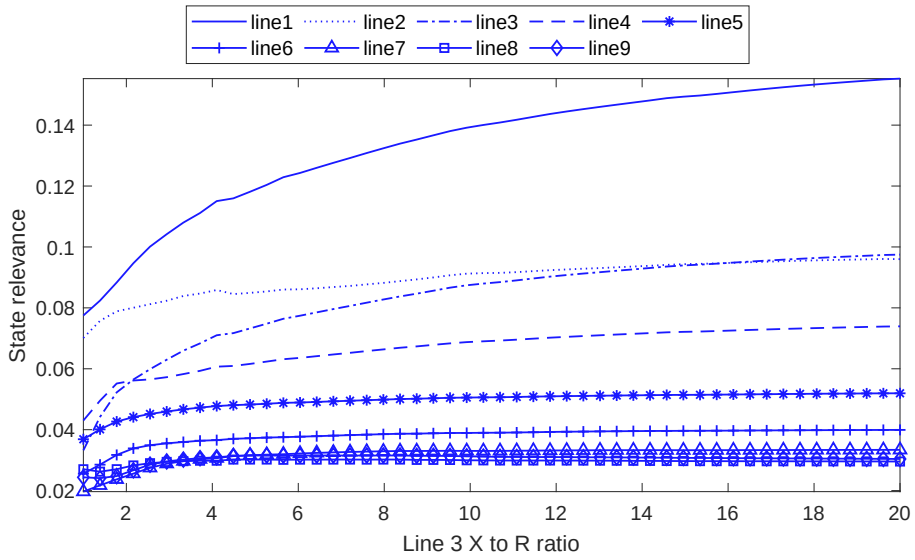

Figure 3.12: Evolution of the state RC of the most relevant state of each line when changing the X/R ratio of line 3 while keeping its impedance modulus constant.

3.5.2 Analysis of the selection of the input and output variables

Since the proposed method takes into consideration the input-output response of the system, results are affected by the input-output pair chosen. Indeed, the selection of the input and output variables affects the RC since it affects the Gramians and consequently the transformation matrix $\mathbf{T}$. In general, the selection of input and output variables may vary according to the study of interest. For example, to analyse the frequency stability of the system of Figure 3.9, the frequency of the centre of inertia (COI) could be considered as an output.

Table 3.6 illustrates the influence of the output selection on the relevance of the 26 most relevant states of the system. It shows that by adding the frequency of the COI to the initial output variable selection, the relevant states and their order hardly change. When choosing the frequency of the COI as the only output, frequency and active power dynamics are, however, the most relevant ones, whereas voltage dynamics are not that relevant. This makes sense since frequency dynamics are mainly affected by active power variations (and much less by voltage and reactive power variations).

Table 3.6: State relevance analysis for different output choices. Case 1 with v, θ, P and Q of all DGs as outputs. Case 2 is the same as case 1, adding the COI frequency as an output. In case 3, the COI frequency is the only output.

Case 1		**Case 2**		**Case 3**	
State name	R_x	**State name**	R_x	**State name**	R_x
$DG10/\theta$	1	$DG10/\theta$	1	$DG10/\theta$	1
$DG8/E^*$	0.99917	$DG8/E^*$	0.99245	$DG9/\theta$	0.66304
$DG7/E^*$	0.96861	$DG7/E^*$	0.96231	$DG4/\theta$	0.46822
$DG9/E^*$	0.96195	$DG9/E^*$	0.95529	$DG3/\theta$	0.44201
$DG6/E^*$	0.91497	$DG6/E^*$	0.90912	$DG8/\theta$	0.43829
$DG5/E^*$	0.87145	$DG5/E^*$	0.86564	$DG5/\theta$	0.43394
$DG10/E^*$	0.84936	$DG10/E^*$	0.84405	$DG3/\omega^*$	0.41449
$DG4/E^*$	0.81012	$DG4/E^*$	0.80456	$DG2/\omega^*$	0.40099
$DG3/E^*$	0.65407	$DG3/E^*$	0.65006	$DG4/\omega^*$	0.3672
$DG9/\theta$	0.64352	$DG9/\theta$	0.64418	$DG1/\omega^*$	0.34421
$DG3/\theta$	0.52128	$DG3/\theta$	0.5206	$DG8/\omega^*$	0.32143
$DG2/E^*$	0.51542	$DG4/\theta$	0.51357	$DG6/\theta$	0.31627
$DG4/\theta$	0.51349	$DG2/E^*$	0.51314	$DG7/\theta$	0.31583
$DG5/\theta$	0.51163	$DG5/\theta$	0.51116	$DG9/\omega^*$	0.3046
$DG2/\omega^*$	0.5023	$DG2/\omega^*$	0.50207	$DG2/\theta$	0.29939
$DG8/\theta$	0.48347	$DG8/\theta$	0.48343	$DG1/P_f$	0.2903
$DG10/PIv_d$	0.47034	$DG3/\omega^*$	0.46884	$DG5/\omega^*$	0.28934
$DG3/\omega^*$	0.46835	$DG10/PIv_d$	0.46762	$DG7/\omega^*$	0.28185
$DG10/PIi_d$	0.46319	$DG10/PIi_d$	0.46051	$DG10/P_f$	0.21092
$DG9/PIv_d$	0.45552	$DG9/PIv_d$	0.45257	$DG10/\omega^*$	0.19797
$DG9/PIi_d$	0.4488	$DG9/PIi_d$	0.44589	$DG6/\omega^*$	0.19175
$DG4/PIv_d$	0.43982	$DG4/PIv_d$	0.43689	$DG4/P_f$	0.16695
$DG4/PIi_d$	0.43279	$DG4/PIi_d$	0.42991	$DG5/P_f$	0.1617
$DG3/PIv_d$	0.42718	$DG3/PIv_d$	0.42456	$DG2/P_f$	0.15137
$DG3/PIi_d$	0.42015	$DG6/\theta$	0.41911	$DG6/P_f$	0.14556
$DG6/\theta$	0.42015	$DG7/\theta$	0.41894	$DG3/P_f$	0.14243

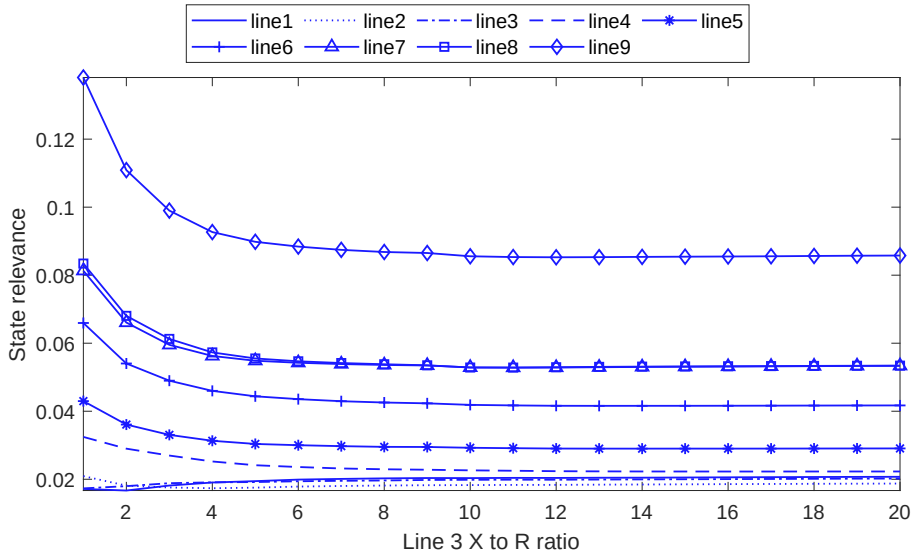

Figure 3.13: Evolution of the state RC of the most relevant state of each line when changing the X/R ratio of line 3 while keeping its impedance modulus constant. Graph from DG10 (leader) to DG1.

To validate this result, the microgrid with 10 GFr-VSCs was reduced by considering the frequency of the COI as the only output and the frequency set point of the leader (DG1) as the input. The reduced model consisted of 26 states: all reference-frame angles but the leader's one (9 states); all secondary-control-related states (10); and those related to active-power filters for all DGs, except DG7, DG8 and DG9 (7 states). The disturbance simulated consisted of a 5% increment in the frequency set point of the leader (DG1). Figure 3.14 shows the response of the frequency of the COI for the original and the reduced[3] nonlinear models to this disturbance. Figure 3.14 also indicates, for each of the considered approaches, the number of states. "Rel." has the fewest states. Figure 3.15 shows the Bode diagram for the linear approximations to the complete and reduced ("Rel.") nonlinear models with the input-output selection considered, to compare the frequency response of both systems.

Since the other approaches ("Rel. approx" and "Eigen") do not focus on the input-output response of the system but only on the state matrix of a linear approximation of the original nonlinear system, they find the same relevant states as when considering the electrical variables of all GFr-VSCs as outputs and fail to follow the

[3] "Rel." removes the states with lower relevance coefficient, "Eig." removes the states with higher participation from the eigenvalues with a more negative real part and "Rel. ap." reduces the states associated with the eigenvalues with a more negative real part.

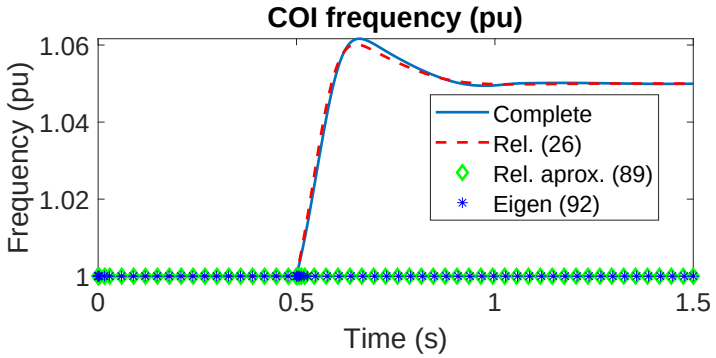

Figure 3.14: Response of the frequency of the COI of the complete and reduced models in case study 2 (10 GFr-VSCs) to a 5% increment in the frequency set point of DG1 (leader). The numbers enclosed within brackets in the legends show the number of states included in the reduced nonlinear models.

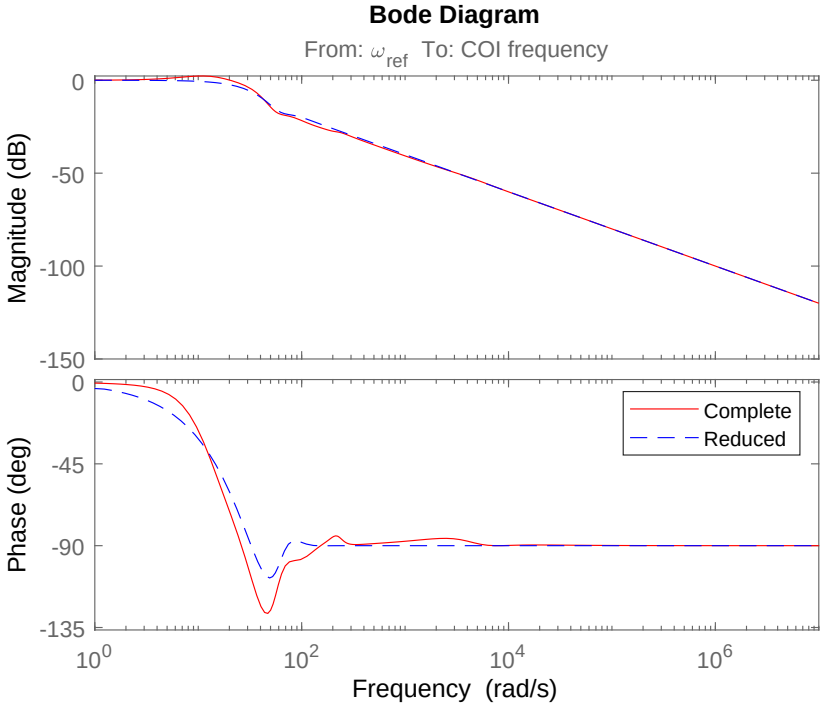

Figure 3.15: Bode diagram of the system using the increment in the frequency set point of DG1 (leader) as input and the frequency of the COI as output.

frequency dynamics with a reduced number of states. This dependence on the input-output selection is one of the key features of the proposed state relevance algorithm.

3.6 Applying state relevance on the IEEE 69 bus test system case study

Table C.2 in Appendix C includes the line and load data for the IEEE 69 bus distribution system presented in Baran and Wu (1989).

The distribution system is operated islanded as a microgrid with seven grid-forming converters connected in the nodes shown in Table C.2.

Table C.1, included in Appendix C, shows the initial operating point for all simulations and linearisations and the parameters used for all the grid-forming converters. For the base case, these parameters were chosen for a clear time-scale separation between control layers.

3.6.1 Performance of the algorithm in a case with clear time-scale separation between control layers.

The microgrid was modelled, initialised and linearised using the author-developed Simulink®tool described in Appendix A. The inputs chosen are current injections in each bus, and the outputs chosen are the frequencies, voltages, and generated active and reactive power of each DG.

Figure 3.16 shows the state relevance of the different states of the linear system. States are grouped as described in Table 3.7. It clearly shows that the most relevant dynamics are the secondary control and the frame calculation of all converters. The state relevance obtained suggests that eliminating the dynamics of all other variables will not significantly change the input-output response of the system. The threshold is set such that only the 20 most relevant states are above, due to the large difference between state number 20 and state number 21.

Figure 3.17 compares the time response of the complete and reduced models of the microgrid to a load change. The load change was produced by disconnecting the most significant load (node 61). Out of 337 state-space initial variables in the complete system, only 20 are considered in the reduced model, i.e. the reduced model is 94% smaller, which reduces the computational burden.

Figure 3.17 confirms the conclusions drawn from the state relevance coefficient: the discarded states do not contribute much to the system dynamics.

3.6.2 Performance of the algorithm in a system close to its stability limit

In this case, the parameters of the voltage controller of converter one (VSC_1) were modified as given by (3.17).

Table 3.7: Nomenclature used for the group of states

Group	Description	State order
E^*	Secondary voltage control	1-7
LPF_P	Active power filter	1-7
LPF_Q	Reactive power filter	1-7
Lines	Line current	d-axis 1-68, q-axis 1-68
Loads	Load current	d-axis 1-48, q-axis 1-48
CC	Current controller	d-axis 1-7, q-axis 1-7
VC	Voltage controller	d-axis 1-7, q-axis 1-7
C_f	Filter capacitor voltage	d-axis 1-7, q-axis 1-7
L_c	Grid-side inductance current	d-axis 1-7, q-axis 1-7
L_f	Converter-side inductance current	d-axis 1-7, q-axis 1-7
ω^*	Secondary frequency control	1-7
frame	Calculation of reference frame	1-7
		Total: 337 States

$$K'_{pv} = 0.005K_{pv} \qquad K'_{iv} = 0.005K_{iv} \tag{3.17}$$

This modification slows down VSC_1 voltage control, reducing the time-scale separation between the control layers of this converter and making the system lightly damped.

Figure 3.18 shows the state relevance of the different states of the linear system. The figure shows that the most relevant dynamics are those of the secondary control, the reference frame calculation of all converters, and the voltage and current controller of VSC_1. Therefore, together with the reduced model, which considers instantaneous changes in power lines, loads, and voltage and current controllers (the conventional model reduction), another reduced model that also includes the dynamics of voltage and current controllers of VSC_1 is added to the comparison, as suggested by the state relevance coefficient (see column bars *CC* and *VC* in Figure 3.18).

Figure 3.19 compares the time response of the complete model with two reduced-order ones to the same load change as in Section 3.6.1. The complete model has 337 states, the conventional reduced model has 20 states, and the reduction suggested by the state-relevance coefficient has 28 states. Notice that including the dynamics of voltage and current controllers also involves the filter capacitor and converter-side inductance.

Results confirm the conclusions obtained with the state relevance coefficient: the discarded states do not contribute much to the system dynamics, except for the voltage and current controller of VSC_1, which must be included for an accurate response.

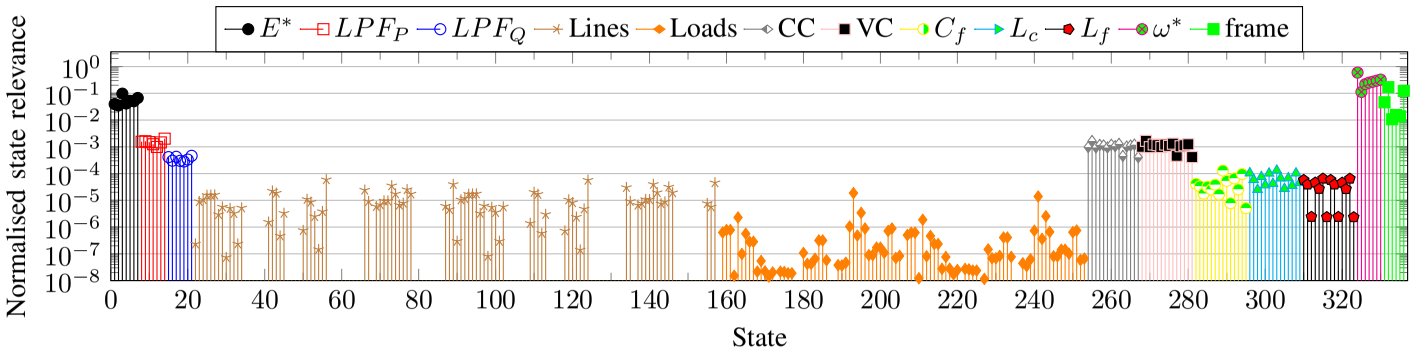

Figure 3.16: Normalised state relevance of the base case study. Values below 10^{-8} are not shown for clarity.

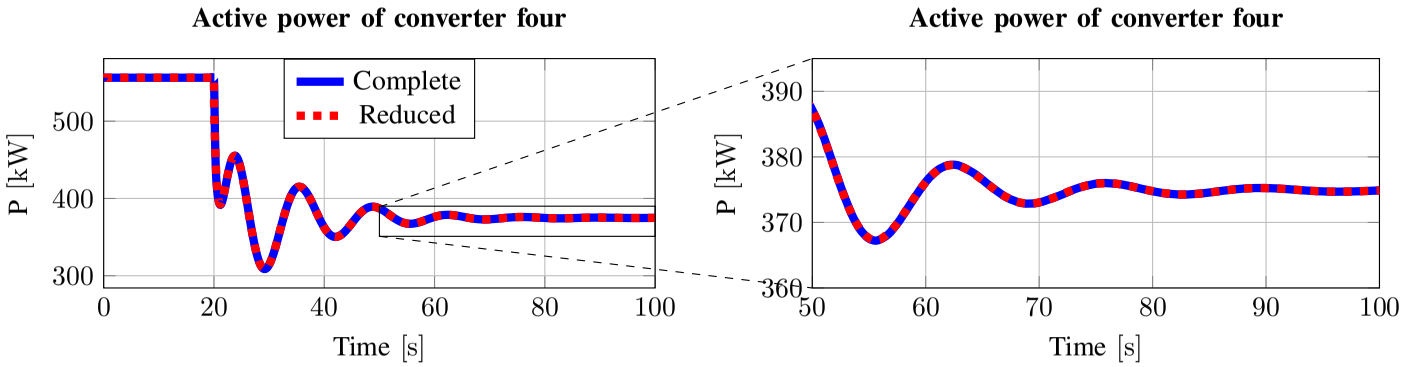

Figure 3.17: Comparison of the time response of the complete and reduced models of the microgrid to a load change. The active power of inverter four VSC_4 is shown.

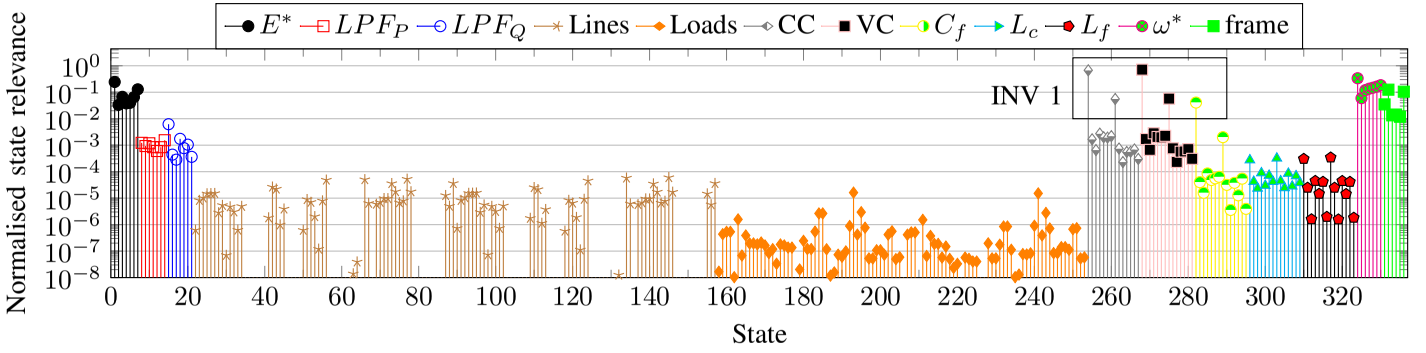

Figure 3.18: Normalised state relevance of the study case with abnormal time-scale separation. Values below 10^{-8} are not shown for clarity.

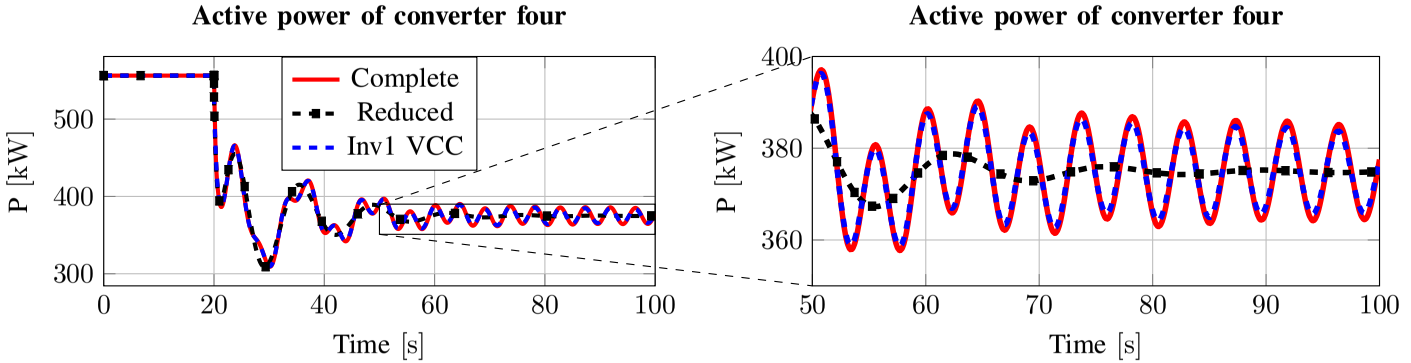

Figure 3.19: Comparison of the time response of the complete and reduced models of the microgrid to a load change. The active power of VSC_4 is shown.

3.7 Conclusions

This chapter has proposed an algorithm to quantify the state relevance of a dynamic system while preserving the physical meaning of the state variables, and has described possible applications to a microgrid with electronic power sources. The algorithm uses a balanced realisation of a linear approximation of the system to calculate the energy of each state variable in the output response. The transformation leading from the original linear system to the balanced realisation is linear, and the system eigenvalues are invariant. Unfortunately, the states of the balanced realisation may not have physical meaning. The relevance of the original states (that have physical meaning)is calculated through the participation factors of the system eigenvalues in the two sets of state variables, namely, before and after the transformation leading to the balanced realisation. In two case studies, the proposed algorithm has been applied to identify the relevant states and reduce the full nonlinear modes, based on this information, by assuming that the derivatives of less-relevant states can be made equal to zero and that controlled variables follow their set points. Results show that the traditional approach of associating relevant states with slow dynamics while fast dynamics are ignored requires reduced-order models of a higher order than those obtained with the proposed state-selection approach, if similar simulation accuracy for small disturbances is sought. The two approaches to state selection produce the same results if there is a clear time-scale separation of the system dynamics; therefore, the proposed state-relevance coefficient can be used to systematically choose the states to include in a reduced model while it provides valuable information for the modal analysis of the system. Needless to say, the state relevance depends on the choice of inputs and outputs (*i.e.*, it is application dependent).

This chapter analyses a multi-agent secondary control system for re-synchronising an electrical microgrid with the main grid, highlighting the effects of communication delays and power flows. Once re-synchronised, the microgrid can follow an exchange power set point given by the system operator accurately. The proposed method was validated using a setup of four 15 kVA converters, a 75 kVA grid emulator, and an industrial communication infrastructure.

4 Application of consensus among agents for reconnecting a microgrid of grid-forming converters to the main grid

4.1 Introduction

A microgrid (MG) is a small-scale power system that can operate either connected to or disconnected from the main grid (i.e., islanded) (Marnay et al., 2015). The transition between island and grid-connected modes need not be extraordinary and should be carried out seamlessly, minimising unwanted transients.

MGs can be reconnected to the main grid by using either asynchronous or synchronous interconnections. For the asynchronous case, a back-to-back electronic power converter is commonly used as the grid interface, and therefore the re-connection is much simpler (Susanto, Shahnia, Ghosh, & Rajakaruna, 2014). Nevertheless, employing an additional device increases the overall cost and the complexity of the installation. In contrast, the synchronous connection is done via a contactor, which is a much cheaper and simpler solution. In this case, the voltages at both sides of the contactor should be accurately synchronised to avoid unwanted transients when the contactor is closed (Rai & C, 2025). This requires precise control of the voltage and frequency of the connection point to the main grid and placing a distributed generator (DG) at that point is a possible alternative to drive the process (Acharya & Vijaya Kumar, 2024). However, this solution may not always be practical, and other alternatives have been sought in the literature for some time already, like the centralised PI-based control presented by J. M. Guerrero et al. (2011). This control should be adapted to the type of MG, e.g., if it consists of grid-forming voltage-source converters (GFr-VSCs) and/or grid-following con-

verters, synchronous generators, etc., and the use of a centralised controller is a typical approach for MGs based on GFr-VSCs. In this case, the angle difference between the grid and the MG is forced to zero by using a proportional+integral (PI) controller that calculates the frequency set point for all the GFr-VSCs. Many types of centralised controllers have been proposed to date to synchronise MGs, and this is still an open research field (Fachini, Bogodorova, Vanfretti, & Boersma, 2024). However, with the current development of DGs and smart grids, conventional centralised controllers could be replaced by multi-agent decentralised controllers, and one of the most common techniques for decentralised control is consensus-based control (Bidram et al., 2017). In applications of consensus algorithms, the only need to reach a global solution is communication between agents, which are commonly called *neighbours*. Consensus algorithms have recently gained attention for applications in AC and DC MGs (Guo et al., 2025).

A consensus-based cooperative synchronisation was proposed by Y. Sun, Zhong, et al. (2017) to synchronise MGs with the main grid. This work includes a synchronisation procedure for the frequency, angle and voltage, but does not analyse the synchronisation transient in active power involved in this type of control (in systems with inductive lines, the active power flow depends mainly on the angle difference. Therefore, angle synchronisation involves active power transients). Shah, Sun, Nikovski, and Zhang (2018) improved this idea by means of an additional low-pass filter (LPF) that smooths the synchronisation transient. A similar approach was presented by Z. Li et al. (2024), but in this case, by using sliding mode voltage and current controllers. These controllers are faster than traditional PI controllers, enabling faster control on all layers with a similar timescale separation. A decentralised algorithm to synchronise MGs based on droop-controlled DGs was presented in Khan, Liu, Shang, and Wang (2023), where one DG was in charge of the synchronisation.

The reviewed literature has presented decentralised approaches for MG synchronisation, but the communication dependency and, in particular, the impact of communication delays have been hardly addressed for synchronisation, which requires precise voltage and frequency control. Communication delays between agents affect the stability of multi-agent algorithms (Olfati-Saber & Murray, 2004). The authors of that reference calculated the maximum delay compatible with a stable secondary controller. This limit depends on the properties of the communication graph between agents and has already been explored in Wong et al. (2021), although the analysis neglected the effect of the controllers of the DGs. In this regard, Coelho et al. (2016) proposed an extension of the small-signal model of a MG with a multi-agent secondary control that includes constant communication time delays. It was found that, by increasing the time delay, some specific system eigenvalues approach the imaginary axis. A similar eigenvalue analysis was conducted in Y. Chen, Wan, Zhao, and Yu (2024) to determine the stability boundaries of a consensus-based secondary control in the presence of communication delays, for a DC MGs. The effect of communication delays in a MG stability has been anal-

ysed for an adaptative triggered consensus algorithm[1] (C. Liu, Wang, & Zhang, 2024). Shahab et al. (2019) highlight the importance of sensor noise in consensus algorithms, in addition to communication delays. This study was later expanded to consider the effect of additive Gaussian noise and time-varying stochastic delays by Dehkordi et al. (2021). In that work, it was shown that DGs may receive incomplete or imprecise information from neighbours due to the fading caused by multi-path propagation. However, these issues are out of the scope of this work since a reliable protocol (TCP/IP) between agents was used, and adequate data integrity can be guaranteed. However, none of these works focuses on synchronisation controllers, which have specific problems such as active power transients. Moreover, in these works, the active power transients between DGs are always addressed from the point of view of the secondary controller, overlooking the ability of the primary controller (e.g., derivative droop)to limit them.

In this chapter, a multi-agent secondary controller for resynchronising MGs formed by GFr-VSCs with the main grid is proposed, analysed, and then implemented and validated in a laboratory. The proposed controller is also capable of imposing the required active-power exchange between the microgrid and the main grid, once the resynchronisation takes place. This chapter focuses on the implementation aspects of this controller, which were not addressed in previous references. More precisely, the effect of communication delays is modelled and explored in detail, together with the active power flow between DGs during the synchronisation process. A detailed small-signal analysis is used to assess the impact of communication delays, while active power transients are studied using a simplified steady-state model of the active power flow. These tools are subsequently used to design a synchronisation controller that guarantees the small-signal stability of the MG and limits the active power flow during the synchronisation process. The results demonstrate that active power flows can be greatly reduced by using a derivative droop controller. In fact, a conventional but carefully designed PI controller, together with the derivative droop, is enough to satisfy all the requirements.

The main features of the proposed controller are first validated by simulations with MATLAB/Simulink (MATLAB, 2019), and then in a laboratory consisting of four 15 kVA power converters (acting as DGs), a 75 kVA grid emulator, electrical lines, loads, and a real communication infrastructure. The main contribution of this chapter compared to state-of-art work is highlighted in Table 4.1.

The rest of the chapter is organised as follows. An overview of the application is presented in Section 4.2, together with the main control and modelling tools used in the chapter. The design of the secondary controller in the presence of communication delays is presented in Section 4.3. Subsequently, the analysis of the active power flow during transients is presented in Section 4.4. A case study and the analytical results are presented in Section 4.5 while the experimental validation is presented in Section 4.6, and the proposed algorithm is validated in the modified IEEE 69 bus test system in Section 3.6.Finally, conclusions are drawn in Section 4.8.

[1] see Chapter 2 for a brief explanation of a triggered consensus algorithm

Table 4.1: Comparison of existing approaches for synchronising MGs. "**C**" means "multi-agent consensus-based algorithm", "**SSA**" "small-signal stability analysis", "**P**" "method to reduce active power during transients", "**D**" "communication delays considered" and "**Lab**" "experimental validation".

Reference	C	SSA	P	Synch. method	D	Lab
J. M. Guerrero, Vasquez, Matas, de Vicuna, and Castilla, 2011				PI + LPF		
Fachini, Bogodorova, Vanfretti, and Boersma, 2024				MPC	✓	
Khan, Liu, Shang, and Wang, 2023	✓			Fuzzy logic control		
Y. Sun, Zhong, et al., 2017	✓	✓		PI control		
Shah, Sun, Nikovski, and Zhang, 2018	✓		✓	PI + LPF		
Z. Li et al., 2024	✓			Integral control		
Tomás-Martín et al., 2023	✓		✓	PI + saturation		
This chapter	✓	✓	✓	PI + deriv. droop	✓	✓

PI: proportional-integral, LPF: low-pass filter, MPC: model predictive control

4.2 Application overview

4.2.1 System description

Figure 4.1 shows the electrical and control diagrams of the MG studied in this work. It can work either connected to (closing the contactor) or disconnected from the main grid. Generation in the MG consists of four DGs that are interfaced with the grid by using voltage-source converters (VSCs) with LCL filters. The voltage at the connection point (v_{mg}) and the main grid voltage (v_g) are measured remotely, and the angle difference between them (θ_{diff}) is calculated and sent only to $DG1$. Each DG (DGi) has a grid-forming controller to control its output voltage. It consists of a voltage controller, an inner current controller (both in dq coordinates, a virtual impedance, and frequency and voltage droops Yazdani and Iravani, 2010. On top of these controllers, a secondary active power-frequency controller is used to generate the output frequency set point for each DG.

When the MG is connected to the grid, the secondary controller is used to control the power exchanged with the grid and guarantee active power sharing among the DGs. However, when the MG is working in island mode, the secondary controller seeks a consensus among the DGs frequencies and their share of supplied active power. In addition, when required, it synchronises the MG with the main grid. Here, a multi-agent active power-frequency secondary controller is used, and it does not require centralised processing of information but only communication

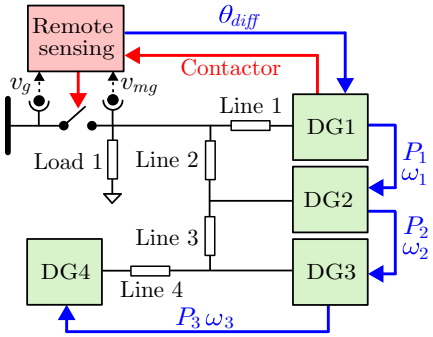

Figure 4.1: Electrical and control system diagram of the MG studied in this work. Four DGs with a decentralised secondary controller.

between neighbours (Bidram et al., 2014).

Each DG is considered as an "agent" whose outputs (P_i and ω_i in Figure 4.1) are calculated based on its local measurements and the information received from its neighbours, exclusively. In this particular setup, there is a maximum of one DG sending information to each DG. This implies that, if a communication link is broken, there is no spanning tree in the system, and consensus is not guaranteed, as explained in Chapter 2. In the scenario of a link loss, the communication graph must be rebuilt such that it contains a spanning tree, using the existing communication infrastructure.

4.2.2 Droop control and consensus final value

This section presents the droop control used for GFr-VSCs and revisits the structure of consensus-based secondary frequency control presented in Chapter 2, applied in this chapter, to clarify the presented algorithm. The droop control for each DG (DGi) in the graph G_r is formulated as (Y. Sun, Hou, et al., 2017):

$$\omega_i(t) = \omega_i^*(t) - m_{Pi}P_i(t) - m_{Di}\frac{dP_i(t)}{dt}, \tag{4.1}$$

where subscript i refers to the DG number, $\omega_i(t)$ is the output frequency and $\omega_i^*(t)$ is its set point, $P_i(t)$ is the measured output power, m_{Pi} is the droop coefficient and m_{Di} is the derivative droop coefficient, introduced to reduce the active power transients among grid-forming converters. To avoid noise amplification and unwanted interactions, the derivative droop is implemented as suggested in the literature (Y. Sun, Hou, et al., 2017), i.e., the angle of the output voltage is imposed rather than the output frequency:

$$\omega_i(t) = \omega_i^*(t) - m_{Pi}P_i(t), \tag{4.2}$$

$$\theta_i(t) = \int \omega_i(t)dt - m_{Di}P_i(t). \tag{4.3}$$

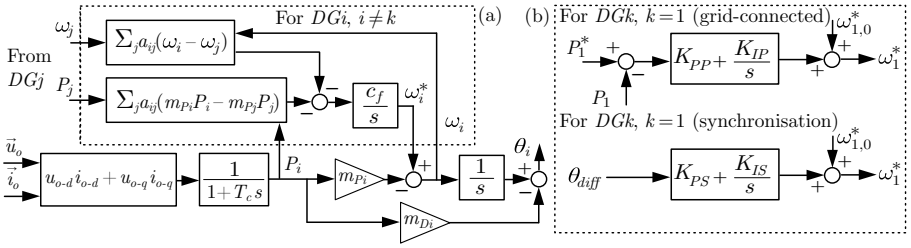

Figure 4.2: Primary and secondary controller of a DG. In (a), for any DG except the leader (k). In (b), for the leader ($k = 1$ in this work).

Since the angle is the derivative of the frequency, this droop control is equivalent to the one described by (4.1).

Using the consensus algorithm, as presented in Chapter 2, the frequency set point for each DG in the MG can be calculated by solving the following differential equation:

$$\frac{d\omega_i^*(t)}{dt} = -c_f \sum_{j \in N_i} a_{ij} \left[\omega_i^*(t) - \omega_j^*(t)\right], \quad i \neq k, \tag{4.4}$$

where $DG_j \in N_i$ if $(DGj, DGi) \in E$ and c_f is the secondary control gain. In other words, DGj sends information (the value of ω_j^*) to DGi, and constants a_{ij} are the weights given to the edge (DGj, DGi).

The control system for the leader (DGk) is different and will be explained in Sections 4.2.4 and 4.2.5. In this work, $DG1$ takes the role of leader and therefore $k = 1$. In general, the leader must be the DG with a lower impedance to the point of connection to the main grid. In the graph shown in Figure 4.1, the edges of the graph form a spanning tree with the root in $DG1$. The calculation of the frequency of the leader is addressed in Section 4.2.4 for resynchronisation, and in Section 4.2.5 for grid-connected mode. For practical reasons (e.g., more visibility of variables, possibility to change droops, etc.), the controller is implemented replacing the steady-state droop characteristic (4.1) in the consensus algorithm (4.4):

$$\begin{aligned}\frac{d\omega_i^*(t)}{dt} = &- c_f \sum_{j \in N_i} a_{ij} \left[m_{Pi}P_i - m_{pj}P_j\right] + \\ &- c_f \sum_{j \in N_i} a_{ij} \left[\omega_i(t) - \omega_j(t)\right], \quad i \neq k.\end{aligned} \tag{4.5}$$

Since the graph has a spanning tree, the DGs will eventually reach a consensus (Bidram et al., 2014):

$$\omega_1^*(t = \infty) = \cdots = \omega_N^*(t = \infty). \tag{4.6}$$

Therefore, the whole MG will reach a common value of frequency in steady state. In this work, $DG1$ (the one that receives the information from the main grid), will force the value of $\omega_1^*(t = \infty)$.

4.2.3 Steady-state operation

In steady state, the frequency of all the DGs will be the same. In addition, as shown in (4.6), the frequency set point of all the DGs will also be the same. Therefore, (4.5) leads to:

$$\omega_1(t=\infty) = \cdots = \omega_N(t=\infty), \tag{4.7}$$

$$m_{P1} \cdot P_1(t=\infty) = \cdots = m_{PN} \cdot P_N(t=\infty). \tag{4.8}$$

and the pair DGi and DGj will work with the same output frequency and will share the power demand according to:

$$P_j(t=\infty) = \frac{m_{Pi}}{m_{Pj}} P_i(t=\infty). \tag{4.9}$$

4.2.4 Synchronisation with the main grid

The synchronisation with the main grid is considered complete when the amplitude, phase and frequency of the voltages at both sides of the grid contactor are the same. In this chapter, voltage amplitude differences are not addressed, although this topic is interesting for further research. As shown in the simulation, there are no large transients caused by voltage amplitude differences after the connection. If required, the voltage amplitude difference can be controlled to zero with a PI control on the leader´s voltage, analogously to the angle. Without loss of generality, $DG1$ was selected as the leader of the synchronisation process and will change its frequency set point (ω_1^*) as (Shah et al., 2018):

$$\omega_1^*(s) = \omega_{1,0}^* + \overbrace{\left(K_{PS} + \frac{K_{IS}}{s}\right)\theta_{diff}(s)}^{\Delta\omega_1^*(s)}, \tag{4.10}$$

where s is the Laplace variable. To simplify the notation, in the remainder of the chapter, the same symbol will be used for signals in the time and the Laplace domains (e.g., $\omega_1^*(s)$ and $\omega_1^*(t)$). The constant $\omega_{1,0}^*$ is the frequency set point of $DG1$ before switching the synchronisation controller on, K_{PS} and K_{IS} are the parameters of a PI controller. The term $\theta_{diff}(s)$ represents the difference between the angles of the space vector of the grid voltage ($\vec{v}_g(t)$) and the MG voltage space vector at the connection point ($\vec{v}_{mg}(t)$). The space vectors are defined using dq components (i.e., $\vec{v}(t) = v_d(t) + jv_q(t)$) and the angle difference is calculated as follows:

$$\theta_{diff}(t) = \theta_g(t) - \theta_{mg}(t) = \text{ang}(\vec{v}_g(t) \cdot [\vec{v}_{mg}(t)]'), \tag{4.11}$$

where $\theta_g(t)$ and $\theta_{mg}(t)$ are the angles of $\vec{v}_g(t)$ and $\vec{v}_{mg}(t)$ with respect to the d axis of the reference frame, respectively. Here, the symbol $'$ indicates "complex conjugate". Note that (4.11) can be calculated in any reference frame since the

relative position between space vectors in the same reference frame is not affected by that choice (dq, $\alpha\beta$, etc.).

When the MG and the main grid are finally synchronised, $\vec{v}_g(t)$ and $\vec{v}_{mg}(t)$ will rotate synchronously and $\theta_{diff}(t)$ will be zero.

4.2.5 Tracking of power set points

When the MG is connected to the main grid, it can follow an active power set point by adding a PI controller to the power injected by the leader ($DG1$):

$$\omega_1^*(s) = \omega_{1,0}^* + \overbrace{\left(K_{PP} + \frac{K_{IP}}{s}\right)(P_1^*(s) - P_1(s))}^{\Delta\omega_1^*(s)}, \tag{4.12}$$

where K_{PP} and K_{IP} are the parameters of the PI controller, and $P_1^*(s)$ is the active power set point of $DG1$. In steady state, the active power injected by the leader will be equal to its set point and the output power of the rest of DGs can be easily calculated with (4.9). Neglecting the losses in the electrical lines of the MG, the total power injected into the grid can be calculated as follows:

$$P_g(t=\infty) = \sum_{i=1}^{N} \frac{m_{Pi}}{m_{Pj}} P_i(t=\infty). \tag{4.13}$$

Then, the active power set point for the leader is:

$$P_1 = \frac{P_g}{\sum_{i=1}^{N} \frac{m_{P1}}{m_{Pi}}} \tag{4.14}$$

If accurate control is needed, the power losses could be estimated and included as a compensation term in the PI controller. Alternatively, the total power injected into the grid can be measured, sent to $DG1$, and used as the controlled signal in the PI controller, in (4.12).

4.3 Synchronisation controller design

4.3.1 Dynamic equivalent of the consensus algorithm

To understand the dynamic relation between the frequencies of DGs, the Laplace transform of the frequency set point of DGi in (4.4) must be calculated:

$$\omega_i^*(s) = -\frac{c_f}{s} \sum_{j \in N_i} a_{ij} \omega_i^*(s) + \frac{c_f}{s} \sum_{j \in N_i} a_{ij} \omega_j^*(s). \tag{4.15}$$

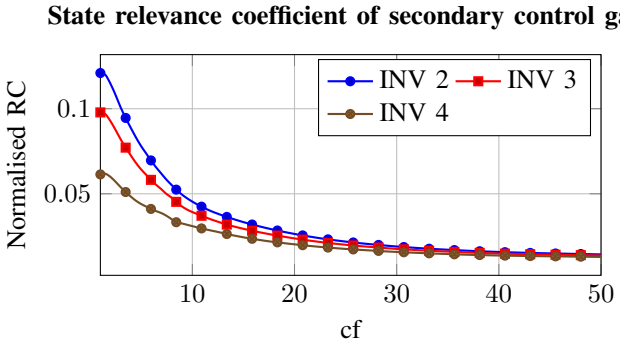

Figure 4.3: Evolution of the state relevance of the LPF state variables in (4.15), while changing the integral gain.

Notice that, in Figure 4.1, only one DG sends information to any given DGi and that $\sum_{j\in N_i} a_{ij} = 1$. Therefore, (4.15) is simplified to:

$$\omega_i^*(s) = \frac{1}{s/c_f + 1}\omega_j^*(s). \tag{4.16}$$

This first-order system relates the frequency set points of DGi and DGj, and proves that frequency set points will not be uniform across the MG during the consensus process. Moreover, if the dynamic associated with (4.16) is slow, the performance of the secondary controller will deteriorate, as it introduces a delay effect in the control. Here, the state relevance presented in Chapter 3 can help to determine the minimum value of c_f to make that delay negligible. If the state relevance finds the LPF state variables in (4.15) negligible, the LPF will not introduce a visible delay. A low value of c_f makes the consensus slow and thus secondary regulation. A quicker control is desirable if the grid to be connected varies significantly (e.g., another microgrid).

Figure 4.3 shows the calculated relevance of the state variable in the filter (4.16), which describes the secondary control. The relevance of the filter is negligible for $c_f \geq 30$.

The expression in (4.16) will be used in the remainder of this work instead of (4.15) because the former is correct for the MG example topology studied in this work. Note that (4.15) is valid to study the dynamics of any pair of DGs in the MG, but not for $DG1$.

4.3.2 Modelling and effect of communication delays

If communication delays exist, each agent i sees its neighbours' frequency (the ones to follow) with a delay. For example, if DGj only communicates its state to DGi,

the equation that relates their frequencies in (4.16) must be updated as:

$$\omega_i^*(s) = \frac{1}{s/c_f + 1} \underbrace{e^{-sT_d}\underline{\omega}_j^*(s)}_{\omega_j^*(s)}, \tag{4.17}$$

where $\underline{\omega}_j^*(s)$ is the frequency before applying the communication delay and T_d is the communication time delay between the two DGs. A large time delay can lead to an unstable consensus secondary control (Olfati-Saber & Murray, 2004). In this scenario, the choice of the graph affects the system dynamics and its robustness against changes in communication delays, as shown in Meng, Dragicevic, Roldán-Pérez, Vasquez, and Guerrero (2016). Therefore, the graph structure is maintained throughout this study to simplify explanations. In addition, even though small communication delays will not jeopardise the stability of the consensus algorithm, its performance will deteriorate. In particular, for MGs formed by GFr-VSCs, delays greatly modify the power injection requested from each DG to synchronise the MG because the droop control of GFr-VSCs described in (4.1) guarantees that DGs share active-power disturbances proportionally to their droop coefficients only if the frequency set points of all the DGs are the same. However, in decentralised secondary controllers, this is only true when the steady state is reached. Consequently, if DGs temporarily have different frequencies (as is the case if communication delays are considered), the angle difference between nodes would also change temporarily, producing unwanted active power transients. These transients may lead to unwanted disconnections of DGs or protection tripping. They can be reduced if changes in the synchronisation angle are made slowly. This issue has been tackled by limiting the rate of change of the frequency set point of the leader in Shah et al. (2018), and by limiting the frequency change given by the PI controller in (4.10) in Tomás-Martín et al. (2023). Alternatively, as suggested later in this thesis, a systematic design of the PI controller speed can be carried out (see Section 4.3.5).

4.3.3 Power exchanged between two DGs

The instantaneous power flow between two DGs (DG_i and DG_j) interconnected by a mainly inductive electrical line can be approximated as follows (Bidram et al., 2017):

$$P_{ij} = \frac{v_i v_j}{X_{ij}} \sin \delta_{ij} \approx \frac{v_i v_j}{X_{ij}} \delta_{ij}, \tag{4.18}$$

where v_i and v_j are the moduli of the DGs output voltages, X_{ij} is the nominal-frequency impedance between them, and δ_{ij} is the angular difference between the output voltages of the DGs. In practice, δ_{ij} is small and $\sin \delta_{ij} \approx \delta_{ij}$. If the impedance between DGs is not mainly inductive (e.g. low-voltage lines), a virtual impedance can be used to adjust its value (Wang, Li, Blaabjerg, & Loh, 2015).

Differentiating (4.18) and assuming that voltages v_i and v_j, and the line

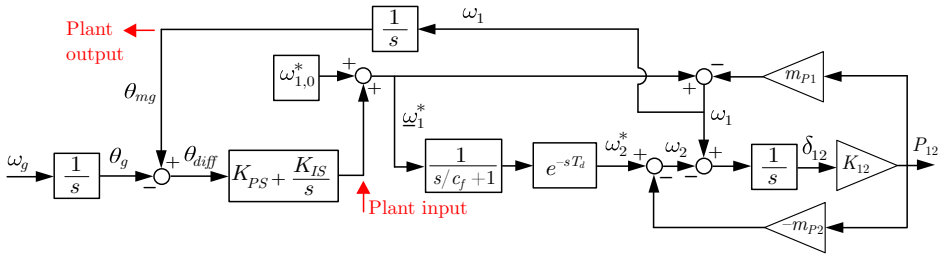

Figure 4.4: Block diagram representing the dynamic model of the agent-based secondary controller applied in this work.

impedances (X_{ij}) are constant gives:

$$\frac{dP_{ij}}{dt} = \frac{v_i v_j}{X_{ij}}(\omega_i - \omega_j). \tag{4.19}$$

which means that the steady state without power oscillations (i.e., $dP_{ij}/dt = 0$) is only reached if $(\omega_i - \omega_j) = 0$.

4.3.4 A complete model of the synchronisation process

Figure 4.4 shows the synchronisation controller, the droop control, the power flow equations between DGs, the secondary controller and the communication delay. This diagram will be used to design the synchronisation controller, and each block within that diagram is explained in the remainder of this subsection using two DGs, namely $DG1$ and $DG2$, where $DG1$ is the leader and it is the only agent that has access to the grid voltage measurements. Note that only two DGs are used to design the synchronisation control. To guarantee that the designed synchronisation control is still valid on larger microgrids with more DGs, the pair of converters to be considered in the analysis must be the worst-case pair. In this study, the worst-case pair is the one with the greatest delay-to-impedance ratio, because the active power transient increases when communication delays increase and/or the impedances between converters are reduced.

The output frequencies of the DGs can be calculated adapting (4.1) to $DG1$ and $DG2$:

$$\omega_1 = \omega_1^* - m_{P1} \cdot P_1 - m_{D1}\frac{dP_1}{dt}, \tag{4.20}$$

$$\omega_2 = \omega_2^* - m_{P2} \cdot P_2 - m_{D2}\frac{dP_2}{dt}. \tag{4.21}$$

The power flow between $DG1$ and $DG2$ can be modelled by setting $i = 1$ and $j = 2$ in (4.18), yielding (if $\delta_{12} \approx 0$):

$$P_{12} = \frac{v_1 v_2}{X_{12}}\sin\delta_{12} \approx \frac{v_1 v_2}{X_{12}}\delta_{12} = K_{12}\delta_{12}, \tag{4.22}$$

In Figure 4.4, communication delays are modelled by using (4.17) with $i = 2$ and $j = 1$, as explained in Section 4.3.2.

4.3.5 PI controller design

In this chapter, the PI controller in Figure 4.4 will be designed using open-loop frequency response techniques because they are well suited for high-order systems with delays (Pagola, 2016). In Figure 4.4, the plant transfer function can be calculated as the equivalent system between the points labelled "Plant input" and "Plant output".

For the design, it was deemed adequate to set the phase margin (ϕ_m) and the cross-over frequency (ω_0) of the open-loop system, since the parameters of the PI controller can then be calculated analytically (Pagola, 2016).

If the frequency responses of the plant ($P(s)$) and the controller ($C(s)$) at ω_0 are:

$$P(j\omega_0) = A_p e^{j\phi_p}, \quad C(j\omega_0) = A_c e^{j\phi_c}. \tag{4.23}$$

If the PI controller in Figure 4.4 is re-written as:

$$C(s) = \frac{sK_{PS} + K_{IS}}{s} = K\frac{1 + Is}{Is} \text{ with } \begin{cases} K = K_{PS} \\ K/I = K_{IS} \end{cases} \tag{4.24}$$

the PI controller can be designed in four easy steps:

1. The required phase of the controller at ω_0 is:

$$\phi_c = \phi_m - \pi - \phi_p. \tag{4.25}$$

2. I is calculated as:

$$I = \frac{\tan(\phi_c + \pi/2)}{\omega_0}. \tag{4.26}$$

3. K is calculated as:

$$K = \frac{I \cdot \omega_0}{\sqrt{1 + (I \cdot \omega_0)^2}} \frac{1}{A_p}. \tag{4.27}$$

4. K_{PS} and K_{IS} are calculated from K and I using (4.24).

Finally, the transient response of the closed-loop system should be checked to validate the design. In this work, the transient response is directly related to the active power flow between DGs during transients, which is investigated in detail in the following section.

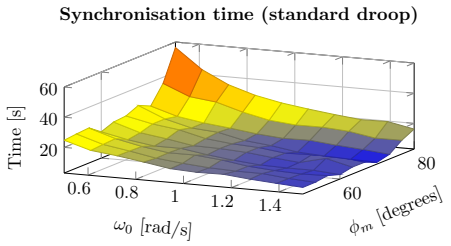

(a) Synchronisation time as a function of the open-loop phase margin and crossover frequency of the system. Standard droop.

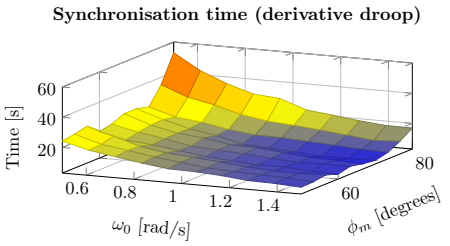

(b) Synchronisation time as a function of the open-loop phase margin and crossover frequency of the system. Derivative droop.

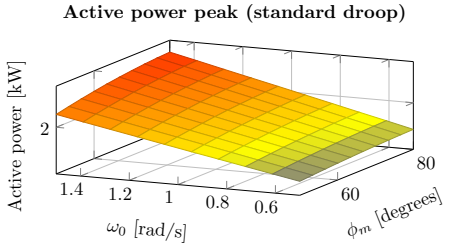

(c) Peak of the active power transient between DGs as a function of the open-loop phase margin and crossover frequency of the system. Standard droop.

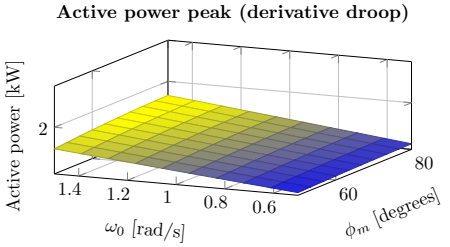

(d) Peak of the active power transient between DGs as a function of the open-loop phase margin and crossover frequency of the system. Derivative droop.

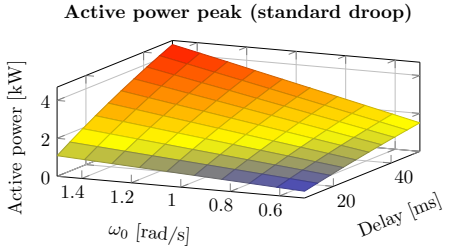

(e) Peak of the active-power transient between DGi and DGj, for different values of the communication delay (T_d) and crossover frequency (ω_0). Standard droop.

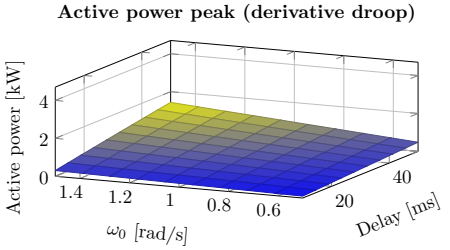

(f) Peak of the active-power transient between DGi and DGj, for different values of the communication delay (T_d) and crossover frequency (ω_0). Derivative droop.

Figure 4.5: Fundamental study of the powerflow between two DGs.

Table 4.2: Parameters used in the simulation study in Section 4.4.

$v_1 = v_2 = 400$ V	$Z_{12} = j \cdot 2\pi 50 \cdot 20e^{-3}\ \Omega$
$\omega^*_{1,0} = \omega^*_{2,0} = 2\pi \cdot 49.5$ rad/s	$\theta_{diff} = \pi$ rad (initial)
$m_{P1} = m_{P2} = 2 \cdot 10^{-4}$ rad/s/W	

4.4 Active-power flow characterisation during transients and its control

In this section, the active-power flow between two DGs (from $DG1$ to $DG2$) during transients is investigated by using numerical simulations to understand the effect of the communication delay (T_d), the phase margin (ϕ_m) and the crossover frequency (ω_0) of the angle-difference controller described in Section 4.3.5. The parameters used in the numerical simulation are presented in Table 4.2. Simulations have been carried out with and without the derivative term to highlight its importance. In this section, every possible design of the PI controller (i.e., phase margin (ϕ_m) and crossover frequency (ω_0)) is evaluated, and the optimal is chosen empirically, because the search space is small. However, in case of a larger search space, an optimisation algorithm can be implemented to design the controller (the objective function would include a minimisation of the transient active power peak and the synchronisation time).

4.4.1 Characterising the active-power flow between DGs

1) Effect of Phase Margin: Figures 4.5a and 4.5c show the synchronisation time and the peak of active-power flow between $DG1$ and $DG2$ when the MG is synchronised with the main grid, respectively. A constant time delay of $T_d = 30$ ms was used. In both cases, the crossover frequency (ω_0) was modified between 0.5 and 1.5 rad/s, and the phase margin (ϕ_m) was modified between 50 and 80 degrees. In Figure 4.5a, the synchronisation time is calculated as the time needed to reach a persistent angle difference (θ_{diff}) smaller than two degrees. Clearly, the synchronisation time can be reduced by increasing the crossover frequency and reducing the phase margin, but this will also increase the active-power flow during transients. The crossover frequency can be reduced as much as needed; however, the phase margin should be kept within adequate margins to avoid unwanted oscillations. In summary, for a proper design of the synchronisation controller, a balance between synchronisation speed and transient active-power flows must be found.
2) Effect of the Time Delay: Figure 4.5e shows the peak of active power needed to synchronise $DG1$ and $DG2$ with the main grid, for different values of the communication delay and the crossover frequency. The phase margin (ϕ_m) was maintained equal to 60 degrees. The active-power peak increases together with the communication delay and the crossover frequency. Therefore, the design of the synchronisation controller should take into account the maximum expected communication

delay and the maximum allowed active-power peak. In this chapter, as all the DGs are similar and there are no limitations in their primary energy source, the limit is established by the pair of DGs with the highest active-power peak. The pair of DGs with the highest active-power peak is the one with the highest delay-to-impedance ratio.

4.4.2 Reduction of the transient active-power peak

As shown in the previous section, the ability of the secondary controller to limit the power during transients is quite limited. A possible solution is to design a fast primary controller to react to changes in the angle of the connection point. In a traditional droop control scheme, this can only be achieved by increasing the droop gain or the virtual impedance. However, the droop gain is typically selected according to the required active power-frequency behaviour, while the virtual impedance should be carefully selected to guarantee adequate dynamic performance of the DG. The use of a derivative term in the droop controller gives an additional degree of freedom (Y. Sun, Hou, et al., 2017). To understand the effect of the derivate droop term, the results obtained for the standard droop in Figures 4.5a, 4.5c and 4.5e, were replicated, including the derivative droop term, in Figures 4.5b, 4.5d and 4.5f. A value of $m_D = 5.33 \cdot 10^{-5}$ was used (the details of how this value was selected are presented in the following section). The results show that the synchronisation time remains almost unaffected, while Figure 4.5d shows that the active-power exchanged between DGs was halved. In addition, Figure 4.5f shows that the effect of the delay is greatly reduced.

4.5 Further details of the case study and analysis

4.5.1 MG description and parameters

The MG presented in Figure 4.1 was modelled in MATLAB/Simulink. The system parameters presented in Table 4.3 were used, where L_c is the converter-side inductance of the LCL filter (R_c its resistance), C_f is the capacitor (R_f is its parallel resistance) and L_o is the output inductance (R_o is its resistance). The switching and sampling frequencies are f_s and f_{sw}, respectively. Figure 4.2 shows a diagram of the primary and secondary controllers implemented for each DG to manage active power. Voltage and current control loops (as described in Chapter 2) are also included. In addition, a virtual impedance (L_V) ensures adequate stability margins and power quality (a stationary implementation was used (Rodríguez-Cabero, Roldán-Pérez, & Prodanovic, 2020)). The information exchange between DGs is depicted in the left-top side of Figure 4.2.

As explained in Section 4.3 value $c_f = 30$ was chosen for the implementation of the secondary control to avoid undesired delays.

Table 4.3: MG hardware and control parameters.

System parameters		
$V_n = 400$ V	$f_n = 50$ Hz	$R_{load} = 16\ \Omega$
$L_{line1} = 0.1$ mH	$L_{line2} = 0.4$ mH	$R_{line}/X_{line} = 0$
$L_{line3} = 0.092$ mH	$L_{line4} = 0.27$ mH	
DG hardware parameters		
$L_c = 1.5$ mH	$C_f = 8.8\ \mu$F	$L_o = 2.2$ mH
$R_c = 48$ mΩ	$R_f = 48$ kΩ	$R_o = 173$ mΩ
$f_{sw} = 10$ kHz	$f_s = 10$ kHz	$L_V = 10$ mH
Initial operating point		
$P_i = 2.502$ kW	$\omega^*_{i,0} = 2\pi 50$ rad/s	
$Q_i = 0.027$ kVAr	$v^*_i = 400$ V	
MG topology and communication definition		
$a_{i(i-1)} = 1\ \forall i \neq 1$	$a_{ij} = 0\ (\forall j \neq i-1)\ \vee\ i = 1$	
Primary control parameters		
$m_P = 2 \cdot 10^{-4}$	$K_{PV} = 0.12$	$K_{PC} = 4.53$
$n_Q = 1 \cdot 10^{-4}$	$K_{IV} = 36.29$	$K_{IC} = 10600$
$m_D = 5.33 \cdot 10^{-5}$	$T_c = 1.5$ ms	
Secondary control parameters		
$K_{PS} = 0.0155$	$K_{PP} = 2 \cdot 10^{-5}$	$T_d = 3.2$ ms
$K_{IS} = 0.0062$	$K_{IP} = 2 \cdot 10^{-4}$	$c_f = 30$

4.5.2 Effect of the derivative droop term

Figure 4.6 shows, in blue, the peak of the active power needed to synchronise the MG, and in black, the synchronisation time.

Different values of the derivative droop term (m_D) were tested (see the horizontal axis). The results obtained for the simplified model presented in Section 4.3.2 are depicted in dashed lines. Meanwhile, the values obtained with the detailed simulation are depicted in solid lines. The results show that the simplified model is an adequate tool for designing the secondary controller, as the results are relatively similar, although the synchronisation time is overestimated slightly with the simplified model. This validates that the active power transient analysis can be simplified by considering only a pair of converters. The active-power peak is greatly reduced by increasing m_D while the synchronisation time remains almost constant. This fact greatly simplifies the design of the derivative droop term, which can be selected before designing the secondary controller. In any case, the stability of the detailed model should be validated for the specific m_D value chosen.

Figure 4.7 shows the system eigenvalues of a linearised version of the complete MG model, when m_D increases. The angle of the eigenvalue ($\mathrm{ang}(\lambda_i)$) is placed at the vertical axis while the modulus ($\mathrm{abs}(\lambda_i)$) is placed at the horizontal axis, in a logarithmic scale. For each complex pair, only the one with a phase between 90

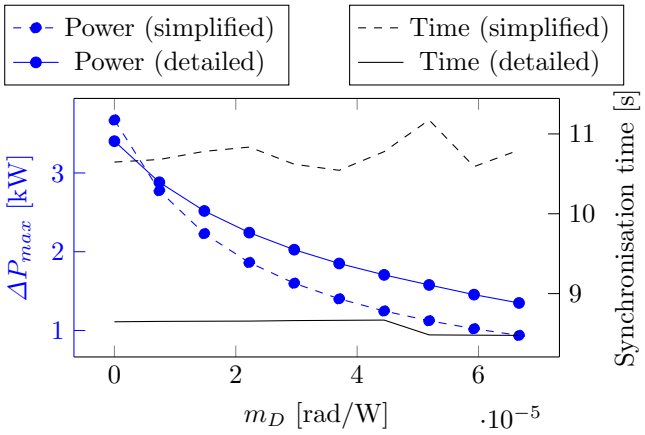

Figure 4.6: (blue) Active power peak needed for synchronisation and (black) synchronisation time, for different values of m_D. (dashed) Simplified and (solid) detailed MG model.

and 180 degrees was plotted. In this representation, all the system eigenvalues fit in a single plot, and critical eigenvalues can be easily spotted. Notice that a pair of complex eigenvalues is unstable if the angle is less than 90 degrees. Meanwhile, real eigenvalues (placed at 180 degrees) tend to "unstable" when reducing their moduli. In Figure 4.7, the eigenvalues affected by m_D are marked with numbers (from $\langle 1 \rangle$ to $\langle 4 \rangle$). The participation factor of each eigenvalue was calculated to understand to which variable it is linked to. The participation factors are calculated as described in Chapter 2. The eigenvalue $\langle 1 \rangle$ is real, and it reduces its modulus when m_D increases. It is mainly related to the integral of the frequency, which is directly related to the output of the PI controller used to synchronise the MG. The eigenvalue $\langle 2 \rangle$ is also real, while $\langle 3 \rangle$ and $\langle 4 \rangle$ are complex. All these eigenvalues are mainly related to the output of the measurement filter (i.e., they are strongly affected by the droop and its derivative).

These results lead to the conclusion that an adequate value of m_D should be selected to guarantee that both $\langle 3 \rangle$ and $\langle 4 \rangle$ are placed adequately.

Theoretically, the system eigenvalues of this example are stable if $m_D \leq 6.7 \cdot 10^{-5}$ rad/W and, to have a compromise between the location of $\langle 3 \rangle$ and $\langle 4 \rangle$ (both with damping factors of around 0.5), a value of $m_D = 5.33 \cdot 10^{-5}$ rad/W was selected.

A zoom on the pair of complex eigenvalues related to the resonance of the LCL filter is included in Figure 4.7. Even though the phases of these eigenvalues are close to 90 degrees (lightly damped), in the practical implementation, these eigenvalues are damped by the parasitic resistances of the DGs and the electrical interconnections. In any case, if these eigenvalues produce undesired resonances, they can be easily damped by using an active damping mechanism. This issue was previously addressed in detail for the VSCs used in Roldán-Pérez, Bueno,

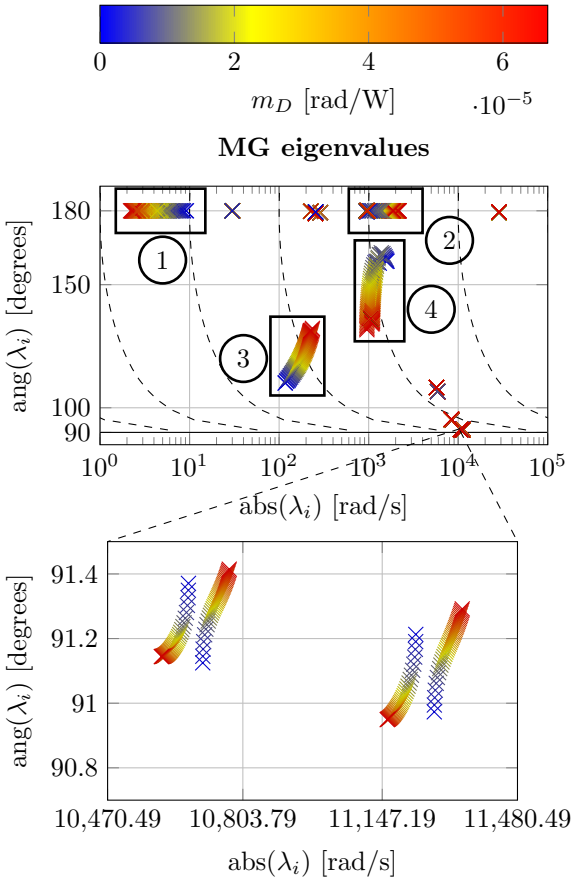

Figure 4.7: Angle versus modulus of the MG eigenvalues, for different values of m_D (see the text for explanations).

Peña-Alzola, and Rodríguez-Cabero (2018).

4.5.3 Numerical simulation to validate the secondary controller

In this section, the results of a set of tests applied to the MGs in Figure 4.1 are presented in Figure 4.8, in blue. The load in that figure consumes both active power (10 kW) and reactive power (10 kVAr). Notice that the generated active power is accurately shared among the DGs of the MG. However, reactive power is not, as this is not addressed by the secondary controller proposed in this work, and reactive power droops do not guarantee accurate sharing of reactive power. Exploring reactive power sharing in detail was left out for further research.

Figure 4.8 (blue) shows the numerical simulation results of the proposed control

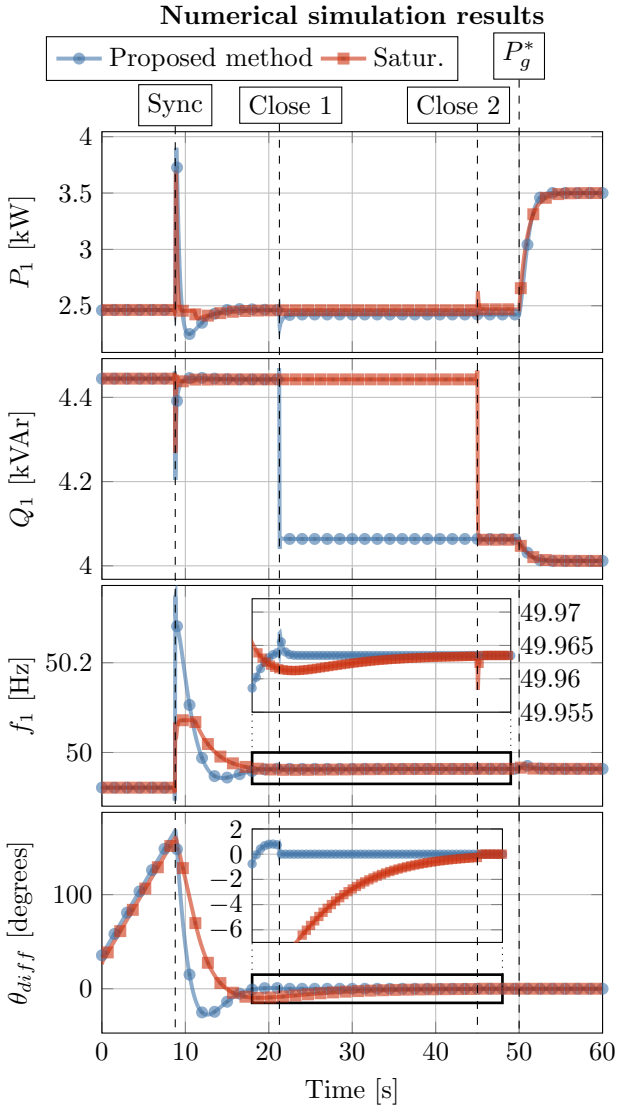

Figure 4.8: Simulation results of (blue) the proposed method and (red) the method based on saturation. From top to bottom, active power, reactive power and frequency of $DG1$, and θ_{diff}. The events are explained in the text.

algorithm. The results obtained with another method are also presented in that figure, in red, which will be explained later. Initially, and on purpose, the MG is operating in steady state below 50 Hz, because the secondary controller does not impose any frequency. At the instant labelled as "synchro", the synchronisation controller of $DG1$ is activated, and the MG starts synchronising with the main grid, which has a constant frequency close to 50 Hz. After some seconds, θ_{diff} becomes zero, meaning that the MG is synchronised with the main grid. Then, at the instant labelled "Close 1", the main contactor is closed (at $t = 20$ s, approximately). The transient in active power is negligible, meaning that the connection was smooth. Meanwhile, the reactive power flow changed rapidly because the voltage was not equal on both sides of the contactor. However, this rapid change is relatively small (0.3 kVAr, approximately) and does not produce any visible transient in the rest of the variables.

After the reconnection to the main grid, the power set point of the MG was modified at the time instant labelled as P_g^* in Figure 4.8. The active power set point of $DG1$ was increased by 1 kW, meaning that the active power injection of the full MG increased by 4 kW (see (4.13)). The active power injection changes rapidly and reaches the new steady-state value.

Figure 4.8 (red) shows the results obtained when a different proposed method, based on saturation, was applied to the MG studied in this work. This method limits the active-power transient by saturating the frequency of the leader during the synchronisation process. Using this method, the main contactor is closed at time instant "Close 2". The saturation is applied to $\Delta\omega_{1,0}^*$ in (4.10). The saturation limits are set to (using per unit values):

$$-0.003 \leq \Delta\omega_{1,0}^* \leq 0.003 \tag{4.28}$$

The application of this method without the consideration of communication time delays is presented in Tomás-Martín et al. (2023). Here, the saturation method was improved by adding the derivative droop. The results show that the modified saturation method also provides adequate results. However, it takes more time to reach the steady state during the synchronisation process. Once the MG is synchronised, the connection transient and the operation in grid-connected mode are similar to those in the previous case. In the future, it would be of interest to include this saturation together with the PI controller proposed in this work.

4.6 Experimental validation

4.6.1 Laboratory description

Hardware elements of the laboratory

The results of previous sections were validated by implementing the microgrid shown in Figure 4.1 in the laboratory facilities of IMDEA Energy. Figure 4.10 shows the main hardware elements used in the validation:

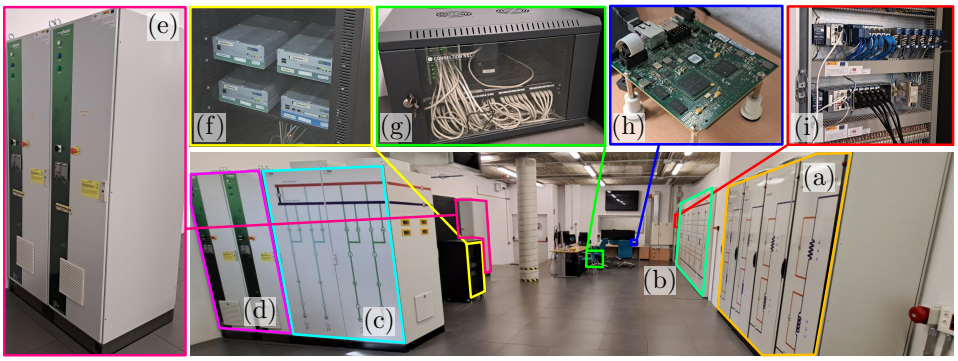

Figure 4.9: Pictures of the elements of the laboratory. (a) Line impedances, (b) AC busbars, (c) DC busbars, (d) 75 kVA VSCs, (e) 15 kVA VSCs, (f) real-time computers, (g) communication network switch, (h) single-board RIO and (i) two compactRIO.

- Four VSCs with LCL output filters were used to emulate the DGs (marked in green as $DG1$, $DG2$, $DG3$ and $DG4$ in Figure 4.10). Each DG was powered by an uncontrolled diode rectifier plus a three-phase transformer, with a transformation ratio of 400/480. These rectifiers were connected to an auxiliary network operating at 400 V and 50 Hz. This gives as a result a constant DC voltage of 680 V, which is enough to perform the pulse-width modulation process of the VSCs.
- The LCL filters of the DGs were all similar, and were connected to the MG by using a contactor.
- The DGs were interconnected using a set of electrical lines (in blue), and AC busbars (in red).
- A programmable load bank (between 0 kW and 30 kW, in steps of 1 kW), was used to emulate the load of the MG (in pink in Figure 4.9).
- The main grid was emulated with a grid emulator, which consisted of a 75 kVA VSC with an LCL output filter. Its output voltage was controlled by using a fast state-space controller so that the effect of the LCL filter was negligible at low frequency. The grid emulator was powered by another 75 kVA VSC connected via an LCL filter to the auxiliary grid. This VSC maintained the voltage of the DC link constant at 680 V and allowed the grid emulator to absorb active power. Therefore, the DGs were able to inject active power into the emulated grid, if needed.

Figure 4.9 shows pictures of the laboratory facilities, where the main elements have been highlighted.

The cabinets used to emulate the electrical lines are in (a), while the AC contactors are in (b). The DC busbars are in (c). The 75 kVA VSCs are in (d) while the

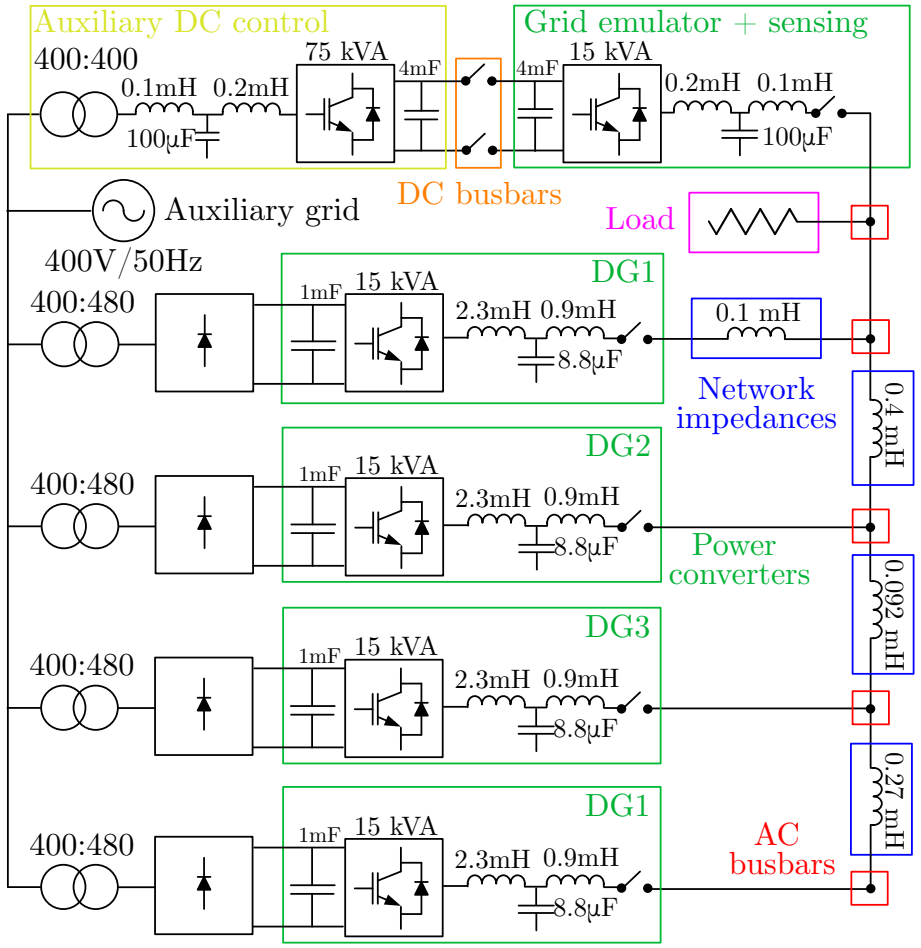

Figure 4.10: Interconnection of the hardware elements in the laboratory. (Green) Power converters, (yellow) auxiliary power converter, (blue) network impedances, (red) AC busbars, (orange) DC busbars and (purple) resistive load.

15 kVA VSCs are in (e). The real-time PCs used to run the control algorithm of DGs is in (f). The communication between those PCs was established via the Ethernet network in (g). A *single-board RIO* platform (h) was used to manage the data-flow between the real-time PCs.

Communication elements of the laboratory

Figure 4.11 shows the schematics of the laboratory control and communication elements. The main element that controls the laboratory is a *CompactRIO (Compact*

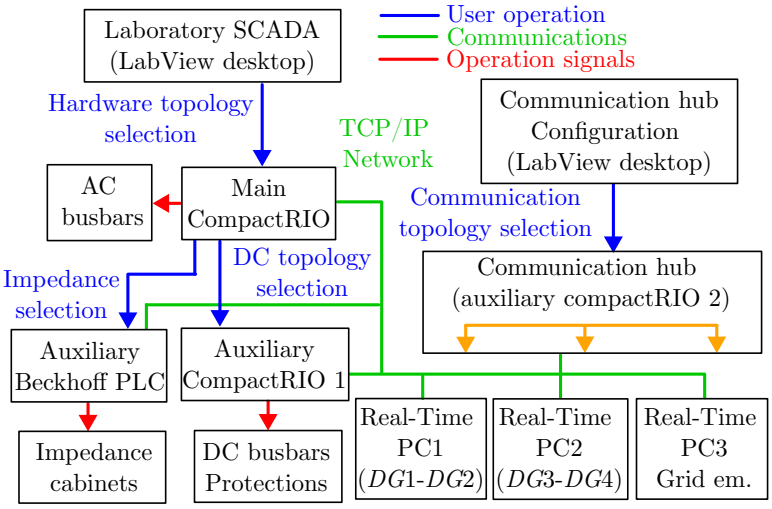

Figure 4.11: Communication infrastructure of the laboratory facilities.

Reconfigurable Input-Ouput). This element is operated from the laboratory SCADA, which is implemented in LabView. The main *CompactRIO* controls the state of the contactors of the AC panel, performs protection actions and coordinates the rest of the laboratory elements. It communicates with a Beckhoff PLC, which coordinates the operation of the network impedances (e.g., it closes/opens contactors to obtain the requested value of inductance and resistance). It also communicates with an auxiliary *compactRIO*, which is in charge of operating the DC contactors and guaranteeing the safe interconnection of DC buses.

The communication between DGs is implemented in a *single-board RIO* platform. It takes all the information from the real-time PCs that control the VSCs, re-route them, and sends it back to the selected real-time PCs. In this way, it is possible to define a communication topology (this is done in a LabView desktop application), and then implement it via the *single-board RIO*.

4.6.2 Experimental results

Measurement of communication delay

The communication delay between DGs was measured before deploying the multi-agent secondary controller. The measurements were done with the real-time PC1 (the one controlling $DG1$ and $DG2$). Figure 4.12 shows a histogram representing the measurements of the communication time delay between $DG1$ and $DG2$. The delay has a stochastic component similar to a normal distribution with a mean value of 3.2 ms. This value is not too long and has been used in the simulation presented to analyse the performance of the control loops, as recommended by

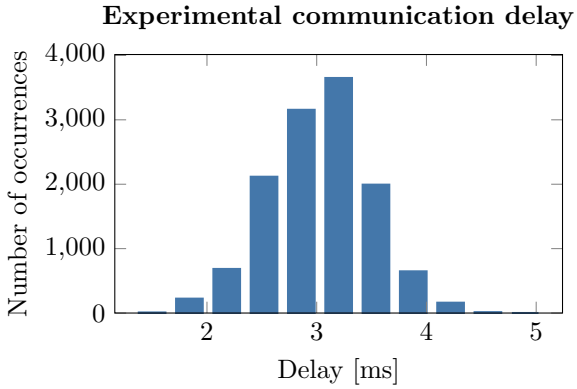

Figure 4.12: Histogram of the experimental measures of the communication delay between $DG1$ and $DG2$ in the laboratory.

(Jankovic et al., 2024).

Figure 4.13 shows the experimental results of the MG. Initially, the MG was operating as an island and the angle difference between the grid and the MG was increasing steadily. At the instant labelled "Sync", the synchronisation controller was activated. From this moment on, the angle difference (θ_{diff}) approaches zero and reaches the steady-state in ten seconds, approximately. The active-power plots show that the synchronisation process does not require an excessive value of active power thanks to the use of the derivative droop. Once the MG was synchronised with the grid, the grid contactor was closed (at the instant labelled "Close"). At this instant, there is a very small transient in the active power and in the frequency. However, it is almost unnoticeable because the MG and the main grid were accurately synchronised. Finally, when the MG was connected to the main grid, a step change of 4 kW was applied to the set point of the MG active power (i.e., $\Delta P_1^* = 4/4 = 1$ kW for $DG1$). Clearly, all the DGs rapidly change their active-power injection and follow the set-point value, accurately.

Figure 4.14 shows, in the same picture, the experimental results and the results obtained from the switched (i.e., the model which includes the pulse width modulation and switching of the electronic converters)and the averaged simulation models. The average simulation model is constructed using the Simulink tool described in Appendix A.

The figure shows the active-power output of $DG1$, its frequency, and the angle difference (θ_{diff}). Notice that the big jump in the angle before 10 seconds occurs only because the angle is wrapped in the range -180° to 180°.The events of the test are the same as those used in Figure 4.13. Clearly, the theoretical and the experimental results are very similar, although in the experimental test (in blue), the power needed to synchronise the MG is slightly higher than in the theoretical models. This happens because the real system has additional losses that were not

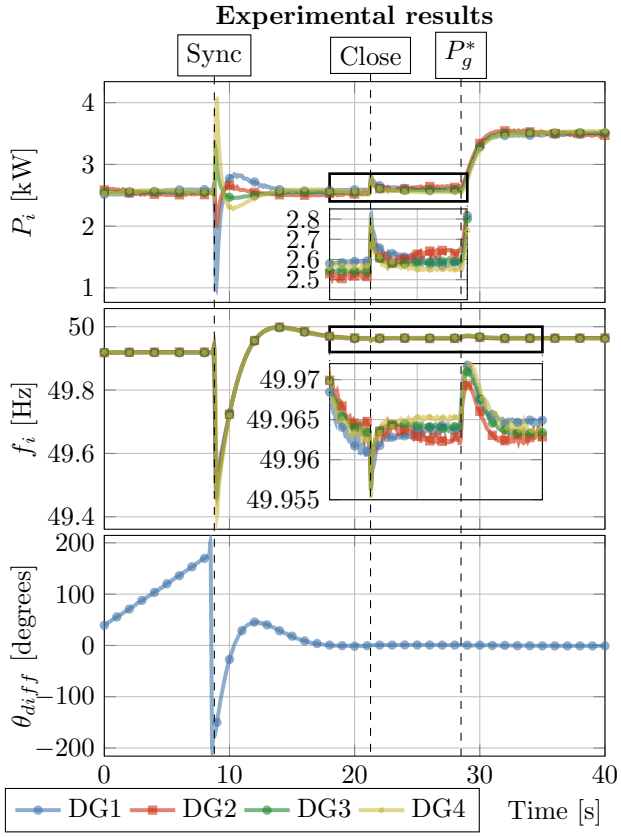

Figure 4.13: Experimental results. Resynchronisation and grid-connected control modes. From top to bottom, active power (P_i), frequency (f_i) and angle difference (θ_{diff}).

considered in the simulation models (e.g., switching losses, etc.).Nevertheless, the shapes of the transients were almost identical, indicating that both the switched and the averaged simulation models are useful tools to predict the dynamic behaviour of the MG.

4.7 A large case study: IEEE 69 bus test system

This section describes the application of the proposed synchronisation method to the modified version of the IEEE 69 test system described in Appendix C. The system is modelled and analysed using the Simulink tool presented in Appendix A. As this is a larger case and might take longer to simulate, the state relevance presented in Chapter 3 is applied to the system to reduce the negligible dynamics.

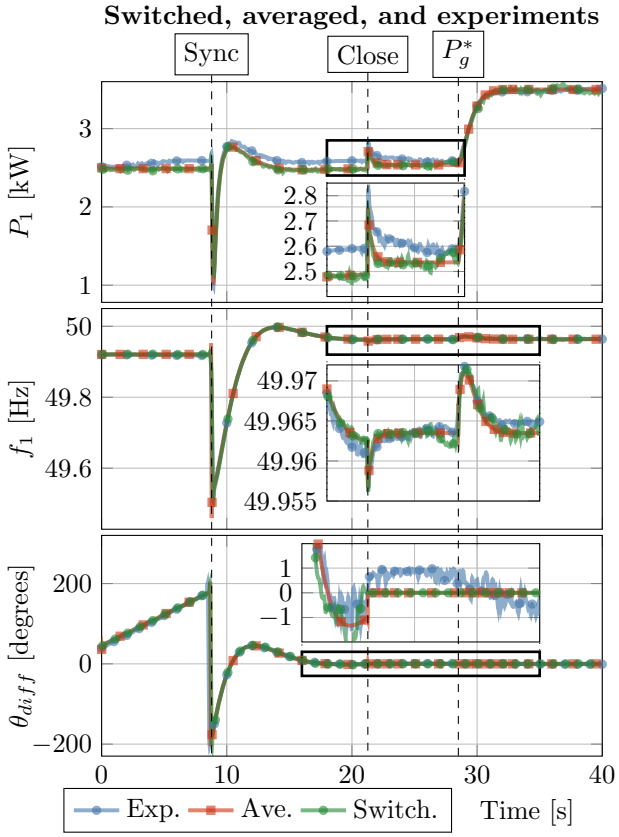

Figure 4.14: Comparison of the switched model, the averaged model and the experimental results. From top to bottom, active power (P_1), frequency (f_1) and angle difference (θ_{diff}).

This allows faster simulation.

Figure 4.15 includes the diagram of the test system. The microgrid will be connected to the main grid (after synchronisation) with a controllable switch connected at bus 33. For this case, a communication time delay of 10 ms was considered between all converters. The synchronisation control structure and parameters are the ones used for the case with four converters.

The synchronisation process is divided into the following stages:

1. **Secondary control activation**: At $t = 10$ s, the secondary control is activated. This guarantees active-power sharing among converters.

2. **Synchronisation starts**: At $t = 30$ s, the synchronisation control is activated. This changes the frequency set point of the leader DG.

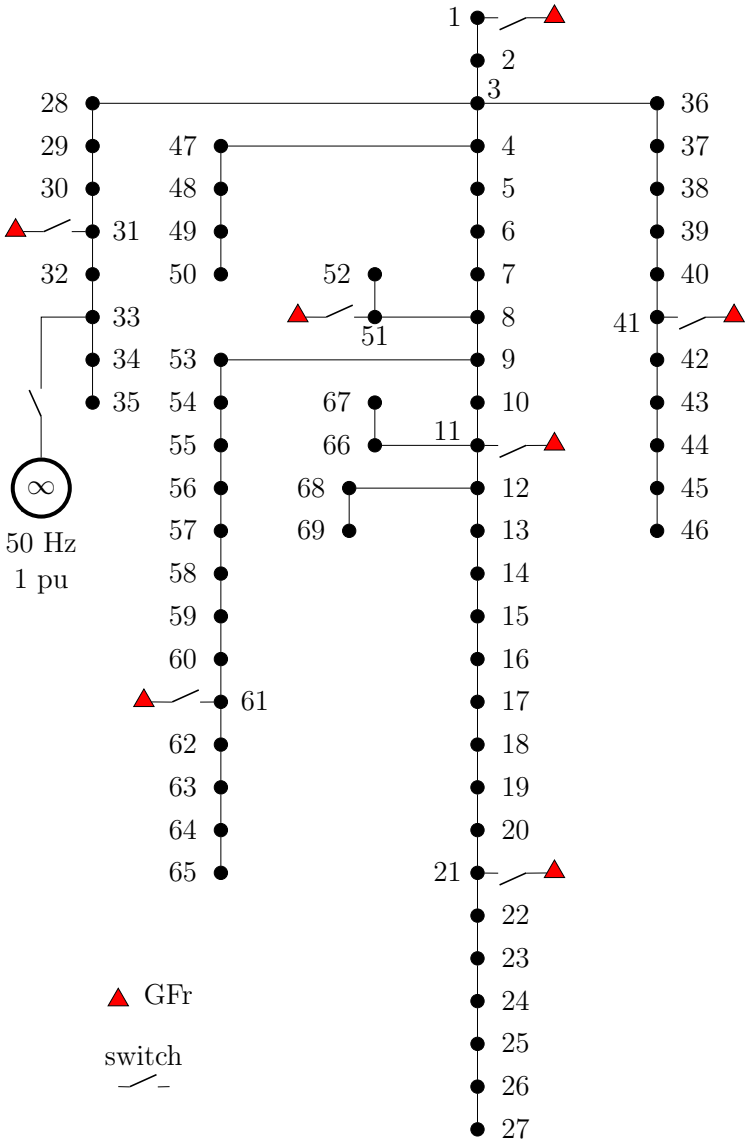

Figure 4.15: Single-line diagram of the modified version of the IEEE 69 bus test system.

3. **Closing the contactor**: After the synchronisation, the controllable switch between the microgrid and the main grid is closed. This occurs when the synchronisation thresholds are met.

4. **Increasing the active-power injection to the main grid**: 10 seconds after the close of the contactor, the microgrid is asked to inject 5.25 MW of active power into the main grid.

Figure 4.16 shows the results of the simulation of the synchronisation process.

Clearly, the results obtained are similar to those in the case of four grid-forming converters. The synchronisation implies an active power transient limited by the design of the proposed control, the angle difference is driven to 0 in a few seconds, avoiding big transients in the connection to the main grid, and the microgrid successfully injects power into the main grid after the connection with the selected active and reactive power sharing among converters. The key difference in this result is that the secondary control in islanded operation before the synchronisation maintains the frequency in its nominal value while guaranteeing active power sharing between converters.

4.8 Summary and conclusion

In this chapter, a multi-agent secondary controller for resynchronising MGs with the main grid was proposed. Two main effects of the communication delays have been studied: their impact on the system dynamics and on the active-power transient required for the resynchronisation. The delays were considered at the design stage of the PI controller so that the transient response of the MG was adequate. In order to reduce the active-power peak, the inclusion of a derivative term in the droop of DGs was proposed. The main findings were validated by using numerical simulations and laboratory experiments carried out in a realistic environment.

The simulation results showed that the communication time delays can greatly affect the power transient needed to synchronise the MG, but it was found that this effect can be reduced by using a faster secondary controller. However, the results showed that the use of a derivative droop term together with an adequate design of the secondary controller is a more effective strategy that can greatly reduce the peak active-power needed to resynchronise the MG while making the system less dependent on communication time delays. The detailed small-signal model revealed the impact of the derivative droop term on different eigenvalues of the MG, and a trade-off between the damping of all of them was established.

The experimental results obtained in the laboratory were very similar to those of the numerical simulation. In fact, the dynamic responses were almost identical, and only some small deviations in the power transients needed to perform the synchronisation were observed. The results obtained emphasise that an adequate modelling of realistic MG elements can lead to accurate models, which can be used to design high-performance controllers for real applications.

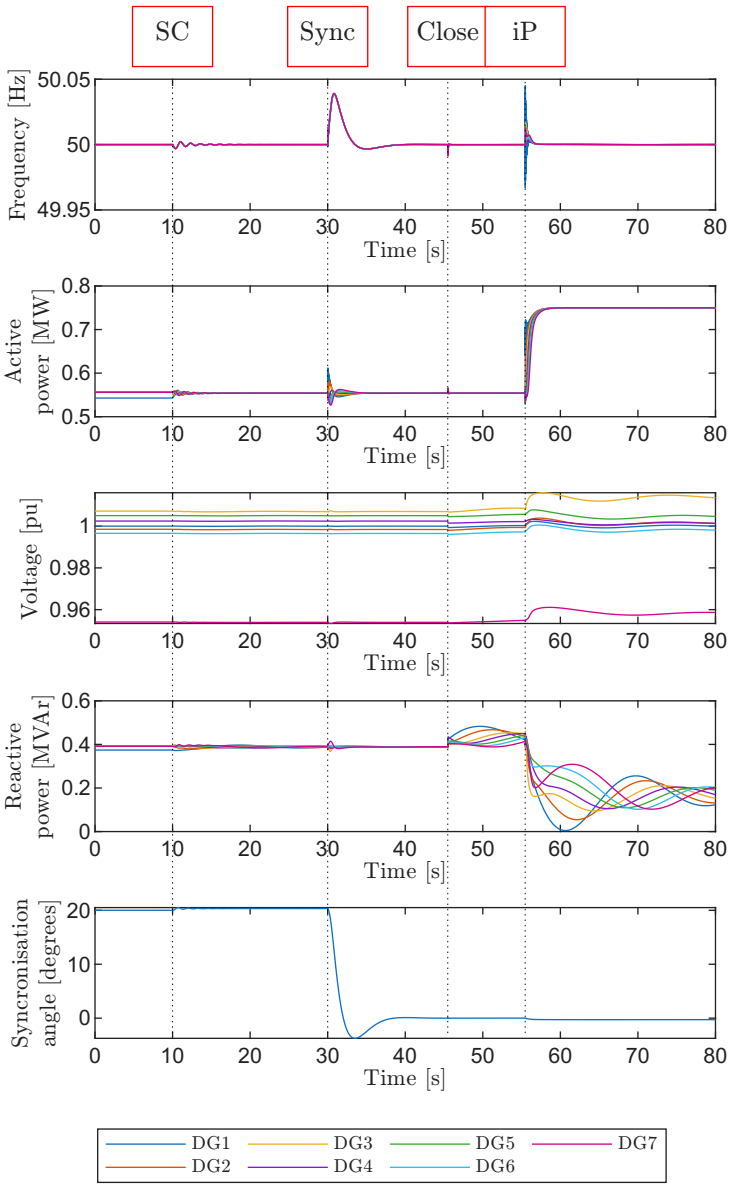

Figure 4.16: Simulation results of the synchronisation of the IEEE 69 bus test system to an infinite grid with the control proposed in this Chapter.

This chapter presents a fully decentralised hierarchical control system for microgrids. It features a consensus-based economic dispatch for the tertiary control layer that remains robust against communication delays and a secondary control layer that manages deviations from set points while considering the active-power limits of generators. The performance and robustness of this approach are compared with conventional centralised and previously published decentralised methods. Stability is validated through nonlinear real-time simulations, Lyapunov-based analysis, and modal analysis.

5 Multi-agent optimal energy management in microgrids

5.1 Introduction

The tertiary control in conventional power systems and microgrids assumes steady-state operation of the power system, since it is only responsible for generating set points for lower layers by planning the use of the different active and reactive power resources. This planning problem can involve different timescales, such as long-term transmission expansion planning, medium-term generation resource scheduling (e.g., unit commitment (Rajabdorri, Kazemtabrizi, Troffaes, Sigrist, & Lobato, 2023)), and short-term operations planning like economic dispatch (Poolla, Hota, Bolognani, Callaway, & Cherukuri, 2021) or optimal power flow problems (Alvarez-Bustos et al., 2021), the latter of which is used for near-real-time operational optimisation (Capitanescu, 2016). To date, this control layer has been mostly addressed in a centralised manner, with some rare exceptions. However, following the central discourse of this thesis, a decentralised tertiary control (an economic dispatch problem, to be more precise), with a decentralised incremental secondary layer, like the one in Chapter 2, is going to be investigated in this chapter.

The economic dispatch problem seeks the optimal allocation of generation among committed units, for example, to minimise the total generation cost while serving the demand (Happ, 1977). Unlike in optimal power flow problems, in the economic dispatch problem, the grid can be reduced or even neglected (e.g., no losses are considered) (W. Chen & Li, 2021). This problem has been analysed for decades, and many solutions have been proposed. Again, most often, the eco-

nomic dispatch is solved using centralised algorithms, but this thesis will discuss distributed and decentralised algorithms.

Centralised algorithms focus on solving a linear or quadratic optimisation problem subject to constraints. Advanced centralised approaches for the economic dispatch problem consider uncertainties by means of applying a robust optimisation[1] formulation (Poolla et al., 2021), and a security-constrained formulation (Roald et al., 2023).

Several studies have implemented distributed and decentralised control algorithms for the economic dispatch problem. For example, decentralised techniques such as adaptive droop control (Dorfler et al., 2016) and distributed algorithms such as consensus-based control (W. Chen & Li, 2021) or game theory (Han, Morstyn, & McCulloch, 2019) have been applied. Distributed algorithms for solving the economic dispatch problem usually require having one coordinating agent that guarantees the generation-demand balance with a global vision (Cruz Victorio et al., 2022). Although the economic dispatch problem is usually implemented without grid consideration, some distributed algorithms consider transmission losses (Binetti, Davoudi, Lewis, Naso, & Turchiano, 2014).

A completely decentralised consensus-based formulation for the economic dispatch problem is proposed in Z. Zhang and Chow (2011). This algorithm is generalised for a directed graph in S. Yang, Tan, and Xu (2013), guaranteeing the demand-generation balance by each agent communicating its demand-generation imbalance to its neighbours, and introducing a learning gain.

Recently, new developments on decentralised economic dispatch have addressed stochasticity using approximate dynamic programming (Xue et al., 2024), the consideration of ramp constraints (Y. He, Wang, & Wu, 2020), and the introduction of line losses (Q. Li, Gao, Zhang, Wu, & Wang, 2019). Ramp constraints are not considered in this chapter, as only one time period is considered in the economic dispatch. The consideration of grid losses, voltage control and reactive-power control is also out of the scope of this chapter, which focuses on the active-power economic dispatch problem.

An analysis of how communication delays impact the performance of the algorithm proposed in S. Yang et al. (2013) is presented in C. Zhao, Duan, and Shi (2020) where the authors find limits for the algorithm convergence based on the maximum expected delay.

The algorithms for the fully decentralised consensus-based economic dispatch in the literature have some limitations: They present limited convergence when communication delays exist and require specific graph properties (the adjacency matrix must be double stochastic, meaning that its columns and rows must sum to one) (S. Yang et al., 2013).

This chapter proposes a fully decentralised consensus-based hierarchical control for a microgrid that tackles the above limitations in the tertiary layer when solving the economic dispatch problem. The algorithm is compared to a previously

[1] robust optimisation seeks an optimal solution for a set of possible scenarios or uncertainties

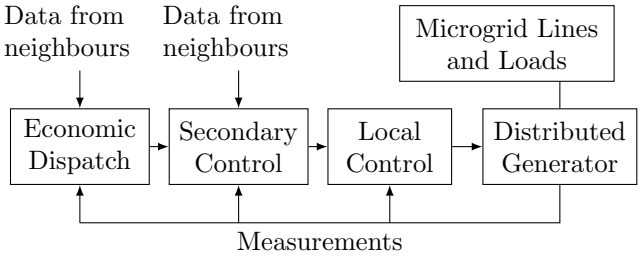

Figure 5.1: Overview of the proposed decentralised hierarchical control for a microgrid, implemented for each generator of the microgrid

well-developed consensus approach (S. Yang et al., 2013) and the conventional centralised solution. The proposed technique decouples the communication delays from the consensus dynamics so that they do not affect the convergence of the algorithm. In addition, an incremental secondary control layer (see Chapter 2) is designed to handle the demand variations considering the costs of generation units (i.e., the active-power sharing among units after a disturbance is proportional to their costs).

The proposed decentralised hierarchical control is validated by the real-time simulation of the full non-linear dynamic model of a microgrid case study.

Figure 5.1 shows a general overview of the proposed hierarchical control applied to one generator of a microgrid. The structure of the tertiary and secondary control layers is the same for each agent (generator) of the microgrid, and there is no need for central coordination. The primary control is implemented locally, and the secondary and tertiary control layers only require communication between some generators, called neighbours. The proposed control keeps a hierarchical control with clear timescale separation to improve compatibility in grid-connected operation (as shown in Chapter 4, the microgrid could synchronise to a larger grid and work as a virtual power plant (VPP) exchanging power with it).

5.2 Economic dispatch formulation

5.2.1 Centralised economic dispatch problem

The economic dispatch problem for a set U of generation units is commonly formulated as in G. Chen, Lewis, Feng, and Song (2015):

$$\begin{cases} \min & \sum_{i\in U} C_i \qquad \text{with } C_i = c_{A_i} {P_i}^2 + c_{B_i} P_i + c_{C_i} \\ s.t. & \sum_{i\in U} P_i = P_L \\ & P_{i,\min} \leq P_i \leq P_{i,\max} \ \ \forall\, i \in U \end{cases} \tag{5.1}$$

where P_i is the active power supplied by the $i-th$ generation unit, C_i is its costs, c_{A_i}, c_{B_i} and c_{C_i} are its cost coefficients, $P_{i,min}$ and $P_{i,max}$ are its minimum and maximum generating limits, respectively and P_L is the total load (or demand).

If generator power limits are not reached (i.e., $P_{i,\min} < P_i < P_{i,\max}, \forall i$), the unconstrained problem can be formulated using the Lagrangian function:

$$L\left(P_{i\in U}\right) = \sum_{i\in U} C_i\left(P_i\right) + \lambda\left(P_L - \sum_{i\in U} P_i\right) \tag{5.2}$$

where λ is the Lagrange multiplier, which can be calculated using the optimality conditions (Karush-Kuhn-Tucker (KKT) conditions) (Wood, Wollenberg, & Sheblé, 2013):

$$\frac{\partial L}{\partial \lambda} = 0 \tag{5.3}$$

$$\lambda = \frac{\partial C_i}{\partial P_i} = 2c_{A_i}P_i + c_{B_i},\ \forall i \tag{5.4}$$

The Lagrange multiplier is the dual variable or shadow price, representing the change in the value of the objective function when there is a unit change in demand. In marginal pricing approaches, the most used nowadays in electricity systems, there is a single price for the system.

If any of the power generation constraints of a generation unit $i \in U$ is reached:

$$\begin{cases} 2c_{A_i}P_i + c_{B_i} < \lambda, & \text{for } P_i = P_{i\,\max} \\ 2c_{A_i}P_i + c_{B_i} > \lambda, & \text{for } P_i = P_{i,\min} \end{cases} \tag{5.5}$$

5.2.2 The economic dispatch as a consensus problem

As shown in the previous section, the optimality conditions are met when $\lambda_i = 2c_{A_i}P_i + c_{B_i}$ of all non-limited units are equal to λ. Therefore, one could formulate the economic dispatch as a fully decentralised problem seeking consensus on the marginal costs that, initially, will be assumed to have different values in each unit ($\lambda_{v,i} \neq \lambda_{v,j}$). If the marginal costs achieve a consensus, the solution is optimal. The consensus on marginal costs is formulated by changing the active power of every unit as:

$$\frac{dP_i^*(t)}{dt} = \gamma_i \overbrace{\sum_{j\in N} a_{ij}^{Ter}\left(\lambda_{v,j}(t) - \lambda_{v,i}(t)\right)}^{\substack{\text{consensus on} \\ \text{virtual marginal cost}}} \tag{5.6}$$

with $P_i^*(t=0) = P_i$ at the instant of running the economic dispatch problem, γ_i is a gain that can be tuned to adapt the speed of convergence (its design is shown

later), and:

$$\lambda_{v,i}(t) = 2c_{A_i}P_i + c_{B_i} \tag{5.7}$$

Proof of convergence of the economic dispatch problem using a Lyapunov function

The objective of this section is to demonstrate that the consensus formulation on equations (5.6)-(5.7) converges to the optimal solution and minimises the global cost:

$$J\left(P^*\right) = \sum_{i \in N} \left(c_{A_i} \left(P_i^*\right)^2 + c_{B_i} P_i^* + c_{C_i} \right) \tag{5.8}$$

The marginal cost of each agent is:

$$\lambda_i(t) = 2c_{A_i}P_i^*(t) + c_{B_i} = \frac{\partial J}{\partial P_i^*} \tag{5.9}$$

Let us consider the following scalar function:

$$W(t) = \frac{1}{2} \sum_{i \in N} \sum_{j \in N} a_{ij}^{\text{Ter}} \left(\lambda_i(t) - \lambda_j(t)\right)^2 \tag{5.10}$$

1. $W(t) > 0$ always, unless $\lambda_i(t) = \lambda_j(t) = \lambda^*$ for all connected generators (graph nodes)
2. λ^* will be the optimal solution for the microgrid at one "equilibrium point".
3. Furthermore,

$$\frac{dW}{dt} = \sum_{i \in N} \sum_{j \in N} a_{ij}^{\text{Ter}} \left(\lambda_i - \lambda_j\right) \left(\dot{\lambda}_i - \dot{\lambda}_j\right) \tag{5.11}$$

where

$$\dot{\lambda}_i = 2c_{A_i} \frac{dP_i^*(t)}{dt} \tag{5.12}$$

which becomes:

$$\dot{\lambda}_i = 2c_{A_i}\gamma_i \sum_{k \in N} a_{ik}^{\text{Ter}} \left(\lambda_k - \lambda_i\right) \tag{5.13}$$

Calling,

$$\delta_i = \sum_{k \in N} a_{ik}^{\text{Ter}} \left(\lambda_i - \lambda_k\right) \tag{5.14}$$

yields,

$$\dot{\lambda}_i = -2c_{A_i}\gamma_i\delta_i \tag{5.15}$$

and taking this result to (5.11):

$$\frac{dW}{dt} = \sum_{i \in N} \sum_{j \in N} a_{ij}^{\text{Ter}} \left(\lambda_i - \lambda_j\right) \left(2c_{A_j}\gamma_j\delta_j - 2c_{A_i}\gamma_i\delta_i\right) \tag{5.16}$$

In other words:

$$\frac{dW}{dt} = -2\sum_{i\in N} c_{A_i}\gamma_i\delta_i \sum_{j\in N} a_{ij}^{\text{Ter}}\left(\lambda_i - \lambda_j\right) + 2\sum_{j} c_{A_j}\gamma_j\delta_j \sum_{i\in N} a_{ij}^{\text{Ter}}\left(\lambda_i - \lambda_j\right) \tag{5.17}$$

and

$$\begin{aligned}\frac{dW}{dt} &= -2\sum_{i\in N} c_{A_i}\gamma_i\delta_i^2 - 2\sum_{j\in N} c_{A_j}\gamma_j\delta_j^2 \\ &= -4\sum_{i\in N} c_{A_i}\gamma_i\delta_i^2\end{aligned} \tag{5.18}$$

4. Since $\gamma_i > 0$, $\delta_i^2 \geq 0$ and $c_{A_i} > 0\ \forall i$, $dW/dt \leq 0$, $W(t)$ has proved to be a Lyapunov function that guarantees that $\lambda_i(t) = \lambda_j(t) = \lambda^*,\ \forall i\ \&\ j$, is a stable equilibrium point and all generator units will reach the consensus solution, eventually.

Requirement of supplying the demand

The demand must be fully supplied by the generation units. This leads to the following constraint in the optimisation problem:

$$\sum_{i\in U} P_i = P_L \tag{5.19}$$

where P_i is the active power supplied by the $i-th$ generator and P_L is the total demand (or load).

In the centralised problem, the total demand P_L is estimated as the sum of the active power supplied by the generators at the operating point:

$$P_L = \sum_{i\in N} P_i^*(t=0) \tag{5.20}$$

In the consensus approach, this is achieved if the total generation power remains constant:

$$\sum_{i\in N} \frac{dP_i^*(t)}{dt} = 0 \tag{5.21}$$

Introducing generation limits for agents

The convergence of a consensus algorithm is usually modified when state variables reach saturations (Chu, Yue, Gao, & Lai, 2021). However, in this case, the

consensus convergence must not be affected by the generation limits. This section demonstrates that the consensus convergence is still reached with generation limits if the demand is between the minimum and maximum active power limits of the microgrid.

When applying the general consensus algorithm, units limit their active power set point in the range $[P_{i,min}, P_{i,max}]$. During this saturation, the unit decides to change its virtual marginal cost as:

$$\lambda_{v,i}(t) = \begin{cases} \dfrac{\sum_{j\in N} a_{ij}^{Ter}\lambda_{v,j}(t)}{\sum_{j\in N} a_{ij}^{Ter}} & \text{for } P_i^*(t) = P_{i,\min} \\ \dfrac{\sum_{j\in N} a_{ij}^{Ter}\lambda_{v,j}(t)}{\sum_{j\in N} a_{ij}^{Ter}} & \text{for } P_i^*(t) = P_{i,\max} \\ 2c_{A_i}P_i + c_{B_i} & \text{for } P_{i,\min} < P_i^*(t) < P_{i,\max} \end{cases} \tag{5.22}$$

From a practical point of view, this is a feedforward of the values received by the neighbours during saturation. This guarantees the consensus between all non-saturated agents that remain communicating their own values. This ensures the generation-demand balance described in the last section.

Convergence under time delays

Communication time delays between agents can affect the convergence of the consensus algorithm (G. Chen & Zhao, 2018). Now, the consensus equation would take the form,

$$\frac{dP_i^*(t)}{dt} = \gamma_i \overbrace{\sum_{j\in N} a_{ij}^{Ter}\left(\lambda_{v,j}(t-\tau_{ji}) - \lambda_{v,i}(t)\right)}^{\substack{\text{consensus on} \\ \text{virtual marginal cost}}} \tag{5.23}$$

where τ_{ji} is the time delay in the communication from unit j to unit i.

Discrete-time implementation

A new discrete-time implementation of the problem is introduced here to avoid the effect of communication delays. To decouple the economic dispatch stability and convergence from the communication delay between agents, at step k, each agent will calculate its response for the next step ($P_i^*(k+1)$) only after all the messages from its neighbours have been received. This discrete-time implementation will be

called "triggered" (do not mistake this triggered version for the one used in the secondary layer in Chapter 2).

$$P_i^*(k+1) = P_i^*(k) + \overbrace{\gamma_i \sum_{j \in N} a_{ij}^{Ter} \left(\lambda_{v,j}(k) - \lambda_{v,i}(k)\right)}^{\Gamma_i, \text{ consensus on cost}} \tag{5.24}$$

Tuning the convergence of the algorithm

The convergence of the proposed consensus-based economic dispatch is governed by γ_i in (5.24). As γ_i increases, the system converges faster, but a high γ_i could make the system unstable. Moreover, the system convergence is strongly affected by the saturation limits. As the proposed algorithm is a discrete system, such as the one outlined in (5.24), the constant γ_i is proposed to be designed such that the states cannot pass from the minimum limit to the maximum limit or vice versa in only one iteration.

Having:

$$P_i^*(k+1) = P_i^*(k) + \Gamma_i \tag{5.25}$$

The bounds of Γ_i that guarantee consensus in the discrete system are:

$$\begin{cases} \max(\Gamma_i) < P_{i,max} - P_{i,min} \\ \min(\Gamma_i) > P_{i,min} - P_{i,max} \end{cases} \tag{5.26}$$

which, using (5.24) and (5.26) and making $\gamma = \gamma_i = \gamma_j \ \forall \ i, j$, for simplicity, gives:

$$\gamma < \frac{\min_i \left(\dfrac{P_{i,max} - P_{i,min}}{c_{B_i} + c_{A_i} P_{i,max}^2} \right)}{\max_i \left(\sum_j a_{ij} \right)} \tag{5.27}$$

5.3 Case study and results

5.3.1 Convergence of the proposed decentralised economic dispatch algorithm under communication delays

This section compares the performance of the proposed method with the method proposed by S. Yang et al. (2013), under different communication delays between agents. The system under study consists of four agents. Each agent is a distributed generator (DG) in the power system of Figure 5.2. This system was already used in Chapter 2 when discussing consensus-based secondary control.

The graph used for the communication between agents, shown in Figure 5.3, has an adjacency matrix as follows:

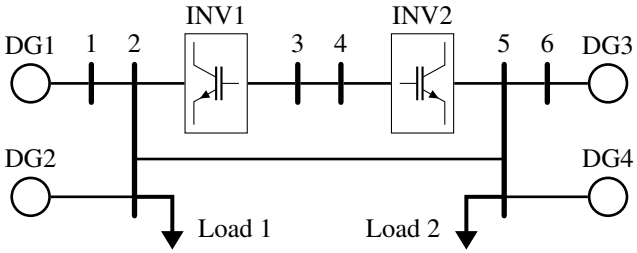

Figure 5.2: 6 bus system with a point-to-point VSC-based DC link between buses 2 and 5.

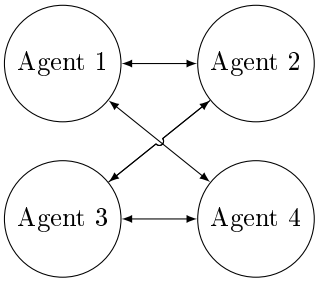

Figure 5.3: Communication graph used for the decentralised economic dispatch algorithm

$$A = \begin{bmatrix} 0 & 1 & 0 & 1 \\ 1 & 0 & 1 & 0 \\ 0 & 1 & 0 & 1 \\ 1 & 0 & 1 & 0 \end{bmatrix} \tag{5.28}$$

Table 5.1 includes each agent's cost coefficients (linear and quadratic terms) and its minimum and maximum active-power limits. Recall that the cost of the active power provided by DG_i is calculated as:

$$c_i = c_{A_i} P_i + c_{B_i} P_i^2 \tag{5.29}$$

Table 5.2 shows the communication time delays included in the simulations for each test carried out with the case study. In each case (I-III), the same delay was used in all communication links.

The results on the convergence of the different algorithms compared are included in Figures 5.4 to 5.6. Table 5.3 includes some numerical details of the results.

Figures 5.4 to 5.6 compare the simulation results of the proposed algorithm with those of the algorithm in S. Yang et al., 2013. Non-triggered (original) and triggered versions, in both cases, are considered (see Figure 5.4 caption for a full

Table 5.1: Cost coefficients and power range for every agent in Figure 5.2.

DG	c_{B_i} [\$/MW]	c_{A_i} [\$/MW^2]	P_{min} [MW]	P_{max} [MW]
1	2	0.04	0	80
2	3	0.03	0	80
3	4	0.035	0	80
4	4	0.03	0	80

Table 5.2: Communication delay implemented for each test case.

Case	Delay (ms)
I	50
II	100
III	200

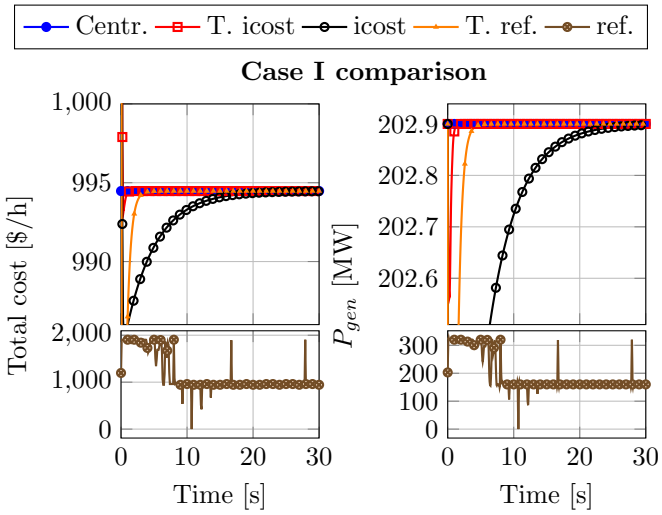

Figure 5.4: Comparison of the evolution of the global operation cost and the power balance obtained using the different approaches for Case I. "Centr." stands for the conventional centralised approach, "T. icost" stands for the triggered version of the proposed approach, "icost" stands for the non-triggered version of the proposed approach, "T. ref." stands for the triggered version of the approach presented in S. Yang, Tan, and Xu (2013) and "ref." stands for the approach presented in S. Yang, Tan, and Xu (2013) (note that this last approach is shown separately in the lower part of each graph due to the large differences in the Y-axis values). Case I.

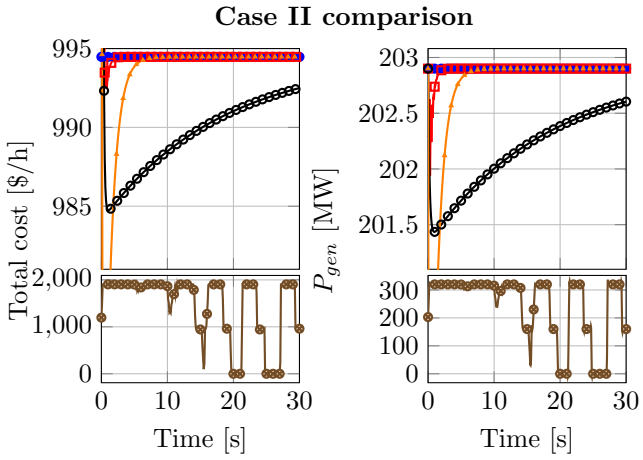

Figure 5.5: Same comparison of Figure 5.4 but for Case II.

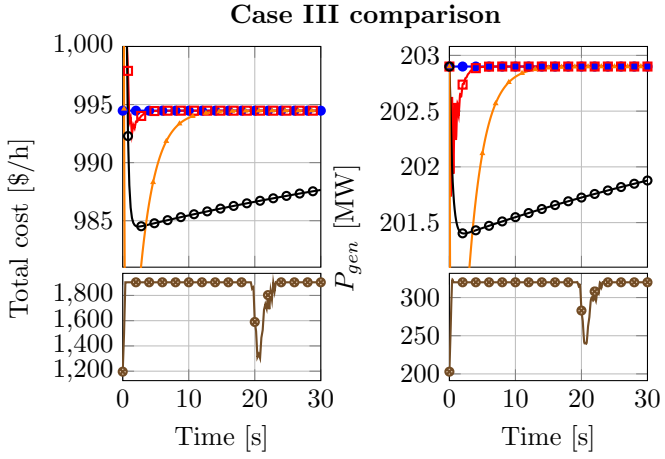

Figure 5.6: Same comparison of Figure 5.4 but for Case III.

Table 5.3: Comparison of the performance of different energy distpach algorithms under different communication delays

Case	Algorithm	cost [$/h]	P_{gen} [MW]
I	Centralised	994.4726	202.9
I	Triggered icost	994.4726	202.9
I	icost	994.3421	202.8805
I	Triggered base	994.4726	202.9
I	Base	0	0
II	Centralised	994.4726	202.9
II	Triggered icost	994.4726	202.9
II	icost	984.4558	201.3981
II	Triggered base	994.4726	202.9
II	Base	1904	320
III	Centralised	994.4726	202.9
III	Triggered icost	994.4726	202.9
III	icost	962.0203	198.0135
III	Triggered base	994.47	202.8996
III	Base	0	0

explanation). A centralised algorithm has also been included for benchmarking. Table 5.3 includes numerical details of the results. Clearly, the original realisations of both algorithms ("icost" and "ref.") are highly affected by communication delays: "icost" reaches consensus despite communications delays but the bigger the delay, the larger the deviation of the solution from the optimum is; and "ref" fails to converge for communication delays above a certain threshold, as shown in C. Zhao et al., 2020. The triggered realisations ("T. icost" and "T. ref.") are more robust. In fact, for each algorithm, the final consensus value was always reached in the same number of iterations. These iterations take longer as the communication delay grows. Nevertheless, the proposed algorithm ("T. icost") always takes fewer iterations than "T. ref." to reach consensus.

Figure 5.7 shows the evolution of the virtual cost and power set point of each agent moving towards the consensus for the communication delay in case I. The final consensus value is the marginal cost of all non-limited units at the optimal solution.

5.3.2 Case study for the implementation of the proposed fully-decentralised hierarchical control: Hybrid AC/DC microgrid

In this section, a fully decentralised hierarchical control based on the decentralised consensus-based economic dispatch proposed in this chapter and the incremental secondary control presented in Chapter 2 is validated with simulations on the test

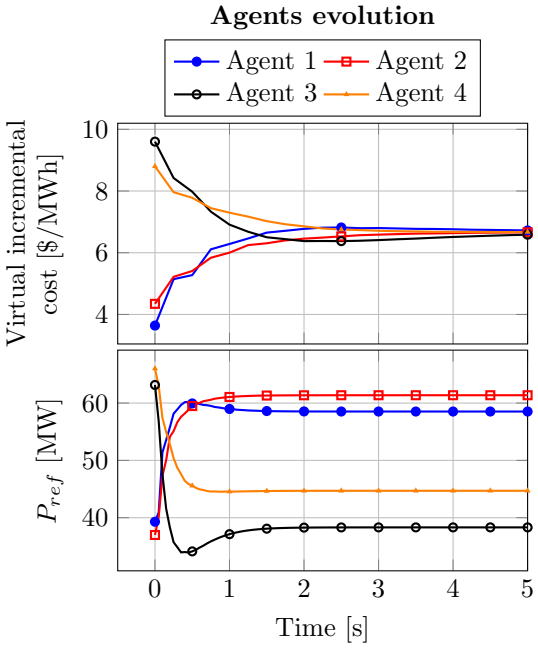

Figure 5.7: Evolution of the virtual cost and power set point of each agent during the consensus process for the communication delay on case I.

system of Figure 5.2. The control structure and parameters of the system are shown in Table 2.5, included in Chapter 2.

To evaluate the performance of the proposed hierarchical control, the active power consumption of both loads is varied. First of all, it is reduced to 5% of the original load and then increased up to 140% of the original load. For simplicity, the load is changed linearly every 20 seconds for 3,600 seconds (1 hour). The costs are varied randomly with a uniform distribution between 2 and 4 for c_{B_i} and between 0.02 and 0.04 for c_{A_i} every 100 seconds, time when also the tertiary control updates the active-power set points. The communication graph used here is the one presented in Figure 5.3, with the same adjacency matrix. Results are shown in Figure 5.8.

Clearly, the saturation of the active power set points works properly. The proposed secondary control structure also manages to recover the frequency to its nominal value after each active-load disturbance. In this scheme, the difference between the scheduled and actual active power is shared by the DGs depending on coefficients a_{ij}^P. To consider the unit costs also in the secondary control, a_{ij}^P coefficients are set as described in Chapter 2.

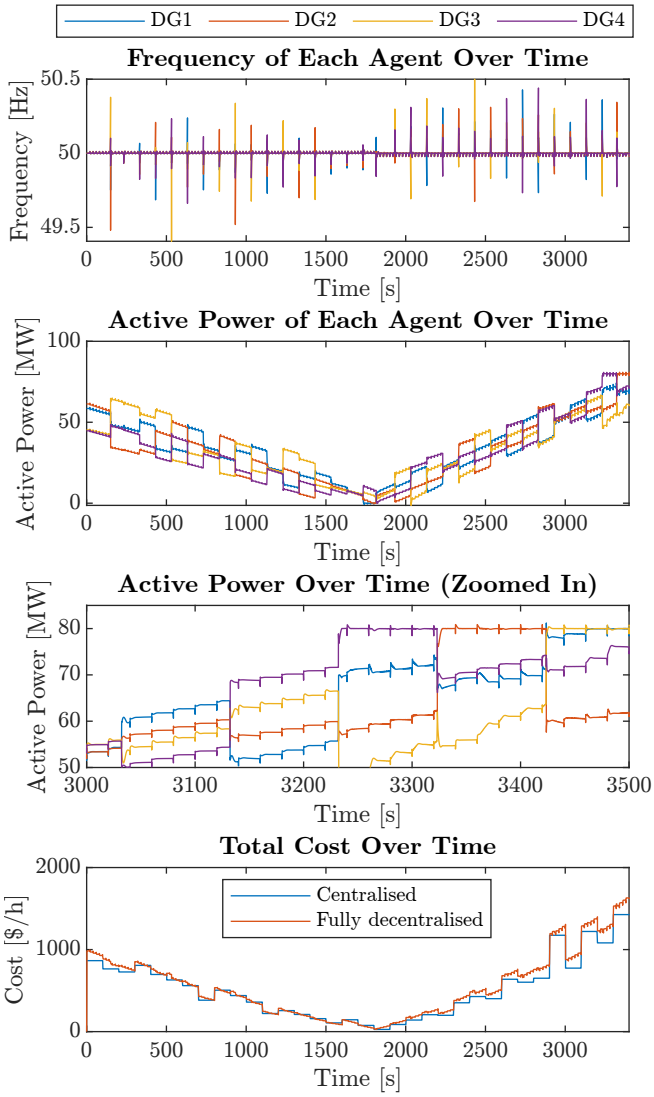

Figure 5.8: Study with demand variation

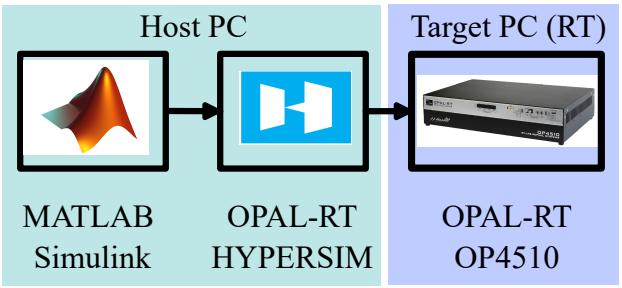

Figure 5.9: Diagram of the process for the real-time simulation of the proposed hierarchical control in the OPAL-RT OP4510 simulator.

5.3.3 Real-time validation of the proposed fully decentralised hierarchical control

For the real-time validation of the proposed fully decentralised hierarchical control, the algorithm was implemented in a real-time simulator, OPAL-RT OP4510. The process followed for the real-time simulation of the proposed algorithm is depicted in Figure 5.9. The non-linear system was modelled using MATLAB Simulink and compiled for OPAL-RT HYPERSIM software (i.e., the Simulink file is translated to C code by the HYPERSIM compiler). Then, the HYPERSIM model is executed in real time on the OP4510.

The real-time simulation results are shown in Figure 5.10.

Regarding the tertiary control, as clearly shown in the figure, the virtual marginal costs reach consensus in a few seconds at every dispatch.

Regarding the secondary control, the voltage and frequency recover their nominal values in a few seconds after each disturbance. The reactive power sharing is set equal to all converters except DG1. The active power sharing of disturbances depends on:

1. The active-power set point set by the decentralised economic dispatch problem.

2. The disturbances (deviations) from the dispatched active-power set points are shared depending on the costs, which can help to understand the deviations from the dispatched set points.

As shown in Figure 5.10, the total operation cost is close to the "Optimal Cost" which is the total cost the system would have with a centralised dispatch immediately after every load and cost change.

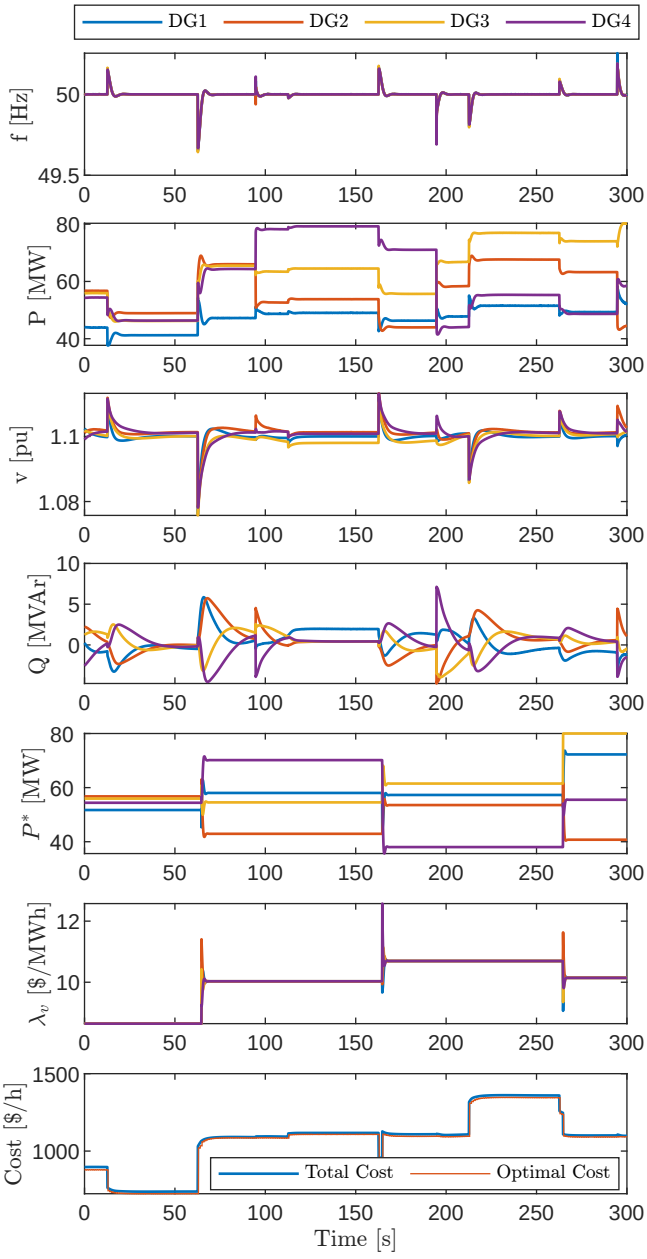

Figure 5.10: Results of the real-time validation of the proposed decentralised hierarchical control.

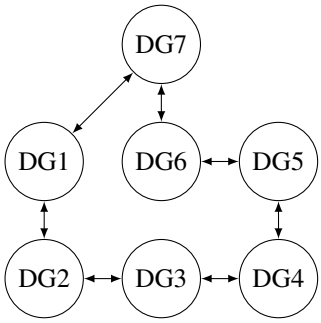

Figure 5.11: Communication graph used for the 69 bus case study.

5.4 Large case study: IEEE 69 bus test system

This section describes the application of the proposed synchronisation method to the modified version of the IEEE 69 test system described in Appendix C. The system is modelled and analysed using the Simulink tool presented in Appendix A.

The parameters of the case study are included in Appendix C. The communication graph used is depicted in Figure 5.11.

The response of the proposed secondary control to gradual load changes was studied by simulation. Like before, the original load was reduced, and was later increased with periodical triggers of the tertiary control. For simplicity, the load is changed linearly every 20 seconds for 3,000 seconds (50 min). The communication graph used here is the one presented in Figure 5.11. Figure 5.12 shows the active power injected by DGs 1-7 during the test described.

In this case study, the saturation of the active power set points also works properly, and the nominal value of the frequency is also recovered after each disturbance.

As this case study involves more power losses than the small case study, and these losses depend on the dispatch of generators, the cost obtained with the proposed control is slightly above the optimal cost obtained with a centralised algorithm. Note that, to evaluate the performance of the secondary control, the centralised algorithm is implemented knowing the actual point, including the losses. However, the cost is still close to the optimal one.

5.5 Conclusion and future work

This chapter proposed a fully decentralised multi-agent hierarchical control of a hybrid AC-DC microgrid. The secondary and tertiary control layers of the proposed control are formulated as a consensus problem. The tertiary control layer calculates the optimal active-power sharing between generators in the microgrid cooperatively in a decentralised manner. The results obtained by the proposed

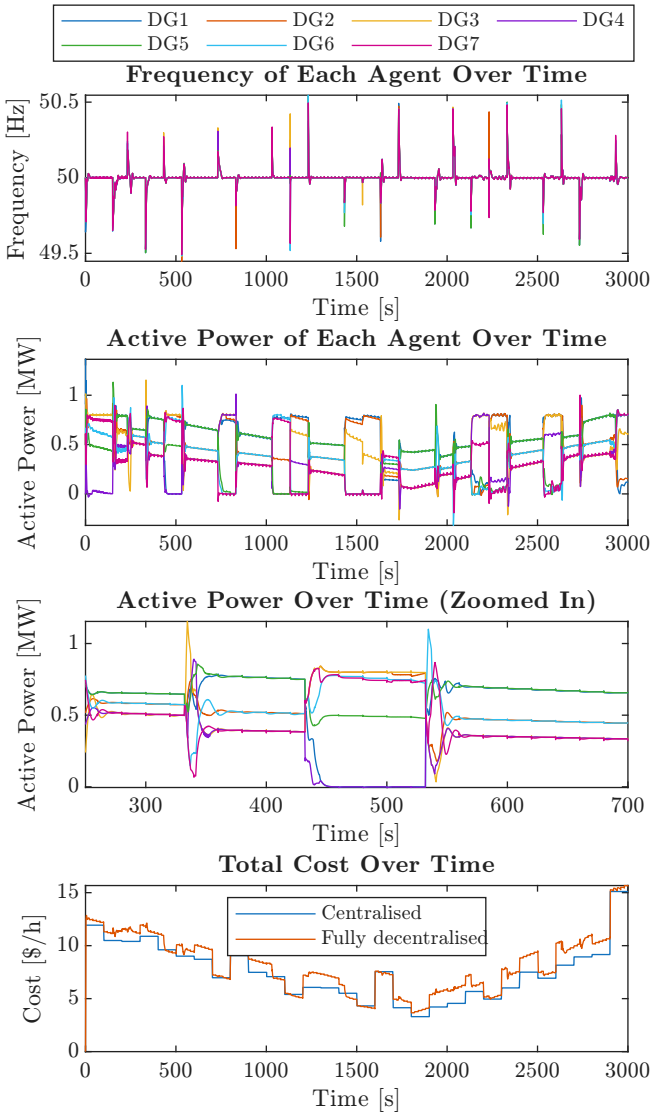

Figure 5.12: Study with demand variation in the large system.

algorithm have been compared against an existing decentralised approach and against the conventional centralised solution. The results show that the communication delays between generators, affecting the convergence of existing methods, do not affect the convergence of the proposed method. The secondary control layer proposed manages the active-power sharing of the deviations from the dispatched operation point. The performance of the proposed algorithm when active-power limits in the generators are included has been investigated in this chapter.

Future work will focus on considering the grid and voltage control on the economic dispatch problem and extending the algorithm to solve a multi-period decentralised economic dispatch problem. In addition, on the secondary control layer, future research will include the design of a trigger mechanism for the proposed incremental secondary control.

This chapter proposes a distributed control to conduct the black start of a microgrid within the distribution level of a power system. The control of the grid configuration is carried out centrally by the distribution system operator, but the decision of when each generator is incorporated into the grid is taken in a decentralised manner. An event-triggered control similar to the one in Chapter 2 is used in the decentralised secondary control layer of the proposed method.

6 Multi-agent-based black start of a microgrid

6.1 Introduction

Failures in power systems, such as voltage sags, faults or disconnection of generating units, can lead to power outages or, in the worst case, the total blackout. Therefore, system operators must establish a power system restoration plan to recover the service as fast as possible after such an event. A power system restoration plan is a list of sequential actions that must be done to recover the service in a specific region of a power system.

Conventional power system restoration plans are top-down approaches: First of all, a large power plant with black-start capability is started, and then other generators and loads are gradually added (Lobato Miguélez, Egido Cortés, Rouco Rodríguez, & López Camino, 2008). In these cases, distribution systems have to wait until the transmission system is fully restored.

However, with the proliferation of renewable energy resources (RERs), future power systems will have a high penetration of distributed generators (DGs). Many of these units will be placed at the distribution level, suggesting that distribution systems may also be actively involved in restoration plans to speed up the process and spare consumers from unnecessarily long outages. A bottom-up approach can help conventional top-down restoration, leading to a faster black-start (Moreira, Resende, & Lopes, 2007)

Only some generators can energise the power grid independently in conventional power systems. They are called "black-start units" (W. Sun, Liu, & Liu, 2011). Meanwhile, non-black-start generators must always work connected to an already-energised grid. Black-start generators in conventional power systems have

a high investment cost and must have periodic checks. The allocation of such units is critical for power system restoration (Patsakis, Rajan, Aravena, Rios, & Oren, 2018).

6.1.1 Technical considerations during the black start

To recover the service quickly but securely, so that no new blackout occurs, special care must be taken with the following aspects:

- When a load is switched on, there can be a significant and fast increase in current demand, such as in the start-up of electric motors. This phenomenon is referred to in the literature as "cold load pickup". The same happens when energising a transformer; a high current increase (inrush current) appears for a short period. Due to these phenomena, it is essential to carry out the service restoration process sequentially making sure that the connected generation can handle these transient current surges at all times.

- Generators with self-starting capability must be able to impose a voltage and energise the grid. If the black-start generator is interfaced with the grid through an electronic converter, it must work with a grid-forming control. In every island system, there must be at least one unit operating with grid-forming control. Since every generator must have a synchronising relay to connect to the grid, and in a black-start (BS) the grid voltage is not present, the synchronising relay must be forced to close, even if the synchronisation requirements are not met.

- When energising a network without load, transient overvoltages may appear on the lines. Generators connected at that time must control these overvoltages by reducing the reactive power injected, or even absorbing reactive power, if necessary (Adibi, Alexander, & Milanicz, 1999).

- These transient phenomena, among others, can put the restoration process at risk if they cause protection tripping (Adibi & Milanicz, 1995). In addition, in a weak network, such as a newly formed island, voltage and frequency will probably exhibit larger variations than those normally considered acceptable, which may lead to underfrequency, overfrequency, undervoltage or overvoltage protection tripping during the restoration process. It may also affect the load-shedding strategy used in the region affected.

- Specific generators may require a minimum load to operate stably (stabilisation loads).

- Each network operation performed is bound to produce a transient disturbance in the grid. In order to carry out the service restoration safely, such operations must be sequential, with a time interval between them to ensure the stabilisation of the network.

Table 6.1: Black start of distribution systems in the literature, specifying the software used for the modelling.

Ref.	Year	Software	Main study
Bassey, Chen, and Butler-Purry (2018)	2018	PSCAD, python	maximum load step and evaluation of transient times
B. Chen (2017)	2017	PSCAD, MATLAB and OpenDSS	Dynamic optimisation of MILP
Ding, Wang, Qu, Wang, and Shahidehpour (2022)	2022	GUROBI	Mixed-Integer Second-Order Cone optimisation
Du, Tu, Lu, Wang, and Lukic (2022)	2022	RT-HIL (OPAL)	microgrid BS and resynchronisation
Sekhavatmanesh and Cherkaoui (2019)	2019	MATLAB Yalmip toolbox	Convex Second-Order Cone optimisation
L. Zhang and Sun (2011)	2011		Multi-agent GA (multiple objectives)
J. Zhao, Zhang, Liu, and Wu (2021)	2021	CPLEX 12.6	mixed integer quadratic programming optimisation
Zhu, Zhou, Wang, Zhou, and Gao (2022)	2022		Pruning algorithm (making decision tree smaller)

- During the restoration process, load blocks are connected sequentially to provide the demand. Naturally, at all times, this demand must be less than the available generation. Moreover, the smoother the load insertion is, the smoother the transient phenomenon experienced by the network will be. Therefore, it is recommended to allow as much flexibility as possible in the demand to be connected.

6.1.2 Specific problems in distribution networks

The characteristics of the distribution system imply that a BS algorithm at this level requires some special considerations.

Table 6.1 includes a brief description of some algorithms to calculate the BS sequence considering distribution systems.

Distribution networks are designed to operate radially. When a blackout occurs, it may have been caused by a fault in a line or transformer. In these cases, the loads (consumers) behind the fault are left without service even after the system is restored. Therefore, alternative supply routes must be provided. For this purpose,

distribution networks include multiple circuit breakers that make reconfiguration possible. However, only some circuit breakers are controllable switches and the actual situation of non-cotrollable ones may not be accessible after the blackout. In fact, some of the latter may have opened after having detected undervoltage.

Moreover, to recover the service as fast as possible, it may be advisable to split the system into various regions and recover the service in all regions in parallel. Therefore, a distribution-level service restoration algorithm would benefit from a method for determining regions (islands) within the system that could be energised independently to be synchronised with each other later on.

Each time a dispatchable generator is connected, it is necessary to communicate set points for its active- and reactive-power injections into the grid to ensure an adequate distribution among generators during a sequential and orderly restoration process.

6.2 Distributed vs centralised service restoration in power systems

Y. Liu, Fan, and Terzija (2016) present a review on BS and network reconfiguration on transmission systems. Although the review does not focus on distribution systems, it explains essential topics related to BS, such as grid reconfiguration and the calculation of a sequence for load recovery. Fan et al. (2021) present a review of service restoration methods for distribution systems. Distribution systems often need to create islands for their BS. The BS process of distribution systems has special technical considerations, and the review also includes algorithms for the preliminary island clustering. However, the review focuses only on centralised optimisation algorithms for calculating the restoration sequence before its application.

Yuan et al., 2022 present a review of decision-making methods for service restoration. The review includes both distributed and centralised approaches and briefly describes each approach without making any assessment.

Pardo and López-Lezama, 2020 present a review of service restoration methods for transmission systems. The review includes both centralised and multi-agent approaches. Interestingly, the review describes the challenge of considering the non-dispatchable nature of RERs.

Table 6.2 summarises the existing reviews for service restoration methods. The table is sorted by year of publication. Columns D and C indicate whether the reviewed paper includes distributed or centralised approaches. DS and TS indicate whether the reviewed papers deal with distribution or transmission systems.

A BS requires, at least, one unit with BS capability. For example, grid-forming voltage-source converters (GFr-VSCs) and synchronous generators can easily have this capability, while grid-following voltage-source converters (GFl-VSCs) cannot have it. RERs do not generally include BS capability. However, a comprehensive

Table 6.2: Comparison of existing reviews for restoration methods. D: distributed, C: centralised, DS: distribution system, TS: transmission system.

Ref.	Year	Reviewed	D	C	DS	TS
Y. Liu, Fan, and Terzija (2016)	2016	2006-2016	✓	✓	×	✓
Fan et al. (2021)	2021	2007-2020	✓	✓	✓	×
Yuan et al. (2022)	2022	1991-2021	✓	✓	✓	✓
Pardo and López-Lezama (2020)	2020	2000-2019	×	✓	×	✓

review of how offshore wind farms can be given BS capability is presented in Pagnani et al. (2020).

The problem of BS can be described as a sequential unit commitment problem (J. Zhao, Zhang, Liu, & Wu, 2021), with the aim of finding the most cost-effective way to restore the service as soon as possible. The unit commitment problem is a well-known optimisation problem in power systems. The objective is to find the optimal commitment of the generation units to meet the demand at the lowest cost. The problem is formulated as a mixed-integer linear programming problem, in general, without considering the grid. The objective function is the total cost of the generation units, and the constraints include the power balance, the ramping limits, and the minimum and maximum generation limits of the units. The key difference between the BS problem and the unit commitment problem is that, in the former, once a generation unit is connected, it cannot be disconnected until the end of the BS process, to increase the system stability and resiliency against outages.

Yao, Chau, Zhang, Iu, and Fernando (2020) formulate the BS as a mixed integer linear programming (MILP) optimisation problem. The algorithm also evaluates the optimal allocation of the BS-capable units.

If the size of the studied region is large, the optimisation problem can be solved using a decomposition approach. For example, Zhu, Zhou, Wang, Zhou, and Gao (2022) propose a pruning algorithm to reduce the size of the decision tree, and Sekhavatmanesh and Cherkaoui (2019) propose a clustering technique to split the whole system into small subsystems that will be energised separately, and will be synchronised later on.

If the blackout stays for a long time, the generation and load profiles in the network can change significantly and are uncertain. In such a case, a forecasting exercise is required to calculate the demand and generation to be included in the optimisation problem (Sharma, Srinivasan, & Trivedi, 2018).

Genetic algorithms (GAs) can be used to solve the BS problem. L. Zhang and Sun (2011) propose a multi-agent approach based on a GA to solve the BS problem. The optimisation problem is formulated to maximise the capacity restored as soon as possible.

The black start of a microgrid has been analysed in several studies. Lopes, Madureira, Gil, and Resende (2013) describes the guidelines to follow in the BS of a microgrid. The process is similar to the BS of an islanded region of a distribution

system. Bassey and Butler-Purry (2020) propose a MILP algorithm to calculate the BS sequence in a microgrid and validate the obtained sequence with a dynamic simulation in PSCAD. Braun et al. (2018) discuss the possible capabilities of distributed generation within grid restoration in future power systems. Conventional restoration plans are calculated through a central controller that knows all the electrical parameters of the grid and generators, and calculates the optimal sequence for service restoration. However, there are several distributed and decentralised approaches in the literature already.

Sekhavatmanesh and Cherkaoui (2019) propose a multi-agent distributed algorithm for the restoration of a distribution network, based on network reduction, in which each feeder agent optimises the sequence of closing controllable switches in its feeder. Sharma et al. (2018) use a similar approach, but considering uncertainty in the forecast of demand and generation, giving a more robust solution.

L. Zhang and Sun (2011) proposes another distributed approach formulated as a genetic algorithm for each agent, with central coordination to ensure the radiality constraint (distributions networks tend to be operated in a radial way).

Future microgrids will include a higher proportion of RERs. The non-dispatchable nature of RERs complicates energy management and generation-load balance. Moreover, some loads, such as electric vehicles, can lead to a higher load uncertainty. Therefore, distributed, decentralised and centralised restoration procedures must consider uncertainty in load and generation (Sharma et al., 2018).

6.2.1 Dynamic analysis of the restoration process

The previously described approaches focus on calculating the sequence offline. However, non-linear issues in the service restoration process can affect the system stability. Therefore, non-linear dynamic simulation is crucial to validate the proposed startup sequence.

McKeever, De Din, Sadu, and Monti (2017) present simulation results of the BS of a microgrid composed of four GFr-VSCs. The connection sequence is known, and the study focuses on the performance of a multi-agent secondary control during the BS process.

Noris, Rueda, Rakhshani, and Korai (2019) present a benchmark model in DIgSILENT PowerFactory to study the BS of a power system with GFr-VSCs. The model includes a centralised secondary control and several battery energy storage systems (BESSs).

Rokrok et al. (2017) include a decentralised multi-agent algorithm to calculate the restoration sequence based on generation capacity and load priority, and studies the performance of the resulting sequence through dynamic simulation. However, it does not consider voltage or grid constraints in the sequence, since each load includes a controllable switch for its connection.

In this chapter, the BS sequence is validated online with detailed non-linear simulations. Moreover, the DGs adapt their operation with dynamic measures. Aspects such as the stability and whether the system has reached its steady state

or not after each grid operation are evaluated by each agent based only on its own electric measurements, without information from a central controller. After each grid operation is completed by the distribution system operator (DSO), the system is considered to be in steady state by each agent if:

$$\psi = A_v(v(t) - v(t-\tau))^2 + A_\omega(\omega(t) - \omega(t-\tau))^2 < 1 \tag{6.1}$$

where ω is the frequency set by each agent at its point of common coupling (PCC) and v is the amplitude of thevoltage set by each agent at its PCC in two different time instants (t and $t-\tau$). A_ω, A_v and τ are parameters to specify the thresholds for the duration of the steady state, the variation in the frequency, and the variation in the voltage, respectively. As described in Chapter 2, the bigger A_ω and A_v are, the smaller the frequency and voltage tolerances are.

6.2.2 Examples of actual service restoration plans

EirGrid (2020) include the guidelines followed by the Irish transmission system operator (TSO) (EirGrid) to design the restoration plan for the Irish power system. These guidelines include information on how resynchronisation between two areas could be carried out.

Morin (1987) describe an approach to service restoration on the Hydro-Québec power system, analysing the possible dynamic problems that may arise.

Lobato Miguélez et al. (2008) describe the general guidelines used by the Spanish TSO for the sequential service restoration of the Spanish power system. On 28 April 2025, the power systems of Spain and Portugal experienced a blackout. ENTSO-E (n.d.) describe briefly the steps that the Spanish and Portuguese TSOs followed, with support from the interconnections of Spain with Morocco and France, to recover the service.

Restoration plans rely on TSO experience and knowledge of the grid to decide the optimal restoration sequence, designed, in general, in a centralised manner.

6.3 Exploring a distributed restoration procedure

Let us consider the situation in which, after a blackout, a region of the distribution system is disconnected from the main grid and is ready to re-energise the existing load in the islanded microgrid.

The sequence of grid operations to be carried out is decided by the DSO in a centralised manner. This is because the DSO is the agent with complete knowledge of the structure and condition of the distribution system after the blackout. Global information on which devices are ready to participate is essential for making the decision on the optimal sequence to follow in a BS. The way in which the DSO calculates the sequence of closing the controllable switches is out of the scope of this thesis. This sequence could be decided by solving an optimisation problem in

which the objective is to minimise the restoration time of critical loads and/or to recover most of the demand as quickly as possible.

The proposed distributed black-start methodology for a microgrid is shown in the flowchart in Figure 6.1. The procedure is structured as a multi-agent system which leverages both centralised and decentralised parts. This approach is particularly suitable for distribution-level restoration, where a central entity possesses system-wide knowledge, while local agents manage their own operational details.

The system is composed of two main types of agents:

1. A single **central agent**, the DSO.
2. Multiple **decentralised agents**, the DGs.

This structure is logical because the DSO is the entity responsible for the entire distribution network's topology and operational state, including monitoring and controlling network assets like controllable switches. In the context of a private or islanded microgrid, this role would be filled by a microgrid central controller. The DGs, in contrast, are responsible for their own start-up and synchronisation.

The proposed distributed algorithm for the optimal restoration of a microgrid represents a first step in exploring fully decentralised restoration, which cuoul offer several advantages in black-start scenarios, including adaptability and robustness to agent failures. However, since in distribution systems, the DSO typically prefers a certain level of centralised control within its system, the proposed algorithm includes a centralised part controlled by the DSO. A fully decentralised restoration could still be an option for small private microgrids, but this topic was postponed for future studies.

The Black-Start Procedure

The restoration process is divided into distinct roles and actions performed by the DSO and the DGs, coordinated through a defined communication protocol.

DSO Role: Centralised Coordination and Grid Management

The left side of the flowchart details the responsibilities of the DSO, which acts as the master coordinator of the restoration.

1. **Calculate Optimal Grid Action:** Following a blackout, the DSO first assesses the overall state of the network, including which loads are critical and which DGs are available for black-start. Based on this global information, the DSO determines an **optimal black-start sequence**. This sequence is a high-level plan that dictates the order in which different sections of the network will be re-energised by closing specific controllable switches. The objective is typically to restore critical loads as quickly and safely as possible, considering the available generation capacity. While the specific algorithm for determining this sequence is beyond our scope, the key point is that the DSO creates a strategic, step-by-step restoration path.

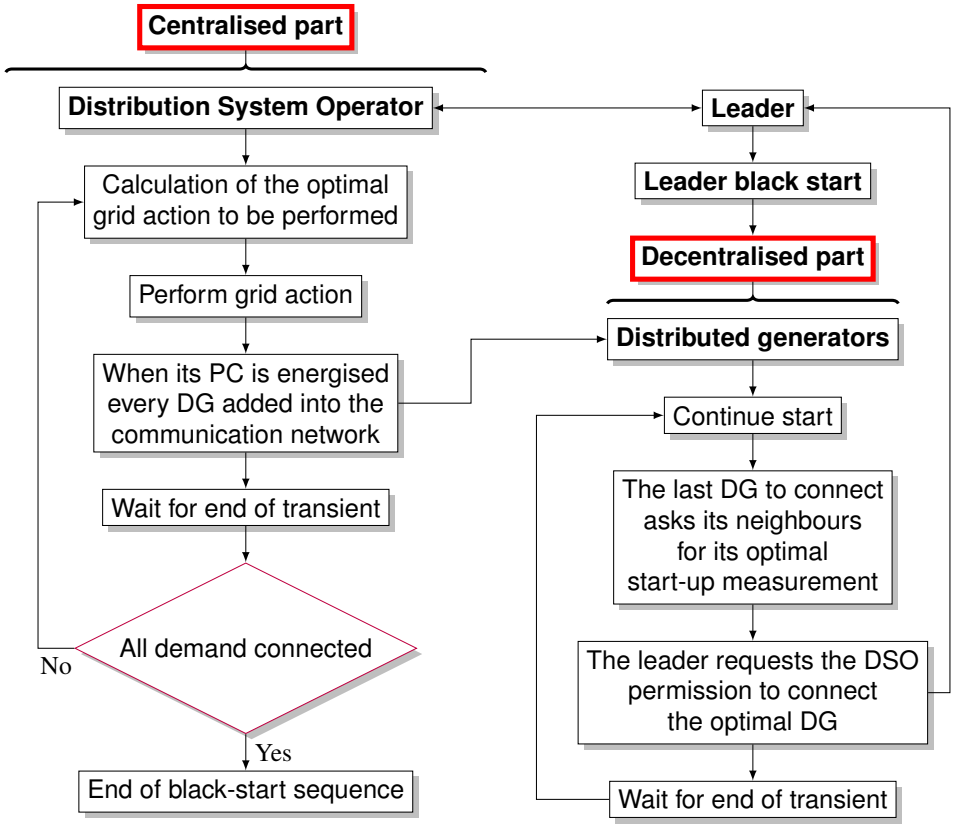

Figure 6.1: Flow chart of the proposed distributed algorithm for the optimal restoration of a microgrid. "Grid action" means closing a controllable switch.

2. **Perform Grid Action:** The DSO initiates the process by executing the first step of its sequence: closing a switch to energise the initial network segment that contains the designated "Leader" DG.

3. **Grant Permission and Expand the Grid:** Throughout the process, the DSO waits for requests from the Leader DG. Upon receiving a request to connect a new DG, the DSO consults its master plan. If the request is aligned with it, the DSO allows the connection. This safely expands the energised portion of the microgrid, allowing more DGs and loads to be connected.

4. **Monitor for Completion:** The DSO is responsible for tracking the overall progress of the restoration. The entire sequence concludes when the DSO confirms that all planned demand has been successfully reconnected.

DG Role: Decentralised and Sequential Start-Up

The right side of the flowchart details the bottom-up, decentralised procedure followed by the DGs.

1. **Leader Black Start:** Once requested by the DSO, the **Leader DG** initiates the process. It performs a "black start," meaning it begins generating power and establishing a stable voltage and frequency set point within the newly formed, isolated island. This leader is typically a DG with inherent black-start capability.

2. **Continue Start (Follower DGs):** The voltage provided by the Leader energises the local communication network and the points of connection for other DGs within the same energised segment. These "follower" DGs can then begin their own start-up procedures ("Continue start").

3. **Optimal Neighbour Selection:** As each new DG comes online and stabilises, it queries its immediate neighbours to identify the next best candidate for connection. This decision is based on the available active power capacity of the generators. This creates a self-organising, bottom-up sequence within the currently energised island.

Information Exchange and the Main Loop

The coordination between the centralised DSO and the decentralised DGs is critical and defines the main operational loop:

1. All the energised DGs identify the next optimal DG to be connected based on local and neighbour information.

2. The **Leader then formally requests permission from the DSO** to connect this new DG. This is the primary point of information exchange from the DGs to the DSO.

3. The DSO receives this request and, as described above, allows the connection.

4. After the switching action, both sides **"Wait for end of transient"** based on local electrical measures (i.e., the measurements of every DG of its frequency and voltage amplitude), to ensure the operation is stable before proceeding.

5. This loop—**Request from Leader, Action by DSO, Stabilisation**—continues, progressively expanding the energised microgrid until the DSO determines the restoration is complete. This ensures that the decentralised, bottom-up decisions of the DGs are always aligned with the restoration strategy of the DSO.

The main characteristic of this procedure is that the communication graph between DGs is calculated dynamically along the restoration process. Moreover, only the communication between the leader DG and the DSO is supposed to work prior to starting to energise the microgrid. The communications between a pair of DGs within the microgrid only work when both DGs have a voltage amplitude at their PCC above a certain threshold. This would be the case when most DG have no energy backup and rely only on the energy supplied by the grid. Only those DG with an alternative power supply will have BS capability. This procedure ensures that the resulting communication graph includes all energised DGs if the communication structure follows a ring.

As discussed previously in this chapter, sudden energisation of the grid leads to problems like transformer inrush currents and cold load pickup. To avoid these issues, the leader is in charge of energising a part of the microgrid by ramping its voltage to the nominal value after the connection. After reaching the voltage nominal value, the DSO continues with the recovery sequence of grid operations.

Since the restoration procedure must be robust and stable, the generators must connect to the grid sequentially. Moreover, the graph is chosen to limit the possibility that the communication delays could turn the system unstable.

Algorithm 1 details the proposed restoration procedure of a microgrid.

Algorithm 1 Restoration procedure

1: $startup(leader)$
2: **Wait until** $\psi = A_v(v(t) - v(t-\tau))^2 + A_\omega(\omega(t) - \omega(t-\tau))^2 < 1$
3: **while** $N_{connected} < N_c$ **do** ▷ Connect all generators in the order decided automatically by the multi-agent algorithm, explained later
4: **if** $\delta_i > 1$ **then** ▷ $\delta_i > 1$ means start-up availability of agent i
5: $startup(i)$, $synchronise(i)$ and $connect(i)$
6: **Wait until** $\psi < 1$
7: **end if**
8: **end while**

The communication systems of generators can work autonomously (e.g., with energy storage) or be supplied by the grid energy. To be generic, in this case study, the model includes, for each generator except the leader, a communication system that needs electrical feeding from the grid to work. This means that every generator can only send and receive messages if the voltage in its PCC is above a specific value. This value is set to 0.5 pu.

The leader is determined before the blackout, and every generator knows their role (leader or follower). The leader must be capable of black-start operation. Every other generator sends a broadcast message of type 0 (new generator) as soon as it has $v > 0.5$ pu at its PCC.

The communications between agents are modelled using the MATLAB toolbox

"SimEvents"[1] for Simulink. While a fixed delay is the conventional modelling of communications in microgrids, SimEvents goes further by providing a discrete-event simulation engine and a comprehensive component library for message-based communication in Simulink. It involves dynamic interactions, queuing, and potential contention that significantly impact system behaviour. SimEvents allows for a detailed analysis of these event-driven system models, enabling the optimisation of critical performance characteristics such as latency, throughput, and packet loss. To reflect realistic network conditions and account for the inherent time taken for message transmission, a fixed communication delay of 100 ms was incorporated into every communication link.

The different message types are:

0. Normal operation (secondary control message) if the destination of the message is a specific neighbour, or to notify the connection of a new agent if the destination of the message is 0[2].
1. The message source wants the message destination to follow it.
2. The message source confirms that it follows the message destination.
3. The message source wants the message destination to follow it and confirms that it is taking the leader's role.
4. The message source does not follow the message destination any longer.
5. The message source asks the message destination to stop following it.
6. The message source requests the startup data (available power capacity) from the message destination and its neighbours.
7. The message source sends startup data to the message destination.
8. The message source sends the message destination a startup order.

The algorithm is based on responding to received messages, according to the generator's role.

Algorithm 2 details how a follower agent must respond to a message.

Algorithm 3 details how the leader must respond to an incoming message.

6.3.1 Synchronisation of grid-forming converters with the main grid

To have a smooth transient after the connection of every grid-forming converter, the difference in voltage amplitude, phase, and frequency between the two sides of the switch to be closed must be small before closing.

[1] More details on the features of the toolbox SimEvents can be found in https://es.mathworks.com/products/simevents.html

[2] a broadcast message, for all neighbours, is defined with destination 0

Algorithm 2 Procedure for received messages for the follower agents

```
1: if mtype == 0 then
2:     if destination == 0 and sending == 0 then                ▷ New DG and I am free
3:         follow me
4:     else                                          ▷ Message with electric variables to follow
5:         Get control set points from message
6:     end if
7: else if mtype == 1 then                                      ▷ It wants follower
8:     if following == 0 and sending ≠ source then
9:         I follow you          ▷ If I am not following anyone and it does not follow me
10:    end if
11: else if mtype == 2 then                                     ▷ It wants to follow me
12:    if following ≠ 0 and ≠ source then                       ▷ I am following someone different
13:        sending = source                                     ▷ It follows me
14:    else
15:        mtype = 5                                            ▷ You cannot follow me
16:    end if
17: else if mtype == 3 then                                     ▷ The leader wants followers
18:    if following ≠ 0 and ≠ source then                       ▷ I am following someone different
19:        mtype = 5                                            ▷ I will no longer follow you
20:    else
21:        mtype == 2                                           ▷ I follow you
22:    end if
23: else if mtype == 4 then                                     ▷ It will no longer follow me
24:    sending = 0
25: else if mtype == 5 then                                     ▷ I cannot follow it
26:    if following == source then                              ▷ I was following it
27:        following = 0
28:        if sending ≠ 0 then                                  ▷ Someone was following me
29:            mtype = 5 and send to = sending                  ▷ Warn follower
30:        end if
31:    end if
32: else if mtype == 6 then                                     ▷ It wants startup data
33:    Collect neighbours' startup data
34:    Get the optimal DG to startup
35:    mtype = 7                                  ▷ Send optimal DG and its startup data
36: else if mtype == 7 then                                     ▷ It sends startup data
37:    if left == 0 then                                        ▷ all neighbours answered
38:        mtype = 8 and send to = optimal DG     ▷ Send start-up message to optimal DG
39:    end if
40: else if mtype == 8 then                                     ▷ Startup
41:    if ID = optimal DG then                                  ▷ If I am the optimal DG
42:        startup
43:    else
44:        Forward to optimal DG
45:    end if
46: end if
```

Algorithm 3 Procedure for received messages for the leader agent

```
1:  if leader == 1 then                                   ▷ If I am the leader
2:      if followers == 0 then                            ▷ If I have no followers
3:          if mtype == 2 then                            ▷ It wants to follow me
4:              follower = origin
5:          else if mtype == 0 then                       ▷ New DG
6:              follow me
7:          end if
8:      else if mtype == 2 then                           ▷ It wants to follow me
9:          mtype = 5                                     ▷ You cannot follow me
10:     else if mtype == 7 then                           ▷ Availability
11:         if left == 0 then                             ▷ all neighbours answered
12:             start-up                                  ▷ Send start-up message to optimum DG
13:         end if
14:     end if
15: end if
```

Two PI controllers were placed to synchronise the voltage amplitude, phase and frequency imposed by the grid-forming converter with those imposed by the grid at its PCCs.

Recalling the droop equations (*i.e.,* primary control) for grid-forming converters:

$$\omega = \omega_{ref} + m_P(P_{ref} - P) \tag{6.2}$$

$$v = v_{ref} + n_Q(Q_{ref} - Q) \tag{6.3}$$

where ω and v are the frequency and voltage set points for the voltage and current controllers, ω_{ref} and v_{ref} are the frequency and voltage set points from the secondary control, P_{ref} and Q_{ref} are the active- and reactive-power set points from the secondary control, P and Q are the measured output active and reactive power of the converter, and m_P and n_Q are the active-power droop coefficient and reactive-power droop coefficient, respectively. These droop equations must be modified for synchronisation, as follows:

$$\omega = \omega_{ref} + m_P(P_{ref} - P) + \left(K_{P,sync,\omega} + \frac{K_{I,sync,\omega}}{s}\right)(\theta_{grid} - \theta_{own}) \tag{6.4}$$

$$v = v_{ref} + n_Q(Q_{ref} - Q) + \left(K_{P,sync,v} + \frac{K_{I,sync,v}}{s}\right)(v_{grid} - v_{own}) \tag{6.5}$$

where $K_{P,sync,\omega}$ and $K_{I,sync,\omega}$ are the proportional and integral coefficients for the frequency synchronisation controller, $K_{P,sync,v}$ and $K_{I,sync,v}$ are the proportional

and integral coefficients for the voltage synchronisation controller, θ_{grid} is the phase of the voltage at the grid-side of the contactor, θ_{own} is the phase of the voltage at the converter-side of the switch, v_{grid} is the amplitude of the voltage at the grid-side of the switch, and v_{own} is the amplitude of the voltage at the converter-side of the switch.

A small voltage magnitude and angle difference are guaranteed if:

$$\forall t \in [t_0, t_0 + \tau_{sync}] \; (|v_{grid} - v_{GFr-VSC}| < \epsilon_v) \; \& \; (|\theta_{grid} - \theta_{GFr-VSC}| < \epsilon_\theta) \quad (6.6)$$

where t_0 is the first time instant when the condition $(|v_{grid} - v_{GFr-VSC}| < \epsilon_v) \; \&(|\theta_{grid} - \theta_{GFr-VSC}| < \epsilon_\theta)$ is met, ϵ_v and ϵ_θ are the voltage amplitude and phase thresholds, respectively, to proceed with the synchronisation, and τ_{sync} is the time for checking the synchronisation condition (if the angle difference is small for some time, then the frequency difference is also small). In fact, if the phase difference of the voltage at both sides of the switch to be closed is kept below its threshold for τ_{sync} seconds, this means that the frequency difference at both sides of the switch is limited to:

$$(|\theta_{grid} - \theta_{GFr-VSC}| < \epsilon_\theta) \rightarrow \left(|\omega_{grid} - \omega_{GFr-VSC}| < \frac{\epsilon_\theta}{\tau_{sync}}\right) \quad (6.7)$$

6.4 Case study: Black start of the IEEE 69 bus test system

The microgrid used for the validation of the proposed BS algorithm is the modified IEEE 69 bus system presented in Appendix C. The location of the controllable switches in the system is shown in Figure 6.2. The model is implemented in the Simulink tool described in Appendix A. Notice that this model does not include non-linear modelling of cold load pickup and inrush current. The graph of available communications is shown in Figure 6.3.

Table 6.3 includes the connection times of controllable switches included in the case study.

Figure 6.4 shows the evolution of the frequency, active power, voltage and reactive power of all DGs in the microgrid in Figure 6.2 during the restoration process. It also includes the total active power served by the generators. Notice that the high transient peaks in the frequency of the DGs (above 51 Hz) is a synchronisation transient that occurs when that DG is energised (before connecting the DG to the grid). Clearly, the trigger-based decentralised secondary control manages to recover the frequency of the microgrid after each grid operation, after the connection of each DG. It also maintains the programmed active- and reactive-power sharing among DGs in the microgrid. The voltage profile changes as a result of the imposed reactive power sharing among DGs.

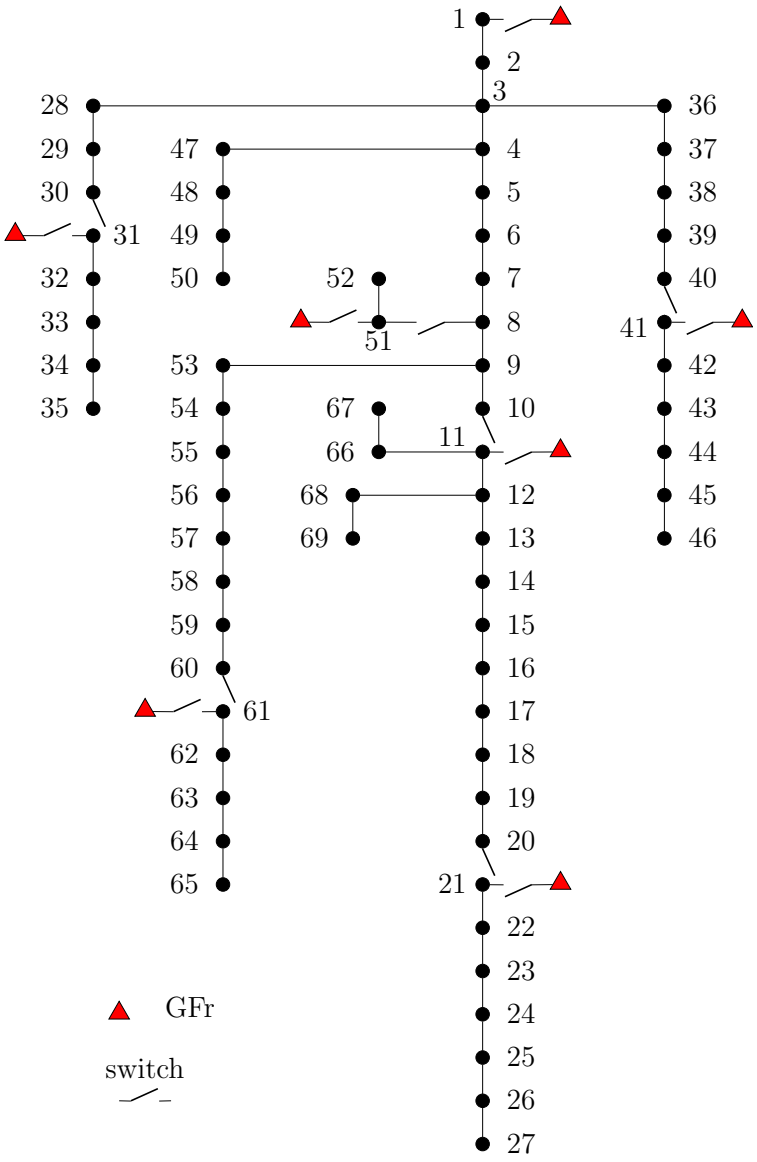

Figure 6.2: Diagram of the modified IEEE 69 bus test system used as the case study. "GFr" stands for grid-forming converter. Every grid-forming converter includes one controllable switch to connect to its PCC. Every open switch embedded in the lines of the system is a controllable switch.

Table 6.3: Switches and GFr-VSCs connection times. Each GFr-VSC is called with its bus number. Agents' numbers are used for the adjacency matrix (i.e., agent i receives information from agent j if $a_{ij} \neq 0$).

Switch	**Time (s)**
10-11	0
20-21	0
30-31	50
40-41	80
8-51	150
60-61	200

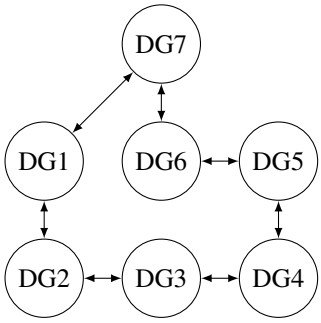

Figure 6.3: Graph of available communication between DGs for the study of the black-start of a microgrid. The used communication graph is automatically constructed using some of the available connections.

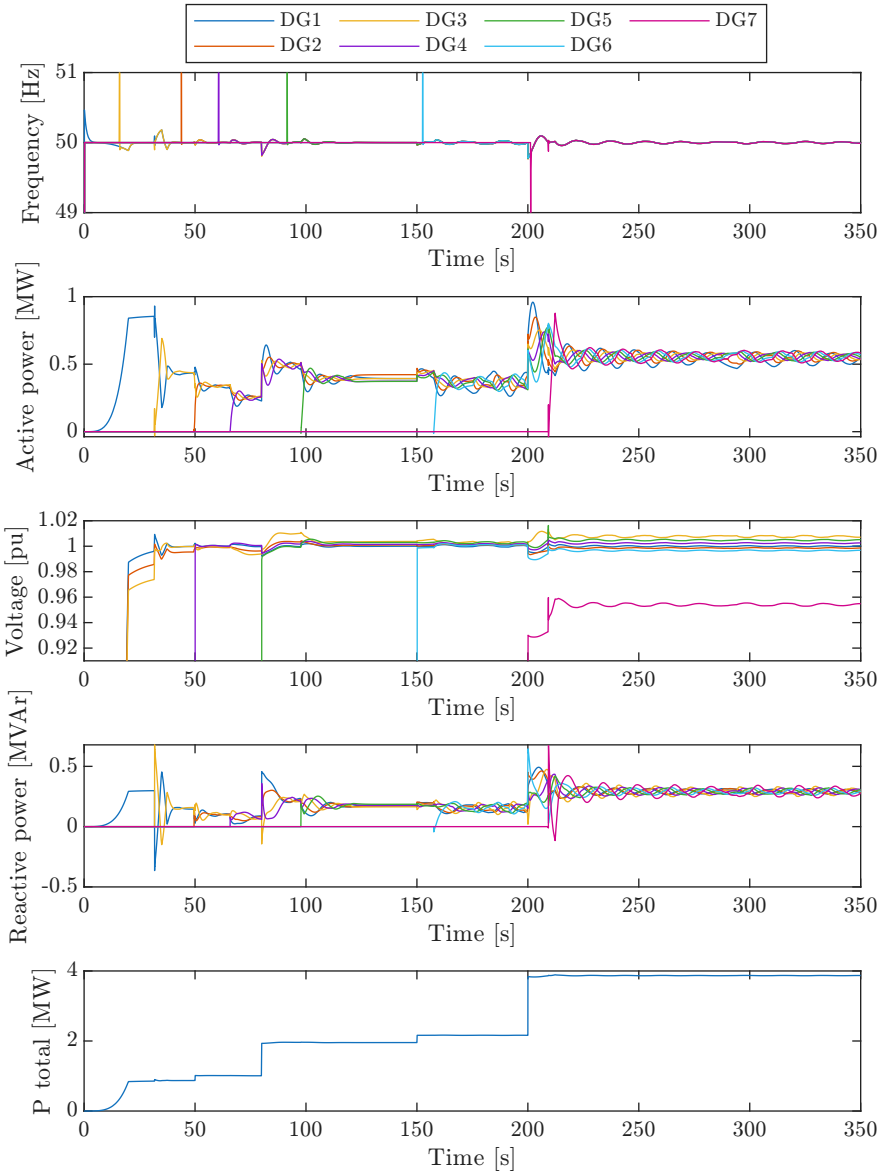

Figure 6.4: Frequency, active power, voltage and reactive power of all DGs in the microgrid.

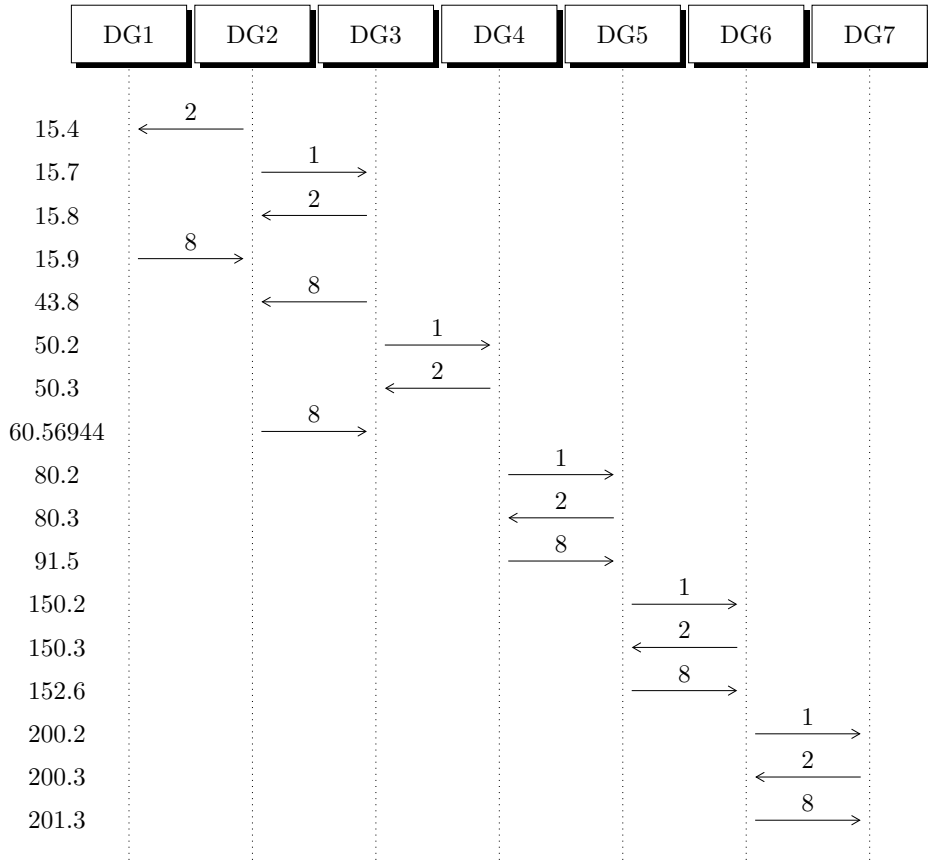

Figure 6.5: Sequence of the messages between DGs in the microgrid. The message type is shown above each message line. For clarity, only types 1 ("follow me"), 2 ("I follow you") and 8 ("start-up") are shown in the figure. The number on the left side is the simulation time at which the message reaches its destination.

Figure 6.4 shows that smooth synchronisation of GFr-VSCs is possible with the proposed control strategy.

Figure 6.5 includes a sequence diagram of the messages between DGs in the microgrid, with the message type shown above each message line. For clarity, only types 1 ("follow me"), 2 ("I follow you") and 8 ("start-up") are shown in the figure. The number on the left side is the simulation time at which the message reaches its destination.

Figure 6.5 shows how the communication graph is built dynamically. Every DG is incorporated into the communication graph after its PCC is energised. As soon as this occurs, it sends a message to all its neighbours and receives a "follow me" request from the ones that are already in the graph. The figure also shows the

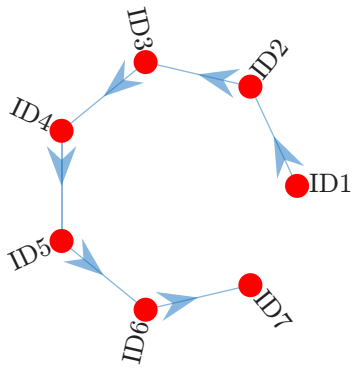

Figure 6.6: Final communication graph among all the DGs in the microgrid after the restoration process has finished. Nodes (in red) indicate DGs, and the arrows indicate the direction of the communications.

sequential decentralised decisions on the next DG to start up. In this specific case, the decision is simple because the grid operations lead to a sequential energisation of the PCC of each DG (i.e., there is only one DG with its PCC energised and available to connect to the microgrid at each moment).

Figure 6.6 includes the final communication graph among all the DGs in the microgrid after the restoration process has finished.

As clearly shown in Figure 6.6, at the end of the synchronisation process, all the DGs are connected to the graph. Therefore, the communication graph meets the conditions stated by Bidram et al. (2017) (*i.e.,* it includes a spanning tree) and the consensus among all DGs is guaranteed.

Figure 6.7 includes the number of messages sent by each DG during the restoration procedure. Clearly, the units that are connected first send more messages than the units that are connected later on.

All messages of Figure 6.7 correspond to secondary control messages, and the number of messages depends on the threshold of the trigger-based secondary control. Figure 6.8 shows the percentage of the total messages sent by each DGs during the restoration process.

6.5 Summary and Conclusions

This chapter presents a distributed method for the sequential multi-agent black start of an islanded microgrid formed in the distribution level of a power system. First of all, it discusses the peculiarities of the service restoration process in distribution systems. Then, the proposed algorithm is described. It coordinates a centralised algorithm implemented by the DSO to calculate the optimal restoration sequence and a decentralised multi-agent algorithm for service restoration among the DGs of

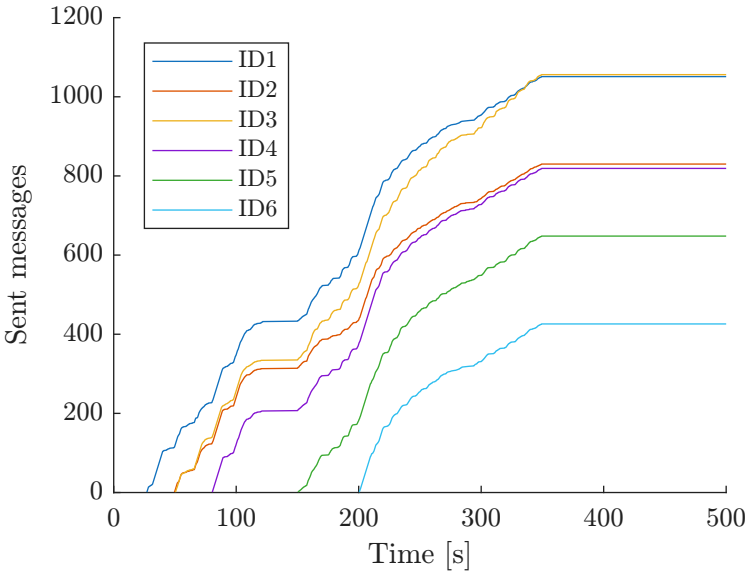

Figure 6.7: Number of secondary control messages sent by each DG during the restoration procedure

the microgrid. A trigger-based control is used for the secondary control layer of the microgrid. Simulation results show a smooth restoration of the microgrid, with a successful graph formation and consensus convergence on active and reactive power, and frequency restoration.

Future studies could focus their attention in aspects such as cold load pickup for the demand inrush current for transformers, current and active power limitation for the grid-forming converters, details of a centralised algorithm to be implemented in the DSO and the evaluation of the algorithm robustness to communication failures or DG outages. The proposed procedure ensures that the resulting communication graph includes all DGs if the communication structure follows a ring. Future research must guarantee consensus for other communication topologies.

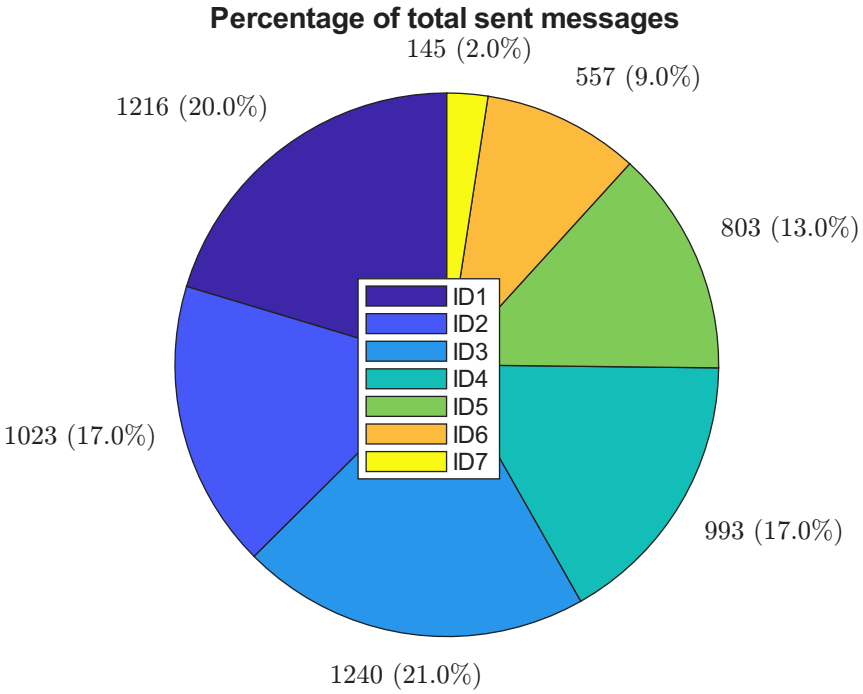

Figure 6.8: Percentages of the messages sent by each DG during the restoration procedure

This chapter details the conclusions drawn from the research carried out. It also remarks the most important contributions of this thesis to the decentralised control of microgrids, and suggests, as future work, aspects related to the work done but not included or examined in detail.

7 Conclusions, contributions, publications and future work

7.1 Conclusions: Decentralised vs centralised control of microgrids

The conclusions drawn from the work done can be summarised as follows:

- The traditional time-scale separation between dynamics may not always be valid in power systems with high penetration of power electronics. In this regard, the proposed state relevance coefficient helps to analyse the relevance of the dynamic of each state variable for each scenario. This measure allows the user to systematically evaluate the interdependence between control layers and devices in a power systems. Applying the state relevance to the multi-agent secondary control of microgrids gives insights into the control design of each loop and the importance of each state variable in the response of the system.

- Fully decentralised control has, in general, worse performance and control capacity than centralised control. Two examples are included in this thesis as chapters:

    1. A microgrid working with multi-agent secondary control based on consensus is still able to synchronise with the main grid successfully, as shown in Chapter 4, but the real implementation of such a feature requires careful consideration and analysis of the communication delays between generators in the control design stage. It has been shown that the effect of communication delays can be reduced by using a derivative droop term and an adequate design of the secondary controller, which can also reduce the peak active-power needed to resynchronise the MG.

2. The economic dispatch problem of a microgrid can be solved in a fully decentralised manner, as shown in Chapter 5, although the centralised solution of the economic dispatch problem is faster and can easily consider more information, such as security constraints and grid structure. Unlike existing methods, the proposed method is able to consider active power limits and its convergence is not affected by communication delays.

The weaknesses and strengths of decentralised multi-agent control for microgrids are clear after the work done in this thesis. A centralised control is nowadays more suitable for the majority of cases. However, with the growth of distributed generation, centralised control may not always be practical, mainly due to bottlenecks and efficiency issues. In this scenario, research on the implementation of traditional control capabilities without centralised control is essential.

7.2 Contributions: Towards an electronically-fed electric microgrid

7.2.1 State relevance in electronically-fed microgrids

This thesis introduces a novel algorithm that quantifies the relevance of states in dynamic systems while preserving the physical meaning of state variables. Its application to microgrids with electronic power sources has been investigated.

The algorithm utilises a balanced realisation of a linear approximation to evaluate the contribution of each state variable to the output response of the system. While the transformation to a balanced realisation is linear and preserves system eigenvalues, the states may lose their physical significance. Relevance is determined through participation factors derived from the eigenvalues of both the original and transformed states.

Applied in several case studies, the algorithm has proven useful in identifying relevant states to guide the reduction of full nonlinear models, by setting the derivatives of less relevant states to zero, while maintaining a sufficiently accurate input-output response in the reduced-order system.

Although traditional methods yield consistent results when there is a clear timescale separation, results show that traditional methods linking relevant states to slow dynamics may require higher-order reduced models for simulation accuracy of small disturbances similar to the one provided by the proposed approach. Therefore, the state-relevance coefficient helps systematically select states for reduced models and provides important insights for modal analysis. The state-relevance coefficient is strongly influenced by the specific inputs and outputs chosen.

The contributions of this algorithm are:

- A systematic approach to measure the relevance of each variable of a linear system in its input-output response.
- The proposed method is valid in complex scenarios where traditional time-scale separation of dynamics cannot be applied.
- Since it depends on the selected inputs and outputs, the algorithm clarifies the relevant dynamics for the desired analysis.
- The physical meaning of the states is preserved, allowing for more intuitive control design and modal analysis.

7.2.2 VFlexP

The work carried out in this thesis has led to the development of VFlexP, an open-source tool for simulating and analysing hybrid AC/DC power systems. VFlexP includes steady-state analysis, non-linear electromagnetic simulation in a d-q synchronously rotating reference frame, accurate linearisation of the non-linear dynamic model, rich eigenvalue analysis of the linear system, and a tool to assess the relevance of state-variable dynamics in an input-output representation of the power system. System data can be introduced in a spreadsheet compatible with MATPOWER, and the user interface of VFlexP makes it possible to make an intuitive selection of the complexity with which each system element is to be represented. All elements of the same type with the same level of detail can be included in a single block in the Simulink workspace, thanks to the vectorised formulation used, to provide a simple and clear view of even mid-to-large power systems. The main contributions of this tool are:

- Built on MATLAB-Simulink, it enables flexible modelling without traditional simplifications and allows for the easy incorporation of new models.
- Key features include relevance analysis of state variables for model simplification and a user-friendly interface that organises system elements efficiently.
- While currently focused on d-q representation of balanced power systems, VFlexP aims to support detailed and nonlinear simulations in evolving energy landscapes.

7.2.3 Decentralised control of microgrids

The continuous growth of distributed renewable energy resources in medium and low-voltage networks reinforces the argument for adopting a distributed architecture for electricity supply that relies on microgrids. While decentralised architectures for the primary and secondary control layers of microgrid hierarchical control have already been discussed in the literature, the tertiary control (economic

dispatch) has primarily been developed as either a centralised system or a distributed approach that depends on a central agent to coordinate operations among distributed generators.

This thesis proposes and evaluates a fully decentralised hierarchical control system for microgrids based on a consensus-driven economic dispatch problem for the tertiary control layer and consensus formulation for the secondary control layer. In addition, this thesis proposes alternative formulations of the secondary control layer. The main contributions of this thesis within decentralised control of microgrids are summarised below.

Decentralised secondary control of microgrids

Regarding the secondary control layer, the control structures included in this thesis are based on the work presented by Bidram et al. (2017) but the analysis is extended by considering the difficulties of having communication time delays in this structure.

An innovative multi-agent secondary control algorithm aimed at synchronising a microgrid with the main grid (another grid in general) is also evaluated and improved. The analysis emphasises the often-overlooked impact of communication delays on active power transients between converters during synchronisation. This thesis analyses the reduction of these transients using a derivative droop control method to enhance system stability. Additionally, how the damping characteristics of the Proportional-Integral (PI) synchronisation controller influence transient behaviour is investigated.

The simulation results are promising and are validated by experimental results from a hands-on laboratory setup, highlighting the applicability and reliability of our findings.

The contributions on this line can be summarised as follows:

- Analysis of the coordination among units to avoid unwanted active-power flows during the synchronisation with the main grid of a microgrid (MG) comprising grid-forming converters working with a multi-agent secondary control.
- Analysis of the impact of communication delays on active-power transients during the synchronisation.
- Implementation in a laboratory set-up of the multi-agent-based synchronisation and validation of the main theoretical results.

Fully decentralised hierarchical control of a microgrid

This thesis presents a fully decentralised multi-agent hierarchical control system for a hybrid AC-DC microgrid. The secondary and tertiary control layers use a consensus formulation. The tertiary layer optimally shares active power among generators in a cooperative manner.

The results show that communication delays do not impact convergence, and the secondary control layer manages active-power sharing for deviations from the dispatched operation point. Simulation results demonstrate the performance of this control system while respecting the active-power limits of the generators.

Nevertheless, the work carried out has focused on active-power/frequency control. Future work should focus on integrating voltage control into the economic dispatch problem and developing an algorithm for multi-period decentralised economic dispatch.

Distributed black-start of a microgrid

This thesis explores a distributed method for the sequential black start of an islanded microgrid at the distribution level. The general algorithm combines a centralised approach by the distribution system operator (DSO) to determine the optimal restoration sequence and a decentralised multi-agent algorithm for voltage restoration among the distributed generators (DGs) in the microgrid. A trigger-based control mechanism is employed for the microgrid secondary control layer.

- This application of consensus-based control may seem rather unusual, but the simulation results obtained indicate smooth voltage restoration, successful graph formation, and consensus convergence for active and reactive power, as well as frequency restoration.

7.3 Future work

This thesis proposes and analyses different algorithms for the multi-agent decentralised control of microgrids and introduces some tools to help analyse microgrids with these controls. As power systems evolve towards a distributed generation model, this control structure is expected to increase in importance in the following years. Therefore, multi-agent structures for microgrid decentralised control may become increasingly important. Some of the research gaps discovered by the work reported here, but not covered in this thesis document, include:

- **The consideration of converter limits for the multi-agent control algorithms:** In this thesis, generation limits are only considered in terms of maximum and minimum active power set points in Chapter 5. In fact, all the converters are considered ideal voltage sources, and the primary energy source limitation is not included. It is recommended that future work investigate current limitations or primary source active-power limitations for the converter.

- **Extending the secondary control to voltage control:** This thesis focused on frequency and active-power control. Voltage control is only considered to recover the voltage to its nominal value after the work of the primary control, but without controlling the voltage profile. Reactive-power sharing

is the chosen objective instead. However, multi-agent voltage secondary control can help to improve the voltage profile of a power system. Moreover, the synchronisation algorithm proposed in Chapter 4 considers only active power analysis. Future work in this topic should include control of the reactive power to ensure an appropriate share among DGs, and stochastic modelling of the communication time delays.

- **Considering DC DGs on the multi-agent secondary control:** In this thesis, only AC DGs are considered in multi-agent control. DC generators, when included (in Chapter 5 and Appendix A), have a fixed active-power set point. However, in the future, the number of DC generators in hybrid power systems is very likely to increase. Therefore, it is interesting to evaluate how they can contribute to the secondary control.
- **Extending the single-period economic dispatch algorithm to multi-period economic dispatch:** This thesis presented a decentralised single-period economic dispatch algorithm in Chapter 5. This algorithm can be extended to consider a multi-period economic dispatch, including battery energy storage system (BESS).

7.4 Publications

7.4.1 Articles published in journals

JCR Q1 Tomás-Martín, A., García-Cerrada, A., Sigrist, L., Yagüe, S. J., & Suárez-Porras, J. (2023a). State relevance and modal analysis in electrical microgrids with high penetration of electronic generation. *International Journal of Electrical Power & Energy Systems*, *147*, 108876. https://doi.org/10.1016/j.ijepes.2022.108876

This paper discusses the need to revisit the conventional time-scale separation of power systems, focusing on the rapid dynamics of electronic power sources. It proposes an algorithm to identify the relevance of different states in a linearised model of an electrical microgrid for input-output responses. By using a non-physical balanced realisation, the algorithm calculates the energy contributions of each state variable and establishes a "relevance coefficient" (RC) to guide the inclusion of dynamics in analyses and simulations. The RC is validated against nonlinear simulations, showing its effectiveness in providing clear recommendations even when system dynamics overlap. This paper is related to the Chapter 3.

JCR Q1 Tomás-Martín, A., Zuluaga-Ríos, C. D., Suárez-Porras, J., Kazemtabrizi, B., García-Aguilar, J., Sigrist, L., & García-Cerrada, A. (2025). A vector-based flexible-complexity tool for simulation and small-signal analysis of hybrid AC/DC power systems. *Sustainable Energy, Grids and Networks*, *43*, 101817. https://doi.org/10.1016/j.segan.2025.101817

This paper, presented at the 12th Bulk Power System Dynamics and Control Symposium - IREP'2025 conference in Sorrento, Italy, discusses VFlexP, an open-source tool for simulating and analysing hybrid AC/DC power systems. Built on MATLAB-Simulink, it enables flexible modelling without traditional simplifications and allows for the easy incorporation of new models. Key features include relevance analysis of state variables for model simplification and a user-friendly interface that organises system elements efficiently. While currently focused on d-q representation of balanced power systems, VFlexP aims to support detailed and nonlinear simulations in evolving energy landscapes. This paper is included in the Appendix A of this thesis.

7.4.2 Articles presented in conferences

- Tomás-Martín, A., García-Cerrada, A., Sigrist, L., Yagüe, S. J., Miguel, D. R., & Martín-Utrilla, F.-D. (2023). Re-synchronisation of a Microgrid to the Main Grid Using Multi-Agent Secondary Control. *2023 IEEE Belgrade PowerTech*, 1–6. https://doi.org/10.1109/PowerTech55446.2023.10202680

  The paper discusses the synchronisation control of self-powered microgrids that can operate independently or be connected to the main electrical grid. It highlights the challenges associated with frequently disconnecting and reconnecting these microgrids, such as maintaining voltage and frequency stability. The proposed control method uses distributed multi-agent systems and does not require additional electronic power converters at the connection point, relying instead on precise measurements. The paper also includes strategies to reduce synchronisation transients and provides simulation results to demonstrate the effectiveness of the proposed approach. This paper was the first approach of the proposed algorithm for the synchronisation of a microgrid to the main grid presented in Chapter 4.

- Tomás-Martín, A., García-Cerrada, A., Sigrist, L., Yagüe, S. J., & Suárez-Porras, J. (2023b). State relevance and modal analysis in electrical microgrids with 100% grid-forming converters [Available on demand.]. *XXX Seminario Anual de Automática, Electrónica industrial e Instrumentación - SAAEI 2023*. Retrieved December 19, 2024, from https://www.iit.comillas.edu/publicacion/congreso/en/12318/

  This paper applies the state relevance method to identify the time-scale separation among different control layers in a microgrid composed of grid-forming converters. It demonstrates that the relevance coefficient captures the importance of the dynamics of each state variable in the linearised system for a wide variety of scenarios. The results included in this paper are also included in Chapter 3.

- Tomás-Martín, A., Roldán-Pérez, J., Jankovic, N., Yagüe, S. J., García-Cerrada, A., & Sigrist, L. (2024). Control secundario multi-agente para reconectar una

microrred de convertidores formadores de red con la red principal [Multi-agent secondary control to reconnect a microgrid of grid-forming converters to the main grid] [Available on demand.]. *XXXI Seminario Anual de Automática, Electrónica industrial e Instrumentación - SAAEI 2024*. Retrieved December 19, 2024, from https://www.iit.comillas.edu/publicacion/congreso/en/12476/

This paper introduces a method to synchronise one microgrid working with multi-agent secondary control based on consensus with the main grid. It proposes a systematic design of the synchronisation controller of the system and analyses how communication time delays affect the performance of the synchronisation. This paper is a preliminary version of the algorithm presented in Chapter 4.

7.4.3 Papers under review

- Tomás-Martín, A., Roldán-Pérez, J., Jankovic, N., Yagüe, S. J., García- Cerrada, A., & Sigrist, L. (2025). Performance of multi-agent secondary control for reconnecting a microgrid of grid-forming converters to the main grid [Preprint available on demand.]

  The paper focuses on the resynchronisation of islanded electrical microgrids with the main grid using a multi-agent secondary control system. It examines the effects of communication delays and instantaneous power flows on the stability of the MG during the re-synchronisation process. The findings suggest that appropriate control parameter design can mitigate the challenges posed by communication delays and optimise power flow management. The study is validated through practical implementation in a real MG setup. The algorithm presented in this paper is included in Chapter 4.

- Tomás-Martín, A., Kazemtabrizi, B., García-Cerrada, A., Sigrist, L., & Bueno, E. J. (2025). Fully decentralised consensus-based hierarchical control of a hybrid AC-DC microgrid [Preprint available on demand.]

  The paper discusses a fully decentralised hierarchical control system for microgrids, focusing on consensus-based economic dispatch. It highlights the advantages of decentralised architectures over traditional centralised control, particularly in the context of increasing distributed renewable energy sources. The proposed approach addresses communication delays and active power limits of generators, demonstrating its robustness and stability through various analyses and comparisons with existing control methods. The control structure presented in this paper is included in Chapter 5.

Bibliography

Acharya, S., & Vijaya Kumar, D. (2024). Frequency stabilization and synchronization between grid and AC microgrid. *Electric Power Systems Research*, *228*, 110045. https://doi.org/10.1016/j.epsr.2023.110045

Adibi, M., Alexander, R., & Milanicz, D. (1999). Energizing high and extra-high voltage lines during restoration. *IEEE Transactions on Power Systems*, *14*(3), 1121–1126. https://doi.org/10.1109/59.780939

Adibi, M., & Milanicz, D. (1995). Protective system issues during restoration. *IEEE Transactions on Power Systems*, *10*(3), 1492–1497. https://doi.org/10.1109/59.466498

Alvarez-Bustos, A., Kazemtabrizi, B., Shahbazi, M., & Acha-Daza, E. (2021). Universal branch model for the solution of optimal power flows in hybrid AC/DC grids. *International Journal of Electrical Power & Energy Systems*, *126*, 106543. https://doi.org/10.1016/j.ijepes.2020.106543

Andreadis, G., Klazoglou, P., Niotaki, K., & Bouzakis, K. (2014). Classification and review of multi-agents systems in the manufacturing section [doi: 10.1016/j.proeng.2014.02.233]. *Procedia Engineering*, *69*, 282–290.

Antoulas, A. C. (2005, January). *Approximation of large-scale dynamical systems*. Society for Industrial; Applied Mathematics.

Avila-Martinez, R. E., Renedo, J., Rouco, L., Garcia-Cerrada, A., Sigrist, L., Qoria, T., & Guillaud, X. (2022). Fast Voltage Boosters to Improve Transient Stability of Power Systems With 100% of Grid-Forming VSC-Based Generation. *IEEE Transactions on Energy Conversion*, 1–12. https://doi.org/10.1109/TEC.2022.3199650

Baran, M., & Wu, F. (1989). Optimal capacitor placement on radial distribution systems. *IEEE Transactions on Power Delivery*, *4*(1), 725–734. https://doi.org/10.1109/61.19265

Bassey, O., & Butler-Purry, K. L. (2020). Black Start Restoration of Islanded Droop-Controlled Microgrids. *Energies*, *13*(22), 5996. https://doi.org/10.3390/en13225996

Bassey, O., Chen, B., & Butler-Purry, K. L. (2018). Sequential service restoration in distribution systems and microgrids integrating frequency response and varying switching interval. *2018 IEEE Texas Power and Energy Conference (TPEC)*, 1–6. https://doi.org/10.1109/TPEC.2018.8312077

Bayo Salas, A. (2018). *Control interactions in power systems with multiple VSC HVDC converters. Analysis, modelling and mitigation of electromagnetic stability problems* [phd]. Ph.D. Thesis / Arenberg Doctoral School, Faculty of Engineering Science.

Beerten, J., & Belmans, R. (2015). MatACDC - an open source software tool for steady-state analysis and operation of hvdc grids. *11th IET International Conference on AC and DC Power Transmission*, 1–9. https://doi.org/10.1049/cp.2015.0061

Beerten, J., D'Arco, S., & Suul, J. A. (2016). Frequency-dependent cable modelling for small-signal stability analysis of VSC-HVDC systems. *IET Generation, Transmission & Distribution*, *10*(6), 1370–1381. https://doi.org/10.1049/iet-gtd.2015.0868

Bidram, A., & Davoudi, A. (2012). Hierarchical Structure of Microgrids Control System. *IEEE Transactions on Smart Grid*, *3*(4), 1963–1976. https://doi.org/10.1109/TSG.2012.2197425

Bidram, A., Davoudi, A., & Lewis, F. L. (2014). A Multiobjective Distributed Control Framework for Islanded AC Microgrids. *IEEE Transactions on Industrial Informatics*, *10*(3), 1785–1798. https://doi.org/10.1109/TII.2014.2326917

Bidram, A., Davoudi, A., Lewis, F. L., & Guerrero, J. M. (2013). Distributed Cooperative Secondary Control of Microgrids Using Feedback Linearization. *IEEE Transactions on Power Systems*, *28*(3), 3462–3470. https://doi.org/10.1109/TPWRS.2013.2247071

Bidram, A., Davoudi, A., Lewis, F. L., & Sam Ge, S. (2014). Distributed Adaptive Voltage Control of Inverter-Based Microgrids. *IEEE Transactions on Energy Conversion*, *29*(4), 862–872. https://doi.org/10.1109/TEC.2014.2359934

Bidram, A., Nasirian, V., Davoudi, A., & Lewis, F. L. (2017). *Cooperative Synchronization in Distributed Microgrid Control*. Springer International Publishing. https://doi.org/10.1007/978-3-319-50808-5

Binetti, G., Davoudi, A., Lewis, F. L., Naso, D., & Turchiano, B. (2014). Distributed Consensus-Based Economic Dispatch With Transmission Losses. *IEEE Transactions on Power Systems*, *29*(4), 1711–1720. https://doi.org/10.1109/TPWRS.2014.2299436

Blondel, A. (1913). *Synchronous Motors and Converters: Theory and Methods of Calculation and Testing* [Google-Books-ID: hQ1ZAAAAYAAJ]. McGraw-Hill Book Company.

Braun, M., Brombach, J., Hachmann, C., Lafferte, D., Klingmann, A., Heckmann, W., Welck, F., Lohmeier, D., & Becker, H. (2018). The Future of Power System Restoration: Using Distributed Energy Resources as a Force to Get Back Online. *IEEE Power and Energy Magazine*, *16*(6), 30–41. https://doi.org/10.1109/MPE.2018.2864227

Capitanescu, F. (2016). Critical review of recent advances and further developments needed in AC optimal power flow. *Electric Power Systems Research*, *136*, 57–68. https://doi.org/10.1016/j.epsr.2016.02.008

Chai, R., Zhang, B., Dou, J., Hao, Z., & Zheng, T. (2016). Unified power flow algorithm based on the NR method for hybrid AC/DC grids incorporating VSCs. *IEEE Transactions on Power Systems*, *31*(6), 4310–4318. https://doi.org/10.1109/TPWRS.2015.2511303

Chen, B. (2017, May). *Black Start Restoration for Electric Distribution Systems and Microgrids* [Thesis]. Texas A & M University [Accepted: 2017-08-21T14:47:11Z]. Retrieved December 12, 2022, from https://oaktrust.library.tamu.edu/handle/1969.1/161665

Chen, G., Lewis, F. L., Feng, E. N., & Song, Y. (2015). Distributed Optimal Active Power Control of Multiple Generation Systems. *IEEE Transactions on Industrial Electronics*, *62*(11), 7079–7090. https://doi.org/10.1109/TIE.2015.2431631

Chen, G., & Zhao, Z. (2018). Delay Effects on Consensus-Based Distributed Economic Dispatch Algorithm in Microgrid. *IEEE Transactions on Power Systems*, *33*(1), 602–612. https://doi.org/10.1109/TPWRS.2017.2702179

Chen, W., & Li, T. (2021). Distributed Economic Dispatch for Energy Internet Based on Multiagent Consensus Control. *IEEE Transactions on Automatic Control*, *66*(1), 137–152. https://doi.org/10.1109/TAC.2020.2979749

Chen, Y., Wan, K., Zhao, J., & Yu, M. (2024). Accurate consensus-based distributed secondary control with tolerance of communication delays for DC microgrids. *International Journal of Electrical Power & Energy Systems*, *155*, 109636. https://doi.org/10.1016/j.ijepes.2023.109636

Chow J.H. (Ed.). (1982). *Time-scale modeling of dynamic networks with applications to power systems* (Vol. 46). Springer-Verlag.

Chu, H., Yue, D., Gao, L., & Lai, X. (2021). Consensus of Multiagent Systems With Relative State Saturations. *IEEE Transactions on Systems, Man, and Cybernetics: Systems*, *51*(4), 2391–2402. https://doi.org/10.1109/TSMC.2019.2912980

Coelho, E. A. A., Wu, D., Guerrero, J. M., Vasquez, J. C., Dragicevic, T., Stefanovic, C., & Popovski, P. (2016). Small-Signal Analysis of the Microgrid Secondary Control Considering a Communication Time Delay. *IEEE Transactions on Industrial Electronics*, *63*(10), 6257–6269. https://doi.org/10.1109/TIE.2016.2581155

Cole, S., & Belmans, R. (2011). MatDyn, A New Matlab-Based Toolbox for Power System Dynamic Simulation. *IEEE Transactions on Power Systems*, *26*(3), 1129–1136. https://doi.org/10.1109/TPWRS.2010.2071888

Cruz Victorio, M. E., Kazemtabrizi, B., & Shahbazi, M. (2022). Real-time resilient microgrid power management based on multi-agent systems with price forecast. *IET Smart Grid*, *6*(2), 190–204. https://doi.org/10.1049/stg2.12089

Cui, H., Li, F., & Tomsovic, K. (2021). Hybrid symbolic-numeric framework for power system modeling and analysis. *IEEE Transactions on Power Systems*, *36*(2), 1373–1384. https://doi.org/10.1109/TPWRS.2020.3017019

D'Arco, S., & Suul, J. A. (2013). Virtual synchronous machines — Classification of implementations and analysis of equivalence to droop controllers for

microgrids. *2013 IEEE Grenoble Conference*, 1–7. https://doi.org/10.1109/PTC.2013.6652456

D'Arco, S., Suul, J. A., & Fosso, O. B. (2015). A Virtual Synchronous Machine implementation for distributed control of power converters in SmartGrids. *Electric Power Systems Research*, *122*, 180–197. https://doi.org/10.1016/j.epsr.2015.01.001

Dehkordi, N. M., Khorsandi, A., Baghaee, H. R., Sadati, N., Moghaddam, S. S., & Guerrero, J. M. (2021). Voltage and Frequency Consensusability of Autonomous Microgrids Over Fading Channels. *IEEE Transactions on Energy Conversion*, *36*(1), 149–158. https://doi.org/10.1109/TEC.2020.3005269

Diestel, R. (2000). *Graph Theory* [Pages: 415 Publication Title: Graduate Texts in Mathematics]. Springer. https://doi.org/10.1007/978-3-662-53622-3

DIgSILENT. (2024). *PowerFactory* (Version 2024) [Last accessed: 27-Oct-2024]. https://www.digsilent.de/en/powerfactory.html

Ding, T., Wang, Z., Qu, M., Wang, Z., & Shahidehpour, M. (2022). A Sequential Black-Start Restoration Model for Resilient Active Distribution Networks. *IEEE Transactions on Power Systems*, *37*(4), 3133–3136. https://doi.org/10.1109/TPWRS.2022.3164589

Dorfler, F., Simpson-Porco, J. W., & Bullo, F. (2016). Breaking the Hierarchy: Distributed Control and Economic Optimality in Microgrids. *IEEE Transactions on Control of Network Systems*, *3*(3), 241–253. https://doi.org/10.1109/TCNS.2015.2459391

Dorri, A., Kanhere, S. S., & Jurdak, R. (2018). Multi-Agent Systems: A Survey. *IEEE Access*, *6*, 28573–28593. https://doi.org/10.1109/ACCESS.2018.2831228

DSATools [Last Accessed: 28-Jun.-2024]. (2024).

Du, Y., Tu, H., Lu, X., Wang, J., & Lukic, S. (2022). Black-Start and Service Restoration in Resilient Distribution Systems With Dynamic Microgrids. *IEEE Journal of Emerging and Selected Topics in Power Electronics*, *10*(4), 3975–3986. https://doi.org/10.1109/JESTPE.2021.3071765

Durić, M., Radojević, Z., & Turković, E. (1997). A practical approach to the order reduction of a power system model for small signal stability analysis. *Electric Power Systems Research*, *41*(1), 13–18. https://doi.org/10.1016/S0378-7796(96)01137-6

Egido, I., Fernandez-Bernal, F., & Rouco, L. (2009). The Spanish AGC System: Description and Analysis. *IEEE Transactions on Power Systems*, *24*(1), 271–278. https://doi.org/10.1109/TPWRS.2008.2007003

EirGrid. (2020, October). *Design of the System Restoration Plan for Ireland* (tech. rep.). EirGrid. Retrieved January 24, 2023, from https://www.eirgridgroup.com/site-files/library/EirGrid/EirGrid_System_Restoration_Plan_Ireland.pdf

ENTSO-E. (n.d.). Iberian Peninsula Blackout - 28 April 2025. Retrieved June 9, 2025, from https://www.entsoe.eu/publications/blackout/9-may-2025-iberian-blackout/

Espina, E., Cárdenas-Dobson, R. J., Simpson-Porco, J. W., Kazerani, M., & Sáez, D. (2023). A Consensus-Based Distributed Secondary Control Optimization Strategy for Hybrid Microgrids. *IEEE Transactions on Smart Grid*, *14*(6), 4242–4255. https://doi.org/10.1109/TSG.2023.3263107

ETAP-Operation Tecnology, Inc. (2024). *ETAP* (Version 2024) [Last accessed: 27-Oct-2024]. https://www.etap.com/

EUROSTAG. (2020). *SMART FLOW* [Last accessed: 27-Oct-2024]. https://www.eurostag.be/

Fachini, F., Bogodorova, T., Vanfretti, L., & Boersma, S. (2024). A microgrid control scheme for islanded operation and re-synchronization utilizing Model Predictive Control. *Sustainable Energy, Grids and Networks*, *39*, 101464. https://doi.org/10.1016/j.segan.2024.101464

Fan, D., Ren, Y., Feng, Q., Liu, Y., Wang, Z., & Lin, J. (2021). Restoration of smart grids: Current status, challenges, and opportunities. *Renewable and Sustainable Energy Reviews*, *143*, 110909. https://doi.org/10.1016/j.rser.2021.110909

Gholami, M., Pilloni, A., Pisano, A., & Usai, E. (2021). Robust Distributed Secondary Voltage Restoration Control of AC Microgrids under Multiple Communication Delays. *Energies*, *14*(4), 1165. https://doi.org/10.3390/en14041165

Ghosh, S., & Senroy, N. (2012). A comparative study of two model order reduction approaches for application in power systems [ISSN: 1944-9925]. *2012 IEEE Power and Energy Society General Meeting*, 1–8. https://doi.org/10.1109/PESGM.2012.6344785

GitHub & OpenAI. (2024, October). GitHub Copilot (v1.243.0 version) [Large language model]. https://github.com/features/copilot

Grammarly. (2024, October). Grammarly (v1.2.110.1501 version) [Large language model]. https://www.grammarly.com/

Grdenić, G., Delimar, M., & Beerten, J. (2020). Assessment of AC network modeling impact on small-signal stability of AC systems with VSC HVDC converters. *International Journal of Electrical Power & Energy Systems*, *119*, 105897. https://doi.org/10.1016/j.ijepes.2020.105897

Grdenić, G., Delimar, M., & Beerten, J. (2022). AC Grid Model Order Reduction Based on Interaction Modes Identification in Converter-Based Power Systems. *IEEE Transactions on Power Systems*. https://doi.org/10.1109/TPWRS.2022.3180426

Griñó, R., Ortega, R., Fridman, E., Zhang, J., & Mazenc, F. (2021). A behavioural dynamic model for constant power loads in single-phase ac systems. *Automatica*, *131*, 109744. https://doi.org/https://doi.org/10.1016/j.automatica.2021.109744

Guerrero, J., de Vicuna, L., Miret, J., Matas, J., & Cruz, J. (2004). Output impedance performance for parallel operation of UPS inverters using wireless and average current-sharing controllers [ISSN: 0275-9306]. *2004 IEEE 35th Annual Power Electronics Specialists Conference*, *4*, 2482–2488 Vol.4. https://doi.org/10.1109/PESC.2004.1355219

Guerrero, J. M., Vasquez, J. C., Matas, J., de Vicuna, L. G., & Castilla, M. (2011). Hierarchical Control of Droop-Controlled AC and DC Microgrids—A General Approach Toward Standardization. *IEEE Transactions on Industrial Electronics*, *58*(1), 158–172. https://doi.org/10.1109/TIE.2010.2066534

Guo, L., Liu, X., Li, X., Wang, R., Ren, H., Wang, Z., & Sun, Q. (2025). A novel adaptive droop-based SoC balancing control strategy for distributed energy storage system in DC microgrid. *International Journal of Electrical Power & Energy Systems*, *165*, 110514. https://doi.org/10.1016/j.ijepes.2025.110514

Gusrialdi, A., & Qu, Z. (2017). Distributed Estimation of All the Eigenvalues and Eigenvectors of Matrices Associated With Strongly Connected Digraphs. *IEEE Control Systems Letters*, *1*(2), 328–333. https://doi.org/10.1109/LCSYS.2017.2717799

Han, L., Morstyn, T., & McCulloch, M. (2019). Incentivizing Prosumer Coalitions With Energy Management Using Cooperative Game Theory. *IEEE Transactions on Power Systems*, *34*(1), 303–313. https://doi.org/10.1109/TPWRS.2018.2858540

Happ, H. (1977). Optimal power dispatch - A comprehensive survey. *IEEE Transactions on Power Apparatus and Systems*, *96*(3), 841–854. https://doi.org/10.1109/T-PAS.1977.32397

Harnefors, L., Zhang, L., & Bongiorno, M. (2008). Frequency-domain passivity-based current controller design. *IET Power Electronics*, *1*(4), 455. https://doi.org/10.1049/iet-pel:20070286

Hatziargyriou, N. (2014). *Microgrids: Architectures and Control*. IEEE Press-Wiley. https://doi.org/10.1002/9781118720677

Hatziargyriou, N., Milanovic, J., Rahmann, C., Ajjarapu, V., Canizares, C., Erlich, I., Hill, D., Hiskens, I., Kamwa, I., Pal, B., Pourbeik, P., Sanchez-Gasca, J., Stankovic, A., Van Cutsem, T., Vittal, V., & Vournas, C. (2021). Definition and classification of power system stability – revisited & extended. *IEEE Transactions on Power Systems*, *36*(4), 3271–3281. https://doi.org/10.1109/TPWRS.2020.3041774

He, J., & Li, Y. W. (2011). Analysis, Design, and Implementation of Virtual Impedance for Power Electronics Interfaced Distributed Generation. *IEEE Transactions on Industry Applications*, *47*(6), 2525–2538. https://doi.org/10.1109/TIA.2011.2168592

He, Y., Wang, W., & Wu, X. (2020). Multi-Agent Based Fully Distributed Economic Dispatch in Microgrid Using Exact Diffusion Strategy. *IEEE Access*, *8*, 7020–7031. https://doi.org/10.1109/ACCESS.2019.2959600

Hossain, M. A., Pota, H. R., Hossain, M. J., & Blaabjerg, F. (2019). Evolution of microgrids with converter-interfaced generations: Challenges and opportunities. *International Journal of Electrical Power & Energy Systems*, *109*, 160–186. https://doi.org/10.1016/j.ijepes.2019.01.038

IEEE-PES. (2023). *Simulation methods, models, and analysis techniques to represent the behaviour of bulk power system connected inverter-based resources* (Technical Report No. PES-TR113). IEEE.

Institute for Automation of Complex Power Systems, EONERC. (2018). *SSMD* (Version 2018) [Last accessed: 27-Oct-2024]. https://www.fein-aachen.org/en/projects/ssmd/

International Energy Agency. (2021, October). *World Energy Outlook 2021 – Analysis* (tech. rep.). International Energy Agency. Retrieved October 28, 2024, from https://www.iea.org/reports/world-energy-outlook-2021

Jamali, M., Baghaee, H. R., Sadabadi, M. S., Gharehpetian, G. B., & Anvari-Moghaddam, A. (2023). Distributed Cooperative Event-Triggered Control of Cyber-Physical AC Microgrids Subject to Denial-of-Service Attacks. *IEEE Transactions on Smart Grid*, *14*(6), 4467–4478. https://doi.org/10.1109/TSG.2023.3259545

Jankovic, N., Roldán-Pérez, J., Prodanovic, M., & Rouco, L. (2024). Centralised Multimode Power Oscillation Damping Controller for Photovoltaic Plants With Communication Delay Compensation. *IEEE Transactions on Energy Conversion*, *39*(1), 311–321. https://doi.org/10.1109/TEC.2023.3317577

Javanmard, B., Tabrizian, M., Ansarian, M., & Ahmarinejad, A. (2021). Energy management of multi-microgrids based on game theory approach in the presence of demand response programs, energy storage systems and renewable energy resources. *Journal of Energy Storage*, *42*, 102971. https://doi.org/10.1016/j.est.2021.102971

Jayawardena, A. V., Meegahapola, L. G., Robinson, D. A., & Perera, S. (2015). Representation of a grid-tied microgrid as a reduced order entity for distribution system dynamics and stability studies. *International Journal of Electrical Power & Energy Systems*, *73*, 591–600. https://doi.org/10.1016/j.ijepes.2015.05.040

Kanerica. (2024). What Are Multi-Agent Systems and Why Are They Important? [Last Accessed: 05-May-2025]. https://kanerika.com/blogs/multi-agent-systems/

Karawita, C., & Annakkage, U. D. (2010). A hybrid network model for small signal stability analysis of power systems. *IEEE Transactions on Power Systems*, *25*(1), 443–451. https://doi.org/10.1109/TPWRS.2009.2036709

Khan, M. Y. A., Liu, H., Shang, J., & Wang, J. (2023). Distributed hierarchal control strategy for multi-bus AC microgrid to achieve seamless synchronization. *Electric Power Systems Research*, *214*, 108910. https://doi.org/10.1016/j.epsr.2022.108910

Khayat, Y., Shafiee, Q., Heydari, R., Naderi, M., Dragicevic, T., Simpson-Porco, J. W., Dorfler, F., Fathi, M., Blaabjerg, F., Guerrero, J. M., & Bevrani, H. (2020). On the Secondary Control Architectures of AC Microgrids: An Overview. *IEEE Transactions on Power Electronics*, *35*(6), 6482–6500. https://doi.org/10.1109/TPEL.2019.2951694

Kokotović, P., Khalil, H. K., & O'Reilly, J. (1999, January). *Singular Perturbation Methods in Control: Analysis and Design*. Society for Industrial; Applied Mathematics. https://doi.org/10.1137/1.9781611971118

Kundur, P., Balu, N. J., & Lauby, M. G. (1994). *Power system stability and control*. McGraw-Hill.

Lara, J. D., Henriquez-Auba, R., Bossart, M., Callaway, D. S., & Barrows, C. (2024). PowerSimulationsDynamics.jl – an open source modeling package for modern power systems with inverter-based resources [Last accessed: 28-Oct.-2024]. https://arxiv.org/abs/2308.02921

Laub, A., Heath, M., Paige, C., & Ward, R. (1987). Computation of system balancing transformations and other applications of simultaneous diagonalization algorithms. *IEEE Transactions on Automatic Control*, *32*(2), 115–122. https://doi.org/10.1109/TAC.1987.1104549

Lewis, F., Zhang, H., Hengster-Movric, K., & Das, A. (2014). *Cooperative control of multi-agent systems: Optimal and adaptive design approaches*. Springer.

Li, Q., Gao, D. W., Zhang, H., Wu, Z., & Wang, F.-y. (2019). Consensus-Based Distributed Economic Dispatch Control Method in Power Systems. *IEEE Transactions on Smart Grid*, *10*(1), 941–954. https://doi.org/10.1109/TSG.2017.2756041

Li, Y., & Li, Y. W. (2009). Virtual frequency-voltage frame control of inverter based low voltage microgrid. *2009 IEEE Electrical Power & Energy Conference (EPEC)*, 1–6. https://doi.org/10.1109/EPEC.2009.5420973

Li, Y., & Gu, Y. (2024). Simplus grid tool [Accessed: 2024-06-26].

Li, Z., Zhang, J., Cheng, Z., Si, J., Wang, Y., & Wang, X. (2024). Distributed cooperative grid synchronization strategy for multiple parallel grid-supporting inverters in AC microgrid. *International Journal of Electrical Power & Energy Systems*, *155*, 109624. https://doi.org/10.1016/j.ijepes.2023.109624

Liu, C., Wang, X., & Zhang, H. (2024). Adaptive event-triggered H∞ consensus secondary control for islanded microgrids under multiple time delays. *Electric Power Systems Research*, *232*, 110367. https://doi.org/10.1016/j.epsr.2024.110367

Liu, T., Liu, Z., Liu, J., & Liu, Z. (2016). Virtual impedance-based active damping for LCL resonance in grid-connected voltage source inverters with grid current feedback. *2016 IEEE Energy Conversion Congress and Exposition (ECCE)*, 1–8. https://doi.org/10.1109/ECCE.2016.7855557

Liu, Y., Fan, R., & Terzija, V. (2016). Power system restoration: A literature review from 2006 to 2016. *Journal of Modern Power Systems and Clean Energy*, *4*(3), 332–341. https://doi.org/10.1007/s40565-016-0219-2

Lobato Miguélez, E., Egido Cortés, I., Rouco Rodríguez, L., & López Camino, G. (2008). An overview of ancillary services in Spain. *Electric Power Systems Research*, *78*(3), 515–523. https://doi.org/10.1016/j.epsr.2007.03.009

Lopes, J. A. P., Madureira, A., Gil, N., & Resende, F. (2013, December). Operation of Multi-Microgrids. In N. Hatziargyriou (Ed.), *Microgrids* (pp. 165–205). John Wiley; Sons Ltd. https://doi.org/10.1002/9781118720677.ch05

Manitoba Hydro International Ltd. (2024). *PSCAD* (Version V5.0.2) [Last accessed: 27-Oct-2024]. https://www.pscad.com

Manshang, W., Tianwen, Z., Laijun, C., Sicheng, D., Shengwei, M., & Zhengming, L. (2018). Active and Reactive Power Sharing under Time Delays in Autonomous Microgrid Using Consensus-Based Distributed Control. *2018 International Conference on Power System Technology (POWERCON)*, 1852–1857. https://doi.org/10.1109/POWERCON.2018.8602039

Marnay, C., Chatzivasileiadis, S., Abbey, C., Iravani, R., Joos, G., Lombardi, P., Mancarella, P., & von Appen, J. (2015). Microgrid Evolution Roadmap. *2015 International Symposium on Smart Electric Distribution Systems and Technologies (EDST)*, 139–144. https://doi.org/10.1109/SEDST.2015.7315197

MathWorks. (2024). MATLAB (24.1.0.2689473 (R2024a) Update 6 version). https://www.mathworks.com

MATLAB. (2019). *Version 9.7.0 (r2019b)*. The MathWorks Inc.

McKeever, P., De Din, E., Sadu, A., & Monti, A. (2017). MAS for automated black start of multi-microgrids. *2017 IEEE International Conference on Smart Grid Communications (SmartGridComm)*, 32–37. https://doi.org/10.1109/SmartGridComm.2017.8340678

Meng, L., Dragicevic, T., Roldán-Pérez, J., Vasquez, J. C., & Guerrero, J. M. (2016). Modeling and Sensitivity Study of Consensus Algorithm-Based Distributed Hierarchical Control for DC Microgrids. *IEEE Transactions on Smart Grid*, *7*(3), 1504–1515. https://doi.org/10.1109/TSG.2015.2422714

Milano, F. (2005). An open source power system analysis toolbox. *IEEE Transactions on Power Systems*, *20*(3), 1199–1206. https://doi.org/10.1109/TPWRS.2005.851911

Milano, F., & Anghel, M. (2012). Impact of Time Delays on Power System Stability. *IEEE Transactions on Circuits and Systems I: Regular Papers*, *59*(4), 889–900. https://doi.org/10.1109/TCSI.2011.2169744

Milano, F. (2010). *Power system modelling and scripting*. Springer.

Mirz, M., Dinkelbach, J., & Vogel, S. (2024). *DPsim* (Version 1.1.1) [Last accessed: 28-Oct-2024]. https://dpsim.fein-aachen.org/docs/

Mohammadi, K., Azizi, E., Choi, J., Hamidi-Beheshti, M.-T., Bidram, A., & Bolouki, S. (2021). Asynchronous Periodic Distributed Event-Triggered Voltage and Frequency Control of Microgrids. *IEEE Transactions on Power Systems*, *36*(5), 4524–4538. https://doi.org/10.1109/TPWRS.2021.3059158

Monteiro, V., Pinto, J. G., Exposto, B., & Afonso, J. L. (2015). Comprehensive comparison of a current-source and a voltage-source converter for three-phase EV fast battery chargers [ISSN: 2166-9546]. *2015 9th International Conference on Compatibility and Power Electronics (CPE)*, 173–178. https://doi.org/10.1109/CPE.2015.7231068

Moore, B. (1981). Principal component analysis in linear systems: Controllability, observability, and model reduction. *IEEE Transactions on Automatic Control*, *AC-26*(1), 17–32. https://doi.org/10.1109/TAC.1981.1102568

Moreira, C. L., Resende, F. O., & Lopes, J. A. P. (2007). Using Low Voltage MicroGrids for Service Restoration. *IEEE Transactions on Power Systems*, *22*(1), 395–403. https://doi.org/10.1109/TPWRS.2006.888989

Morin, G. (1987). Service Restoration Following a Major Failure on the Hydro-Québec Power System. *IEEE Transactions on Power Delivery*, *2*(2), 454–463. https://doi.org/10.1109/TPWRD.1987.4308129

Naval, N., & Yusta, J. M. (2021). Virtual power plant models and electricity markets - A review. *Renewable and Sustainable Energy Reviews*, *149*, 111393. https://doi.org/10.1016/j.rser.2021.111393

Noris, L., Rueda, J., Rakhshani, E., & Korai, A. W. (2019). Power System Black-Start and Restoration with High Share of Power-Electronic Converters. *2019 IEEE Power & Energy Society General Meeting (PESGM)*, 1–5. https://doi.org/10.1109/PESGM40551.2019.8973828

Olfati-Saber, R., & Murray, R. (2004). Consensus Problems in Networks of Agents With Switching Topology and Time-Delays. *IEEE Transactions on Automatic Control*, *49*(9), 1520–1533. https://doi.org/10.1109/TAC.2004.834113

Olfati-Saber, R., Fax, J. A., & Murray, R. M. (2007). Consensus and Cooperation in Networked Multi-Agent Systems. *Proceedings of the IEEE*, *95*(1), 215–233. https://doi.org/10.1109/JPROC.2006.887293

O'Malley, M., Bowen, T., Bialek, J., Braun, M., Cutululis, N., Green, T., Hansen, A., Kennedy, E., Kiviluoma, J., Leslie, J., Li, Y., Matevosyan, J., McDowell, J., Miller, N., Pettingill, P., Ramasubramanian, D., Robinson, L., Schaefer, C., & Ward, J. (2021). Enabling power system transformation globally: A system operator research agenda for bulk power system issues. *IEEE Power and Energy Magazine*, *19*(6), 45–55. https://doi.org/10.1109/MPE.2021.3104078

OPAL-RT. (2024). *Real-time simulation solutions* [Last accessed: 27-Oct-2024]. https://www.opal-rt.com/

OPAL-RT TECHNOLOGIES, Inc. (2024). HYPERSIM (2024.3.0 version). https://www.opal-rt.com/systems-hypersim/

OpenAI. (2024, October). ChatGPT (Oct 30 version) [Large language model]. https://chatgpt.com/

Pagnani, D., Blaabjerg, F., Bak, C. L., Faria da Silva, F. M., Kocewiak, Ł. H., & Hjerrild, J. (2020). Offshore Wind Farm Black Start Service Integration: Review and Outlook of Ongoing Research. *Energies*, *13*(23), 6286. https://doi.org/10.3390/en13236286

Pagola, F. L. (2016). *Control Systems*. Universidad Pontificia Comillas.

Pagola, F., Perez-Arriaga, I., & Verghese, G. (1989). On sensitivities, residues and participations: Applications to oscillatory stability analysis and control. *IEEE Transactions on Power Systems*, *4*(1), 278–285. https://doi.org/10.1109/59.32489

Paquette, A. D., & Divan, D. M. (2015). Virtual Impedance Current Limiting for Inverters in Microgrids With Synchronous Generators. *IEEE Transactions on Industry Applications*, *51*(2), 1630–1638. https://doi.org/10.1109/TIA.2014.2345877

Parang, B., Mohammadi, M., & Arefi, M. M. (2019). Residualisation-based model order reduction in power networks with penetration of photovoltaic re-

sources. *IET Generation, Transmission & Distribution*, *13*(13), 2619–2626. https://doi.org/10.1049/iet-gtd.2018.6172

Pardo, R. A., & López-Lezama, J. M. (2020). Revisión de metodologías de arranque óptimo de generación para el restablecimiento de sistemas de potencia considerando fuentes de energía convencionales y renovables no convencionales. *Revista Ingenierías Universidad de Medellín*, *19*(36), 187–204. https://doi.org/10.22395/rium.v19n36a9

Park, R. H. (1929). Two-reaction theory of synchronous machines generalized method of analysis-part I. *Transactions of the American Institute of Electrical Engineers*, *48*(3), 716–727. https://doi.org/10.1109/T-AIEE.1929.5055275

Patsakis, G., Rajan, D., Aravena, I., Rios, J., & Oren, S. (2018). Optimal Black Start Allocation for Power System Restoration. *IEEE Transactions on Power Systems*, *33*(6), 6766–6776. https://doi.org/10.1109/TPWRS.2018.2839610

Pérez-Arriaga, I., Verghese, G., & Schweppe, F. (1982). Selective Modal Analysis with Applications to Electric Power Systems, PART I: Heuristic Introduction. *IEEE Transactions on Power Apparatus and Systems*, *PAS-101*(9), 3117–3125. https://doi.org/10.1109/TPAS.1982.317524

Poolla, B. K., Hota, A. R., Bolognani, S., Callaway, D. S., & Cherukuri, A. (2021). Wasserstein Distributionally Robust Look-Ahead Economic Dispatch. *IEEE Transactions on Power Systems*, *36*(3), 2010–2022. https://doi.org/10.1109/TPWRS.2020.3034488

Prodanovic, M., Rodríguez-Cabero, A., Jiménez-Carrizosa, M., & Roldán-Pérez, J. (2017). A rapid prototyping environment for DC and AC microgrids: Smart energy integration Lab (SEIL). *2017 IEEE Second International Conference on DC Microgrids (ICDCM)*, 421–427. https://doi.org/10.1109/ICDCM.2017.8001079

PSI Neplan AG. (2024). *NEPLAN* (Version 360) [Last accessed: 27-Oct-2024]. https://neplan.ch/en-products/

PyACDCPF [Last Accessed: 26-Jun.-2024]. (2016).

Qoria, T., Gruson, F., Colas, F., Kestelyn, X., & Guillaud, X. (2020). Analysis of the coupling between the outer and inner control loops of a Grid-forming Voltage Source Converter. *2020 22nd European Conference on Power Electronics and Applications (EPE'20 ECCE Europe)*, P.1–P.10. https://doi.org/10.23919/EPE20ECCEEurope43536.2020.9215688

Qoria, T., Cossart, Q., Li, C., Guillaud, X., Colas, F., Gruson, F., & Kestelyn, X. (2018, December). *WP3 - Control and Operation of a Grid with 100% Converter-Based Devices. Deliverable 3.2: Local control and simulation tools for large transmission systems* (tech. rep.). MIGRATE project. Retrieved May 5, 2022, from https://www.h2020-migrate.eu/downloads.html

Rai, I., & C, S. (2025). Microgrid and grid synchronization: A critical analysis of challenges and opportunities. *Electric Power Systems Research*, *242*, 111434. https://doi.org/10.1016/j.epsr.2025.111434

Rajabdorri, M., Kazemtabrizi, B., Troffaes, M., Sigrist, L., & Lobato, E. (2023). Inclusion of frequency nadir constraint in the unit commitment problem of

small power systems using machine learning. *Sustainable Energy, Grids and Networks*, *36*, 101161. https://doi.org/10.1016/j.segan.2023.101161

Ramirez, A., Mehrizi-Sani, A., Hussein, D., Matar, M., Abdel-Rahman, M., Jesus Chavez, J., Davoudi, A., & Kamalasadan, S. (2016). Application of Balanced Realizations for Model-Order Reduction of Dynamic Power System Equivalents. *IEEE Transactions on Power Delivery*, *31*(5), 2304–2312. https://doi.org/10.1109/TPWRD.2015.2496498

Rasheduzzaman, M., Mueller, J. A., & Kimball, J. W. (2015). Reduced-Order Small-Signal Model of Microgrid Systems. *IEEE Transactions on Sustainable Energy*, *6*(4), 1292–1305. https://doi.org/10.1109/TSTE.2015.2433177

Roald, L. A., Pozo, D., Papavasiliou, A., Molzahn, D. K., Kazempour, J., & Conejo, A. (2023). Power systems optimization under uncertainty: A review of methods and applications. *Electric Power Systems Research*, *214*, 108725. https://doi.org/10.1016/j.epsr.2022.108725

Rodríguez-Cabero, A., Roldán-Pérez, J., & Prodanovic, M. (2020). Virtual impedance design considerations for virtual synchronous machines in weak grids. *IEEE Journal of Emerging and Selected Topics in Power Electronics*, *8*(2), 1477–1489. https://doi.org/10.1109/JESTPE.2019.2912071

Rokrok, E., Shafie-khah, M., Siano, P., & Catalão, J. (2017). A Decentralized Multi-Agent-Based Approach for Low Voltage Microgrid Restoration. *Energies*, *10*(10), 1491. https://doi.org/10.3390/en10101491

Roldán-Pérez, J., Bueno, E. J., Peña-Alzola, R., & Rodríguez-Cabero, A. (2018). All-pass-filter-based active damping for vscs with lcl filters connected to weak grids. *IEEE Transactions on Power Electronics*, *33*(11), 9890–9901.

Rouco, L., & Zamora, J. (2006). Dynamic patterns and model order reduction in small-signal models of doubly fed induction generators for wind power applications. *2006 IEEE Power Engineering Society General Meeting*, pp. 1–8. https://doi.org/10.1109/PES.2006.1709515

Sauer, P. W., & Pai, M. A. (1998). *Power system dynamics and stability*. Prentice Hall.

Sekhavatmanesh, H., & Cherkaoui, R. (2019). Distribution Network Restoration in a Multiagent Framework Using a Convex OPF Model. *IEEE Transactions on Smart Grid*, *10*(3), 2618–2628. https://doi.org/10.1109/TSG.2018.2805922

Serrano-Jiménez, D., Unamuno, E., Gil-de-Muro, A., Aragon, D., Ceballos, S., & Barrena, J. (2022). Stability tool for electric power systems with a high penetration of electronic power converters. *Electric Power Systems Research*, *210*, 108115. https://doi.org/https://doi.org/10.1016/j.epsr.2022.108115

Shah, S., Sun, H., Nikovski, D., & Zhang, J. (2018). Consensus-based Synchronization of Microgrids at Multiple Points of Interconnection. *2018 IEEE Power & Energy Society General Meeting (PESGM)*, 1–5. https://doi.org/10.1109/PESGM.2018.8586167

Shahab, M. A., Mozafari, B., Soleymani, S., Dehkordi, N. M., Shourkaei, H. M., & Guerrero, J. M. (2019). Stochastic Consensus-Based Control of uGs With Communication Delays and Noises. *IEEE Transactions on Power Systems*, *34*(5), 3573–3581. https://doi.org/10.1109/TPWRS.2019.2905433

Sharma, A., Srinivasan, D., & Trivedi, A. (2018). A Decentralized Multi-Agent Approach for Service Restoration in Uncertain Environment. *IEEE Transactions on Smart Grid*, *9*(4), 3394–3405. https://doi.org/10.1109/TSG.2016.2631639

Shu, D., Xie, X., Dinavahi, V., Zhang, C., Ye, X., & Jiang, Q. (2018). Dynamic phasor based interface model for emt and transient stability hybrid simulations. *IEEE Transactions on Power Systems*, *33*(4), 3930–3939. https://doi.org/10.1109/TPWRS.2017.2766269

Siemens PTI. (2024). *PSS/E* (Version 35-6-3) [Last accessed: 27-Oct-2024]. https://www.siemens.com/global/en/products/energy/grid-software/planning/pss-software/pss-e.html

Simpson-Porco, J. W., Dörfler, F., & Bullo, F. (2013). Synchronization and power sharing for droop-controlled inverters in islanded microgrids. *Automatica*, *49*(9), 2603–2611. https://doi.org/10.1016/j.automatica.2013.05.018

Simpson-Porco, J. W., Shafiee, Q., Dorfler, F., Vasquez, J. C., Guerrero, J. M., & Bullo, F. (2015). Secondary Frequency and Voltage Control of Islanded Microgrids via Distributed Averaging. *IEEE Transactions on Industrial Electronics*, *62*(11), 7025–7038. https://doi.org/10.1109/TIE.2015.2436879

Singhal, A., Vu, T. L., & Du, W. (2021, October). Coordinated Frequency and Voltage Regulation of Grid-Following and Grid-Forming Inverters [arXiv:2012.06685 [cs, eess]]. Retrieved August 25, 2022, from http://arxiv.org/abs/2012.06685

Sun, Q., Han, R., Zhang, H., Zhou, J., & Guerrero, J. M. (2015). A Multiagent-Based Consensus Algorithm for Distributed Coordinated Control of Distributed Generators in the Energy Internet. *IEEE Transactions on Smart Grid*, *6*(6), 3006–3019. https://doi.org/10.1109/TSG.2015.2412779

Sun, W., Liu, C.-C., & Liu, S. (2011). Black start capability assessment in power system restoration. *2011 IEEE Power and Energy Society General Meeting*, 1–7. https://doi.org/10.1109/PES.2011.6039752

Sun, Y., Hou, X., Yang, J., Han, H., Su, M., & Guerrero, J. M. (2017). New Perspectives on Droop Control in AC Microgrid. *IEEE Transactions on Industrial Electronics*, *64*(7), 5741–5745. https://doi.org/10.1109/TIE.2017.2677328

Sun, Y., Zhong, C., Hou, X., Yang, J., Han, H., & Guerrero, J. M. (2017). Distributed cooperative synchronization strategy for multi-bus microgrids. *International Journal of Electrical Power & Energy Systems*, *86*, 18–28. https://doi.org/10.1016/j.ijepes.2016.09.002

Susanto, J., Shahnia, F., Ghosh, A., & Rajakaruna, S. (2014). Interconnected microgrids via back-to-back converters for dynamic frequency support. *2014 Australasian Universities Power Engineering Conference (AUPEC)*, 1–6. https://doi.org/10.1109/AUPEC.2014.6966616

Tabernero, J., & Rouco, L. (2007). Dynamic Patterns in Small-signal Models of Multipole Synchronous Generators for Wind Power Applications. *2007 IEEE Lausanne Power Tech*, 225–231. https://doi.org/10.1109/PCT.2007.4538321

Tomás-Martín, A., García-Cerrada, A., Sigrist, L., Yagüe, S. J., Miguel, D. R., & Martín-Utrilla, F.-D. (2023). Re-synchronisation of a Microgrid to the Main Grid Using Multi-Agent Secondary Control. *2023 IEEE Belgrade PowerTech*, 1–6. https://doi.org/10.1109/PowerTech55446.2023.10202680

Tomás-Martín, A., García-Cerrada, A., Sigrist, L., Yagüe, S. J., & Suárez-Porras, J. (2023a). State relevance and modal analysis in electrical microgrids with high penetration of electronic generation. *International Journal of Electrical Power & Energy Systems*, *147*, 108876. https://doi.org/10.1016/j.ijepes.2022.108876

Tomás-Martín, A., García-Cerrada, A., Sigrist, L., Yagüe, S. J., & Suárez-Porras, J. (2023b). State relevance and modal analysis in electrical microgrids with 100% grid-forming converters [Available on demand.]. *XXX Seminario Anual de Automática, Electrónica industrial e Instrumentación - SAAEI 2023*. Retrieved December 19, 2024, from https://www.iit.comillas.edu/publicacion/congreso/en/12318/

Tomás-Martín, A., Kazemtabrizi, B., García-Cerrada, A., Sigrist, L., & Bueno, E. J. (2025). Fully decentralised consensus-based hierarchical control of a hybrid AC-DC microgrid [Preprint available on demand.].

Tomás-Martín, A., Roldán-Pérez, J., Jankovic, N., Yagüe, S. J., García- Cerrada, A., & Sigrist, L. (2025). Performance of multi-agent secondary control for reconnecting a microgrid of grid-forming converters to the main grid [Preprint available on demand.].

Tomás-Martín, A., Roldán-Pérez, J., Jankovic, N., Yagüe, S. J., García-Cerrada, A., & Sigrist, L. (2024). Control secundario multi-agente para reconectar una microrred de convertidores formadores de red con la red principal [Multi-agent secondary control to reconnect a microgrid of grid-forming converters to the main grid] [Available on demand.]. *XXXI Seminario Anual de Automática, Electrónica industrial e Instrumentación - SAAEI 2024*. Retrieved December 19, 2024, from https://www.iit.comillas.edu/publicacion/congreso/en/12476/

Tomás-Martín, A., Zuluaga-Ríos, C. D., Suárez-Porras, J., Kazemtabrizi, B., García-Aguilar, J., Sigrist, L., & García-Cerrada, A. (2025). A vector-based flexible-complexity tool for simulation and small-signal analysis of hybrid AC/DC power systems. *Sustainable Energy, Grids and Networks*, *43*, 101817. https://doi.org/10.1016/j.segan.2025.101817

Van Ness, J., Boyle, J., & Imad, F. (1965). Sensitivities of large, multiple-loop control systems. *IEEE Transactions on Automatic Control*, *10*(3), 308–315. https://doi.org/10.1109/TAC.1965.1098163

Verghese, G., Pérez-Arriaga, I., & Schweppe, F. (1982). Selective Modal Analysis With Applications to Electric Power Systems, Part II: The Dynamic Stability Problem. *IEEE Transactions on Power Apparatus and Systems*, *PAS-101*(9), 3126–3134. https://doi.org/10.1109/TPAS.1982.317525

Wang, X., & Blaabjerg, F. (2019). Harmonic stability in power electronic-based power systems: Concept, modeling, and analysis. *IEEE Trans. Smart Grid.*, *10*(3), 2858–2870. https://doi.org/10.1109/TSG.2018.2812712

Wang, X., Li, Y. W., Blaabjerg, F., & Loh, P. C. (2015a). Virtual-impedance-based control for voltage-source and current-source converters. *IEEE Transactions on Power Electronics*, *30*(12), 7019–7037. https://doi.org/10.1109/TPEL.2014.2382565

Wang, X., Li, Y. W., Blaabjerg, F., & Loh, P. C. (2015b). Virtual-Impedance-Based Control for Voltage-Source and Current-Source Converters. *IEEE Transactions on Power Electronics*, *30*(12), 7019–7037. https://doi.org/10.1109/TPEL.2014.2382565

Wong, Y. C. C., Lim, C. S., Cruden, A., Rotaru, M. D., & Ray, P. K. (2021). A Consensus-Based Adaptive Virtual Output Impedance Control Scheme for Reactive Power Sharing in Radial Microgrids. *IEEE Transactions on Industry Applications*, *57*(1), 784–794. https://doi.org/10.1109/TIA.2020.3031884

Wood, A. J., Wollenberg, B. F., & Sheblé, G. B. (2013, November). *Power Generation, Operation, and Control* [Google-Books-ID: JafyAAAAQBAJ]. John Wiley & Sons.

Xiong, M., Wang, B., Vaidhynathan, D., Maack, J., Reynolds, M. J., Hoke, A., Sun, K., & Tan, J. (2024). ParaEMT: An open source, parallelizable, and HPC-compatible EMT simulator for large-scale IBR-rich power grids. *IEEE Transactions on Power Delivery*, *39*(2), 911–921. https://doi.org/10.1109/TPWRD.2023.3342715

Xue, X., Fang, J., Ai, X., Cui, S., Jiang, Y., Yao, W., & Wen, J. (2024). A Fully Distributed ADP Algorithm for Real-Time Economic Dispatch of Microgrid. *IEEE Transactions on Smart Grid*, *15*(1), 513–528. https://doi.org/10.1109/TSG.2023.3273418

Yague, S. J., García-Cerrada, A., & Farré, P. P. (2023). Comparison between Modal Analysis and Impedance-Based Methods for Analysing Stability of Unbalanced Microgrids with Grid-Forming Electronic Power Converters. *Journal of Modern Power Systems and Clean Energy*, 1–13. https://doi.org/10.35833/MPCE.2022.000669

Yagüe Yagüe, S. J. (2024, April). *Stability Analysis of Unbalanced Microgrids with Grid-Forming and Grid-Following Electronic Power Converters* [Ph.D. Thesis]. Universitat Ramon Llull [Accepted: 2024-04-19T07:04:02Z Publication Title: TDX (Tesis Doctorals en Xarxa)]. Retrieved July 8, 2024, from https://www.tdx.cat/handle/10803/690653

Yang, C., Zheng, T., Bu, M., Li, P., & Guerrero, J. M. (2024). Distributed Model-Free Adaptive Control Strategy for Hybrid AC/DC Microgrid With Event-Triggered Mechanism. *IEEE Transactions on Industrial Electronics*, *71*(8), 9077–9086. https://doi.org/10.1109/TIE.2023.3331158

Yang, S., Tan, S., & Xu, J.-X. (2013). Consensus Based Approach for Economic Dispatch Problem in a Smart Grid. *IEEE Transactions on Power Systems*, *28*(4), 4416–4426. https://doi.org/10.1109/TPWRS.2013.2271640

Yao, F., Chau, T. K., Zhang, X., Iu, H. H.-C., & Fernando, T. (2020). An Integrated Transmission Expansion and Sectionalizing-Based Black Start Allocation of BESS Planning Strategy for Enhanced Power Grid Resilience. *IEEE Access*, *8*, 148968–148979. https://doi.org/10.1109/ACCESS.2020.3014341

Yazdani, A., & Iravani, M. R. (2010). *Voltage- Sourced Converters in Power Systems: Modeling, Control, and Applications*. Wiley-IEEE Press. https://doi.org/10.1002/9780470551578

Yazdani, A., & Iravani, R. (2010). Grid-imposed frequency VSC system: Control in dq-frame. In *Voltage-sourced converters in power systems: Modeling, control, and applications* (pp. 160–203). John Wiley; Sons, Ltd.

Yi, Z., Xu, Y., Gu, W., & Fei, Z. (2021). Distributed Model Predictive Control Based Secondary Frequency Regulation for a Microgrid With Massive Distributed Resources. *IEEE Transactions on Sustainable Energy*, *12*(2), 1078–1089. https://doi.org/10.1109/TSTE.2020.3033320

Yuan, G., Li, Z., Zheng, Y., Su, F., He, Z., & Yu, C. (2022). A Review on Decision-making Methods for Restoration Control of Transmission and Distribution Systems. *Journal of Physics: Conference Series*, *2166*(1), 012044. https://doi.org/10.1088/1742-6596/2166/1/012044

Zhang, J., Sun, B., & Zhao, D. (2023). A Novel Event-Triggered Secondary Control Strategy for Distributed Generalized Droop Control in Microgrid Considering Time Delay. *IEEE Transactions on Power Electronics*, *38*(5), 5963–5978. https://doi.org/10.1109/TPEL.2023.3241063

Zhang, L., & Sun, L. (2011). Multi-Objective Service Restoration for Blackout of Distribution System with Distributed Generators based on Multi-Agent GA. *Energy Procedia*, *12*, 253–262. https://doi.org/10.1016/j.egypro.2011.10.035

Zhang, Y., Mohammadpour Shotorbani, A., Wang, L., & Mohammadi-Ivatloo, B. (2021). Enhanced PI control and adaptive gain tuning schemes for distributed secondary control of an islanded microgrid. *IET Renewable Power Generation*, *15*(4), 854–864. https://doi.org/10.1049/rpg2.12074

Zhang, Z., & Chow, M.-Y. (2011). Incremental cost consensus algorithm in a smart grid environment [ISSN: 1944-9925]. *2011 IEEE Power and Energy Society General Meeting*, 1–6. https://doi.org/10.1109/PES.2011.6039422

Zhao, C., Duan, X., & Shi, Y. (2020). Analysis of Consensus-Based Economic Dispatch Algorithm Under Time Delays. *IEEE Transactions on Systems, Man, and Cybernetics: Systems*, *50*(8), 2978–2988. https://doi.org/10.1109/TSMC.2018.2840821

Zhao, J., Zhang, Q., Liu, Z., & Wu, X. (2021). A Distributed Black-Start Optimization Method for Global Transmission and Distribution Network. *IEEE Transactions on Power Systems*, *36*(5), 4471–4481. https://doi.org/10.1109/TPWRS.2021.3056096

Zhao, K., Xiao, F., Li, S., Wang, X., & Wei, B. (2024). Distributed Secondary Control of Microgrids via a Time-Event Switching Triggered Mechanism. *IEEE*

Control Systems Letters, *8*, 2463–2468. https://doi.org/10.1109/LCSYS.2024.3491416

Zheng, Q., Gao, F., Li, Y., Zhu, Y., & Gu, Y. (2024). Equivalence of impedance participation analysis methods for hybrid ac/dc power systems. *IEEE Transactions on Power Systems*, *39*(2), 3560–3574. https://doi.org/10.1109/TPWRS.2023.3288018

Zhou, J., Kim, S., Zhang, H., Sun, Q., & Han, R. (2018). Consensus-Based Distributed Control for Accurate Reactive, Harmonic, and Imbalance Power Sharing in Microgrids. *IEEE Transactions on Smart Grid*, *9*(4), 2453–2467. https://doi.org/10.1109/TSG.2016.2613143

Zhu, Y., Zhou, Y., Wang, Z., Zhou, C., & Gao, B. (2022). A terminal distribution network black-start optimization method based on pruning algorithm considering distributed generators. *Energy Reports*, *8*, 237–244. https://doi.org/10.1016/j.egyr.2021.11.040

Zimmerman, R. D., Murillo-Sánchez, C. E., & Thomas, R. J. (2011). MATPOWER: Steady-State Operations, Planning, and Analysis Tools for Power Systems Research and Education. *IEEE Transactions on Power Systems*, *26*(1), 12–19. https://doi.org/10.1109/TPWRS.2010.2051168

This appendix presents VFlexP, an open-source tool for the simulation and analysis of hybrid AC/DC power systems using MATLAB-Simulink. VFlexP is the tool used to model, analyse and simulate all the case studies included in this thesis. Unlike other tools, VFlexP allows flexible device representation without simplifications and supports easy integration of new models. It includes a module for analysing the relevance of state variables to aid model simplification and ensures efficient initialisation from power-flow analysis to avoid prolonged initial transients. Its user-friendly interface groups similar power system elements, making it suitable for detailed analysis of large hybrid systems. This tool has been developed in collaboration with Carlos-David Zuluaga Ríos, Jorge Suárez Porras, Behzad Kazemtabrizi and Javier García Aguilar. This appendix has been published in Tomás-Martín, Zuluaga-Ríos, et al. (2025).

A A Vector-Based Flexible-Complexity Power System Tool for Simulation, Static and Modal Analysis of Hybrid AC/DC Power Systems

A.1 Introduction

As many countries transition towards low-carbon or net zero-carbon energy systems, renewable energy sources (RESs) are playing an increasingly important role in the energy mix, transforming the way power systems are operated. RESs present unique new challenges: they are often not readily dispatchable; require inverter-based interfaces with the grid (i.e, inverter-base resources or IBRs); and are typically distributed across the grid as distributed energy resources (DERs) (O'Malley et al., 2021).

In response to these challenges, hybrid AC/DC systems have become increasingly important for integrating diverse energy sources into the grid, thanks to the advances in electronic power converters. The combination of AC and DC technologies should improve grid flexibility, stability, and resilience, facilitating a smoother

transition to renewable-dominated power systems and supporting long-term sustainability.

Conventional tools for the analysis of AC electric power systems address one or more of the following aspects (Milano, 2010):

- Static analysis, mainly power flow (PF) and optimal power flow (OPF), that determines the system voltages, currents, and power flows under stable steady-state operating conditions.
- Dynamic analysis consisting of time-domain (TD) simulation and/or small-signal analysis (SSA).

There are two distinctive approaches among time-domain simulators. On the one hand, Transient Stability (TS) Simulators, also called Electromechanical (EM) Simulators, study the effects of disturbances on synchronous generator dynamics. They neglect the dynamics of the electrical grid (which is assumed to be in a quasi-steady state) because they are very fast and generally well-damped and focus on the dynamics of electromechanical components with often lightly-damped low-frequency oscillations. These simulators provide phasor information for voltages and currents and this is why they are often called RMS simulators. However, many references highlight the limitation of RMS models when studying fast transients (see Chow J.H. (1982) and IEEE-PES (2023)), and propose the use of Electromagnetic Transient (EMT) simulators with detailed models of all components. Unfortunately, this modelling can be computationally intensive (Xiong et al., 2024).

Finally, SSA is a method for evaluating system stability and dynamic response to small disturbances by linearising the system around an operating point. This tool is often used by engineers to design controllers to tackle oscillations in power systems (Kundur et al., 1994).

Gradually, most analysis tools have incorporated, in one way or another, hybrid AC/DC systems. For example, static analysis can be carried out with MATPOWER (Zimmerman et al., 2011) and its extension FUBM (Alvarez-Bustos et al., 2021), MatACDC (Beerten & Belmans, 2015), and PyACDC (2016). In addition, EMT and/or EM simulation is possible with PowerFactory (DIgSILENT, 2024), PSCAD (Manitoba Hydro International Ltd., 2024), ETAP (ETAP-Operation Tecnology, Inc., 2024) and PSS/E (Siemens PTI, 2024). SSA can be carried out with PowerFactory, CSTEP (Serrano-Jiménez et al., 2022) and DSATools (2024). The capabilities of several of these important tools have been summarised in Table A.1 indicating whether they are commercial $\mathbb{P}$, open-source $\mathbb{O}$, or toolboxes of MATLAB-Simulink, which is a commercial software package $\mathbb{OM}$.

Nowadays, IBRs (or, in other words, fast-acting electronics-based generators) are becoming increasingly present in electric power systems, and the question of whether the time-scale separation between generators and the grid can be taken for granted may not always have a unique answer (Hatziargyriou et al., 2021). However, none of the above-mentioned software tools addresses this question

Table A.1: Overview of simulation and analysis tools for hybrid AC/DC power systems. In License: 𝕆 means open-source, ℙ means commercial, and 𝕆𝕄 means open-source tools that rely on MATLAB and/or Simulink.

Tool	PF	OPF	SSA	SR	License	EMT	RMS
DSATools (2024)	✓		✓		ℙ		
ETAP (ETAP-Operation Tecnology, Inc., 2024)	✓	✓			ℙ	✓	✓
Neplan (PSI Neplan AG, 2024)	✓	✓	✓		ℙ	✓	✓
PowerFactory (DIgSILENT, 2024)	✓	✓	✓		ℙ	✓	✓
PSCAD (Shu et al., 2018)	✓				ℙ	✓	
PSS/E (Siemens PTI, 2024)	✓	✓	✓		ℙ		✓
Smart Flow (EUROSTAG, 2020)	✓	✓	✓		ℙ		✓
ANDES (Cui, Li, & Tomsovic, 2021)	✓		✓		𝕆	✓	
DPsim (Mirz, M., Dinkelbach, J., & Vogel, S., 2024)	✓				𝕆	✓	✓
PowerSimulationsDynamics.jl (Lara, Henriquez-Auba, Bossart, Callaway, & Barrows, 2024)	✓		✓		𝕆	✓	
Pypower and PyACDC (2016)	✓	✓			𝕆		
CSTEP (Serrano-Jiménez et al., 2022)			✓		𝕆𝕄	✓	✓
MATPower (Zimmerman, Murillo-Sánchez, & Thomas, 2011) and MATACDC (Beerten & Belmans, 2015)	✓	✓			𝕆𝕄		
MATLAB/Simulink and MatDyn (Cole & Belmans, 2011)					𝕆𝕄	✓	✓
PSAT (Milano, 2005)	✓		✓		𝕆𝕄		✓
SimplusGT (Y. Li & Gu, 2024)	✓		✓		𝕆𝕄	✓	
SSMD (Institute for Automation of Complex Power Systems, EONERC, 2018)			✓		𝕆𝕄		
VFlexP	✓	✓	✓	✓	𝕆𝕄	✓	✓

directly. This new scenario underscores the need for more flexible and multi-purpose tools.

This appendix presents VFlexP, an open-source tool for hybrid AC/DC power system analysis and simulation built upon MATLAB/Simulink. Component data are fed into the system description with a file similar to the one used in MATPOWER, and the electrical system is described using a synchronously rotating d-q reference frame with Simulink dynamic blocks. Only elementary blocks such as integrators, sums, products, gains, and trigonometric functions are used for device-model building to ease linear analysis. Static analysis of the electrical system, such as PF and OPF, can be performed using a modified version of MATPOWER, as outlined by Alvarez-Bustos et al. (2021), enabling support for hybrid AC/DC systems. Additionally, the proposed tool supports SSA for hybrid systems with a high penetration of IBRs, facilitating deep system insights. As part of this analysis, it also quantifies the state relevance (SR) in the input-output response of dynamic hybrid AC/DC systems and the result can later be used for an informed model reduction. VFlexP accommodates flexible modelling with options for varying levels of detail in the component models. EMT simulation is carried out by default, but the use of simplified component models makes less cumbersome simulation possible. Simulations can be conducted using either the original non-linear model or a linearised approximation, with the flexibility of selecting from a full-order model or several reduced-order approximations.

If compared to other tools included in the literature survey, the following features can be highlighted:

- The static analysis can deal with AC and DC systems seamlessly. Several devices are already available in the library. Some of them are to be connected to the DC side.
- Grid-forming or grid-following control of IBRs and AC/DC interface converters can be represented and used.
- Special care has been taken to derive an accurate calculation of the operating point of the full system starting from the PF results of MATPOWER. This avoids unrealistic and time-consuming transients when starting a simulation and makes it possible for seamless system linearisation.
- Primary and secondary frequency and voltage control layers for generators are included, with flexible architecture choices.
- Most blocks used in the Simulink workspace already have linearised versions in Simulink original library, and MATLAB uses them for reliable linearisation. Those not in the library have been linearised using a Taylor expansion and stored for subsequent use. This avoids calculating the linear approximation by finite differences.

The following contributions of the tool can be highlighted:

- In addition to a full-featured SSA of the system (i.e. calculation of participations, eigenvalue sensitivity, mode shapes, etc.), the user can analyse the relevance of all state variables in the input-output response of the non-linear system. This is an excellent starting point towards the order reduction of the original model.
- Only one block is necessary in Simulink workspace to represent all devices of the same type, and the same level of detail, even if they have different parameters. This is possible thanks to the vectorisation of all the differential equations used, which largely reduces computational effort.
- Each device block can host several levels of detail for a given component. The level to be used, according to a previous relevance analysis, can be easily selected by using a GUI, which implements the concept of flexible complexity and allows improving computation efficiency further.

The rest of the appendix is organised as follows: Section A.2 details the vector-based and flexible-complexity approach of hybrid power systems used in VFlexP. Section A.3 describes how the SSA and simulations are carried out after initialising the system around an operating point. In Section A.4, SSA and simulation results are shown by comparing VFlexP with another simulation tool and considering different grid sizes. Moreover, a reduced-order model of a large power system is validated. Finally, Section A.5 concludes the appendix.

A.2 Vector-based modelling of hybrid power systems with flexible complexity

A.2.1 Scalable and Vectorisable Modelling of power systems

The simplest components included in VFlexP's library are inductors (L-R series connected) and capacitors (C-R parallel connected). The differential equations governing the behaviour of a series RL in a synchronous d-q frame are typically written as follows in per unit (pu):

$$v_d = \frac{1}{\omega_{base}} L \frac{di_d}{dt} - \omega L i_q + R i_d, \tag{A.1}$$

$$v_q = \frac{1}{\omega_{base}} L \frac{di_q}{dt} + \omega L i_d + R i_q, \tag{A.2}$$

where, v_d and v_q are the d- and q-axis voltages, respectively, across the RL element, i_d and i_q are the d- and q-axis currents, respectively, ω_{base} is the base frequency of the system (in rad/s), ω is the angular speed of the synchronously rotating frame, and R and L are the resistance and inductance values of the series RL element, respectively. If v_d and v_q (inputs) are known, differential equations (A.1) and (A.2) can be integrated to calculate i_d and i_q (outputs and state variables).

These differential equations can be easily built using elementary Simulink blocks (integrators, sums, and gains with the parameters), and they can be included in a user-defined block. However, a power system is bound to have a large number of RL elements as part of power lines and/or loads, for example, and including a block for each line in Simulink's workspace is not practical. Instead, a single block can be used to contain all the elements of the system with equations like (A.1) and (A.2), if those equations are vectorised as follows:

$$\mathbf{v_d} = \frac{1}{\omega_{base}}\mathbf{L} \odot \frac{d\mathbf{i_d}}{dt} - \omega\mathbf{L} \odot \mathbf{i_q} + \mathbf{R} \odot \mathbf{i_d}, \tag{A.3}$$

$$\mathbf{v_q} = \frac{1}{\omega_{base}}\mathbf{L} \odot \frac{d\mathbf{i_q}}{dt} + \omega\mathbf{L} \odot \mathbf{i_d} + \mathbf{R} \odot \mathbf{i_q}, \tag{A.4}$$

where voltages, currents and each type of parameter are grouped in vectors (i.e., $\mathbf{v_d}$, $\mathbf{v_d}$, $\mathbf{i_d}$, $\mathbf{i_q}$, $\mathbf{L}$, and $\mathbf{R}$); and multiplications and sums are carried out element-by-element (i.e., Hadamard product $\odot$).

Similarly, all elements included so far in VFlexP (capacitors, loads, synchronous generators, electronic power converters, etc.) can be represented in vector form. Therefore, only one block needs to be included in Simulink's workspace to contain all elements of the same type and model.

A.2.2 Flexible-complexity models for power systems

In traditional power systems, the slow electromechanical dynamics of synchronous generators could be decoupled from the fast response of inductors and capacitors that power lines consist of (Hatziargyriou et al., 2021). Nowadays, this separation is challenged by the fast response of electronic-based generation or IBRs, and it cannot be taken for granted that all fast dynamics (e.g., inductors) can always be simplified. The same type of element may require a different level of detail depending on its position in the power grid or even on the operating point where the study is being carried out. Bearing this in mind, VFlexP has been designed so that each element can be included with a different level of detail. For example, if the dynamics of a number of inductors can be neglected (i.e., $di_{dq}/dt = 0$), equations (A.3) and (A.4) can easily be simplified into vectorise algebraic equations where currents can be calculated if voltages are known. Each block of the library in VFlexP offers multiple suggested levels of detail, allowing easy selection of the appropriate level. However, within the Simulink workspace, each block can only contain elements of the same type represented with identical level of detail. For instance, if M inductors require the description in (A.1) and (A.2), while D inductors can be represented with $di_{dq}/dt = 0$, two separate blocks will be needed in the Simulink workspace: one for M inductors and another for D inductors. Selector and assignment blocks have been used for each component model to select its level of detail, as shown in Figure A.1 for a typical load. In this figure, the load models are organised into two levels of detail (e.g., A and B) to represent different modelling complexities. The voltage ($\mathbf{v}$) and current ($\mathbf{i}$) vectors are structured with

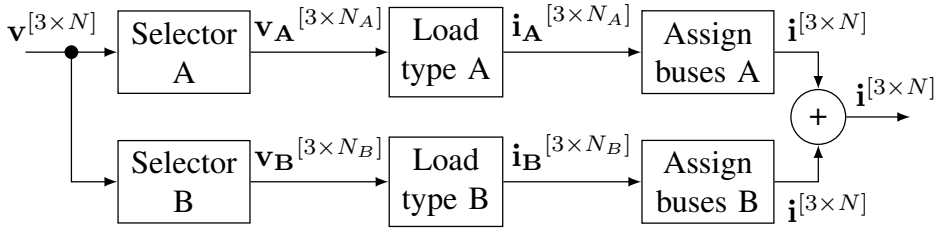

Figure A.1: Loads, selectors and assignments. Array dimensions are indicated in square brackets. All arrays have 3 rows, direct (d), quadrature (q) and homopolar (neglected for the time being) components. N is the number of buses in the system, N_A, N_B and N_C are the number of Loads of type A, B and C in the system, respectively.

three rows, representing the direct (d), quadrature (q), and homopolar components (with the homopolar component neglected in this example). Each load type, such as A and B, is connected to different groups of buses, where N denotes the total number of buses in the system, and N_A and N_B represent the number of buses with load types A and B, respectively. For each load type, voltage and current vectors are labelled according to load type and bus assignment. For instance, the notation $\mathbf{v}_A^{[3\times N_A]}$ and $\mathbf{i}_A^{[3\times N_A]}$ designates the dimensions of the voltage and current array corresponding to type A loads across N_A buses. This notation specifies a clear vector structure that accommodates varying load models across buses. The current vector through each load is calculated from its parameters and voltage vector, depending on the load model. To consolidate the currents of all load types into a single current array $\mathbf{i}^{[3\times N]}$, an assignment block is employed. This block assigns each load type's current at a given bus k to the corresponding position in $\mathbf{i}^{[3\times N]}$. If no load of type A is connected at bus k, the 3 rows of the k-th column of the current array are set to zero; otherwise, it contains the current value for the load connected at that bus. This approach to array assignment applies similarly to other elements in VFlexP, such as generators, transmission lines, and both AC and DC loads. A comprehensive list of the models included in VFlexP, detailing components like generators and converters, is provided in Figure A.2 and Table A.2, highlighting the modularity and flexibility of VFlexP's modelling framework.

A.3 Simulation of hybrid power systems and SSA in VFlexP

This section describes VFlexP capabilities to simulate and analyse hybrid power systems. VFlexP runs a power flow to initialise the state variables accurately, which is needed for non-linear time-domain simulations and SSA. With respect to SSA, VFlexP derives a linear approximation of the non-linear system included in the

Table A.2: Summary of elements included in VFlexP.

Element	**Implemented model**
Synchronous Generators	Eighth-Order model with Governor and AVR (Kundur, Balu, & Lauby, 1994) Second-Order model (Y. Li & Gu, 2024) Multi-pole model (Tabernero & Rouco, 2007)
Induction Generators	Conventional model (Kundur, Balu, & Lauby, 1994)
Synchronous Compensators	Conventional model (Kundur, Balu, & Lauby, 1994)
Doubly Fed Induction Generators	Conventional model (Rouco & Zamora, 2006)
AC Loads	Static Loads (Kundur, Balu, & Lauby, 1994) Dynamic Loads (Kundur, Balu, & Lauby, 1994) Induction Motors (Kundur, Balu, & Lauby, 1994)
AC Transformers	Conventional model (Kundur, Balu, & Lauby, 1994)
DC loads	Static Loads (Kundur, Balu, & Lauby, 1994) Dynamic Loads (Griñó, Ortega, Fridman, Zhang, & Mazenc, 2021)
Converters	Grid-forming converter (droop) (Bidram, Davoudi, & Lewis, 2014) GFr (Virtual Synchronous Machine) (D'Arco & Suul, 2013) Grid-following converters (Bidram, Davoudi, & Lewis, 2014) Grid-following interface converters (Bidram, Davoudi, & Lewis, 2014) Buck DC-DC converters (Y. Li & Gu, 2024)

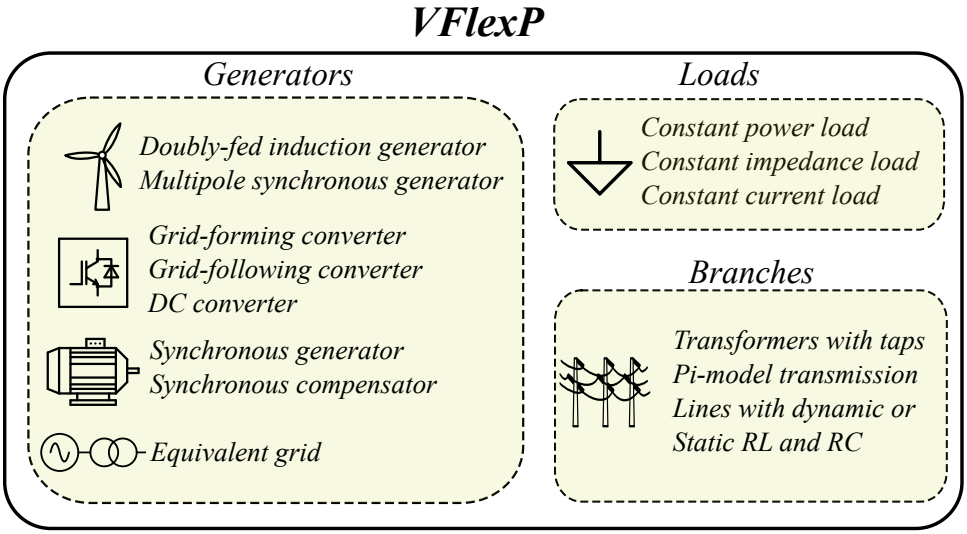

Figure A.2: Summary of elements included in VFlexP.

Simulink workspace, and it can carry out a comprehensive eigenvalue analysis of the resulting linear system. The tasks corresponding to these capacities are addressed in the following sections.

A.3.1 Powerflow and Initialisation

Before linearising a Simulink model, the target steady-state operation point must be calculated, i.e., the initial values of all the state variables of the system must be determined. This can be done directly with the original tools in MATLAB/Simulink (e.g., *findop*), but they are not very efficient when dealing with large dynamic systems. Alternatively, VFlexP uses the following strategy:

1. Grid currents and voltages are initialised by running a power-flow algorithm based on MATPOWER (Zimmerman et al., 2011), which is a well-known open-source MATLAB tool originally developed to be applied on AC power systems, only. This tool has been extended with the flexible universal branch model (FUBM) (Alvarez-Bustos et al., 2021) to seamlessly deal with hybrid AC/DC power systems. The power flow solution includes the values for voltage amplitude and angle, and active and reactive power injections of all generators at their bus of connection. However, it does not include the value of internal state variables, for example those associated with current or voltage controllers in electronic generators.

2. State variables not calculated by the initial PF run can be calculated automatically using a gradient-based optimisation in MATLAB for each one of

the blocks in the Simulink workspace. The results of the PF run are the restrictions to be satisfied by the optimisation process. In addition, for simple blocks, the equations to calculate the initial conditions can be calculated manually in advance and stored in the block for future use. The impedance value of constant-impedance loads is recalculated in this process to ensure that they consume the active and reactive power given by the PF solution.

A.3.2 Linearisation

For linearisation, VFlexP uses MATLAB function `linearize(mdl, io, op)`, where `mdl` is the name of the Simulink model, `io` is the set of inputs and outputs to consider in the linear model (previously set using `setlinio` function), and `op` is the operation point used for the linearisation. Considering that operating point, MATLAB calculates the input and state values for each block and requests its Jacobian. The models included in VFlexP mainly include Simulink basic blocks (*e.g.*, integrators, products, sums, switches, etc.). These blocks have a predefined Jacobian for linearisation. For other more complex blocks used, the Jacobian in the operating point is provided. With the Jacobian for all blocks, Simulink considers how the blocks are connected with each other to compute the complete linear model of the system. The final linear system obtained using this method is of the form:

$$\begin{cases} \dot{x} = \mathbf{A}x + \mathbf{B}u \\ y = \mathbf{C}x + \mathbf{D}u \end{cases} \tag{A.5}$$

where x is the system state column vector, u is the input vector, y is the output vector, and $\mathbf{A}$, $\mathbf{B}$, $\mathbf{C}$ and $\mathbf{D}$ are the system matrices.

A.3.3 Small signal analysis

The mode-in-state participation factors normalised as by Milano (2010) and Sauer and Pai (1998) (based on Pérez-Arriaga et al. (1982)) are used, as defined in Chapter 2.

The state relevance presented in Chapter 3 is included in this tool and its use is further demonstrated in this appendix.

The tool also includes eigenvalue sensitivities (as described in Chapter 2 and mode-shape calculations. For a given eigenvalue λ_i of matrix $\mathbf{A}$ in (A.5), the mode shapes are the complex numbers that form the right eigenvector corresponding to that eigenvalue (one complex number per state variable). Mode shapes illustrate the relative phase of mode oscillations which has application in power system stabiliser design and inter- and intra-area oscillation analysis.

A.3.4 Simulation of non-linear and linear models

VFlexP models each element of hybrid power systems using basic Simulink blocks such as sums, products, and integrators to define the differential equations. As a

result, it leverages all the capabilities of native Simulink. For example, variable-step solvers can be used. They are particularly useful when steady state is reached since the variables of a balanced three-phase power system remain constant in the d-q reference frame. Additionally, Simulink solvers for stiff differential equations can significantly speed up simulations, especially given the different time scales often involved in the system dynamics. Another important feature is that Simulink supports real-time simulation on some RT boxes available on the market, including OPAL-RT (OPAL-RT, 2024).

Linearised models are simulated using `lsim(linearised_system,u,t)` command of MATLAB, where `u` is the input to the system and `t` is the time vector for the simulation. Command `lsim` discretises the linear system with `c2d` function, using, by default, a zero-order hold and then calculates the response to the input.

A.4 Case studies using VFlexP

This section demonstrates the main features of VFlexP through case studies on small and large hybrid AC/DC power systems. The performance is compared with the Simplus Grid Tool (Y. Li & Gu, 2024), a recently presented open-source tool also based on MATLAB-Simulink. Four test systems are analysed, focusing on voltage and frequency responses, power delivery, and eigenvalue analysis. VFlexP's ability to handle non-linearities and SSA is demonstrated. The usefulness of the concept of state relevance for model-order reduction without compromising accuracy is also discussed.

A.4.1 Case study: small power systems

This section explores the application of VFlexP in three small power systems (see Figures. A.3, A.5 and A.7).

All the parameters for the systems shown in Figures A.3 and A.7 can be found in the examples in SimplusGT repository (Y. Li & Gu, 2024) but have also been included in A.6. For comparison, a 50-second dynamic simulation was carried out in all three small systems starting from an operating point determined by the load values shown in Figures A.3, A.5 and A.7. The load in each of the three systems was increased between 25 and 26.2 seconds. Simulation results for the two simulation tools applied to the three systems were recorded, and voltage, speed, active, and reactive power of the synchronous machine are shown in Figures A.4, A.6 and A.8. The blue line is the response obtained using SimplusGT, and the red dotted line is the one obtained with VFlexP.

The first test system (Figure A.3) includes a synchronous generator connected to a load. Figure A.4 shows the simulation results of this system. Simplus calculates the voltage behaviour of a synchronous machine with adequate accuracy in the dynamic simulation. However, the tool lacks an accurate procedure to compute the initial operating point of the dynamic simulation and an unnecessary initial

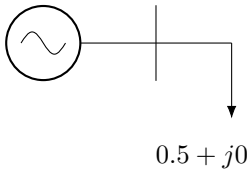

Figure A.3: Single-line diagram of a synchronous generator feeding a load

transient takes place. The voltage response on the machine using Simplus remains close to 1 pu during the simulation, which reflects good control and stability of the system. VFlexP accurately calculates the initial operating point and produces dynamic simulation results very close to those produced by Simplus without the unnecessary initial transient. The transient response, when the load changes, is very similar in the two simulation tools, even in those variables that show important oscillations (Notice the close response of the two tools in the zoomed windows in Figs A.4-(c) and (d)). Figure A.4 shows the location of five eigenvalues of the linear approximation of the system shown in Figure A.3. Simplus and VFlexP produce very similar results. However, both tools must add extra elements to include all the state variables of interest. For example, VFlexP adds a small shunt capacitor (i.e., 1×10^{-6} pu) at each of the buses so that bus voltages become state variables and, in this case, it adds a transmission line with a very small resistance (0.1×10^{-6} pu) between the generator and the load. These additional state variables produce additional eigenvalues in the linear approximation of the original system (see Table A.3 for a comparison of the eigenvalues calculated by the two tools). The additional eigenvalues produced by VFlexP can be spotted very easily due to their unreasonably large moduli. However, the extra eigenvalues produced by Simplus are unstable or very close to becoming unstable. Finally, Figure A.4-(f) shows the response of the system frequency for the non-linear simulation and its linear approximation using the proposed tool. The two curves agree closely.

In the second system (Figure A.5), data from the first system were reused, and a purely inductive transmission line with a reactance of 0.65 pu ($X_{12} = 0.65$ pu) was added. Simplus and VFlexP were compared in this setup. Again, a load change was introduced from 25 to 26.2 seconds, and the results are shown in Figure A.6. Figure A.6-(a), A.6-(c), and A.6-(d) highlight initialisation issues associated with Simplus. Meanwhile, Figure A.6 (e) presents some of the eigenvalues for the system in Figure A.5. In this case, some of the eigenvalues calculated with Simplus have positive real parts (Table A.4). This table also shows that Simplus employs 15 state variables, whereas the proposed tool uses only 11. An analysis of the simulation results in Figures A.6-(e) and A.6-(f) demonstrates that the proposed tool accurately models the system, confirming its local stability around the operating point. Figures A.6-(e) and A.6-(f) show that linearisation provides a good approximation of the nonlinear system in the vicinity of the operating point.

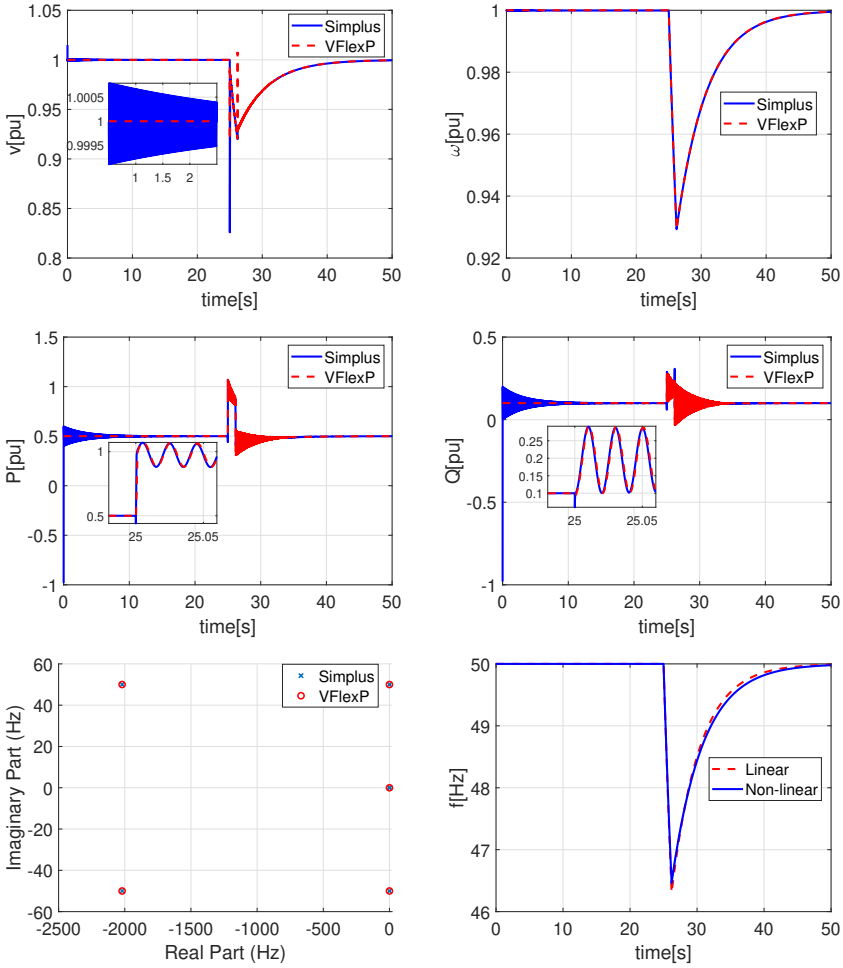

Figure A.4: (a) Bus-1 voltage, (b) Speed of the SG in pu, (c) Active power of the SG, (d) Reactive power of the SG, (e) eigenvalues of the system and (f) Comparison of the frequency response of non-linear and linearised system shown in Figure A.3.

Table A.3: Eigenvalues for the system shown in Figure A.3.

	Simplus		**VFlexP**	
	Re (λ)	Im (λ)	Re (λ)	Im (λ)
1	0.0000	0.0000	–	–
2	$-2.8e-09$	0.0000	–	–
3	$\mathbf{-0.0341}$	$\mathbf{0.0000}$	$\mathbf{-0.0340}$	$\mathbf{0.0000}$
4	$\mathbf{-0.0495}$	$\mathbf{-50.00}$	$\mathbf{-0.0487}$	$\mathbf{-49.99}$
5	$\mathbf{-0.0495}$	$\mathbf{50.00}$	$\mathbf{-0.0487}$	$\mathbf{-49.99}$
6	$\mathbf{-2019.9}$	$\mathbf{-50.00}$	$\mathbf{-2020.2}$	$\mathbf{-50.00}$
7	$\mathbf{-2019.9}$	$\mathbf{50.00}$	$\mathbf{-2020.2}$	$\mathbf{50.00}$
8	–	–	$-1e15$	0.0000
9	– –	–	$-1e15$	0.0000
10	–	–	$-1.2e07$	-49.96
11	–	–	$-1.2e07$	49.96

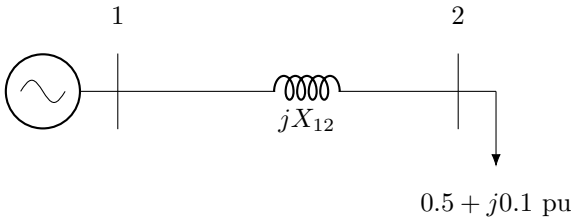

Figure A.5: Single-line diagram of a synchronous generator feeding a load through a transmission line.

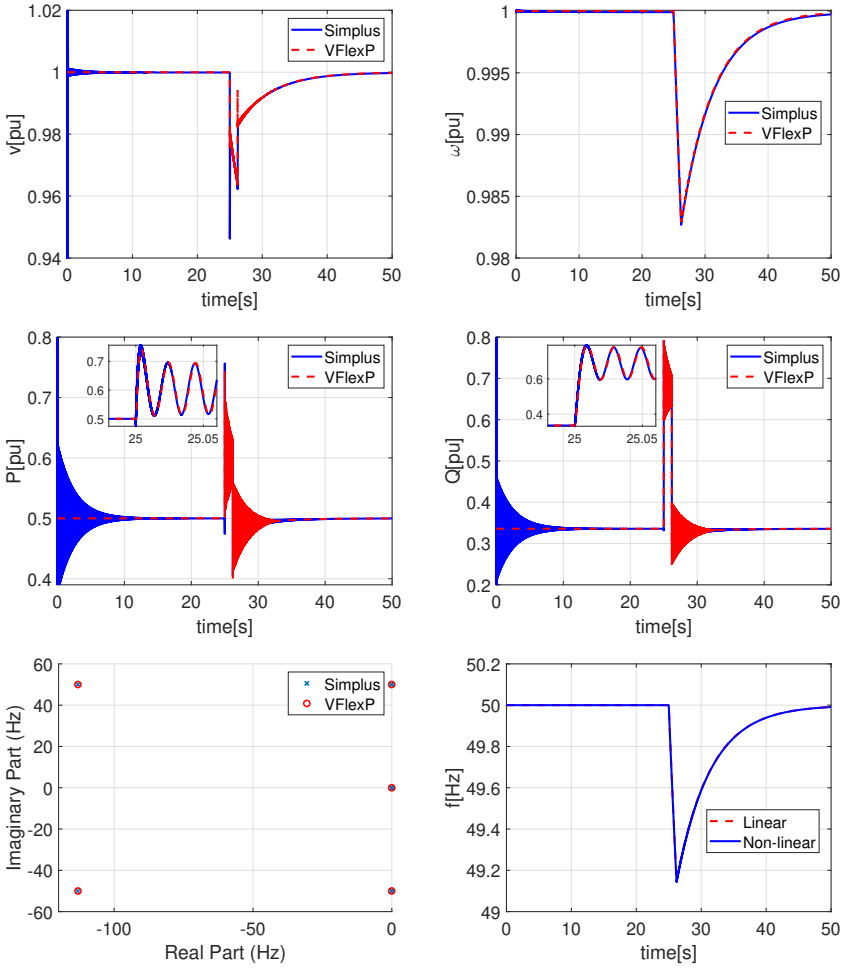

Figure A.6: (a) Bus-1 voltage, (b) Speed of the SG in pu, (c) Active power of the SG, (d) Reactive power of the SG, (e) eigenvalues of the system and (f) Comparison of the system (Figure A.5) frequency with non-linear and linearised models.

Table A.4: Eigenvalues for the system shown in Figure A.5.

	Simplus		**VFlexP**	
	Re (λ)	Im (λ)	Re (λ)	Im (λ)
1	0.0000	0.0000	–	–
2	$-2.0e-15$	-50.00	–	–
3	$-2.0e-15$	50.00	–	–
4	$2.9e-14$	-50.00	–	–
5	$2.9e-14$	50.00	$-3.5e07$	-50.00
6	$-5.3e-14$	-50.00	$-3.5e07$	50.00
7	$-5.3e-14$	50.00	$-3.3e01$	$-2.3e05$
8	$-9.8e-16$	0.0000	$-3.3e01$	$2.3e05$
9	$4.4e-06$	0.0000	$-3.3e01$	$-2.3e05$
10	$-4.9e-06$	0.0000	$-3.3e01$	$2.3e05$
11	**−0.0304**	**0.0000**	**−0.0304**	**0.0000**
12	**−0.0632**	**−50.00**	**−0.0632**	**−50.00**
13	**−0.0632**	**50.00**	**−0.0632**	**50.00**
14	**$-1.1e02$**	**−50.00**	**$-1.1e02$**	**−50.00**
15	**$-1.1e02$**	**50.00**	**$-1.1e02$**	**50.00**

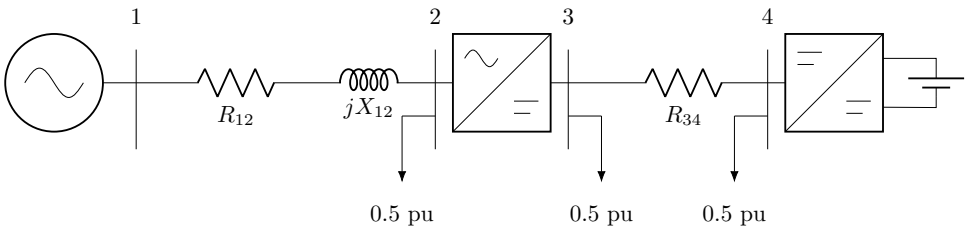

Figure A.7: Single-line diagram of the 4-bus hybrid AC-DC system presented by Zheng, Gao, Li, Zhu, and Gu (2024)

Table A.5: Computation time when Simplus and VFlexP simulate the systems shown in Figures A.3, A.5 and A.7.

Tool	Computation time $[s]$		
	SG	**Two Bus System**	**Hybrid System**
Simplus	33.625	36.843	103.84
VFlexP	12.312	15.953	11.687

Finally, the 4-bus hybrid AC/DC power system presented by Zheng, Gao, Li, Zhu, and Gu (2024) was also studied (see Figure A.7). A synchronous generator is connected to bus 1 (AC side), a buck converter is connected to bus 4 (DC side), and AC and DC sides are connected by a grid-following interface converter placed between buses 2 and 3 with a traditional droop control and PI voltage and current controllers in cascade, with a LCL output filter. The generator and the two electronic converters in Figure A.7 feed three active power loads. Figure A.8 shows the behaviour of this system when using Simplus and VFlexP. Due to the aforementioned comments regarding the number of eigenvalues, only the time responses to load variations at bus 2 were compared. Figures from A.8-(a) to A.8-(d) demonstrate the close agreement between the simulation results using Simplus and those using VFlexP. In addition, Figure A.8-(e) shows that the simulations of the non-linear system and its linear approximation carried out using VFlexP agree closely.

The computation times (CT) required for both tools to perform the dynamic simulations presented in Figures A.4, A.6 and A.8 are written in Table A.5. To ensure a fair comparison with VFlexP, Simplus was adjusted to use a variable integration step instead of its default fixed discrete time step. All simulations were performed on an Intel Core i7 PC with a 2.8 GHz processor. VFlexP consistently outperforms Simplus across all three systems in terms of computation time. The difference is most pronounced in the Hybrid System, where VFlexP requires only 11.687 seconds, compared to 103.84 seconds required by Simplus (i.e., a reduction of about 89%). Both tools take longer to simulate the hybrid system due to its intricate dynamics involving both AC and DC elements.

A.4.2 Case study: Large hybrid AC/DC power system

Exploring reduced order models for a large hybrid power system

To validate the performance of the proposed tool on large hybrid AC/DC power systems, the hybrid power system introduced by Chai, Zhang, Dou, Hao, and Zheng (2016) was implemented in the tool. Figure A.9 shows the schematic diagram of that power system, automatically generated by the tool, consisting of two AC areas connected through two DC grids by means of several DC/AC converters, controlled in grid-following mode in their AC interface. VFlexP includes

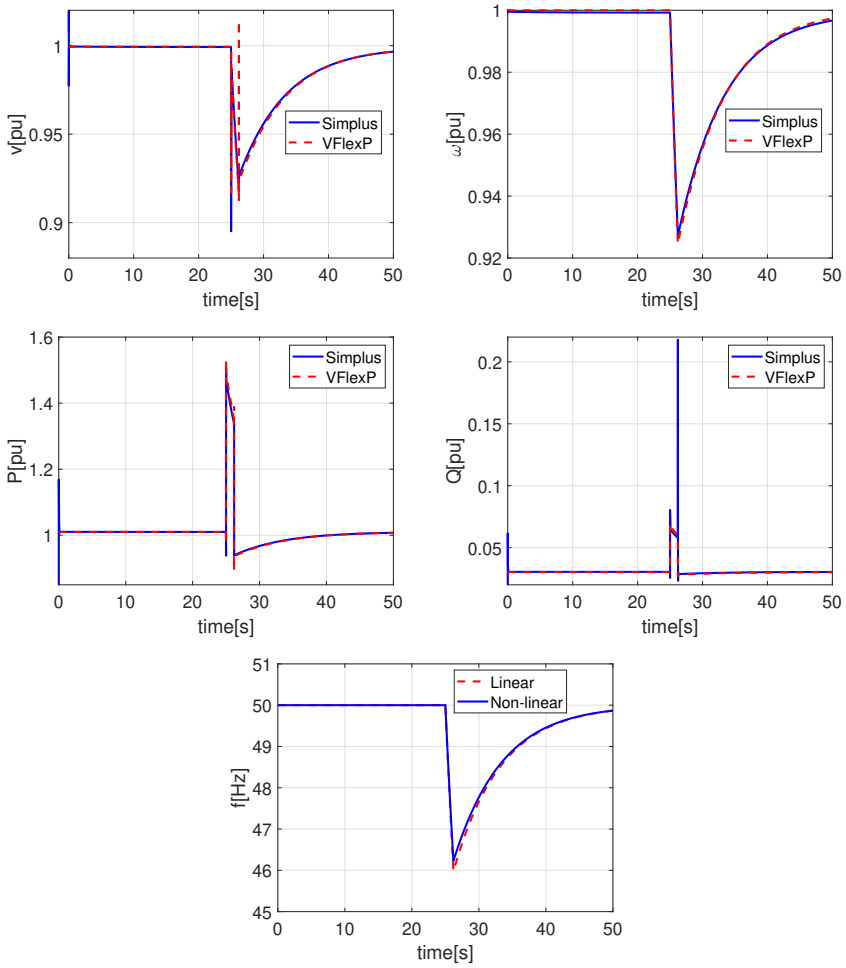

Figure A.8: (a) Bus-1 voltage, (b) Speed of the synchronous generator in pu, (c) Active power, (d) Reactive power and (e) Frequency in the non-linear and linearised simulations of the system in Figure A.7.

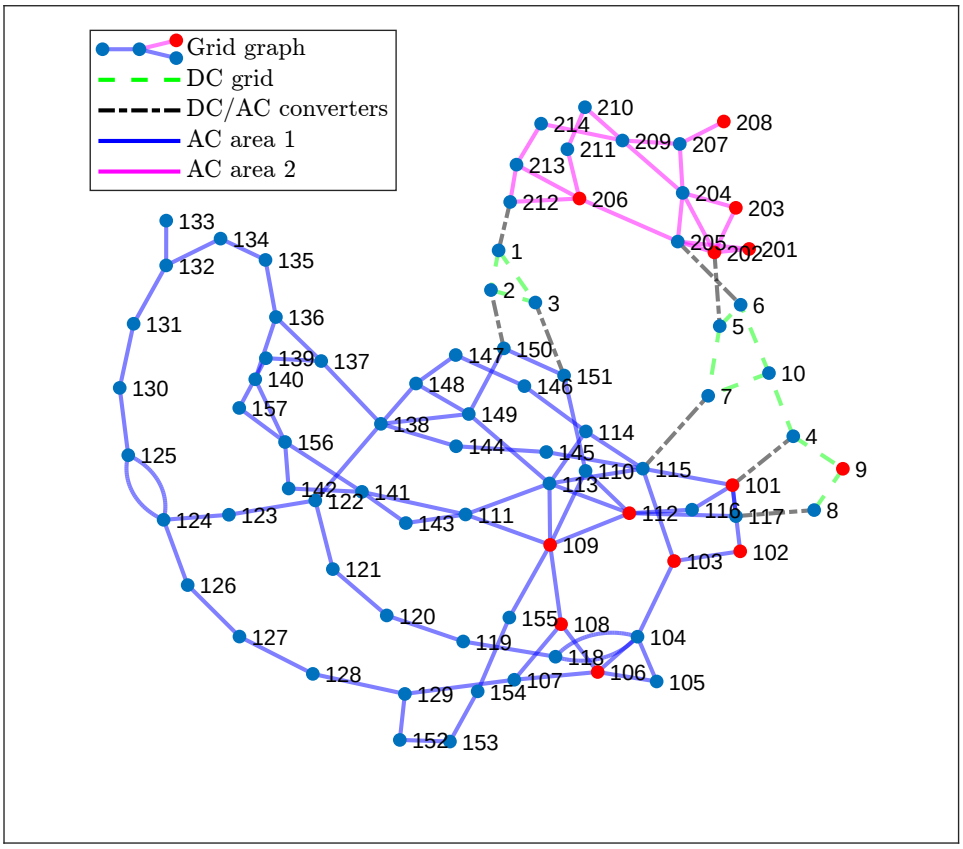

Figure A.9: Graph representing the grid used for the case study. Buses highlighted in red include generation.

as "datatips"[1] in this graph the values of active and reactive power generated by generation units and consumed by loads at every bus. These are results from the power flow calculation.

AC area 1 is the IEEE 57-bus system, and AC area 2 is the IEEE 14-bus system. Buses with generators are highlighted in red. All the static data of the test case were taken from Chai et al. (2016). The model and parameters for the generator included in bus 9 of the DC grid are the ones used for the DC generator in Zheng et al. (2024). All the generators on the AC grids are modelled as grid-forming converters with the traditional droop control and PI voltage and current controllers in cascade, with a LCL output filter. The details of the control structure of the converters can be found in Bidram et al. (2014). To illustrate the advantages of the vectorisation used in VFlexP, Figure A.10 shows one screenshot of the Simulink workspace containing

[1]Data tips are small text boxes that display information about individual data points.

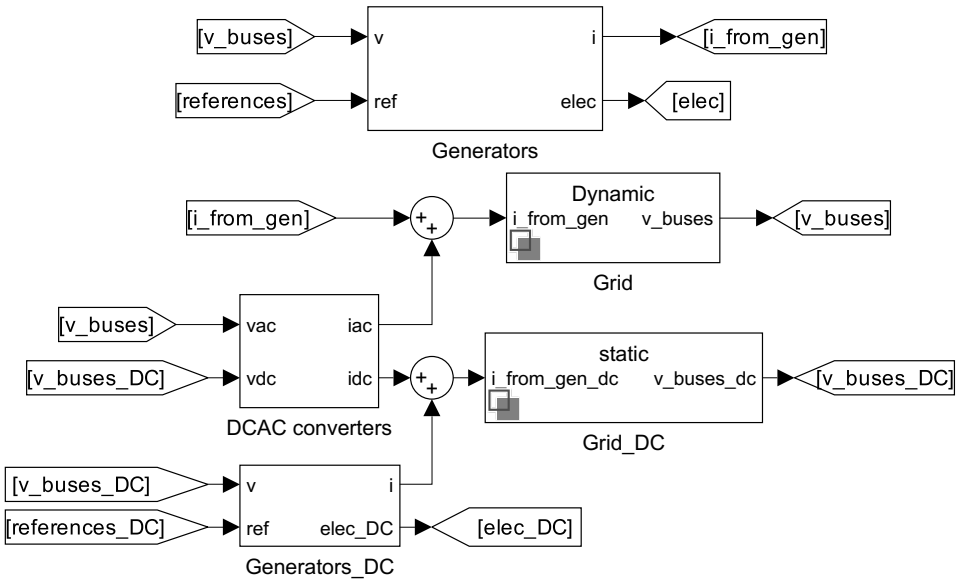

Figure A.10: Screenshot of the Simulink workspace for the hybrid system implemented in VFlexP.

the hybrid system implemented in VFlexP. The blocks used to implement the large hybrid system shown in Figure A.9 are the same as the ones used to implement the small hybrid system used in Figure A.7 (with the only difference that the synchronous generator block was replaced by the grid-forming block). Notice that, in the system of Figure A.9, the resulting vectors are larger because the system implemented is larger, but the number of Simulink blocks does not change.

The system was linearised in the operating point calculated by the initialisation of all variables from the results of the power-flow analysis given by Alvarez-Bustos et al. (2021) with the set points of Chai et al. (2016). Then, the state relevance of each state of the linear system in the system input-output response is calculated as described by Tomás-Martín et al. (2023) and grouped by type of element as shown in Figure A.11. The inputs chosen for the linear model are current injections on each AC bus, and the outputs are the frequencies of all grid-forming converters.

As shown in Figure A.11, the dynamics of all DC elements, load dynamics and some dynamics of the grid-forming converters (GFrs) have very little contribution to the input-output response of the linear system. However, some dynamics of the GFrs, branches and buses can not be neglected because they have a considerable contribution to the input-output response (*i.e.*, not negligible state relevance).

To show the usefulness of the state relevance measure, the following scenario is proposed: the system in this large case study is modified by changing the voltage controller of DG1.

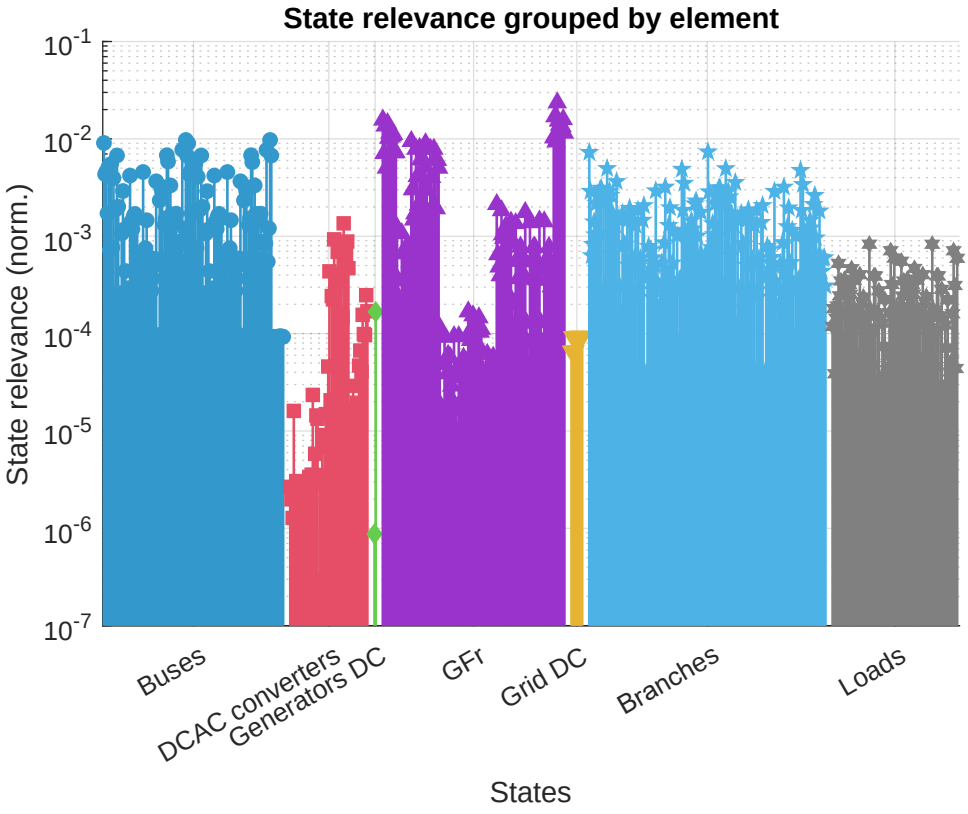

Figure A.11: State relevance of the linearised system, grouped by element. The state relevance is normalised to sum one and shown in a logarithmic scale for clarity.

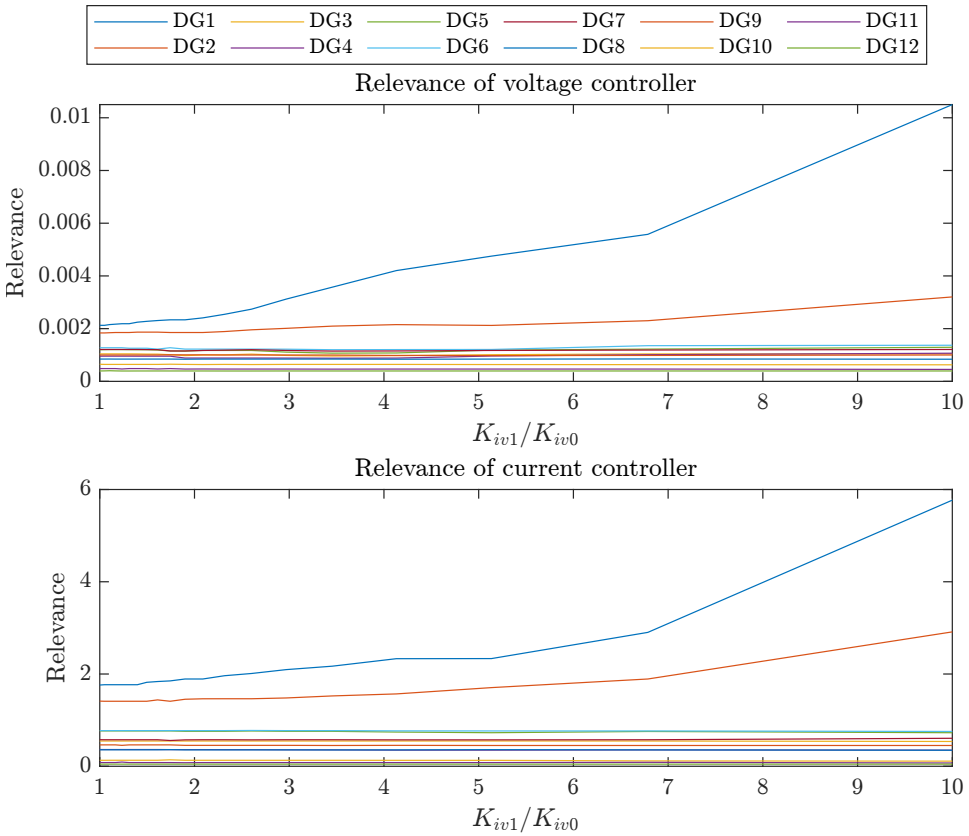

Figure A.12: Evolution of the state relevance of the voltage and current controllers for all converters of the system under study when varying the voltage controller of converter DG1. In K_{iv1}/K_{ivO}, K_{iv1} is the varying gain of DG1 and K_{ivO} is its initial value.

Figure A.12 shows the evolution of the state relevance of the voltage and current controllers for all converters of the system under study when varying the voltage controller of converter DG1. First, the voltage and current controllers of all grid-forming converters have the same parameters. Then, the integrator gain of the voltage controller of DG1 was increased from its initial value to 10 times its initial value. Meanwhile, the parameters of all other DGs were left unchanged.

Figure A.12 clearly shows that the state relevance of the states of the voltage and current controllers of DG1 increase with the integrator gain of the voltage controller of DG1. This result can be understood by considering that the varying control system is approaching instability. In addition, the state relevance of the states of the voltage and current controllers of DG2 also increase with the integrator gain of

the voltage controller of DG1. This is due to the fact that DG2 is close to DG1 in terms of electrical distance.

To further validate the state relevance analysis, the response of the complete non-linear system to a load change is compared with the response of several non-linear models with different levels of complexity reduction:

- VCC 1-12: Complete model.
- VCC 1-2: The dynamics of AC branches, loads and grid-forming converter voltage and current controls with state relevance below 0.0012 are neglected.
- VCC 1: The dynamics of AC branches, loads and grid-forming converter voltage and current controls with state relevance below 0.004 are neglected.
- No VCC: The dynamics of AC branches, loads and grid-forming converter voltage and current controls are neglected.

Figure A.13 shows the comparison of the complete and reduced models to a load increment in bus 10. The variable compared is the frequency of DG1 (grid-forming converter at bus 101).

Figure A.13 clearly shows that the frequency of DG1 has a lightly damped oscillation when the load change is applied. This oscillation is only properly captured when the dynamics of the states with relatively high relevance are not neglected. In any reduced-order model, the dynamics of the states with higher state relevance must be included.

An example of the use of the "state relevance" calculated by VFlexP

The connection of a grid-following converter at bus 101 has been explored with the use of the concept of "state relevance". The complete non-linear model of the power system can be used to study the performance of the control loops designed for a grid-following converter. However, this may be computationally expensive or even impractical in some cases. Instead, the use of reduced-order models of the power system based on the information given by the state relevance can be proposed. In this section, simulation results using a full-order linear approximation of the whole system in Figure A.9 at an operating point when bus 101 is perturbed by a grid-following converter will be compared with simulation results using several reduced-order models of the same power system. State relevance has been calculated by injecting a current perturbation at bus 101 and measuring the voltage response of the same bus.

Figure A.14 shows the comparison of the response of the frequency measured by the PLL of the grid-following converter to an increment of the active power injected by the grid-following converter placed at bus 101. It includes a comparison between the different linear models described below:

- Full-order approximation to the non-linear system: This is the complete linear model, using the exact block-by-block linearisation of MATLAB/Simulink.

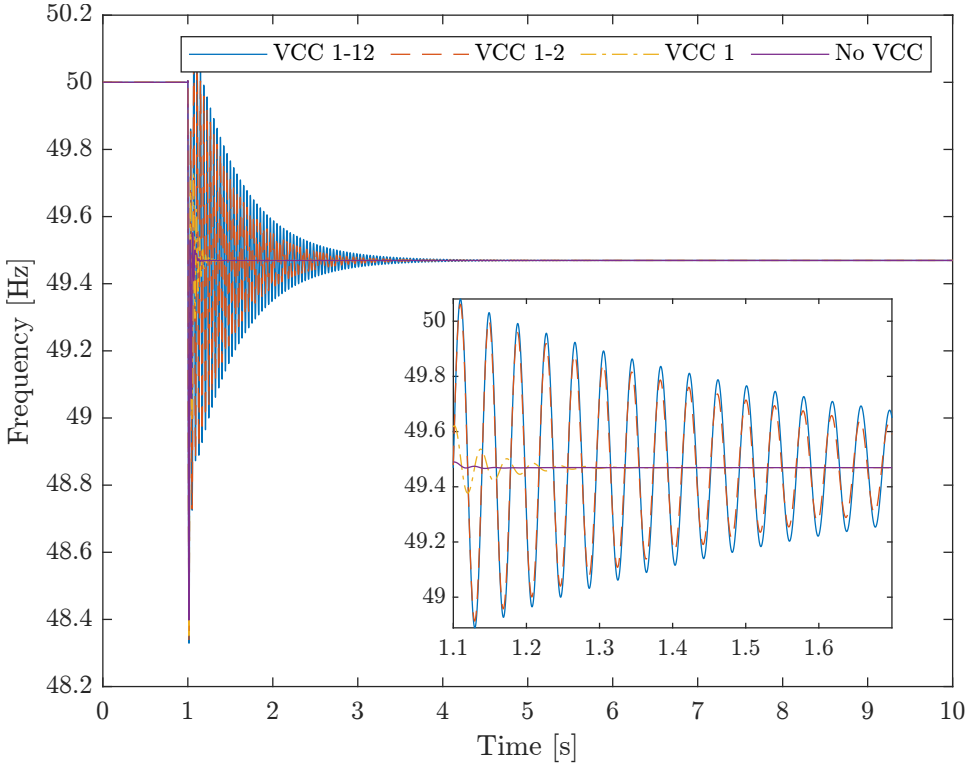

Figure A.13: Response of the frequency of DG1 to a load change. Comparison between the complete model and different reduced-order non-linear models.

- Reduced-order balanced realisation: A balanced realisation of the system was calculated following the procedure in Laub et al. (1987). Then, the dynamics of the states of the system contributing less to the input-output response were discarded by making their derivatives equal to 0. The states of the system contributing less to the input-output response can be easily identified in this transformation. However, those states are linear combinations of the states of the original system and no longer have a physical meaning.

- Reduced diagonal: The states of the system are transformed with the eigenvectors of the state matrix of the full-order system to have a complex diagonal state matrix with the system eigenvalues on the diagonal. Then, the dynamics of the states of the system contributing less to the input-output response are discarded by making their derivatives equal to 0. The states of the system contributing less to the input-output response are the ones that have large participations from the eigenvalues contributing less to the input-output response. As in the "reduced balanced", the states of the transformed system no longer have the same physical meaning as in the original system.

- Truncated original: The state matrix of the full-order linear system was split into relevant and non-relevant states, and only the piece corresponding to the relevant states was taken. In this approach, the steady-state value of the response of the full-order system is not matched, but the states of the reduced-order system retain their physical meaning.

A.5 Conclusion

This appendix presented VFlexP, a MATLAB/Simulink-based tool for simulation and analysis of hybrid AC/DC power systems. It includes steady-state analysis, non-linear electromagnetic simulation in a d-q synchronously-rotating reference frame, accurate linearisation of the non-linear dynamic model, rich eigenvalue analysis of the linear system, and a tool to assess the relevance of state-variable dynamics in an input-output representation of the power system. This last feature is unique, to the best of the author's knowledge, and can be used to investigate reduced-order models for further studies. System data can be introduced in a spreadsheet compatible with MATPOWER, and the user interface of VFlexP makes it possible to make an intuitive selection of the complexity with which each system element is to be represented. All elements of the same type with the same level of detail can be included in a single block in Simulink workspace, thanks to the vectorised formulation used. This provides a simple and clear view of even mid-to-large power systems.

The capabilities of VFlexP have been compared with those of a recently published tool, namely, Simplus. The former achieves a more accurate initialisation, which is very useful to avoid unnecessary initial transients when simulating and

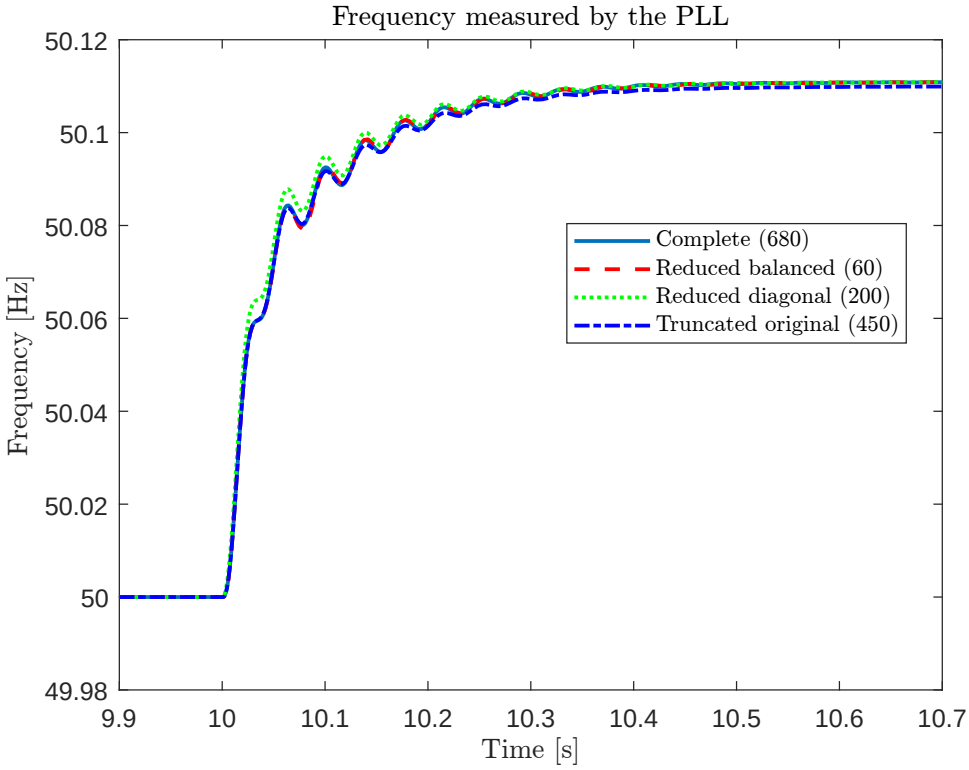

Figure A.14: Response of the frequency measured by the PLL of the grid-following converter to an increment of the active power injected by the grid-following converter. Comparison between the complete model and different reduced-order linear models. The number of states of each linear system is shown in brackets.

calculating the operating point for linearisation. In addition, the results of the linearisation process of the former are also more explicable than those of the latter.

Although VFlexP already shows useful features and efficient simulation to address many challenges in modern power systems with a rapidly increasing contribution of electronic power converters in the generation mix, the tool will be extended to address, for example, unbalanced systems as described by Yague, García-Cerrada, and Farré (2023).

A.6 Test System Parameters

The parameters for the systems depicted in Figures A.3 and A.7 are provided in Tables A.6 and A.7, respectively.

Table A.6: Parameters for the system shown in Figure A.3, which can be found in Y. Li and Gu (2024).

Synchronous Generator			
H	3.500 s	L_{m_d}	0.04 pu
D	1.00 pu	L_{m_q}	0.04 pu
f	50.0 Hz	R_f	0.01 pu
D	1.00 pu	L_f	0.01 pu
R_s	0.01 pu	L_s	0.05 pu
Load			
P_d	0.50 pu	Q_d	0.10 pu

A.7 Electronic converter modelling

The control parameters used for grid-forming converters are shown in Table A.8.

All lines were modelled with a Π block, and all loads were modelled as series RL with constant impedance consuming the active and reactive power calculated by the power flow, with the bus voltage also calculated by the power flow solution. The DC/AC interface converters are controlled as grid-following converters, tracking the voltage and angle at their point of connection by means of a phase-locked loop (PLL), with a PI current control loop and a L output filter. The details of the control structure of the converters can be found in Bidram et al. (2014). Converter losses were included as in Alvarez-Bustos et al. (2021) and Chai et al. (2016) as a function of the AC output active power:

$$P_{\text{loss},i} = \alpha_i + \beta_i P_i^{AC} + \gamma_i (P_i^{AC})^2 \tag{A.6}$$

Table A.7: Parameters for the system depicted in Figure A.7, which can be found in Y. Li and Gu (2024).

Synchronous Generator			
H	3.500 s	L_{m_d}	0.04 pu
D	1.00 pu	L_{m_q}	0.04 pu
f	50.0 Hz	R_f	0.01 pu
D	1.00 pu	L_f	0.01 pu
R_s	0.01 pu	L_s	0.05 pu
Load			
P_1	0.50 pu	P_2	0.50 pu
P_3	0.50 pu		
Branches			
R_{12}	0.01 pu	X_{12}	0.03 pu
R_{34}	0.01 pu		
Buck Converter			
R	0.01 pu	L	0.00016 pu
K_P	0.6	K_I	565
Interface Converter			
R_f	0.0001 pu	L_f	0.15 pu
K_{PC}	1	K_{IC}	10
$K_{P,PLL}$	1	$K_{I,PLL}$	20
α	0	β	0
γ	0		
$K_{P,DC}$	0.5	$K_{I,DC}$	10

Table A.8: Parameters used for the simulation of the large hybrid power system. Control parameters are valid for per-unit variables. The base power is $Sb = 100$ MVA, and the base voltage for every bus can be found in Chai, Zhang, Dou, Hao, and Zheng (2016).

Grid-forming converters			
m_P	0.0159 pu	n_Q	0.0083 pu
R_f	0.001 pu	L_f	0.01 pu
C_f	1 pu	R_{cf}	1000 pu
R_c	0.001 pu	L_c	0.01 pu
K_{PV}	0.028	K_{IV}	0.28
K_{PC}	34.72	K_{IC}	347.2
F_i	1	LPF_{const}	0.01 s
R_{VI}	0	L_{VI}	0
Interface converters			
$R_{f_{1,4}}$	0.051 pu	$L_{f_{1,4}}$	0.033 pu
$R_{f_{2,3,5,6,7,8}}$	0.0765 pu	$L_{f_{2,3,5,6,7,8}}$	0.05 pu
K_{PC}	1	K_{IC}	10
$K_{P,PLL}$	1	$K_{I,PLL}$	10
α	0.0001	β	0.005
γ	0.05		
$K_{P,DC_{1,4}}$	0.5	$K_{I,DC_{1,4}}$	10

where $P_{loss,i}$ is the active power loss of the converter in per unit, P_i^{AC} is its active power measured on the AC side in per unit, and α_i, β_i, and γ_i are constant values used in all converters:

$$\alpha_i = 0.0001 \quad \beta_i = 0.005 \quad \gamma_i = 0.05 \tag{A.7}$$

Grid-following converters orientate their d-q injected current with respect to the voltage at their AC point of connection and adjust their injected current to meet specific active and reactive power requirements. This alignment is achieved using a phase-locked loop.

The set points for the d- and q-axis currents are calculated using the voltage values on the d and q axes, v_{odi} and v_{oqi}, measured at the connection point, along with the active and reactive power set points P_i^{ref} and Q_i^{ref}:

$$i_{ldi}^* = \frac{v_{odi}P_i^{\text{ref}} + v_{oqi}Q_i^{\text{ref}}}{v_{odi}^2 + v_{oqi}^2} \tag{A.8}$$

$$i_{lqi}^* = \frac{v_{oqi}P_i^{\text{ref}} - v_{odi}Q_i^{\text{ref}}}{v_{odi}^2 + v_{oqi}^2} \tag{A.9}$$

The active and reactive power set points P_i^{ref} and Q_i^{ref} for INV(2,3,5-8), as well as the reactive power set points for INV1 and INV4, were maintained constant with the values derived from the power flow result.

For INV1 and INV4, the active power set points were adjusted to maintain their DC voltage using a PI controller:

$$P_2^{\text{ref}}(s) = (v_{DC,2} - v_{DC,2}^{\text{ref}})\left(K_{P,DC,2} + \frac{K_{I,DC,2}}{s}\right) \tag{A.10}$$

This appendix includes a description of the method used for the reduction of the dynamics of non-relevant state variables in the linear models used in this thesis.

B Elimination of dynamics for model order reduction

B.1 Reducing the number of states in linear models

Once the relevant states are known, one can start with the model reduction.

To complete the model reduction, the system states are divided into r relevant states ($\dot{\mathbf{x}}_r$) and m less relevant states ($\dot{\mathbf{x}}_{lr}$):

$$\begin{bmatrix} \dot{\mathbf{x}}_r \\ \dot{\mathbf{x}}_{lr} \end{bmatrix} = \begin{bmatrix} \mathbf{A}_{11}^{r\times r} & \mathbf{A}_{12}^{r\times m} \\ \mathbf{A}_{21}^{m\times r} & \mathbf{A}_{22}^{m\times m} \end{bmatrix} \cdot \begin{bmatrix} \mathbf{x}_r \\ \mathbf{x}_{lr} \end{bmatrix} \tag{B.1}$$

Pérez-Arriaga et al. (1982) divide the system into relevant and less relevant dynamics (see Figure B.1).

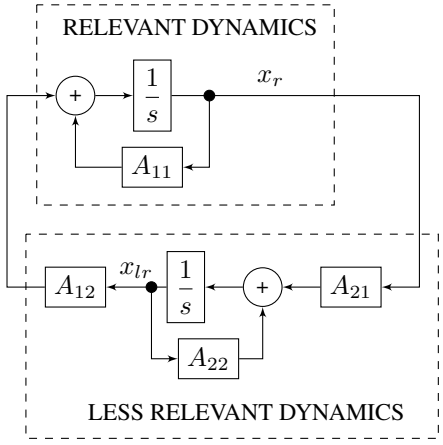

Figure B.1: Relevant and less relevant dynamics. Adapted from Verghese, Pérez-Arriaga, and Schweppe (1982)

The simplest model reduction approach is to completely neglect the $\mathbf{A}$ matrix rows and columns corresponding to non-relevant states:

$$\begin{bmatrix} \dot{\mathbf{x}}_r \\ \dot{\mathbf{x}}_{lr} \end{bmatrix} = \begin{bmatrix} \mathbf{A}_{11}^{r\times r} & \mathbf{0}^{r\times m} \\ \mathbf{0}^{m\times r} & \mathbf{0}^{m\times m} \end{bmatrix} \cdot \begin{bmatrix} \mathbf{x}_r \\ \mathbf{x}_{lr} \end{bmatrix} \tag{B.2}$$

where $\mathbf{x}_{lr}$ are completely forgotten.

However, most approaches consider the less relevant states with no dynamics (they are very fast and reach steady state immediately) but keep track of them in the system model. Then, if a general linear system has the matrix form:

$$\begin{cases} \begin{bmatrix} \dot{\mathbf{x}}_r \\ \dot{\mathbf{x}}_{lr} \end{bmatrix} = \begin{bmatrix} \mathbf{A}_{11} & \mathbf{A}_{12} \\ \mathbf{A}_{21} & \mathbf{A}_{22} \end{bmatrix} \begin{bmatrix} \mathbf{x}_r \\ \mathbf{x}_{lr} \end{bmatrix} + \begin{bmatrix} \mathbf{B}_1 \\ \mathbf{B}_2 \end{bmatrix} \mathbf{u} \\ \\ y = \begin{bmatrix} \mathbf{C}_1 & \mathbf{C}_2 \end{bmatrix} \begin{bmatrix} \mathbf{x}_r \\ \mathbf{x}_{lr} \end{bmatrix} + \mathbf{D} \cdot \mathbf{u} \end{cases} \tag{B.3}$$

and the dynamics of $\mathbf{x}_{lr}$ are neglected (i.e., $d\mathbf{x}_{lr}/dt = 0$):

$$\begin{cases} \dot{\mathbf{x}}_r = \mathbf{A}_{11} \cdot \mathbf{x}_r + \mathbf{A}_{12} \cdot \mathbf{x}_{lr} \\ 0 = \mathbf{A}_{21} \cdot \mathbf{x}_r + \mathbf{A}_{22} \cdot \mathbf{x}_{lr} \end{cases} \tag{B.4}$$

Taking $\mathbf{x}_{lr}$ from the second equation in (B.4) to the first one:

$$\dot{\mathbf{x}}_r = \underbrace{\left(\mathbf{A}_{11} - \mathbf{A}_{12} \cdot \mathbf{A}_{22}^{-1} \cdot \mathbf{A}_{21}\right)}_{\mathbf{A}_{red}} \cdot \mathbf{x}_r \tag{B.5}$$

and the reduced-order model of the the system becomes:

$$\begin{cases} \dot{\mathbf{x}}_r = \left[\mathbf{A}_{11} - \mathbf{A}_{12}\mathbf{A}_{22}^{-1}\mathbf{A}_{21}\right] \mathbf{x}_r + \left[\mathbf{B}_1 - \mathbf{A}_{12}\mathbf{A}_{22}^{-1}\mathbf{B}_2\right] \mathbf{u} \\ \\ y = \left[\mathbf{C}_1 - \mathbf{C}_2\mathbf{A}_{22}^{-1}\mathbf{A}_{21}\right] \mathbf{x}_r + \left[\mathbf{D} - \mathbf{C}_2\mathbf{A}_{22}^{-1}\mathbf{B}_2\right] \mathbf{u} \end{cases} \tag{B.6}$$

B.2 Reducing the number of states in the nonlinear models used

Electrical elements with no dynamics

The differential equations of a balanced inductor with an inductance value L and a series resistance R in a $d-q$ reference frame which rotates with a variable angular speed $\omega(t)$ are (Qoria et al., 2018):

$$\begin{cases} v_d(t) = L\dfrac{di_d(t)}{dt} - \omega(t)Li_q(t) + Ri_d(t) \\ \\ v_q(t) = L\dfrac{di_q(t)}{dt} + \omega(t)Li_d(t) + Ri_q(t) \end{cases} \tag{B.7}$$

Notice that d and q components of electrical variables can be gathered together in a complex number to have a compact expression:

$$\mathbf{v}(t) = L\frac{d\mathbf{i}(t)}{dt} + j\omega(t)L\mathbf{i}(t) + R\mathbf{i}(t) \tag{B.8}$$

where $\mathbf{v}(t) = v_d(t) + jv_q(t)$ is the instantaneous voltage difference between the inductor terminals, and $\mathbf{i}(t) = i_d(t) + ji_q(t)$ is the instantaneous current through the inductor. The term $j\omega(t)L\mathbf{i}$ calculates the cross-coupling between the d and q components of the inductor differential equations.

If the inductor dynamics are very fast, currents quickly reach their steady-state value (where $d\mathbf{i}(t)/dt = 0$) and can be calculated from the applied voltage as the following complex number:

$$\mathbf{i}(t) = \frac{\mathbf{v}(t)}{j\omega(t)L + R} \tag{B.9}$$

where $j\omega(t)L + R$ is not a typical frequency-dependent impedance but the operator that relates instantaneous $d-q$ voltage components with instantaneous $d-q$ current components in a reference frame that rotates with an angular speed equal to $\omega(t)$.

Similarly, $d-$ and $q-$axis differential equations for a balanced capacitor of capacitance C and a parallel resistance R can be obtained, respectively, from the real and imaginary parts of :

$$\mathbf{i}(t) = C\frac{d\mathbf{v}(t)}{dt} + j\omega(t)C\mathbf{v}(t) + \frac{\mathbf{v}(t)}{R} \tag{B.10}$$

where $\mathbf{v}(t) = v_d(t)+jv_q(t)$ is the voltage difference between the capacitor terminals, and $\mathbf{i}(t) = i_d(t) + ji_q(t)$ is the total current through the capacitor.

If the capacitor dynamics are very fast, the voltage will quickly reach its steady state value (where $d\mathbf{v}(t)/dt = 0$), yielding:

$$\mathbf{v}(t) = \frac{\mathbf{i}(t)}{j\omega(t)C + 1/R} \tag{B.11}$$

where $j\omega(t)C + 1/R$ is not a typical frequency-dependent admittance, either, but allows the calculation of the $d-$ and $q-$axis instantaneous voltage components immediately after the instantaneous current components through the capacitor are known.

Notice that d and q components of all balanced electrical variables will have a constant value in steady state if and only if $\omega(t)$ is eventually equal to the power system frequency.

Voltage and current controllers

If current-controller dynamics are not relevant, but the voltage-controller dynamics are relevant, the model of a grid-forming converter (GFr) can be simplified by assuming that the converter output currents follow their set points (*) instantaneously (see Figure C.2 in Appendix C for details in the control structure used for GFrs):

$$i^*_{ldi} = i_{ldi} \;\; \& \;\; i^*_{lqi} = i_{lqi} \tag{B.12}$$

Similarly, if the dynamics of the voltage controllers are not relevant, the model of a GFr can be simplified further as:

$$v^*_{odi} = v_{odi} \;\; \& \;\; v^*_{oqi} = v_{oqi} \tag{B.13}$$

where the output voltages ($d-q$ components) reach their set points (*) immediately.

Primary control

If the dynamics of the low-pass filters of the active- and reactive-power measurements are not found to be relevant, those filters can be omitted.

This appendix includes a description of the largest case power system used in this thesis, a modified version of the IEEE 69 bus test system.

C IEEE 69 BUS TEST SYSTEM

This appendix includes a description of the largest case power system used in this thesis, a modified version of the IEEE 69 bus test system described by Baran and Wu (1989). The modified version is shown in Figure C.1. It is a radial distribution system composed of 69 buses and 68 branches. The total system load is 3.802 MW and 2.694 MVAr. Grid-forming converters (GFrs) DGs 1-7 are connected at buses 1, 11, 21, 31, 41, 51 and 61, respectively. The bases and parameters used for the test system and grid-forming voltage-source converters (GFr-VSCs) are included in Table C.1. Figure C.2 shows the detailed control diagram used for GFr-VSCs in this test system, as explained in Chapter 2. The communication graph used for this test case study, unless otherwise stated, is shown in Figure C.3. The default constant communication delay between converters is set to 10 ms. The delay is modelled using a third-order Padé approximation in linearised models.

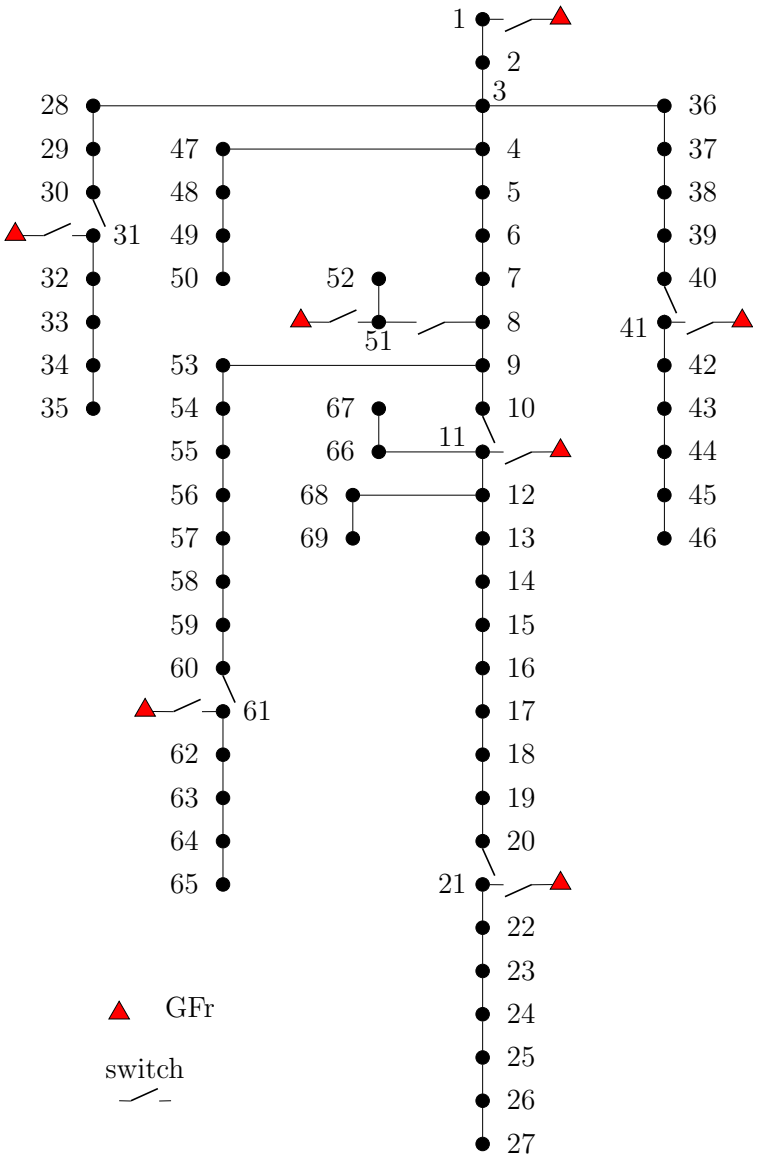

Figure C.1: One-phase diagram of the modified IEEE 69 bus test system used as the case study. "GFr" stands for grid-forming converter. Every grid-forming converter includes one controllable switch to connect to its PCC.

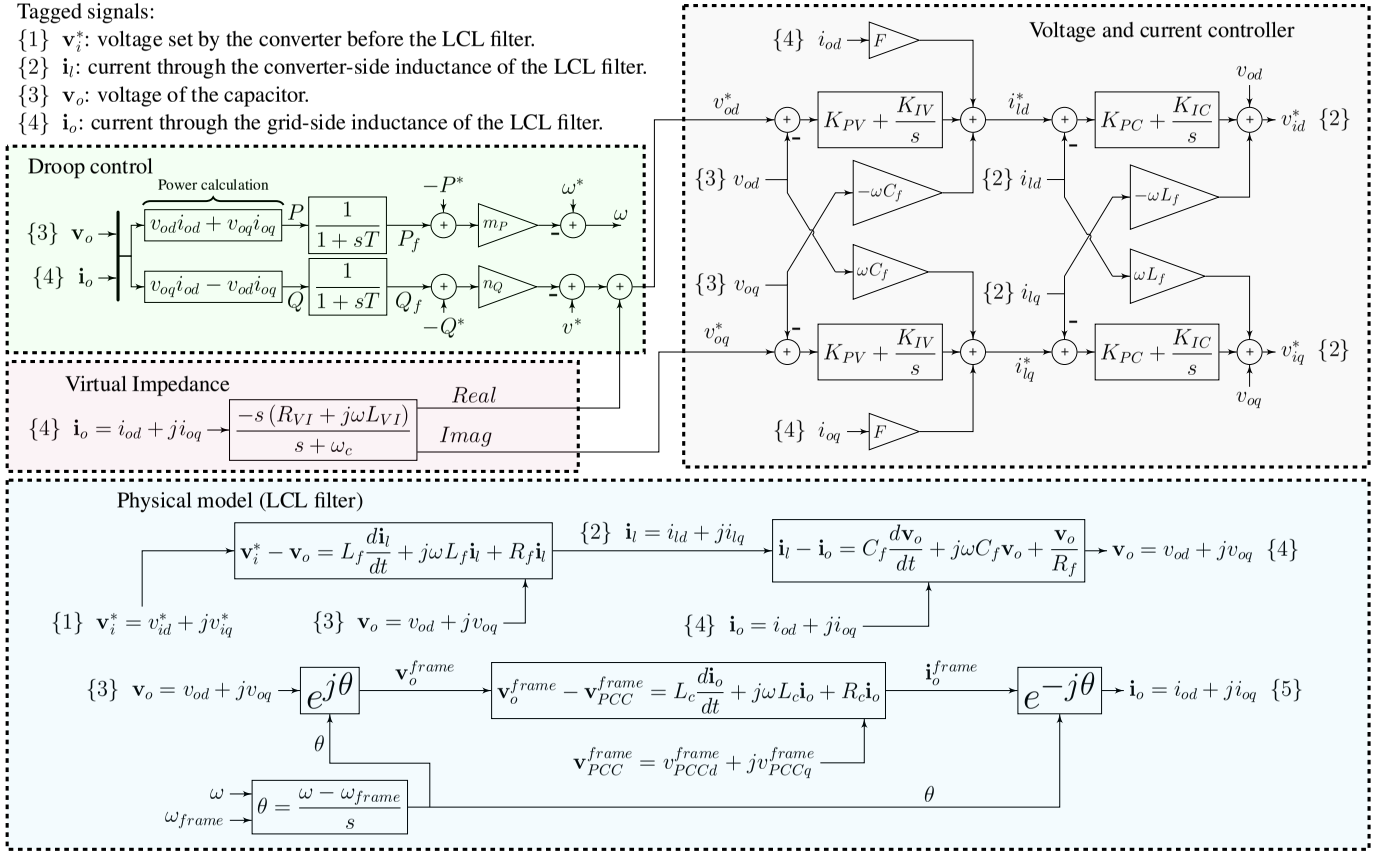

Figure C.2: Model of a grid-forming converter

Table C.1: Parameters used for the simulation of the modified IEEE 69 bus test system.

GFr			
m_P	$1 \cdot 10^{-7}$ rad/s·W	n_Q	$1 \cdot 10^{-4}$ V/VAr
R_f	0.048 Ω	L_f	1.5 mH
C_f	66.32 μF	R_{cf}	48 $k\Omega$
R_c	0.048 Ω	L_c	1.5 mH
K_{PV}	0.02	K_{IV}	0.2
K_{PC}	50	K_{IC}	500
F_i	1	LPF_{const}	0.01 s
Sec. control parameters and bases			
c_f	1	c_v	1
f_{base}	50 Hz	S_{base}	3 MVA
delay (T_d)	0 s	$V_{nom} = V_{base}$	12.6 kV
β	0	B	1
$g_1 = 1$	$g_i = 0 \; \forall \; i \neq 1$	$a_{ij} = 1 \; \forall \; i \neq 1, j = i - 1$	
ω_{ref}	1 pu	v_{ref}	1 pu
Initial operation point ($i \in [1 - 7]$)			
P_i	532.54 kW	Q_i	374.82 kVAr

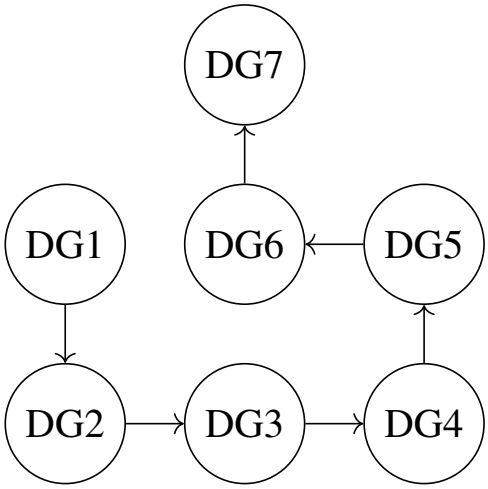

Figure C.3: Communication graph used for the modified IEEE 69 bus test system used as the case study.

Table C.2: IEEE 69-bus system data (Baran & Wu, 1989). Loads connected at "to" node. DGs connected at "from" node.

from	to	R (Ω)	X (Ω)	P (kW)	Q (kVAr)	DGs
1	2	0.0005	0.0012	0	0	INV1
2	3	0.0005	0.0012	0	0	
3	4	0.0015	0.0036	0	0	
4	5	0.0251	0.0294	0	0	
5	6	0.366	0.1864	2.6	2.2	
6	7	0.3811	0.1941	40.4	30	
7	8	0.0922	0.047	75	54	
8	9	0.0493	0.0251	30	22	
9	10	0.819	0.2707	28	19	
10	11	0.1872	0.0619	145	104	
11	12	0.7114	0.2351	145	104	INV2
12	13	1.03	0.34	8	5.0	
13	14	1.044	0.345	8	5.5	
14	15	1.058	0.3496	0	0	
15	16	0.1966	0.065	45.5	30	
16	17	0.3744	0.1238	60	35	
17	18	0.0047	0.0016	60	35	
18	19	0.3276	0.1083	0	0	
19	20	0.2106	0.0696	1	0.6	
20	21	0.3416	0.1129	114	81	
21	22	0.014	0.0046	5.0	3.5	INV3
22	23	0.1591	0.0526	0	0	
23	24	0.3463	0.1145	28	20	
24	25	0.7488	0.2475	0	0	
25	26	0.3089	0.1021	14	10	
26	27	0.1732	0.0572	14	10	
3	28	0.0044	0.0108	26	18.6	
28	29	0.064	0.1565	26	18.6	
29	30	0.3978	0.1315	0	0	
30	31	0.0702	0.0232	0	0	
31	32	0.351	0.116	0	0	INV4
32	33	0.839	0.2816	14	10	
33	34	1.708	0.5646	19.5	14	
34	35	1.474	0.4873	6	4	
3	36	0.0044	0.0108	26	18.55	
36	37	0.0640	0.1565	26	18.55	
37	38	0.1053	0.1230	0.0	0.0	
38	39	0.0304	0.0355	24.0	17.0	
39	40	0.0018	0.0021	24.0	17.0	
40	41	0.7283	0.8509	1.2	1.0	
41	42	0.310	0.3623	0.00	0.0	INV5
42	43	0.041	0.0478	6.0	4	
43	44	0.0092	0.0116	0	0.0	
44	45	0.1089	0.1373	39	26	
45	46	0.00	0.0012	39	26	
4	47	0.0034	0.008	0	0	
47	48	0.0851	0.2083	79	56.4	
48	49	0.2898	0.7091	384.7	274.5	
49	50	0.0822	0.2011	384.7	274.5	
8	51	0.0928	0.0473	40.5	28.3	
51	52	0.332	0.1114	3.6	2.7	INV6
9	53	0.1740	0.0886	4.35	3.5	
53	54	0.203	0.1034	26.4	19	
54	55	0.2842	0.1447	24	17.2	
55	56	0.2813	0.1433	0	0	
56	57	1.5900	0.5337	0	0	
57	58	0.7837	0.2630	0	0	
58	59	0.3042	0.1006	100	72	
59	60	0.386	0.1172	0	0	
60	61	0.5075	0.259	1244	888	
61	62	0.0974	0.0496	32	23	INV7
62	63	0.1450	0.0738	0	0	
63	64	0.7105	0.3619	227	162	
64	65	1.04	0.5302	59	42	
11	66	0.201	0.0611	18	13	
66	67	0.0047	0.0014	18	13	
12	68	0.7394	0.2444	28	20	
68	69	0.0047	0.0016	28	20	